

CRPP

CENTRE DE RECHERCHES EN PHYSIQUE DES PLASMAS
FACULTÉ DES SCIENCES DE BASE
ASSOCIATION EURATOM - CONFÉDÉRATION SUISSE



ÉCOLE POLYTECHNIQUE
FÉDÉRALE DE LAUSANNE

ANNUAL REPORT

2007

Table of content

FOREWORD

1 INTRODUCTION	1
1.1 THE INTERNATIONAL SITUATION	1
1.2 THE CRPP	1
1. INTRODUCTION	3
1.1 LA SITUATION INTERNATIONALE	3
1.2 LE CRPP	3
1 EINLEITUNG	5
1.1 DIE INTERNATIONALE LAGE IN DER FUSIONSFORSCHUNG	5
1.2 DAS CRPP	5
1. INTRODUZIONE	7
1.1 LA SITUAZIONE INTERNAZIONALE	7
1.2 IL CRPP	7
2 RESEARCH ACHIEVEMENTS OF THE CRPP IN 2007	9
2.1 THE TCV TOKAMAK	9
2.1.1 <i>Scenarios with internal transport barriers</i>	9
2.1.2 <i>Plasma edge characterisation and modelling</i>	13
2.1.3 <i>H-mode physics</i>	16
2.1.4 <i>Plasma rotation</i>	16
2.1.5 <i>Heat and particle transport in TCV</i>	19
2.1.6 <i>Physics of ECH, ECCD and of suprathermal electrons</i>	22
2.1.7 <i>Electron Bernstein Wave Heating</i>	25
2.1.8 <i>Plasma shape stabilization of current rise MHD instabilities in TCV</i>	26
2.2 THEORY AND NUMERICAL SIMULATION	27
2.2.1 <i>Physics underlying anomalous transport</i>	27
2.2.2 <i>RF waves</i>	31
2.2.3 <i>Operational limits</i>	31
2.2.4 <i>Optimisation of 3D configurations</i>	33
2.2.5 <i>Tokamak discharge simulation</i>	34
2.2.6 <i>Integrated Tokamak Modelling</i>	36
2.3 OPERATION OF A SPECIALISED BASIC PLASMA PHYSICS DEVICE, TORPEX	37
2.3.1 <i>Linear and nonlinear properties of interchange and drift-interchange instabilities naturally occurring in TORPEX</i>	37
2.3.2 <i>Drift wave antenna excitation in TORPEX</i>	39
2.3.5 <i>Blob physics: Scenario and mechanism for blob formation</i>	40
2.3.6 <i>Blob physics: Role of pressure gradients on the formation of blobs and turbulent structures</i>	44
2.3.7 <i>Characterisation of transport in the scenario with turbulence and blobs</i>	44
2.3.8 <i>Measurement of plasma flows with turbulence and blobs</i>	45
2.3.9 <i>Universal aspects of fluctuations and turbulence</i>	46
2.3.10 <i>Theory supporting basic plasma physics studies</i>	47
2.4 MATERIALS RESEARCH	48
2.4.1 <i>Irradiation Experiments</i>	50
2.4.2 <i>Underlying Technology Tasks</i>	50
2.4.3 <i>EFDA Technology Tasks</i>	57
2.5 SUPERCONDUCTIVITY	72

2.5.1	<i>Underlying Technology</i>	72
	<i>Interstrand resistance measurement on ITER size electrical termination</i>	74
2.5.2	<i>Technology Tasks</i>	78
2.6	INDUSTRIAL PROCESS PLASMAS	101
2.6.1	<i>Microcrystalline silicon for thin film photovoltaic solar cell application</i>	102
2.6.2	<i>Problems in industrial thin-film silicon deposition by plasma processes</i>	104
2.6.3	<i>From conventional plasma spraying to reactive thermal plasma CVD</i>	105
2.6.4	<i>Optimisation of the plasma enhanced chemical vapour deposition (PECVD) process for the deposition of SiO_x barrier coatings on polymers.</i>	107
2.6.5	<i>Arc phenomena in space environment and equipment</i>	108
2.6.6	<i>Influence of a weakly-ionised boundary layer on transonic and supersonic air flow</i>	109
2.6.7	<i>Plasma diagnostics for electrical discharge machining (EDM)</i>	111
2.6.8	<i>Other collaborations and industrial mandates</i>	112
3	TECHNICAL ACHIEVEMENTS OF THE CRPP IN 2007	113
3.1	TCV OPERATION	113
3.2	SHUTDOWN ACTIVITIES AND DIAGNOSTIC UPGRADE	113
3.2.1	<i>Thomson Scattering</i>	114
3.2.2	<i>X-Ray Tomography</i>	114
3.2.3	<i>FIR polarimeter</i>	115
3.2.4	<i>Diagnostic Neutral Beam</i>	115
3.2.5	<i>Tangential X-Ray detector array</i>	117
3.2.6	<i>Tangential phase contrast imaging</i>	119
3.2.7	<i>Microwave reflectometer</i>	120
3.2.8	<i>Lower-Hybrid Parametric Instability Probe</i>	120
3.2.9	<i>Oblique ECE receiver</i>	121
3.2.10	<i>Plasma edge diagnostics</i>	122
3.2.11	<i>Compact NPA</i>	123
3.2.12	<i>Charge Exchange Spectroscopy</i>	123
3.2.13	<i>SPRED UV-Spectrometer</i>	124
3.2.14	<i>First wall tile cleaning</i>	124
3.3	PRELIMINARY STUDIES IN VIEW OF POSSIBLE TCV UPGRADES	124
3.3.1	<i>Neutral beam heating</i>	124
3.3.2	<i>X3 Upgrade</i>	126
3.3.3	<i>Ergodisation coils</i>	128
3.3.4	<i>Fast ion physics tools</i>	128
3.4	CONTROL AND ACQUISITION	129
3.4.1	<i>Plant control and data acquisition</i>	129
3.4.2	<i>Plasma control system</i>	129
3.5	HEATING SYSTEMS	130
3.5.1	<i>X2 heating system</i>	130
3.5.2	<i>X3 heating system</i>	130
3.6	TORPEX TECHNICAL DEVELOPMENTS AND DIAGNOSTIC UPGRADES	131
3.6.1	<i>New Magnetron</i>	131
3.6.2	<i>LIF</i>	131
3.6.3	<i>Double Gridded Energy Analyzer for fast ion detection</i>	132
3.6.4	<i>Fast Camera</i>	132
3.6.5	<i>Ohmic system</i>	133
3.6.6	<i>Acquisition system</i>	133
3.7	SUPERCONDUCTIVITY	133
3.7.2	<i>Commissioning of the new 15 T solenoid for small size experiments</i>	134
3.8	ITER 170GHZ GYROTRON AND ITS TEST FACILITY	135
3.8.1	<i>Gyrotron components</i>	135
3.8.2	<i>C-GT170 test facility</i>	136
3.9	GYROTRON FOR DYNAMIC NUCLEAR POLARIZATION ENHANCED MAGIC ANGLE SPINNING NUCLEAR MAGNETIC RESONANCE	137
4	INTERNATIONAL AND NATIONAL COLLABORATIONS	139
4.1	EXPLOITATION OF THE JET FACILITIES	139
4.1.1	<i>Control of MHD instabilities</i>	139

4.1.2	<i>JET, S1 support for NTM avoidance</i>	139
4.1.3	<i>Particle transport</i>	141
4.1.4	<i>Collaboration on Alfvén waves and fast particles studies</i>	141
4.2	ITER	145
4.2.1	<i>Superconductivity</i>	145
4.3	COLLABORATIONS ON OTHER TOKAMAK EXPERIMENTS	146
4.4	PLASMA SURFACE INTERACTIONS IN COLLABORATION WITH THE UNIVERSITY OF BASEL	146
4.5	SOCIO-ECONOMIC STUDIES	147
4.6	COLLABORATIONS WITH OTHER EURATOM ASSOCIATIONS	148
4.7	OTHER INTERNATIONAL COLLABORATIONS	150
4.8	OTHER COLLABORATIONS WITHIN SWITZERLAND	151
5	THE EDUCATIONAL ROLE OF THE CRPP	153
5.1	UNDERGRADUATE COURSES GIVEN BY CRPP STAFF	153
5.2	UNDERGRADUATE WORK PERFORMED AT THE CRPP	154
5.3	EPFL MASTER DEGREES AWARDED IN 2007	155
5.4	POSTGRADUATE STUDIES	156
	APPENDICES	174
APPENDIX A	ARTICLES PUBLISHED IN REFEREED SCIENTIFIC REVIEWS DURING 2007	174
APPENDIX B	CONFERENCES AND SEMINARS	181
B.1	<i>Conference and conference proceedings published in 2007</i>	181
B.2	<i>Seminars presented at the CRPP in 2007</i>	190
B.3	<i>Other external presentations in 2007</i>	193
APPENDIX C	EXTERNAL ACTIVITIES OF CRPP STAFF DURING 2007	194
C.1	<i>National and international committees and ad-hoc groups</i>	194
C.2	<i>Editorial and society boards</i>	196
C.3	<i>EPFL committees and commissions</i>	196
APPENDIX D	LAUSANNE REPORTS (LRP)	198
APPENDIX E	THE BASIS OF CONTROLLED FUSION	199
E.1	<i>Fusion as a sustainable energy source</i>	199
E.2	<i>Attractiveness of fusion as an energy source</i>	200
APPENDIX F	GLOSSARY	201
APPENDIX G	SOURCES OF FINANCIAL SUPPORT	215

Foreword

The Centre de Recherches en Physique des Plasmas (CRPP) performed its activities in 2007 along the lines of the strategy proposed to and endorsed by the Review Panel chaired by Dr. R. Aymar in 2005.

This strategy encompasses:

- An active role in fusion physics both in experiments (TCV and TORPEX) and in theory and in simulations;
- contribution to ITER construction and the preparation of the demonstration reactor DEMO;
- activities in plasma processing for industrial application;
- education and training of young scientists and engineers.

It is a pleasure for me to present to you this Annual Report of the CRPP in all these domains. It describes in detail our achievements in scientific research and technology as well as our contributions to education.

I would like to take this opportunity to thank all my co-workers for their dedication. The financial support of our funding agencies is also acknowledged.

Lausanne, June 2008

Prof. M.Q. Tran, Director General

1 INTRODUCTION

1.1 *The international situation*

Two major events occurred in 2007: the formal ratification by the seven ITER parties of the ITER Agreement and the completion of the ITER Design Review (IDR). The IDR is necessary since the final design was completed in 2001 and therefore it is necessary to take into account the latest scientific and technology developments. The process of the IDR was conducted with the contribution from scientists from all Parties and was reviewed by the ITER Scientific and Technical Advisory Committee (STAC). After an assessment, a set of specific questions was endorsed by STAC for further evaluation by ITER Organisation in 2008.

In parallel, the different activities in the frame of the "Broader Approach" (BA), an agreement signed between the European Union and Japan to accelerate the realisation of fusion energy, were launched. Nearly all activities under the BA are performed by and supported by Voluntary Donors (France, Germany, Italy, Spain and Switzerland). They encompass the design of the International Fusion Material Irradiation Facility (IFMIF) and the construction of some key elements, the joint construction of a superconducting tokamak JT-60 SA in Japan and R+D related to material science for DEMO. In this frame, a high performance computer will also be installed in a new centre located in Rokkasho.

The European Domestic Agency in charge of the delivery of ITER procurements was formally established as a Joint Undertaking named Fusion for Energy (F4E). It is based in Barcelona.

F4E is also in charge of the Broader Approach. A smooth transfer between F4E and the European Fusion Development Agreement (EFDA) Technology Programme was organised in 2007. EFDA research responsibility will be focused on the operation of JET and the continuation of the programmes (physics and emerging technologies) of the Associations.

1.2 *The CRPP*

In 2007, a member of the CRPP, Dr. Nadine Baluc, was nominated as Adjunct Professor (Professeure titulaire) by the Council of the Swiss Federal Institute of Technology. Professor Baluc is the head of the Fusion Materials Group. Professor Fasoli became Executive Director of the CRPP in charge of all administrative aspects of the laboratory.

The CRPP continued to follow the strategy which was endorsed by the Review Panel chaired by Dr. Aymar in 2005. It encompasses:

- An active role in fusion physics both in experiments (TCV and TORPEX) and in theory and in simulations;
- contribution to ITER construction and the preparation of the demonstration reactor DEMO;
- activities in plasma processing for industrial application;
- education and training of young scientists and engineers.

The CRPP also plays a key role in the implementation of the Broader Approach on behalf of the Swiss Government.

The results of our research are presented in this report which is structured as follows:

- Chapter 2: Research achievements
- Chapter 3: Technical achievements
- Chapter 4: International and national collaborations
- Chapter 5: Education role.

Since it is also the annual report of the activities of the Association Euratom- Swiss Confederation, we have included the work performed by other Swiss laboratories and institutions, which have contributed to the European Fusion Programme.

Activities which do not belong to the Workprogramme of the Association Euratom-Swiss Confederation is clearly marked in the report.

1. INTRODUCTION

1.1 *La situation internationale*

Deux événements majeurs ont eu lieu en 2007: la ratification formelle par les sept Parties du projet ITER de l'Accord ITER (ITER Agreement) et la réalisation de l'ITER Design Review (Examen de la conception d'ITER, IDR). L'IDR était nécessaire dans la mesure où la conception finale a été achevée en 2001 et il était donc essentiel de prendre en compte les dernières données scientifiques et l'évolution des technologies. Le processus de l'IDR a été mené à bien avec la contribution de scientifiques de toutes les Parties et a été examiné par le Comité consultatif scientifique et technique d'ITER (Scientific and Technical Advisory Committee, STAC). Après évaluation, une série de questions spécifiques a été approuvée par le STAC pour appréciation ultérieure par l'Organisation d'ITER (ITER Organisation) en 2008.

En parallèle, différentes activités dans le cadre de l'approche élargie (Broader Approach, BA), un accord signé entre l'Union européenne et le Japon pour accélérer la réalisation de l'énergie de fusion, ont été lancées. Presque toutes ces activités sont réalisées et soutenues par des donateurs volontaires (France, Allemagne, Italie, Espagne et Suisse). Elles englobent la conception de l'Installation internationale d'irradiation des matériaux pour la fusion (International Fusion Material Irradiation Facility, IFMIF) et la construction de certains de ses éléments clés, le projet commun de construction d'un tokamak supraconducteur JT-60 SA au Japon et de Recherche et Développement liées à la science des matériaux pour DEMO. Dans ce cadre, un ordinateur de haute performance sera également installé dans un nouveau centre situé à Rokkasho.

L'agence domestique européenne en charge de la livraison des achats pour ITER a été officiellement établie comme une entreprise commune nommée Fusion pour l'énergie (Fusion for Energy, F4E). Elle est basée à Barcelone.

F4E est également chargée de l'Approche élargie. Un transfert progressif entre F4E et le Programme de technologie de l'Accord européen de développement de la fusion (European Fusion Development Agreement, EFDA) a été organisé en 2007. La responsabilité de l'EFDA dans la recherche sera désormais axée sur le fonctionnement du JET et la poursuite des programmes de physique et de technologies émergentes de l'Association.

1.2 *Le CRPP*

En 2007, un membre du CRPP, le Dr Nadine Baluc, a été nommé professeur titulaire par le Conseil des Écoles Polytechniques Fédérales. Madame la Professeur Baluc est chef du Groupe Matériaux pour la Fusion. Le Professeur Fasoli est devenu Directeur exécutif du CRPP en charge de tous les aspects administratifs du laboratoire.

Le CRPP a continué de suivre la stratégie approuvée par le comité d'examen présidé par le Dr Robert Aymar en 2005. Elle comprend:

- Un rôle actif en physique de la fusion dans ses aspects expérimentaux (TCV et TORPEX), théoriques et en simulation;
- Contribution à la construction d'ITER et la préparation du réacteur de démonstration DEMO;
- Des activités de traitement par plasma pour des applications industrielles;
- L'éducation et la formation de jeunes scientifiques et ingénieurs.

Le CRPP joue également un rôle clef dans la mise en œuvre de l'Approche élargie au nom du Gouvernement Suisse.

Les résultats de nos recherches sont présentés dans ce rapport qui est structuré comme suit:

- Chapitre 2: résultats scientifiques
- Chapitre 3: réalisations techniques
- Chapitre 4: collaborations nationales et internationales
- Chapitre 5: éducation

Comme ce rapport est également le rapport annuel des activités de l'Association Euratom-Confédération Suisse, nous avons inclus le travail effectué par d'autres laboratoires suisses et institutions qui ont contribué au programme européen sur la fusion.

Les activités qui n'appartiennent pas au travail de l'Association Euratom-Confédération Suisse sont clairement indiquées dans le texte.

1 EINLEITUNG

1.1 Die internationale Lage in der Fusionsforschung

Das Jahr 2007 hat für die Fusionsforschung zwei wichtige Ereignisse gebracht:

- Die formelle Ratifizierung des ITER-Abkommens durch die 7 Partner
- Die Neuauflage des Abschlussberichts zur Konstruktion von ITER (ITER Design Review, IDR).

Eine Neuauflage des Abschlussberichts war erforderlich geworden, um neuere wissenschaftliche und technologische Ergebnisse zu berücksichtigen, denn die bisher gültigen Konstruktionsunterlagen stammten aus dem Jahr 2001. Der Bericht wurde der wissenschaftlich-technischen Berater-Kommission für ITER (STAC) vorgelegt und beinhaltet Beiträge von Wissenschaftlern aus allen Partnerorganisationen. Nach einer allgemeinen Beurteilung beauftragte diese Kommission die ITER-Organisation für 2008 mit weiteren Untersuchungen zu speziellen Fragestellungen.

Gleichzeitig wurden im Rahmen der zwischen der Europäischen Union und Japan abgeschlossenen Vereinbarung "broader approach" (BA) verschiedene Aktivitäten gestartet, die darauf abzielen, die Verwirklichung der Energieerzeugung durch Kernfusion zu beschleunigen.

Nahezu alle Aktivitäten innerhalb des "broader approach" wurden als freiwillige Beiträge der Partner (Frankreich, Deutschland, Italien, Spanien, Schweiz) durchgeführt. Sie umfassen die Planung der Intern. Strahlungsquelle für Materialuntersuchungen (IFMIF) und dazu erforderlicher Komponenten, die Beiträge zum Bau des mit supraleitenden Spulen ausgerüsteten Tokamaks JT-60 SA in Japan, sowie Forschungs- und Entwicklungsarbeiten für DEMO auf dem Gebiet der Materialwissenschaften. Dazu gehört auch die Installierung eines Hochleistungsrechners in einem neu eingerichteten Zentrum in Rokkasho, in Japan.

Als Agentur der europäischen Partner wurde in Barcelona das gemeinschaftliche Unternehmen "Fusion for Energy" (F4E) gegründet, das für die Bereitstellung der europäischen Beiträge zu ITER zuständig sein wird.

Das Unternehmen F4E wird auch die Aktivitäten innerhalb des "broader approach" koordinieren. Im Lauf des Jahres 2007 fand ein reibungsloser Übergang von der Organisation EFDA zu F4E statt. Die Verantwortlichkeit von EFDA wird sich von nun an auf den Betrieb von JET sowie auf die Fortführung der Forschungsprogramme innerhalb der Assoziationen konzentrieren.

1.2 Das CRPP

Im Lauf des Jahres 2007 wurde Dr. Nadine Baluc vom Rat der Eidgenössischen Technischen Hochschulen der Professorentitel verliehen (adjunct professor). Prof. Baluc leitet am CRPP die Gruppe Materialforschung für die Fusion.

Prof. Ambrogio Fasoli wurde zum geschäftsführenden Direktor (executive director) des CRPP ernannt und ist nunmehr für alle Verwaltungsangelegenheiten am Institut zuständig.

Das CRPP setzt die Strategie fort, die bereits 2005 durch die von Dr. Aymar geleitete Kommission bestätigt wurde. Sie umfasst :

- Aktivitäten in der Fusionsforschung in Theorie, numerischer Simulation und Experiment, gestützt auf die Anlagen TCV und TORPEX
- Beiträge zum Bau von ITER und zur Vorbereitung des Fusionsreaktors DEMO
- Aktivitäten auf dem Gebiet der Plasmatechnologie für industrielle Anwendungen
- Ausbildung und Fortbildung von jungen Wissenschaftlern und Ingenieuren.

Im Auftrag der Schweizer Regierung hat das CRPP eine Schlüsselrolle bei der Durchführung des als "broader approach" definierten Forschungsprogramms übernommen.

Dieser Jahresbericht stellt die Ergebnisse unserer Aktivitäten vor und gliedert sich in folgende Kapitel :

- Kapitel 2 : Ergebnisse aus der Forschung
- Kapitel 3 : Ergebnisse aus der Technologieentwicklung
- Kapitel 4 : nationale und internationale Zusammenarbeit
- Kapitel 5 : Beiträge zur Ausbildung.

Da dieser Jahresbericht gleichzeitig als Tätigkeitsbericht der Assoziation Schweizer Eidgenossenschaft – EURATOM dient, wird auch über Aktivitäten berichtet, die an anderen schweizerischen Instituten und Laboratorien durchgeführt wurden und zum europäischen Kernfusionsprogramm beigetragen haben.

Aktivitäten, die ausserhalb des Programms der Assoziation Schweizer Eidgenossenschaft – EURATOM durchgeführt wurden, sind speziell gekennzeichnet.

1. INTRODUZIONE

1.1 *La situazione internazionale*

Il 2007 è stato caratterizzato da due eventi di grande importanza: la ratifica formale dell'accordo su ITER da parte dei sette membri e il completamento della Rivista del Progetto ITER (IDR). L'IDR è stata resa necessaria dal tempo trascorso dal 2001, anno in cui fu terminata la progettazione, imponendo un confronto con gli ultimi sviluppi scientifici e tecnologici. L'IDR è stata condotta con il contributo del personale scientifico di tutti i membri e con la valutazione finale del Comitato Consultivo Scientifico e Tecnico (STAC) di ITER, risultata in una serie di interrogazioni specifiche presentate all'Organizzazione ITER per il 2008.

In parallelo sono state lanciate le diverse attività contemplate dal "Broader Approach" (BA), un accordo firmato dall'Unione Europea e dal Giappone per accelerare l'impiego pratico dell'energia di fusione. Quasi tutte queste attività sono svolte e sostenute dai Donatori Volontari (Francia, Germania, Italia, Spagna e Svizzera). Le attività principali sono la progettazione del Centro Internazionale di Irradiazione dei Materiali per la Fusione (IFMIF) e la costruzione di alcuni elementi chiave, la costruzione collaborativa del tokamak superconduttore JT-60 SA in Giappone e infine lavori di ricerca legati alla scienza dei materiali per DEMO. In questo quadro, un computer di grande potenza di calcolo sarà inoltre installato in un nuovo centro situato a Rokkasho.

L'Agenzia Domestica Europea incaricata della consegna dei componenti per ITER è stata formalmente inaugurata nella forma di un'impresa collettiva chiamata "Fusion for Energy" (F4E), con sede a Barcellona.

F4E è anche incaricata della gestione del Broader Approach. La redistribuzione delle consegne tra F4E e l'Accordo Europeo per lo Sviluppo della Fusione (EFDA) è stata organizzata e completata agevolmente nel 2007. Le responsabilità di ricerca di EFDA si concentreranno sull'operazione del JET e sulla continuazione dei programmi di fisica e di tecnologie emergenti delle Associazioni.

1.2 *Il CRPP*

In 2007, un membro del CRPP, Dr. Nadine Baluc, è stata nominata Professore Titolare dal Consiglio Federale Svizzero delle Scuole Politecniche. La Prof. Baluc dirige il gruppo di ricerca sui materiali per la fusione. Il Prof. Fasoli è divenuto Direttore Esecutivo del CRPP con l'incarico di gestire l'amministrazione del laboratorio nella sua totalità.

Il CRPP ha continuato a perseguire la strategia raccomandata dalla Commissione di Verifica diretta da Dr. Aymar nel 2005, che comprende i seguenti elementi:

- un ruolo attivo nella fisica della fusione, sia nel campo sperimentale (TCV e TORPEX) che in quello teorico e delle simulazioni numeriche;
- contributi alla costruzione di ITER e alla preparazione del reattore di dimostrazione DEMO;
- attività di ricerca nei processi al plasma per applicazioni industriali;
- educazione e formazione di giovani scienziati e ingegneri.

Il CRPP gioca inoltre un ruolo di primo piano nell'implementazione del Broader Approach per conto del governo svizzero.

I risultati della nostra ricerca sono presentati in questo rapporto, che si articola come segue:

- Capitolo 2: Risultati di ricerca
- Capitolo 3: Traguardi tecnici
- Capitolo 4: Collaborazioni internazionali and nazionali
- Capitolo 5: Ruolo educativo.

Poiché il presente rapporto raccoglie le attività dell'Associazione Euratom-Confederazione Svizzera, vi è incluso anche il lavoro effettuato da altri laboratori e istituzioni svizzeri che hanno contribuito al programma di fusione europeo.

Le attività che non fanno parte del Programma di Lavoro dell'Associazione Euratom-Confederazione Svizzera sono chiaramente segnalate come tali nel rapporto.

2 RESEARCH ACHIEVEMENTS OF THE CRPP IN 2007

2.1 *The TCV tokamak*

The operation of TCV in 2007 was limited to the first two months of the year, as a major shutdown started in March. This shutdown will last until the early 2008, and has been devoted to the installation of new diagnostic systems and to performing important maintenance work, including a complete dismantling and cleaning of the more than 1600 graphite tiles forming the TCV first wall. To compensate for the planned unavailability of TCV, operation during January and February 2007 was intensified, with a pace of nine sessions per week. During this period, the second harmonic (X2) system was available up to full power (3MW). As only two of the three gyrotrons of the third harmonic system (X3) were available, with the 3rd gyrotron under repair due to an RF window failure, the experimental campaign focused on scenarios using X2 heating and current drive schemes.

This period concluded the experimental campaign launched at the beginning of 2006, which was conducted according to the scientific missions defined and agreed during general discussions in December 2005. These missions addressed a number of specific issues within a few themes of relevance for ITER and for the improvement of the tokamak concept in general. The TCV research weighting evolved somewhat with respect to the original definition, following the interests of the international fusion community, and included the study of scenarios with internal transport barriers, the characterisation and modelling of the plasma edge, plasma rotation and heat and particle transport, the physics of ECH, ECCD and the related suprathreshold electrons, an assessment of the potential of Electron Bernstein waves for heating and current drive, and the influence of the plasma shape on MHD stability issues. Highlights of the results obtained on these themes are reported below.

In parallel with the scientific exploitation of TCV, based both on the relatively short 2007 campaign and on the analysis and theoretical modelling of previously collected data, part of the team dedicated some effort to exploring possible medium term developments and upgrades, in particular in view of the European facilities review. These studies address the possibility of direct ion heating by NBI, of operating at slightly higher magnetic field, of increasing the ECRH X3 power, of installing additional tools for error field and ELM control, and of performing fast ion physics experiments on TCV.

2.1.1 *Scenarios with internal transport barriers*

Steady-state, fully bootstrap-sustained discharges

We succeeded in creating stationary discharges with a 100% bootstrap current fraction by applying strong ECRH during the initial plasma current ramp-up and clamping the current in the Ohmic transformer primary to a constant value a few ms after breakdown in order to remove all external volt-second input. A 55kA current was sustained for 1s by 2.7MW second-harmonic X-mode ECRH power at a line-averaged density of $1 \times 10^{19} \text{ m}^{-3}$ (see Fig. 2.1.1). Using only half of the available power (1.35MW), a stationary 35kA discharge was sustained for 0.6s. The duration of these steady-state phases is significantly longer than the current redistribution

and the L/R time and orders of magnitude longer than the confinement time. The EC waves have zero parallel wave number and thus supply no current drive. The initial heating generates a strong internal transport barrier (ITB), which evolves naturally to a stationary state once all the external current sources are removed. This self-organized state is characterized by a narrow electron ITB with a reduced confinement enhancement of 2.5-3 (Fig. 2.1.2).

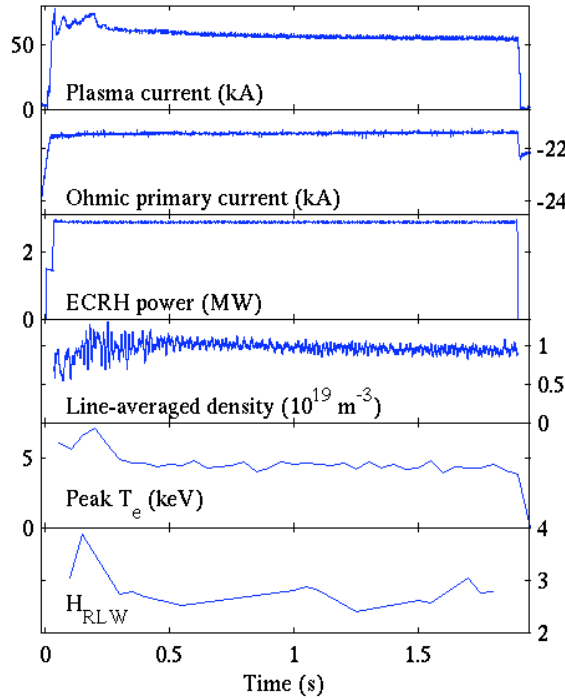


Fig. 2.1.1 TCV discharge 34428. There are no external current sources from 0.02 to 1.9s. A stable current of 55kA (to within 2%) is supplied by the bootstrap mechanism from 0.9 to 1.9s. The confinement enhancement factor in the bottom box is scaled to the TCV L-mode confinement scaling (the Rebut-Lallia-Watkins scaling).

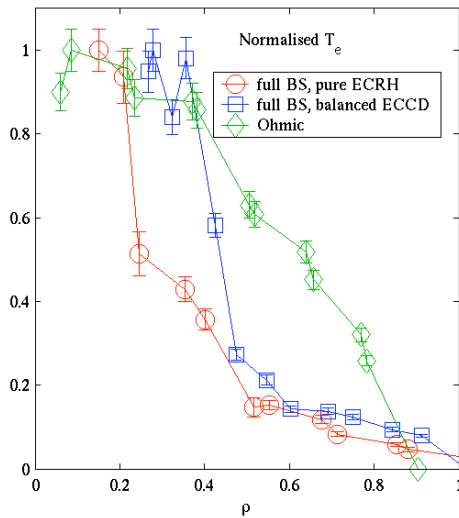


Fig. 2.1.2 Normalised electron temperature profiles for TCV discharges 34428 (narrow eITB with no ECCD and 100% bootstrap; red), 34175 (broad eITB with balanced co- and counter-ECCD and 100% bootstrap; blue) and 34508 (Ohmic; green).

Quasi-stationary discharges with zero net nominal injected current were also obtained by adding counter-ECCD to a pre-existing stationary non-inductive eITB discharge sustained initially by off-axis co-ECCD. In these cases a broader and stronger barrier (confinement enhancement ~ 4) is observed, resulting in strong MHD activity and a more turbulent state with cyclic confinement variations, as in the example shown in Fig. 2.1.3, which displays a quasi-stationary phase starting at 1.7s.

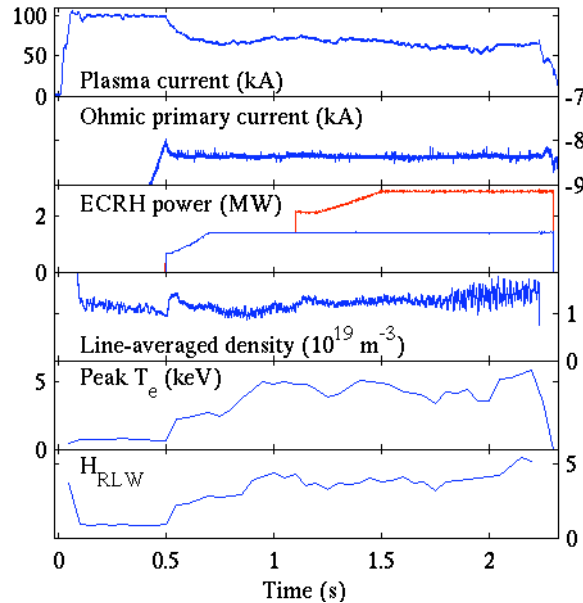


Fig. 2.1.3 TCV discharge 34175. The ECRH power traces correspond to co- (blue) and counter- (red) current drive. The total nominal driven current after 1.5s is zero.

Global plasma oscillations in eITB regimes

Both in non-inductive and inductive eITB scenarios, slow oscillations of the electron temperature, with frequency ~ 10 Hz and full poloidal and toroidal symmetry ($m=n=0$), are observed, coexisting with MHD modes and with oscillations of the total plasma current. This phenomenon appears akin to the oscillatory (O-) regime on the Tore Supra tokamak, occurring in fully or nearly non-inductive discharges with lower hybrid current drive and negative central magnetic shear.

The MHD activity and reversed magnetic shear are key requirements for the Oscillatory regime (O-regime) to occur on TCV. The O-regime can be effectively suppressed (together with MHD activity) by ECCD-induced local current density perturbation. In 2007 experiments, MHD activity has been modified through current density profile tailoring rather than local deposition within an island. A transition from resistive to ideal type of MHD activity with increased local pressure gradient in the O-regime has been shown.

By adding co-ECCD (0.25MW) well inside the barrier at 1.5s, the O-regime is suppressed, although an MHD mode continues until the end of the plasma. As the current density profile becomes less hollow compared with the phase with oscillations, the barrier loses its strength at 1.6s (with a delay comparable with the current redistribution time), as proved by a drop in the energy confinement time

enhancement factor, H_{RLW} , from 3 (during the O-regime) to 2. The MHD mode has been identified as $m/n=3/1$ from Mirnov coils and is located at $r/a=0.45$, just outside the foot of the eITB, confirmed by ECE measurements.

Alternatively, we demonstrate that removing the MHD activity contributes to the suppression of the O-regime even if the transport barrier is preserved. In discharge #33897 (Fig. 2.1.4) the total power of co-ECCD off-axis beams has been continuously decreased from 1.5MW at 1.5s down to 0.6MW at 2.2s. In order to maintain the strength of the transport barrier, a counter-ECCD on-axis beam has been added from 1s to 2.2s with a constant power of 0.25MW. Although the off-axis co-driven current decreases, thus raising the value of q_{min} , the central shear remains negative. At 1.7s, the $m/n=3/1$ MHD mode is completely stabilized, as confirmed by the analysis of correlation ECE spectra. At the same time, global plasma oscillations disappear. The value of H_{RLW} clearly increases from 3 to 3.5 after the suppression of the O-regime, indicating a strengthening of the transport barrier.

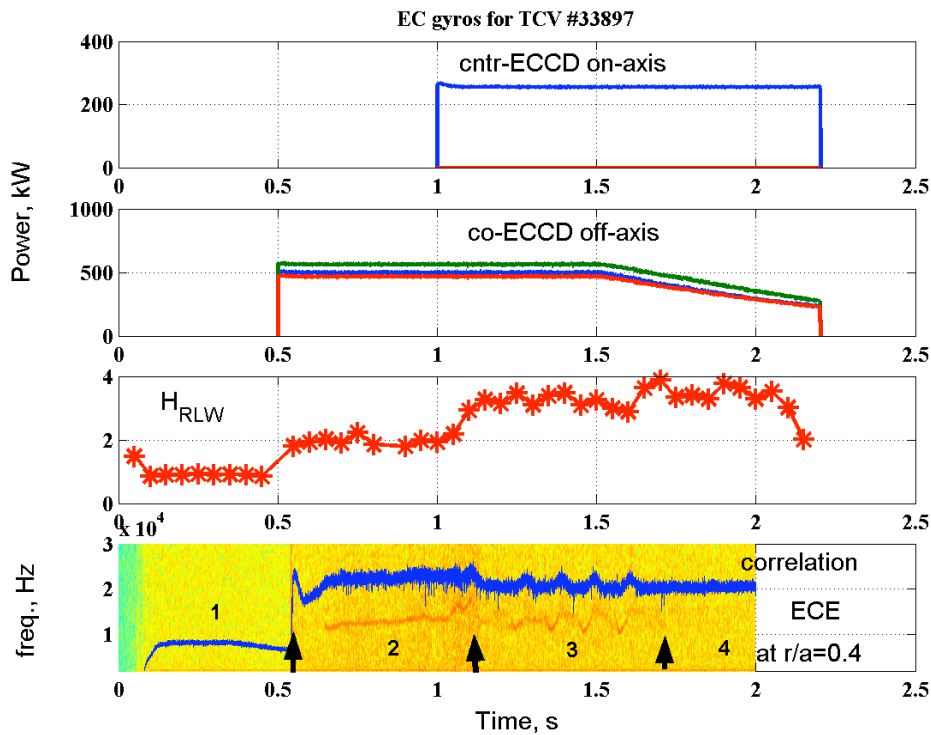


Fig. 2.1.4 *Suppression of the O-regime by stabilizing $m/n=3/1$ mode at 1.7s (shot #33897). Top: ECH power and H-factor evolution during the discharge. Bottom: correlation ECE spectrogram at $r/a=0.45$.*

The O-regime can be triggered if modulated ECRH power (10Hz, 0.5MW) is added inside the barrier, after it has been sustained by 1MW of off-axis co-ECCD (Fig. 2.1.5). The MHD mode frequency evolution follows these “induced” oscillations. Interestingly, when the imposed modulation is finished and ECRH power inside the barrier remains constant, the O-regime continues with the same frequency (10Hz). Evidence for a mode in the electron fishbone frequency range, as well as for the broadband temperature fluctuations between 30–200kHz, has been obtained by means of high-resolution correlation ECE diagnostic. These modes co-exist with the O-regime and lower-frequency resistive/ideal MHD activity. Their influence on the confinement degradation will be the subject of future study.

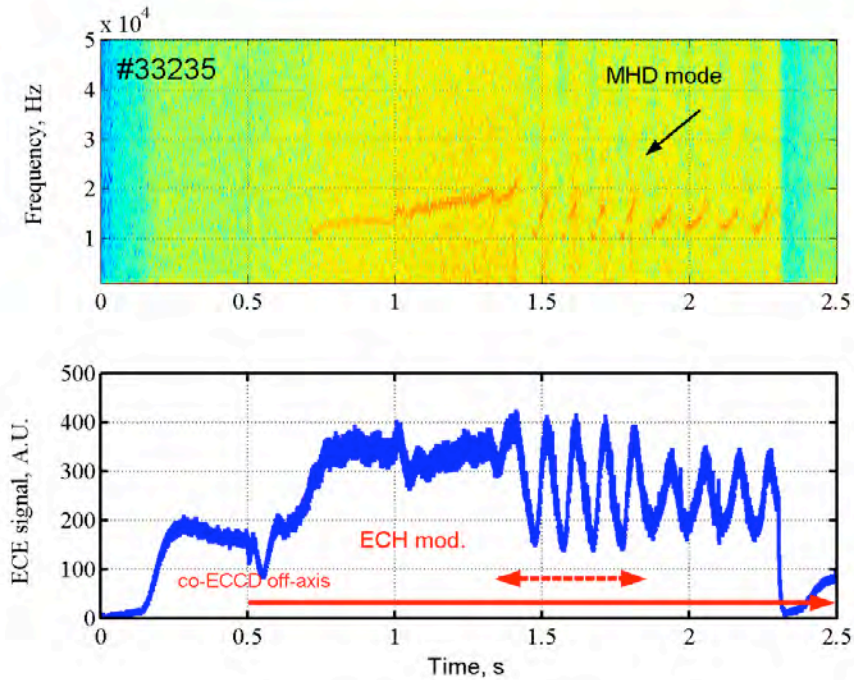


Fig. 2.1.5 Excitation of the O-regime by modulated ECH power (0.5MW) inside the barrier. The O-regime continues after the modulation stops at 1.8s.

2.1.2 Plasma edge characterisation and modelling

The first measurements of parallel scrape-off layer (SOL) flow on TCV were described in the 2006 Annual Report. There it was shown how the radial flow profile in the outer midplane SOL comprises a magnetic field direction dependent component, dominant at low to medium plasma densities, and a smaller contribution independent from the field direction and the plasma density. The former was clearly shown to be driven by classical Pfirsch-Schlüter (P-S) return flows in the SOL due to poloidal drifts arising as a result of radial gradients in edge electric field and plasma pressure. Radial, interchange driven turbulent transport was proposed as the driving mechanism for the latter, with two dimensional fluid turbulence simulations in quantitative support. Nevertheless, the completely open nature of the TCV vacuum vessel (i.e. no baffled divertor) left open one alternative process that could explain the field independent flow: a drive by the presence of a divertor target sink. To eliminate this possibility required more measurements, at different locations in the SOL.

Varying the measurement location usually means moving the diagnostic. But on TCV, the possibility of variable plasma shape allows the plasma to be moved with the diagnostic fixed in place. The reciprocating Mach probe which is used to make the flow measurements is thus fixed on the machine midplane and further experiments have been performed in SNL and SNU magnetic configurations to shift the position of the probe with respect to the plasma midplane. The results are compiled in Fig. 2.1.6 in the form of averaged parallel flow profiles for varying plasma density. "Averaging" is to be taken in the sense of the arithmetic mean of flows measured for forward and reversed toroidal field in separate discharges matched for plasma current and shape. Here, forward (or negative) toroidal field denotes the most often used field direction in tokamak experiments in which the ion ∇B drift direction is downwards. By averaging the measurements obtained for

both field directions, any field direction dependent flow is eliminated, leaving only the field independent component.

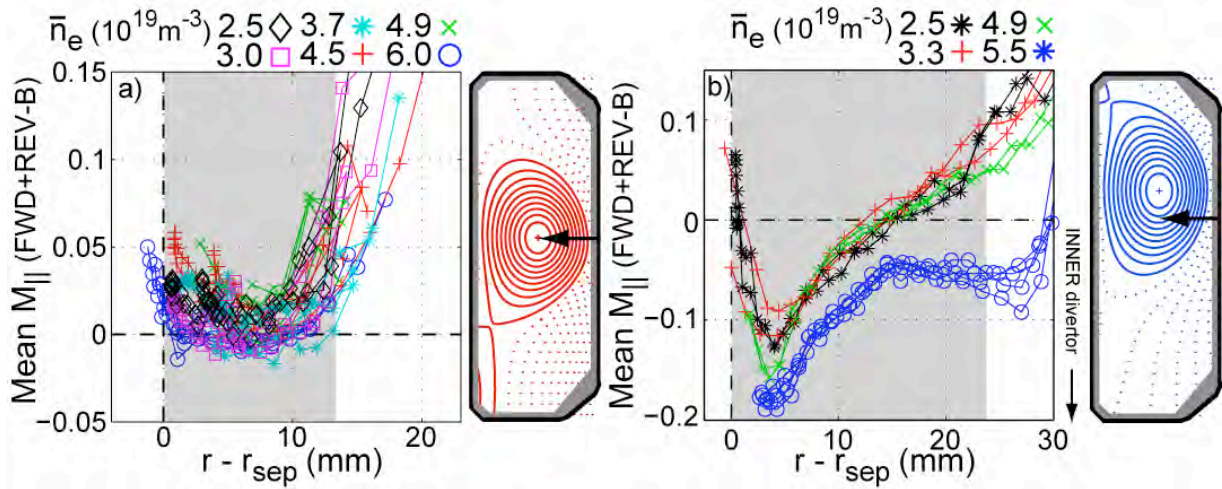


Fig. 2.1.6 (a,b) Average of parallel flows (expressed as a Mach number, where the fluid velocity is normalised to the local plasma sound speed) measured for forward and reversed toroidal field directions in a series of matched ohmic discharges in which the plasma density is varied and for both SNL and SNU diverted configurations in SNL (see reconstructed magnetic equilibria to the right of each figure). These “average” flow profiles (plotted in terms of distance from the separatrix mapped to the low field side midplane) reveal any magnetic field direction independent flow component. The grey shaded areas delimit the region of SOL plasma in which field lines fully connect from outer to inner divertor target without first intersecting wall surfaces. Negative flows are always directed downwards, towards the outer target for SNL (a) and the inner target for SNU (b). The reciprocating probe location, fixed on the vacuum vessel midplane, is indicated on the magnetic configurations by the horizontal arrows.

Measurements on the midplane (Fig. 2.1.6a) reveal that the field independent component is close to zero at all densities when the probe is located on the outside midplane in SNL, whilst for SNU, when the probe is effectively above the plasma midplane (relative to the X-point), there is an offset in the flow directed towards the inner divertor. This flow has a distinct radial profile shape and appears to be density dependent. Both of these observations are consistent with those obtained previously (see 2006 Annual Report) for a variant of the SNL configuration in which the probe was located below the outboard midplane. They further support the conjecture of a field independent flow component driven by interchange turbulent-driven radial convective transport of plasma filaments in a region of the poloidal cross-section localised in the outboard midplane region. Excess pressure (compared with the SOL background plasma) in these filaments is released by parallel transport along field lines in the SOL region. This leads to the appearance of a parallel flow in locations poloidally separated from the origin of the enhanced cross-field transport. A probe measurement on the plasma midplane is a “neutral point” for this flow and does not sense it.

A new fast infra-red (IR) camera diagnostic to replace the slower, micro-bolometric device viewing the outer divertor targets. The aim was to observe the time dependence, spatial profile and magnitude of the transient power loads provoked by

ELMs on the divertor target. This new device came into operation during the latter part of the period covered by this report and has provided the first observations of this kind on TCV. Some first examples are provided in Fig. 2.1.7, showing the surface temperature and power flux densities for individual ELMs at the outer divertor of SNL plasmas. These measurements are obtained in sub-array mode, in which a thin radial slice of the divertor is viewed at high speed, allowing time resolution of $40\mu\text{s}$ with integration time of $4\mu\text{s}$. This provides excellent tracking of the ELM power rise phase, the most critical in determining the physics of ELM parallel transport and the maximum power load experienced at the target. The preliminary observations in Fig. 2.1.7 show how the Type III ELM appears to have a faster rise time than the more powerful large X3 ELM. This is in apparent contradiction to the scaling commonly observed in tokamaks for a rise time linearly dependent on the parallel transport time for an ELM outflux originating upstream and travelling to the targets along SOL field lines at the acoustic speed. The hotter X3 upstream plasma should provide for faster parallel transit than in the ohmic case and hence a faster, or at least comparable rise time to the Type III ELM. Both fluid (SOLPS5 code) and kinetic (BIT1 particle-in-cell code) simulations are underway to study the parallel SOL transport during these ELMs, using the IR power flux measurement as constraint at the target.

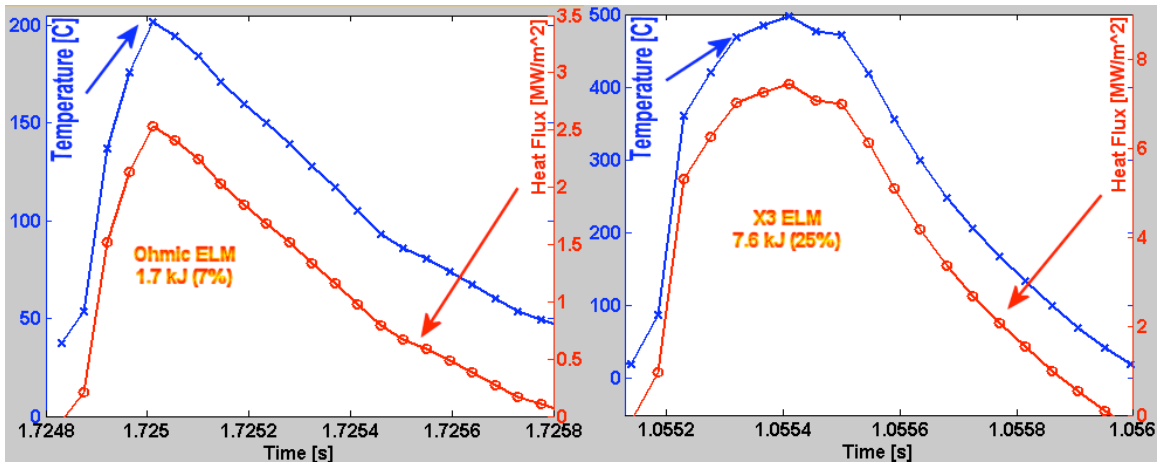


Fig. 2.1.7 Time dependence of power flux density and surface temperature at the TCV outer divertor targets for two separate ELMs obtained in a SNL H-mode discharge heated with X3 ECRH (a) Type III ELM, $\Delta W_{ELM}=1.7\text{kJ}$ (7%) from the ohmic H-mode phase and (b) large ELM, $\Delta W_{ELM}=7.6\text{kJ}$ (probably Type I) from the X3 heated phase.

These new data also show clearly the effect of deposited surface layers on the outer target tiles – the surface temperature rise provoked even by the relatively small Type III ELM is $\sim 150^\circ\text{C}$, far higher than would be produced by an ELM of only $\sim 2\text{kJ}$ depositing its energy on a clean bulk graphite surface ($\sim 30^\circ\text{C}$). Energy accounting at the outer target during these ELMs also reveals that at most only $\sim 25\%$ of the plasma stored energy drop associated with each ELM is found at the outer target. Even accounting for plasma radiation during the ELM itself, the implication is that the inner target loading (which is not observed) must be considerably higher, indicating that TCV data is consistent with the important recent observations from the ASDEX Upgrade and JET tokamaks of an in-out asymmetry of the ELM energy deposition.

2.1.3 H-mode physics

ELM control experiments were performed in plasmas with the ion VB drift directed away from the X-point, the so-called ‘unfavourable direction’ for H-mode access. After reversing the magnetic field direction, some effort was dedicated to finding the operational domain of a stationary ELMy discharge. This year some experiments were dedicated to the study of the relative role of sawteeth and magnetic perturbation on the ELM cycle.

The first step consisted of producing the perturbation signal with a new wave form generator. Then, perturbations were applied to the vertical position feedback control loop to add quick vertical displacements of the plasma. In all discharges, the natural delay between ELMs was rather irregular. This was probably due to the bad conditioning of the vacuum vessel which was also diagnosed by the large amount of dust observed in the divertor (in the vicinity of the separatrix leg striking the vessel floor). This effect resulted in a difficulty of choosing a perturbation frequency capable of dragging the ELM cycle to a new, faster, fixed, frequency. As a consequence, the synchronisation of ELMs with the perturbation was not good enough to address the question of the role of the sawteeth.

2.1.4 Plasma rotation

TCV has continued with the measurement and analysis of plasma rotation with Charge Exchange Spectroscopy (CXRS) using a diagnostic neutral beam that only induces a small (<1km/s) plasma rotation. These measurements of “intrinsic” or “spontaneous” rotation are of particular interest since toroidal rotation is found to stabilise the resistive wall mode instability that is of concern in upcoming fusion grade devices such as ITER, where the plasma rotation may not be set by neutral beam momentum injection.

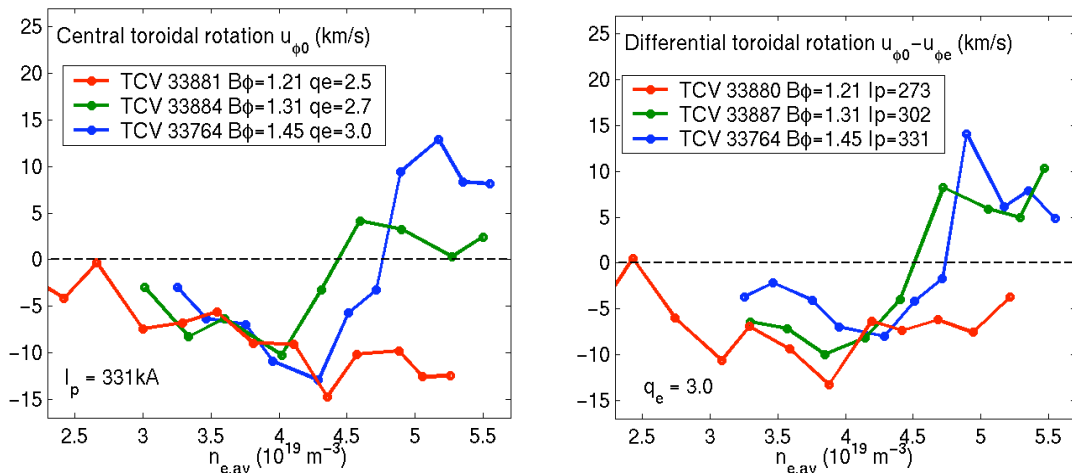


Fig. 2.1.8 a) Core toroidal rotation as a function of average plasma density for three toroidal magnetic field values for a plasma current of 330kA. b) The core toroidal rotation for three magnetic fields where the plasma current has been adapted to keep a constant edge safety factor of 3. The density at which the toroidal inversion occurs was little changed for a constant edge safety factor.

Observations of an inversion in the toroidal rotation profile on TCV both for limited and diverted observations, and the difficulty in finding an appropriate theoretical explanation, led to experiments in which both the plasma rotation and the rotation inversion were measured as a function of a number of plasma parameters.

Figure 2.1.8 shows a plot of the core plasma rotation for a sequence of discharges with a varying toroidal field, where the plasma current was kept constant or was adjusted to keep the edge safety factor constant. Although no inversion in the toroidal rotation was observed for the lowest 1.2T toroidal field, the density at which the toroidal rotation occurred was similar for a constant edge safety factor, i.e. the same magnetic field structure.

Figure 2.1.9 shows the toroidal rotation profile in two discharges with and without 500kW of off-axis second harmonic EC heating. ECH modifies the current density profile in the plasma column by displacing the position of the sawtooth inversion radius (associated with the first rational magnetic surface) from a flux normalised radius of ~ 0.35 to ~ 0.2 . Without ECH, the rotation profile is flat within the inversion radius with a maximum value of ~ 25 km/s. By displacing the inversion radius inwards, the toroidal rotation profile now continues rising up to the new inversion radius position with a peak rotation of ~ 40 km/s.

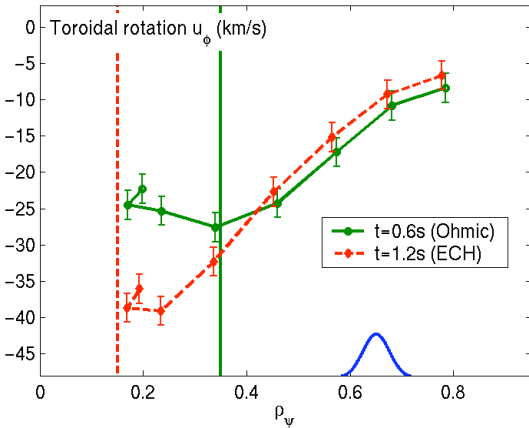


Fig. 2.1.9 The toroidal rotation profile with and without 500kW of off axis second harmonic X2 heating. With EC heating the inversion radius is displaced closer to the axis and the core rotation peaking increases with the maximum rising from ~ 25 km/s to ~ 40 km/s.

In Fig. 2.1.10, the toroidal rotation profile is shown for two values of the shape parameter measuring plasma triangularity across the density range for which a toroidal velocity inversion is observed. Although some discontinuity in the evolution of the central rotation velocity is discernable at a plasma density $\sim 3.5 \times 10^{19}/\text{m}^3$, it is strongly reduced with low triangularity. The difference in the toroidal velocity profile is even more pronounced. The rotation inversion with positive triangularity is peaked in the core with the plasma velocity in the edge region close to zero. For low triangularity, the toroidal rotation profile is close to zero in the core with strong counter plasma current rotation in the edge region that no longer shows a rotation inversion as a function of plasma density. This example of the scaling of the toroidal velocity with plasma shape was extended by the first data from the poloidal CXRS observation system, Fig. 2.1.11, so that the toroidal and poloidal velocities are now simultaneously available.

CXRS also provides the impurity density profile which may then be combined with the toroidal and poloidal velocity profiles to obtain the radial electric field profile using the ion force balance equation.

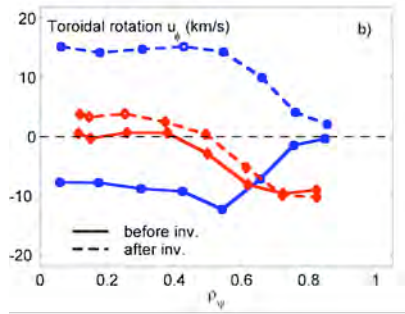
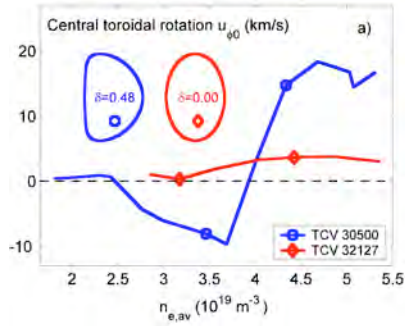


Fig. 2.1.10

a) The core toroidal rotation as a function of the average plasma density for a plasma triangularity of 0.48 and 0. b) The toroidal rotation profiles for the two triangularities at 3.5 and $4 \times 10^{19} / \text{m}^3$. The profile and its evolution with the plasma density are a strong function of the plasma shape.

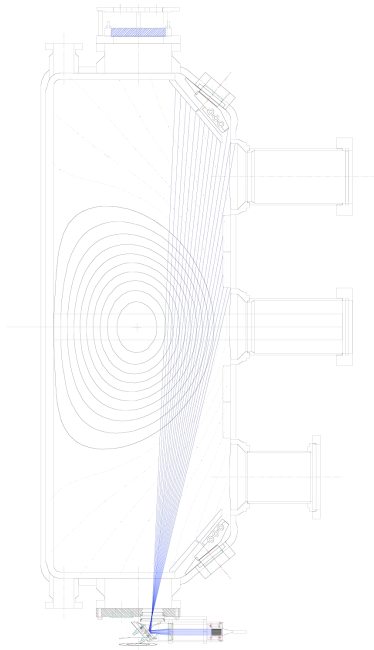


Fig. 2.1.11

Schematic of the poloidal rotation CXRS observation camera.

Figure 2.1.12 shows the radial electric field before and after the toroidal velocity inversion illustrated in Fig. 2.1.10. The contributions from the toroidal rotation, poloidal rotation and ion pressure are represented together with the total electric field. Dominated by the toroidal rotation, the radial electric field changes sign in the plasma core across the toroidal rotation inversion, whereas the potential well in the edge region remains negative and is noticeably stronger after the toroidal velocity reverses.

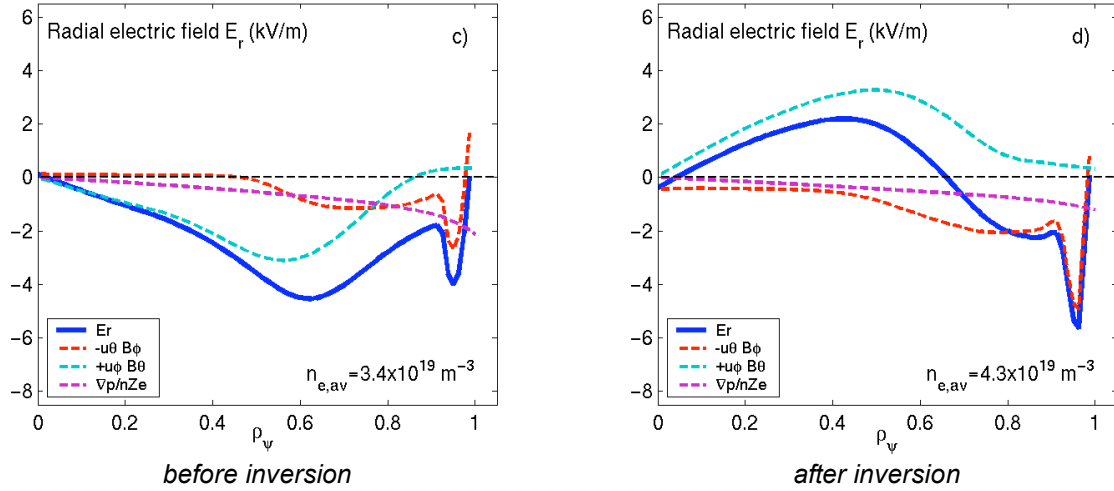


Fig. 2.1.12 Radial electric field in the plasma across a toroidal rotation reversal. The contributions from the toroidal rotation, the poloidal rotation and the ion pressure are shown together with the total radial electric field.

It is expected that these scalings and further experiments in which the plasma shape will be further exercised will help provide a basis for a physical explanation for these rather unique measurements, and to contribute to understand fundamental aspects of the physics of plasma rotation in tokamaks.

2.1.5 Heat and particle transport in TCV

Effect of triangularity on heat transport in ECH L-mode discharges

A strong dependence of heat flux on plasma triangularity and collisionality in ECH heated L-mode experiments has previously been reported. For otherwise identical discharges, the heat flux necessary to sustain the same profiles and stored energy in a discharge with $\delta = -0.4$ is half of that required for a discharge with $\delta = +0.4$. This behaviour has now been modelled by quasilinear and by non-linear collisional calculations, using the local gyrokinetic code GS2 in the electrostatic approximation. These plasmas are found to be unstable to trapped electron mode (TEM) microturbulence. The results obtained for the nonlinear heat flux are in remarkable agreement with observations, reproducing both the increase of heat diffusivity towards lower collisionalities and the effect of triangularity. Nevertheless the latter tends to vanish as the simulated flux tube approaches the magnetic axis, due to the finite radial penetration length of triangularity. Since experimentally the improvement in confinement is roughly independent of the spatial position, further modelling including global effects is necessary to account for the discrepancy.

Linear numerical experiments have allowed us to pinpoint the effect of triangularity as being due to a combined effect of reduced drive from grad-B-curvature drifts and of enhanced effective k_{perp} , acting differently on barely and deeply trapped particles, at lower (and negative) triangularity. At high collisionality, TEM's are stabilized, the magnetic drifts become unimportant and heat conductivities tend to become independent of triangularity, as experimentally observed.

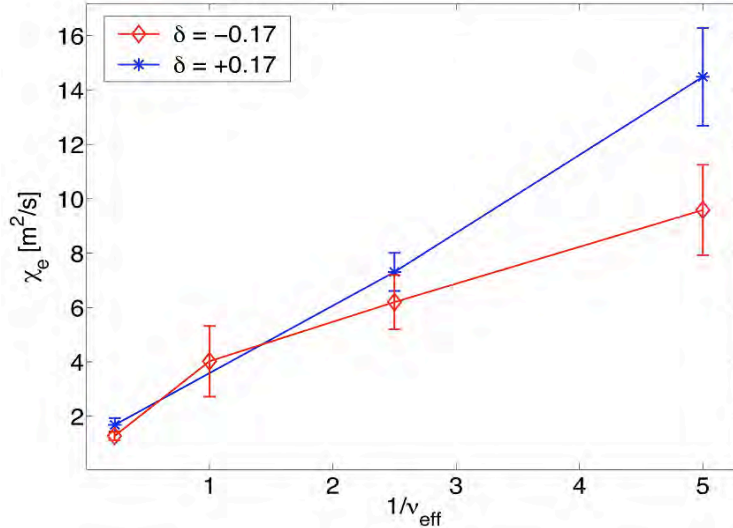


Fig. 2.1.13 Quasilinear GS2 calculations of electron heat conductivity versus inverse collisionality for plasmas with positive and negative triangularity under otherwise identical conditions (in particular density and temperature scale lengths).

Transport in EC-heated H-modes

H-mode operation with ECH heating at the third harmonic (X3) has allowed access to H-modes parameters and regimes not achievable with Ohmic heating only. The microwave power is injected nearly vertically, at a shallow angle to the X3 resonance, to maximize first pass absorption. Experiments were performed with two and three available gyrotron sources at 118GHz, allowing up to 1.4MW of power to be launched into the vessel. TORAY calculations show that first pass absorption exceeding 75% is obtained in these H-modes, which have $\langle n_e \rangle \approx 6 \times 10^{19} \text{m}^{-3}$, achieving $T_e(0) \geq 2 \text{keV}$, $\beta_N \leq 2$, $\beta_T \leq 2.5\%$ and a confinement enhancement factor $H_{\text{IPB98(y,2)}}$ up to 1.4, as determined from diamagnetic measurements (Fig. 2.1.14).

The most remarkable changes compared with Ohmic H-modes are observed in the behaviour of the ELMs. They are larger than the type III ELMs observed in Ohmic conditions and correspond to type I ELMs. On the other hand, stationary ELM-free H-modes are also observed. These stationary ELM-free H-modes have impurity content and radiative power loss comparable to ELMy H-modes ($Z_{\text{eff}} \approx 2.5$, $P_{\text{rad}}/P_{\text{tot}} \approx 20\%$). Ongoing linear stability analysis of such H-modes, comparing several codes (the gyrokinetic GENE, GS2 and KINEZERO codes, the fluid Weiland and GLF23 models) show that the plasma is unstable to trapped electron modes (TEM), electron temperature gradient modes (ETG), and marginally to ion temperature gradient (ITG) modes. The latter depends on the ion temperature gradient sustained by electron to ion heating and thus depends on density. Since these H-modes exhibit all these instabilities, non-linear simulations are required in order to evaluate the effective transport modes due to these modes. First IFS-ETG nonlinear simulations indicate that ETG can drive significant transport.

X3-heated H-modes are also observed to have moderately peaked density profiles at all collisionalities. However, collisionality cannot be the main control parameter for peakedness in these discharges, since plasmas with flat and peaked profiles are observed at the same collisionalities, the more peaked ones being obtained with higher ECH heating power and higher density. In order to help interpret these observations, a series of quasilinear gyrokinetic simulations was undertaken using the GS2 code. The results suggest that in these conditions the ITG mode may be

responsible for the inward particle pinch, which results in peaked density profiles. The experimental observations of reduced peaking at lower density is tentatively interpreted as due to the weaker coupling between electrons and ions and associated reduced ion heating. The reduced ion heating may in turn reduce ITG mode activity, allowing TEM modes to dominate. This would reduce (or reverse) the associated thermodiffusive component of the particle pinch and the peakedness of the density profile.

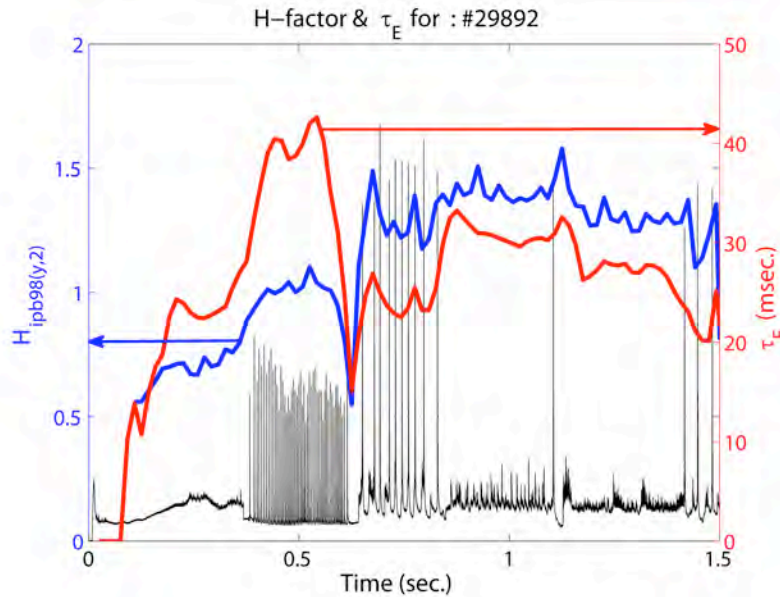


Fig. 2.1.14 Confinement time (red) and H factor (blue) in a discharge exhibiting a phase with large ELMs and two stationary ELM-free phases. The black trace is D_α light intensity. The plasma was heated with 1.4MW of ECH from 0.6s onwards.

Impurity transport

The aim of this work was to document and interpret the intrinsic carbon density profile behaviour in the TCV tokamak in the framework of different transport models. The experimental information from 2005-2007 was compiled into a database of carbon density profiles in steady state, measured using Charge Exchange Spectroscopy. The database contains nearly 800 samples and covers a wide range of discharge conditions, including Ohmic, ECH and some eITB discharges. The database documents in detail a previously reported correlation between the carbon density profile and the current density profile in Ohmic L-mode discharges. In high q_{95} Ohmic discharges, the carbon density profile is considerably more peaked than the electron density profile. In ECH discharges with ECH power larger than 500kW, we found an additional dependence on the ECH deposition radius, but not on the deposited ECH power. This behaviour is similar to that of the electron density profile. Attempts to interpret this behaviour in terms of dominant turbulent drift modes, using the gyrokinetic codes KINZERO and GS2, are under way.

2.1.6 Physics of ECH, ECCD and of suprathermal electrons

Characterisation of electron distribution function asymmetry during ECCD with oblique ECE

A new low-field-side electron-cyclotron-emission (ECE) receiver has been put into operation and connected to an existing 24-channel, 65-100GHz radiometer. The receiver is a spare ECRH launcher, providing the same flexibility in 2D angular orientation characteristic of the ECRH launching system. In particular, measurements have been performed with the viewing chord oriented in a near-tangential direction to the magnetic field in order to investigate asymmetries in the electron distribution function (EDF) with respect to the parallel velocity during the application of ECCD. Oblique ECE is itself asymmetrically generated by virtue of the Doppler shift of the cyclotron frequency: emission detected by looking along the co-current direction is from electrons contributing positive current, and vice versa. Thus, a direct comparison of co- and counter-emission can yield information on the distribution function asymmetry, which is essential for the mechanism of current generation. The asymmetry is revealed clearly in Fig. 2.1.15, displaying the ratio of co- to counter-emission for ECCD going from co- to counter. The two orientations are exactly symmetric with an angle of 65° to the poloidal plane at the antenna and the polarization is nearly exactly X-mode. The driven current is estimated by linear ray-tracing calculations and ranges from +23 to -23kA in the scan. As illustrated by Fig. 2.1.16, the results agree quantitatively with calculations by the ECE radiation transport code NOTECTCV using a simple drifting suprathermal population superimposed on a bulk Maxwellian electron distribution, with densities and temperatures constrained by a variety of experimental measurements.

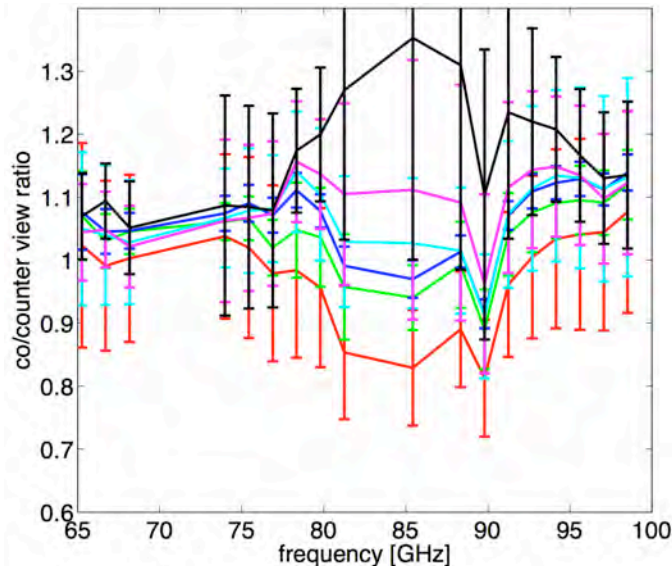


Fig. 2.1.15 The ratio of the co-/counter viewing receiver signals as a function of frequency. The driven current is increased from counter- to co-ECCD (red to black curves). The central frequencies (81.25 – 88.34GHz) are from the region of current generation. The EDF is seen to be asymmetric and emits more radiation in the direction of driven current.

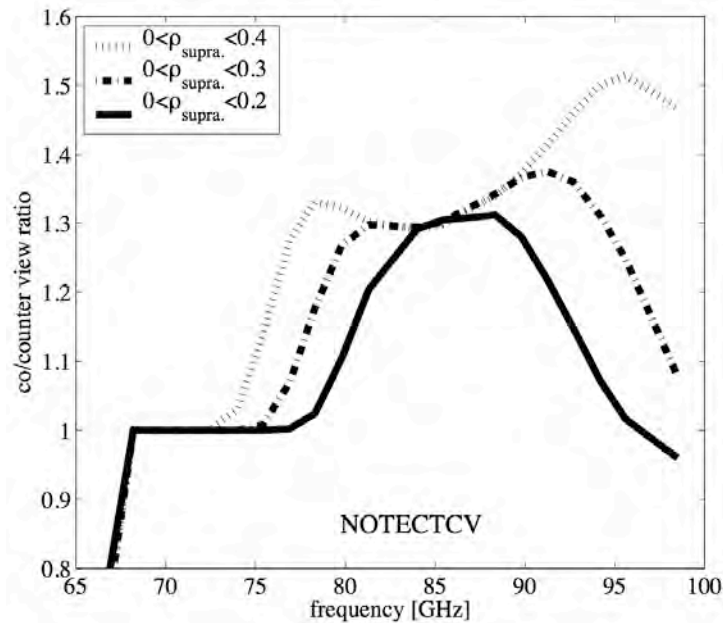


Fig. 2.1.16 *The ratio of the co-/counter viewing receiver signals calculated by NOTECTCV. The amplitude is consistent with a value of +23kA in Fig. 2.1.15 for the case in which the supra-thermal electrons are restricted to the region of calculated ECCD ($\rho < 0.2$). The other curves show the change in the profile for simulations in which supra-thermals are spread farther, resulting in higher current.*

Real-time control of plasma current and elongation with ECRH actuators

Feedback control of 2nd harmonic ECRH actuators was demonstrated for the first time on TCV. The plasma current was successfully controlled in fully non-inductive conditions by operating on the ECRH power. With the external loop voltage clamped at zero, the current was varied by several tens of kA in the 150-200kA range with 2.7MW power, as illustrated by Fig. 2.1.17. The controller increases the ECRH power in response to the change in the reference signal, driving more plasma current and minimizing the error.

In a separate experiment, control of the plasma elongation was demonstrated by heating the plasma far off-axis and operating both on the power and on the launcher orientation. Off-axis heating reduces the local resistivity and draws current away from the plasma centre, flattening the current profile and ultimately causing the plasma to elongate, at constant shaping magnetic field. The elongation can thus be controlled by regulating the applied power. An example is shown in Fig. 2.1.18, where ECRH power is applied in a constant shaping field from 0.3 to 1.5s and is varied by the control system to minimize the error signal and follow the requested steps in the elongation reference. Additionally, a second control loop operated on the launcher orientation in order to keep the beam at approximately the same normalised radius as the plasma elongation changed. These experiments, performed with the present linear analogue plasma control system, offer strong promise for ECRH control in TCV with the new digital control system coming on line in 2008.

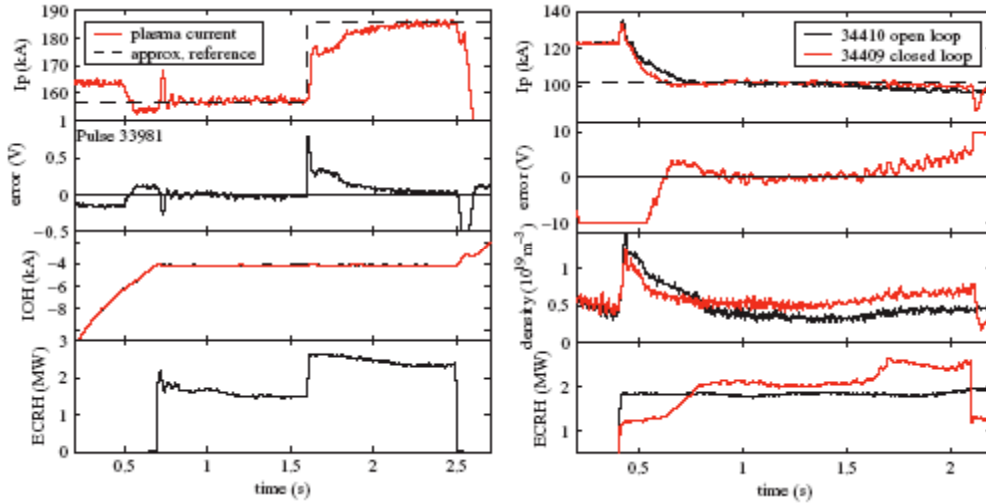


Fig. 2.1.17 (Left) Plasma current control with a step increase in the current reference. Also shown is the current in the Ohmic coils which is flat during the control phase from 0.7 to 2.5s. (Right) Comparison of open and closed loop (with a constant current reference) control cases. The close loop case responds faster to the initial reference and maintains a constant current for a longer time. There is a gyrotron arc at 2.2s, removing one cluster (half the power).

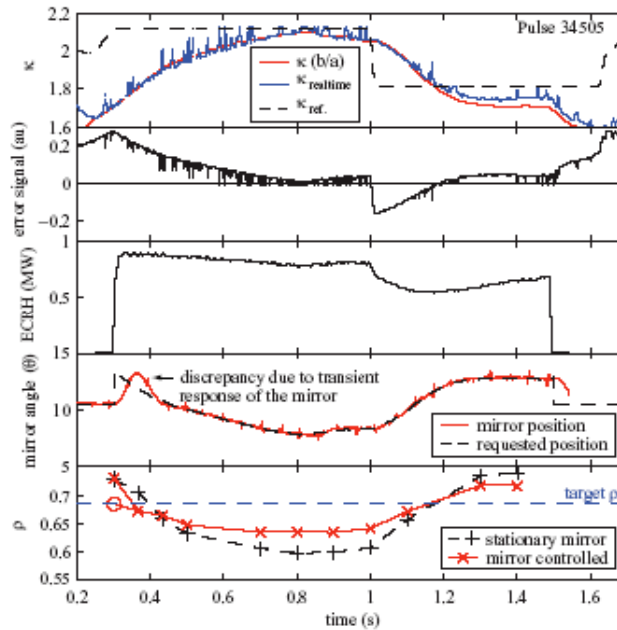


Fig. 2.1.18 Feedback control of the plasma elongation and ECRH deposition location. The reconstructed elongation trace is shown at the top together with the elongation observer and reference. The κ error signal is used in the ECRH power control algorithm only. The fourth trace shows the actuator signal for the mirror controller together with the measured mirror position. A ray-tracing calculation of the deposition ρ is shown in the bottom trace (solid line) and compared with the expected deposition ρ given by a constant mirror angle at the feed forward value of 11.25° (dashed line). The target ρ is also shown, which is simply the initial deposition radius at ECRH power-on.

2.1.7 Electron Bernstein Wave Heating

Previous experiments in TCV have demonstrated Electron Bernstein Wave Heating (EBWH) allowing local power deposition at densities far above the conventional O-mode cut-off density. At the optimum injection angle maximising the O-X transmission and subsequent absorption, the deposition of modulated power was found inside the O-mode cut-off layer, a clear signature of the O-X-B scheme. Up to 1MW of EBW power step was injected on top of 1MW of CW heating power, giving rise to a clearly measurable increase in central temperature (on Thomson scattering and on the soft X-rays). These results represent the first demonstration of EBWH in a medium aspect ratio tokamak using the O-X-B double mode conversion scheme. In the modulated EBWH experiments, the total power absorption efficiency was typically 60% and the deposition was made far off-axis to avoid the large central sawtooth perturbation that would prevent a clear detection of the deposition location. Central power deposition is however needed to maximize the global Electron Bernstein (EB) heating effects. Therefore, initial experiments have been conducted to optimize central deposition using an equatorial rather than oblique launch. A toroidal field scan allowed us to determine an optimal field for central deposition in equatorial launch (Fig. 2.1.19), in preparation for dedicated central high power deposition. The deposition location in the core could be determined in the presence of strong sawteeth using a slope-breaking analysis of soft X-ray traces. The difference between the experimental results and the non-relativistic calculations of deposition locations appears more significant than in the earlier far off-axis deposition experiments, which provides a good opportunity for the determination of relativistic ray propagation effects.

To increase the coupling efficiency, an understanding of the loss channels is required. A small part of the power may be lost in the Lower Hybrid wave generated by parametric instability at the X-B conversion layer. The installation of a magnetic probe to reveal its presence is under way and will also help optimizing the launcher angle at high power in heating experiments. The additional launcher mirror system installed on TCV for use as a steerable reception antenna will allow a more efficient determination of the optimal injection angle directly from the EB emission (EBE) of the plasma, due to the quasi-reciprocity of absorption and emission (Kirchoff's law) in TCV plasmas.

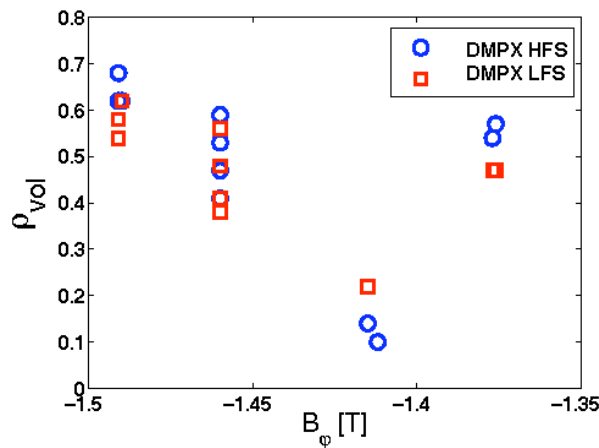


Fig. 2.1.19 EBW deposition location in a toroidal magnetic field scan, determined from the slope break of soft X-ray traces (DMPX) at EC power switch-on.

2.1.8 Plasma shape stabilization of current rise MHD instabilities in TCV

The potentially disruptive plasma current rise instabilities have been studied as a function of the plasma shape in TCV, varying elongation and triangularity, see Fig. 2.1.20. Disruptions typically occur in quasi-circular plasmas at $q_a \sim 3$ in both non-sawtoothed and sawtoothed discharges with peaked current profiles. The perturbations in the plasma parameters before disruption are characterized, and the main unstable modes identified as coupled $m/n = 2/1$ and $3/2$ rotating tearing modes. In the early phase, the coupling between $3/1$ external mode and the $2/1$ mode is found to play a major role in determining whether or not the disruption will occur. Plasma cross-section shaping is found to reduce or to completely stabilize the disruptive mode and is regularly used in TCV operation as a tool for safe initial current ramp-up. Plasma elongation, positive and negative triangularity prevent the growth of a large $2/1$ mode at $q_a, \sim 3$ thus reducing or even suppressing the disruptions.

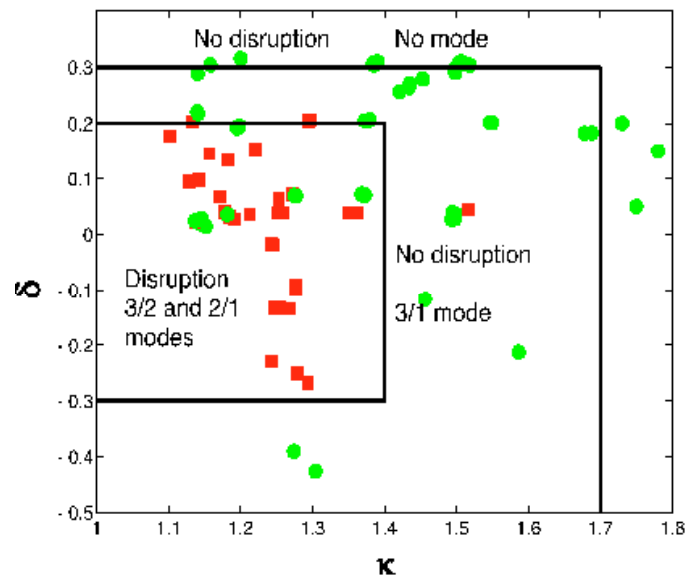


Fig. 2.1.20 Disruption events in the δ - κ plane at $q_a \sim 3$, with the dominant mode numbers m/n indicated. The dots represent non-disruptive discharges whereas the squares represent disruptive discharges. Large elongation and triangularity values strongly reduce the risk of disruptions during the current rise, maintaining low amplitude $m/n = 2/1$ tearing mode, or even completely suppressing it.

To interpret the experimental results, full-geometry resistive linear (single-mode) calculations of the tearing-mode stability parameter Δ' have been made with the PEST-3 code. Surprisingly, these calculations indicate a destabilising effect of elongation and triangularity, in contrast with the experiment. This suggests the dominant role of toroidal mode coupling in the destabilization of the $m/n=2/1$ mode in quasi-circular TCV plasmas. Single-mode theory does not provide a good description of the effect of plasma shaping on tearing stability. Other stabilizing mechanisms must be taken into account, which could contribute to the safe crossing of $q_a=3$ in shaped plasmas.

Two possibilities can be suggested. First, the effect of the conducting wall. This strongly depends on the plasma shape and may inhibit the external mode potentially destabilizing the $m=2$ tearing mode by toroidal coupling (see Fig. 2.1.21). Second, the effect of mode coupling with vacuum flux surfaces at $q=3$, $q=4$ and $q=5$. A complete theoretical interpretation of this effect for plasma parameters relevant to

the TCV case (finite shaping), is still missing. Both stabilizing mechanisms act simultaneously and independently, and may be used in TCV and other tokamaks to mitigate or suppress plasma disruptions.

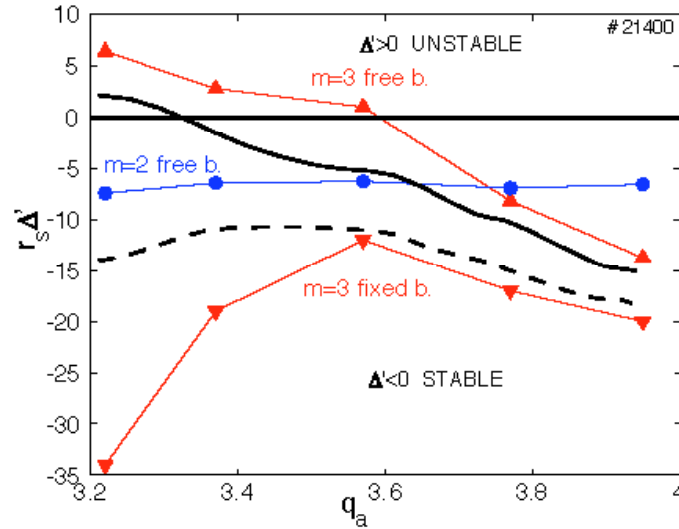


Fig. 2.1.21 Tearing Δ' -stability (PEST-3) as a function of edge safety factor q_a , for a 'low shaping' case ($\kappa \sim 1.3$ and $\delta \sim 0.2$). The $m = 2$ mode is always stable. The $m = 3$ modes, unstable at low q_a with free boundary, is stabilized by fixed boundary conditions. The solid and dashed black lines are just meant to suggest plausible but arbitrary paths in the $m = 3$ tearing stability diagram, when taking into account the real TCV-wall geometry, for quasi-circular and strongly shaped plasmas, respectively

2.2 Theory and numerical simulation

Research activities have been pursued in the areas of first-principles based simulations of turbulence based on gyrokinetic theory, investigations of tokamak and stellarator MHD stability with extensions to include fast particle kinetic effects, application of RF waves to tokamaks and stellarators, optimization of 3D magnetic configurations and full to tokamak simulations.

2.2.1 Physics underlying anomalous transport

Global gyrokinetic simulations

The first simulations of decaying turbulence with the global gyrokinetic code ORB5 including the non-adiabatic response of trapped electrons have been performed. In the linear regime, benchmark comparisons have been made with other local and global codes for both Ion Temperature Gradient (ITG) and Trapped Electron Mode (TEM) dominant drive. The first nonlinear results indicate that the numerical noise is increased compared with adiabatic electron simulations but remain tractable. A numerical cost has to be paid in terms of a 10-fold decrease in the time step required. Studies have begun on the trapping/detrapping of electrons due to the turbulent field and on the interaction of zonal flows with TEM turbulence.

Sources have been included in the ORB5 code. Extensive numerical tests have been performed with different formulations for the source term: a standard Krook operator, a modified Krook operator and a density preserving “heating” operator. The modification to the Krook operator enables a good preservation of the zero frequency branch of the zonal flows. Damping tests have been successfully compared to the analytical theory of Rosenbluth and Hinton. Most importantly, very long simulations have been performed with a controlled level of numerical noise, Fig. 2.2.1, with averaged temperature gradients well above their marginal stability value. This allows us to obtain a statistically relevant description of turbulence. The probability distribution function (PDF) of heat flux shows a marked non-Maxwellian tail, signature of large events (avalanches). Investigations are in progress in order to characterize these avalanches and to quantify what proportion of the time-averaged flux is due to these large events.

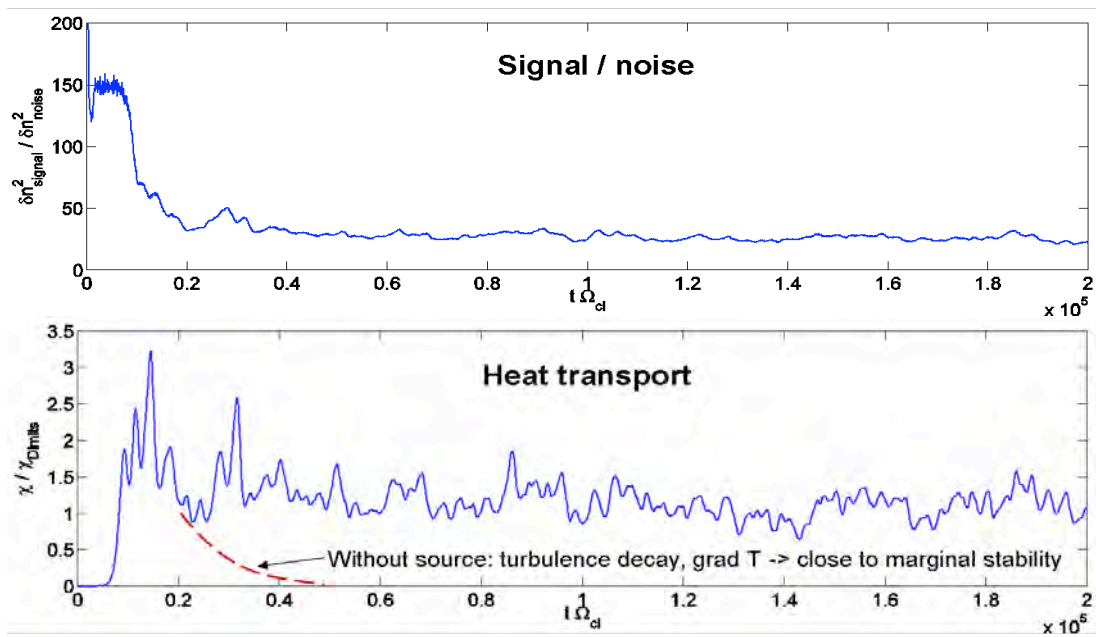


Fig. 2.2.1 Heat transport (top) and signal to noise ratio (bottom) in a global gyrokinetic simulation of ITG turbulence with the ORB5 code including forcing with sources. The control of noise enables long enough simulations to have a statistically relevant analysis of turbulent transport.

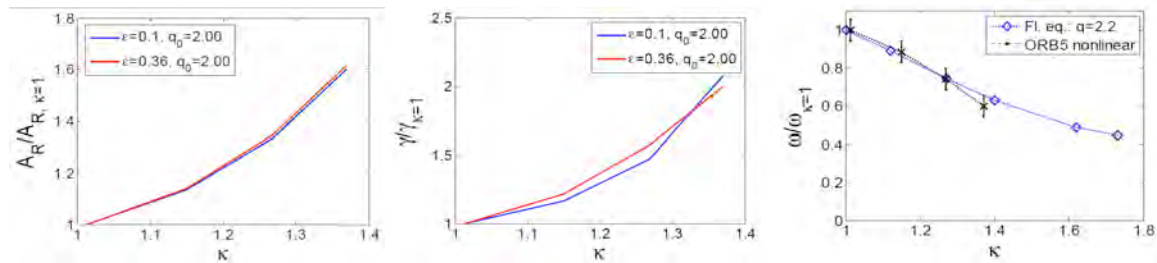


Fig. 2.2.2 GAM Frequency (left, with a comparison with a fluid dispersion relation), damping rate (middle), and undamped residual zonal flow (right) as a function of elongation, for a series of simulations with the ORB5 code.

A study of the influence of tokamak plasma elongation (κ) on zonal flows, geodesic acoustic modes (GAM), ITG stability and turbulence has been undertaken with the

ORB5 code. The GAM frequency is found to decrease with κ , in agreement with an analytical dispersion relation and with experimental observations. The GAM damping rate increases with κ (it doubles when κ goes from 1.0 to 1.4). The undamped zonal flow residual also increases with κ by about 60% when κ goes from 1.0 to 1.4, Fig. 2.2.2. Linear ITG growth rates are systematically lower with increasing κ , with a marginal critical T_i gradient (when measured on the equatorial plane) increasing with elongation. A systematic scan in κ from 1 to 1.75 and temperature gradient was performed: results indicate that the growth rates are a function of a rescaled temperature gradient: $R/L_T \langle \kappa \rangle^{1/2}$ (Fig. 2.2.3). In nonlinear simulations with the temperature gradient rescaled so as to have the same linear drive, the perturbed field energy level and the effective heat diffusivity decrease with increasing κ , thus showing the importance of nonlinear effects (Fig. 2.2.4). These findings are consistent with the increased GAM damping and increased steady zonal flow component with increasing κ .

In collaboration with the CEA in Cadarache, the Lagrangian PIC code ORB5 and the semi-Lagrangian code GYSELA have been benchmarked for a nonlinear ITG turbulence case with reasonably good agreement. The merits and drawbacks of both approaches have been confirmed.

In order to address the specific problems of the semi-Lagrangian approach, a new drift kinetic code has been developed based on a modular approach including the following elements: (a) 2D time integration of the characteristics in the poloidal plane; (b) a spline module with arbitrary orders for 1D and 2D interpolation and Poisson solver on non-equidistant meshes; (c) modules that facilitate the distributed data handling on parallel platforms; (d) 2D domain decomposition and parallelisation.

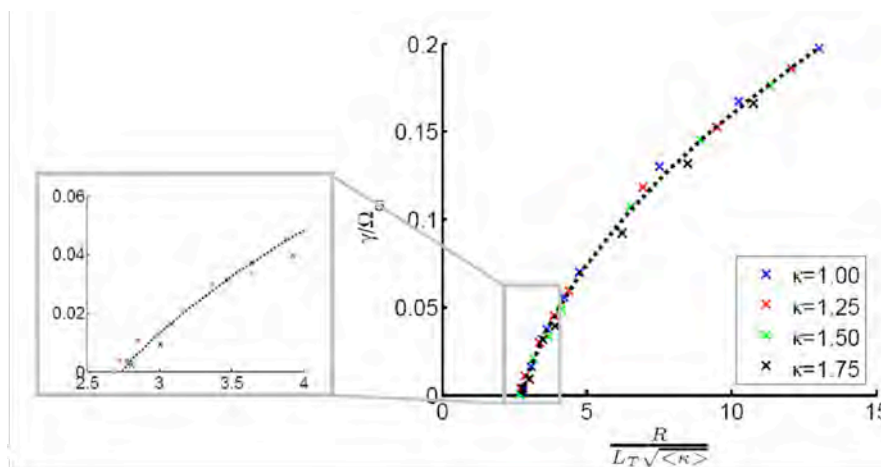


Fig. 2.2.3 ITG growth rate versus renormalized temperature gradient for various elongations.

The Eulerian flux tube code GENE has been linked to the ideal MHD stability code CHEASE. This enables the computation of more realistic configurations. Comparisons of these equilibria with the standard s -alpha equilibrium approximation that was made in GENE before have shown that growth rates are strongly affected: up to a factor of 2 has been found for the standard tokamak parameters of the CYCLONE base case. This study has pointed to finite aspect ratio terms in the metric tensor that are neglected in the s -alpha model, in particular the non-orthogonality of the straight-field line coordinate system. A study of the effects of plasma triangular shaping on microturbulence has started.

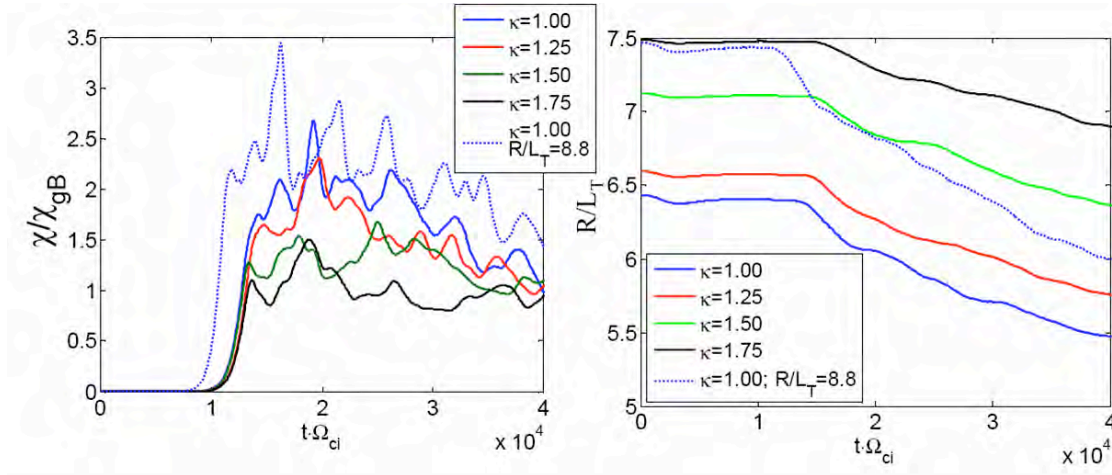


Fig. 2.2.4 *ITG turbulent heat transport (left) and normalised temperature gradient (right) versus time for various elongations. The initial temperature gradients are chosen such as to give the same linear growth rates for all elongations. The observed reduction of heat transport with elongation is thus a consequence of nonlinear effects.*

Turbulent transport of fast ions

Anomalous transport of heat and particles is known to be a key issue for fusion devices. Fast ions occur in burning plasmas in the form of fusion produced alpha particles. Another origin of fast ions is the neutral beam injection (NBI), which is widely used to heat and to drive current. The fast particles have a strong velocity along the field lines. To investigate the turbulent transport of these ions, we used an asymmetric Maxwellian equilibrium distribution function, together with gyrokinetic ITG background turbulence. With this setting, we found a significant fast ion particle transport due to the turbulence. The simulation of the turbulence in the presence of fast ions has been done with the GENE flux tube code. The beam ions are treated as passive tracers but obey the full gyrokinetic dynamics. The influence of different parameters on the fast ion diffusivity has been investigated. The main result is the fact that there is a significant contribution of the superthermal particle energies to the particle diffusivity. Between an energy of 3 and 10 times the thermal energy, the diffusivity of the fast ions is remarkable. This also gives a possible explanation of results reported from Asdex Upgrade.

Electron transport and current profile modelling

The effect of the predicted local ECCD driven by the equatorial and upper launcher on ITER has been evaluated. The equatorial launcher can very efficiently control the value of q within $r/a=0.2-0.3$, in particular if there is also the option to drive counter-CD. If only co-CD is driven, as soon as the gyrotrons will be used, for example to heat the center, it can remove the reverse shear. Therefore if one cannot do heating or counter-CD, central gyrotrons will probably be useless for advanced and hybrid scenarios. Simulations on the effect of local current drive, via the upper launcher, on the shear at $q=1$ have also been performed. It is found that sawteeth can be stabilized or destabilized, changing the sawtooth period by about a factor of two. However, it is much easier to destabilize the sawteeth, i.e. to increase the shear at $q=1$, rather than to keep the shear at $q=1$ at low values. For the latter, one needs to be within the current deposition width outside the $q=1$ surface. Given that the deposition width is very small this is rather difficult to achieve practically.

Quasilinear simulations with the CQL3D code have been performed for scenarios which exhibit temperature oscillations. These are more difficult to analyse since they are not in steady-state. The calculated current density profile, j_{cd} , is then used in ASTRA or CRONOS time evolution modeling. These should provide insight on the relation between current profile, MHD modes and transport near the electron internal transport barrier. The simulations with CRONOS are performed in collaboration with CEA/Cadarache.

Particle transport modeling

The theoretical analysis of particle transport characteristics in electron Internal Transport Barriers has continued with analytical and numerical work using the gyrokinetic GS2 code. The main achievement has been to show that the anomalous pinch is of a thermodiffusive nature and is carried by the trapped electrons. The pinch usually called 'Turbulent Equipartition Pinch' is found to be negligible. The resulting density peaking is maximized at the transition between the two main turbulent instabilities, namely the ion temperature gradient (ITG) mode and the trapped electron mode (TEM): the latter has to be subdominant. The passing electrons start to contribute at finite and high collisionality. The comparison of theoretical results with experimental observations requires the detailed knowledge of the ion parameters, thus new experiments have been planned for the next experimental campaign in TCV.

2.2.2 RF waves

Alfvén and ICRF waves in 2D and 3D configurations

The LEMan full wave global code has been adapted to run on an IBM SP5 cluster. As the memory is shared between all processors of a single node, Open MP was used to obtain an efficient parallelisation of the solver. But MPI is still used for the communication between the nodes. The code is now able to reach a total of 2000 Fourier modes for the description of the perturbed field. This should allow simulations in the IC domain for a wider range of stellarators. The computation of the warm dielectric tensor with exact determination of the parallel wave vector has been optimized to reach good convergence with an improvement of the CPU time dependence on the number of Fourier modes. This was made by avoiding computing negligible terms. A comparison between the versions with exact computation and with different approximated parallel wave vectors has been performed for the case of a JET equilibrium. It points out the importance of this quantity to influence the results, the approximation being more or less appropriate depending on the different cases considered (e.g. inside the TEA gap or the continuum).

2.2.3 Operational limits

Kinetic effects on MHD modes

Studies continue to identify kinetic modifications to modes which are essentially of MHD origin. Pressure anisotropy has recently been considered in the equilibrium and linear fluid perturbations and in the drift orbits of particles (see section 2.2.4).

An analytical calculation of average toroidal drift orbits in an anisotropic plasma has been made. Solutions are obtained for both trapped and passing orbits in fully shaped geometry. The results are expected to be important in understanding electron and ion fishbone instabilities with various mode numbers, in conventional, hybrid and advanced scenarios. Furthermore, the inclusion of shaping effects could help explain contrasting anomalous transport phenomena in, for example, TCV with differing geometry. In parallel to this, the VENUS code has recently been generalised to include pressure anisotropy following the Hamiltonian formulation described in Section 2.2.4. VENUS takes the equilibrium from VMEC, which in turn is being compared with analytical solutions for the anisotropic equilibria. Comparisons between the equilibrium analytical work and VMEC, as well as the orbit analytical work and VENUS, are excellent.

Sawtooth behaviour and internal ideal stability

The bi-Maxwellian model employed in VMEC and TERPSICHORE has been compared favourably with the code SELFO used to post-process ICRH distributions of fast ions in JET discharges. A scheme has been implemented which obtains a best fit of the SELFO data in terms of the model distribution function. Very good fits are obtained for a JET demonstration discharge which are of particular interest for testing sawtooth control in the presence of energetic trapped ions in the core. This work has been extended to include distribution functions that are not symmetric in the sign of the parallel velocity, which is of interest when ICRH is used without dipole antennas. It is then necessary to model the kinetic effects associated with having more or fewer co passing ions than counter passing ions, and the resulting effect on the internal kink mode and sawteeth. It is foreseen that this extension will enable an explanation of empirical results demonstrating the sensitivity of the sawtooth period to the deposition of ICRH and ICCD.

Recent work treats the ideal internal kink stability with realistic q -profiles in a toroidal plasma. The result serves as a generalization to the well known result by Bussac et al. Analytical work on the stability of the ideal internal kink mode has been extended to ideal Mercier and Infernal modes in hybrid scenarios. Mercier type modes occur in a region of the plasma where the safety factor is less than one, and we have an infinite number of global (non-local) Mercier modes in the region where the shear vanishes. The infernal type modes are studied in equilibria with a large region of vanishing shear, but with the safety factor above one. We again find an infinite spectrum of modes, but only one of them can be unstable. This mode is driven unstable when the pressure gradient is sufficiently large, and could thus invoke operational limits in hybrid scenarios in the form of sawtooth-like reconnections, and fishbone-like behaviour.

Edge Localised Modes (ELMs)

The analysis of ELM triggering and ELM pacing experiments in TCV and Asdex Upgrade has been pursued. The effect of applying an external magnetic perturbation has been shown to deform high order moments of the plasma shape. Therefore the question of how this deformation can affect the ideal MHD stability limits has been examined. Our analysis has focused on edge localised instabilities of the external kink and ballooning types. The ideal MHD global stability code KINX has been used and it takes into account the presence of a separatrix in a consistent manner. The stability diagrams obtained show an effect of deformation that is potentially large enough to affect type-I ELM triggering experiments. Quasi-equilibrium modelling of Asdex Upgrade ELM pacing experiments with different

patterns of plasma movement shows that the corresponding changes in the stability limits are consistent with experimental findings.

In order to improve the accuracy and efficiency of equilibrium reconstruction, in particular with pedestal profiles near the edge, a free-boundary code using a grid adaptive technique taking into account the bootstrap current in the pedestal has been developed. It will be applied to ELMy TCV shots using high resolution temperature and density profile Thomson scattering measurements.

Tokamaks with reversed current density

The problem of axisymmetric stability of tokamaks with reversed current density and non-nested flux surfaces (equilibria with islands) was investigated with the development a new unstructured grid code. The unstructured nature of the grid is better suited for such cases that exhibit topology changes and a variable number of axisymmetric islands and/or dipole type configurations. Unstable $n=0$ modes were found in some cases even with a conducting wall right at the plasma boundary.

2.2.4 Optimisation of 3D configurations

Exact Hamiltonian formalism for guiding centre drift orbits

A Hamiltonian formulation of the guiding centre drift orbits is extended to pressure anisotropy and field perturbations in axisymmetric systems. The Boozer magnetic coordinates are shown to retain canonical properties in anisotropic pressure plasmas with finite electrostatic perturbations and electromagnetic perturbed fields that solely affect the parallel component of the magnetic vector potential. The equations of motion developed in the Boozer coordinate frame are satisfied exactly through direct verification of the drift velocities. A numerical application has been performed to illustrate the significance of retaining all second order terms some of which have been ignored in previous theoretical models.

Optimisation of quasi-isodynamic stellarator configurations

Novel geometry quasi-isodynamic (QI) stellarator configurations have been devised with vanishing dipole secondary current in the plasma. In a first step, model investigations were undertaken to identify the Fourier spectrum of the magnetic field strength which simultaneously satisfy the QI and zero dipole current conditions. Secondly, the geometry at the boundary corresponding to such a magnetic field spectrum was found, showing that the cross sections were purely elliptical therefore displaying an absence of magnetic well. In the last stage, some boundary magnetic surfaces were generated for which the plasma was stable to Mercier, resistive interchange and strong symmetric ballooning criteria which were also close to QI.

Neoclassical transport in 3D Systems

The VENUS- δf code has been applied to the super dense core plasmas that are achieved in the LHD device with pellet injection to compute the bootstrap current. Under these highly collisional conditions, the bootstrap current is quite small in

LHD. Comparisons of the bootstrap current in a very large range of collisionalities between VENUS- δf and the DKES code shows excellent agreement with discrepancies only appearing at very large mean free path. A benchmark study of the mono-energetic bootstrap current coefficients on three different stellarator configurations has been performed with the VENUS- δf , DKES, NEO-MC and NEO-2 codes and very good agreement has been obtained. The VENUS- δf code demonstrates convergence of the bootstrap current coefficient to the semi-analytical Shaing-Callen limit in the extreme long mean-free-path regime. Different filter values have been explored to provide the Monte Carlo noise/variance reduction.

Fluid MHD Stability in a Heliotron with Anisotropic Fast Particles

The fluid stability models with anisotropic fast particle species, implemented in the TERPSICHORE code, have been applied to investigate the properties of on-axis and off-axis hot particle deposition and large parallel versus large perpendicular pressure anisotropy in a Heliotron system. With central deposition, the non-interacting hot particle model predicts stability at $\beta=4\%$ (with the energetic particles contributing 1/3 of the total β) while the fully interacting model also predicts stability if the hot particle deposition is sufficiently peaked. Off-axis deposition deteriorates the stability properties in both models and yields similar results for all the cases considered except for low field side deposition with large perpendicular anisotropy which is significantly more unstable. The mode structures are core-localised for the non-interacting model and more edge-localised in the fully interacting hot particle model.

Free-boundary 3D equilibria with anisotropic pressure

A free boundary version of the 3D VMEC equilibrium code coupled with the NESTOR code for the vacuum computation has been extended to include pressure anisotropy driven by fast particle species described with the variant of a bi-Maxwellian distribution function that satisfies the lowest order solution of the Fokker-Planck equation. A steepest descent energy minimisation technique coupled with a preconditioned algorithm is applied to compute the minimal energy state. The plasma-vacuum interface is varied to guarantee the continuity of the total pressure across it and the vacuum magnetic field must satisfy the Neumann boundary condition that its component normal to this interface surface vanishes. To obtain the vacuum magnetic field, a Green's function method is employed. Off-axis energetic particle deposition in a 2 field period quasi axisymmetric stellarator reactor system has shown that the perpendicular hot particle pressure localises in the region of the fast particle deposition layer for large perpendicular anisotropy, while for large parallel anisotropy the energetic particle pressures remain more or less uniform around the flux surfaces.

2.2.5 Tokamak discharge simulation

The previously proposed ITER reference scenarios still have uncertainties, mainly from the plasma transport and boundary evolution during the plasma current ramp-up phase. While the plasma current ramp-up phase plays an important role to reach the desired flat-top tokamak operation conditions, the complexity of non-linear plasma evolution and operational constraints on CS and PF coils makes it difficult to study the feasibility of the scenarios. The combined DINA-CH and CRONOS simulator has been upgraded for plasma current ramp-up phase

simulation, fulfilling all requirements. As a first practical application, the current ramp-up phase of ITER reference scenario 2 has been studied. The ITER reference scenario 2 is designed to use the maximum inductive current ramp-up capability. Therefore, the risks of violating operational coil current limits and limiting the duration of plasma burn still exist in the previously proposed reference scenario.

The plasma current was ramped up from 0.4MA to 15MA over about 100 sec and the plasma density was assumed to increase linearly in time (Fig. 2.2.5). The plasma is initially limited on the outboard side, expands and reaches its fully diverted shape through the X-point formation. Initially applied vertical position control with a virtual radial position control stabilizes the plasma position until the X-point formation, and then shape control turns on with a smooth transition for the control of 6 gaps (Fig. 2.2.6). Heat transport is assumed to follow an ohmic energy confinement scaling law and sawtooth events are triggered simultaneously for the rearrangement of plasma current and heat in both codes.

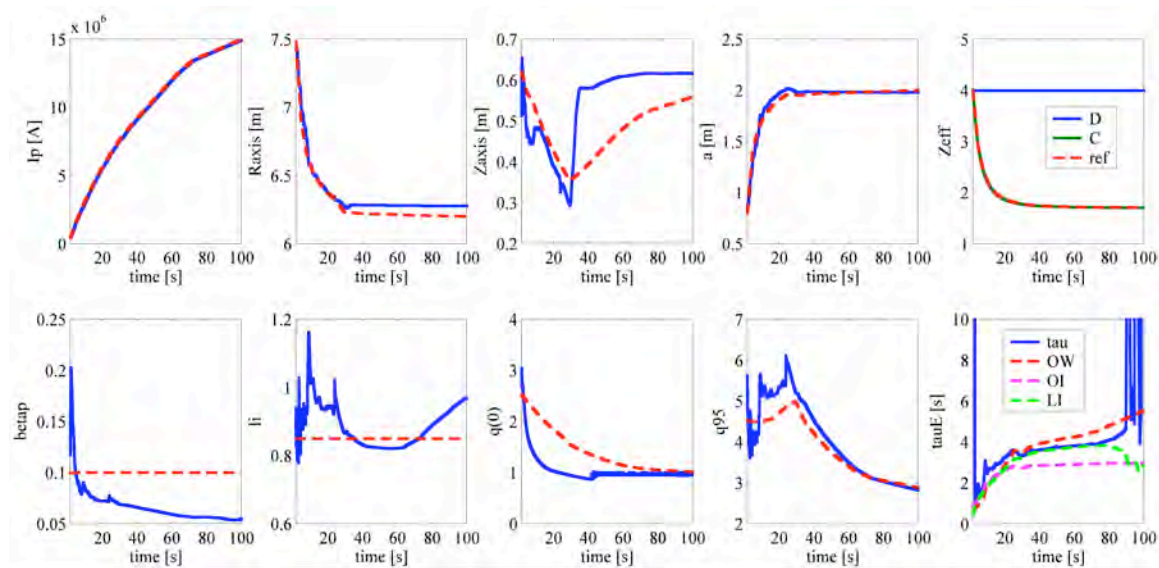


Fig. 2.2.5 Time traces of plasma parameters, plasma current, R_{axis} , Z_{axis} , minor radius, effective charge, beta poloidal, internal inductance, safety factors (q_0 and q_{95}), and energy confinement times (blue lines: DINA-CH / CRONOS combined simulator; dashed red lines: ITER reference scenario 2 except the ohmic confinement time scaling)

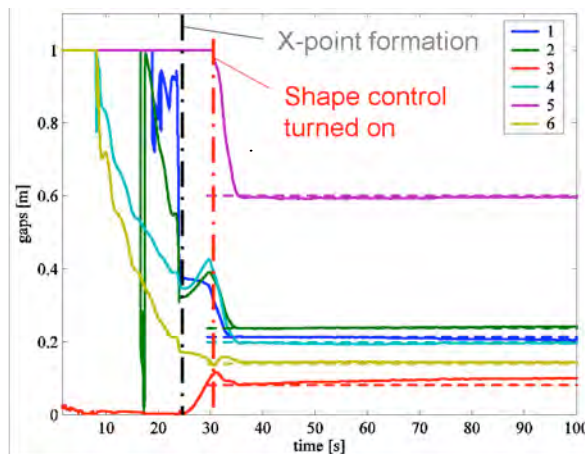


Fig. 2.2.6 Time traces of 6 gap measurements (continuous lines: DINA-CH / CRONOS simulation; dashed lines : reference gaps).

Non-linear plasma current ramp-up simulations show that the evolution of plasma parameters, such as the plasma poloidal beta and internal inductance, is not as optimistic as those in the previously proposed reference scenario 2. The plasma poloidal beta which is related to the ohmic flux consumption causes the CS1 coil current (Fig. 2.2.7) to cross its limit, and restricts the duration of plasma burn. Either the application of additional heating power during the current ramp-up phase or a modification of the reference coil current inputs for control has been shown to a practical solution. Though the vertical movement is more unstable with a higher plasma inductance, the level of instability was still controllable.

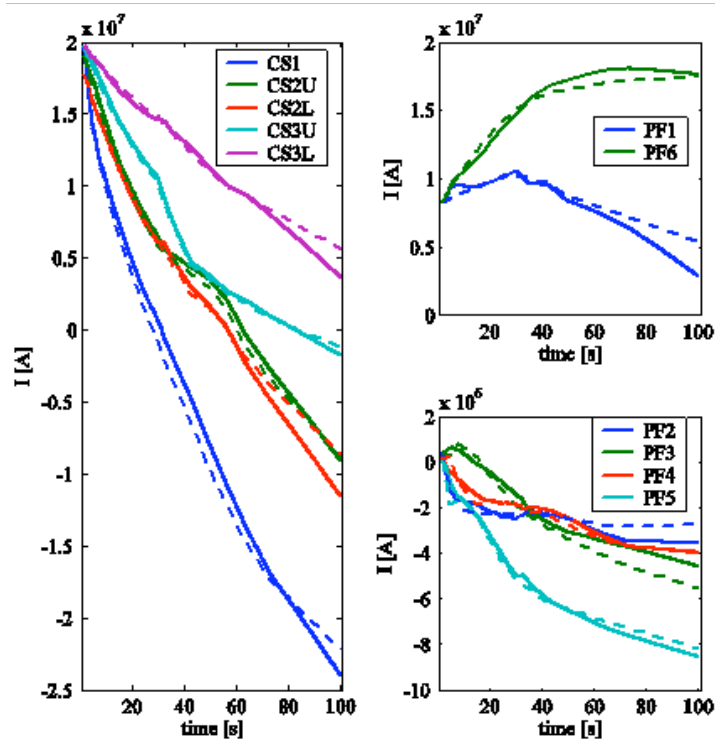


Fig. 2.2.7 Time traces of coil currents (dashed lines: ITER reference scenario 2)

2.2.6 Integrated Tokamak Modelling

The various contributions of CRPP to the Integrated Modelling Projects (IMP's) are summarized below.

Significant contributions to the IMP#2 project have been provided by the CRPP. In particular, a first version of a sawtooth module to be included in transport simulations has been delivered. It still needs to be adapted to the ITM data structure; however, it is already available on the CRPP public svn server at the following address: <http://crppsvn.epfl.ch/repos/sawtoothmodel/>. Collaboration with CNR-Milan has been started in order to provide a NTM module. The latter will provide the predicted island width and frequency evolution from the plasma parameters provided by data analysis or transport simulations.

The KINX ideal MHD stability code with magnetic separatrix, and its companion equilibrium code CAXE have been transferred to the ITM Code Platform. Studies of the ideal MHD limits in the presence of holes in walls have been performed with the resistive wall mode version of KINX (KINX/RWM) as a part of IMP#1.

The Alfvén and ICRF global wave code LION has been optimized in view of its frequent usage in the frame of IMP#5.

The CRPP will also contribute to the 3D-MHD project of the TF-ITM as well as to the effects of pressure anisotropy on MHD equilibrium and stability.

2.3 Operation of a specialised basic plasma physics device, TORPEX

The CRPP Basic Plasma Physics group addresses fundamental aspects of the physics of fluctuations, turbulence and related transport phenomena in toroidal magnetised plasmas. The experiments are conducted on the TORPEX device, characterized by low plasma densities and temperatures, allowing high-resolution measurements of plasma parameters and wave fields throughout the plasma cross-section. Plasmas are confined by a toroidal magnetic field up to $B_T=0.1T$, and a smaller vertical component, $B_z \leq 50mT$, corresponding to a simple configuration incorporating the main ingredients for drift wave instabilities and turbulence in fusion relevant scenarios, namely pressure gradients and magnetic field line curvature. Highly reproducible discharges of different noble gases with electron density and temperature in the range $n_e \sim 10^{16}-10^{17}m^{-3}$ and $T_e \sim 5-10eV$ are driven during more than 2s by microwaves ($P < 50kW$) at $f=2.45GHz$, in the electron cyclotron (EC) range of frequencies. Parameters such as the neutral gas pressure, the location of the EC resonance and the amount of injected power can be varied to control density and temperature profiles.

Following previous preparation efforts, a number of physics studies were completed in 2007, including the identification of the effect of the vertical magnetic field (or connection length) on the nature of the dominant instability, the nonlinear interactions of the fluctuations and the spectral energy cascade on the way to the turbulence, a full reconstruction of the mechanisms behind the generation of turbulence structures or blobs, their propagation, statistical properties, transport effects and link with background plasma profiles. In addition, a significant effort of theoretical interpretation of TORPEX plasma scenarios using a 2D fluid model has been conducted. Several technical developments and preparation for diagnostic upgrades were also undertaken, as discussed at the end of this Section. The second and third PhD theses of the first generation of graduate students working on TORPEX were completed successfully in 2007.

2.3.1 Linear and nonlinear properties of interchange and drift-interchange instabilities naturally occurring in TORPEX

Instabilities of different nature develop and propagate on TORPEX. For a wide range of values of the vertical field they can coexist on the low field side of the maximum background density. This is shown in Fig. 2.3.1, which represents the power spectrum of density, δn , and electrostatic potential fluctuations $\delta\phi_p$ for different values of the vertical field, $B_z=[0.6,1.8] mT$. The power spectra shown in the figure correspond to measurements taken on the high field side, at $R-R_0=-9 cm$, and on the low field side, at the position of maximum level of density fluctuations.

Two low frequency modes with different properties are detected in the power spectra of δn . The first one is measured both on the high and on the low field side. Its frequency ($\sim 4kHz$) and amplitude are barely affected by the value of B_z . This mode is identified as a drift-interchange, whose linear dispersion relation is consistent

with that of a drift wave and whose instability threshold is strongly affected by the curvature of the magnetic field lines.

The second mode is measured only on the low field side, in a layer of radial extension of 5 to 8cm. Its spectral features are strongly affected by the magnitude of the vertical field. The peak associated with this mode is broad in frequency and has low amplitude at the lowest B_z . With increasing B_z , the mode becomes narrower and its amplitude increases up to a point (for $B_z > 1.0\text{mT}$) where it dominates the power spectrum of fluctuations. This instability has been identified as a pure interchange mode, destabilized by the curvature of the magnetic field in the region where the magnetic field gradient and the pressure gradient are co-linear. It propagates mostly across the magnetic field with a perpendicular wavelength fixed by the value of the vertical displacement of the magnetic field line after a complete toroidal turn. The development of turbulence from a linear state has been studied for both instabilities and was found to be independent of the exact nature of the mode. It has been observed that the power spectrum broadens during convection and that the broadening of the spectrum is mainly due to wave-wave nonlinear interactions between the unstable mode and the other spectral components. The first step of the process is the generation of higher order harmonics from the fundamental mode, then the filling of the spectral regions in between harmonics follows via nonlinear three-wave interactions. Only at a later stage is the range of nonlinear interactions extended to spectral components with frequencies significant larger than the frequency of the mode. Figure 2.3.2 shows the variation of spectral power due to nonlinear interactions relative to the total variation of power, calculated with two probes separated by 0.6cm along the direction of convection. The figure refers to the case of the drift-interchange instability, for $B_z=0.6\text{mT}$. As shown by the negative value of $\Delta P_{\text{NL}}/\Delta P_{\text{TOT}}$ at 4kHz, the instability loses its energy to the other spectral components through nonlinear interactions, which correspond to a direct cascade mechanism.

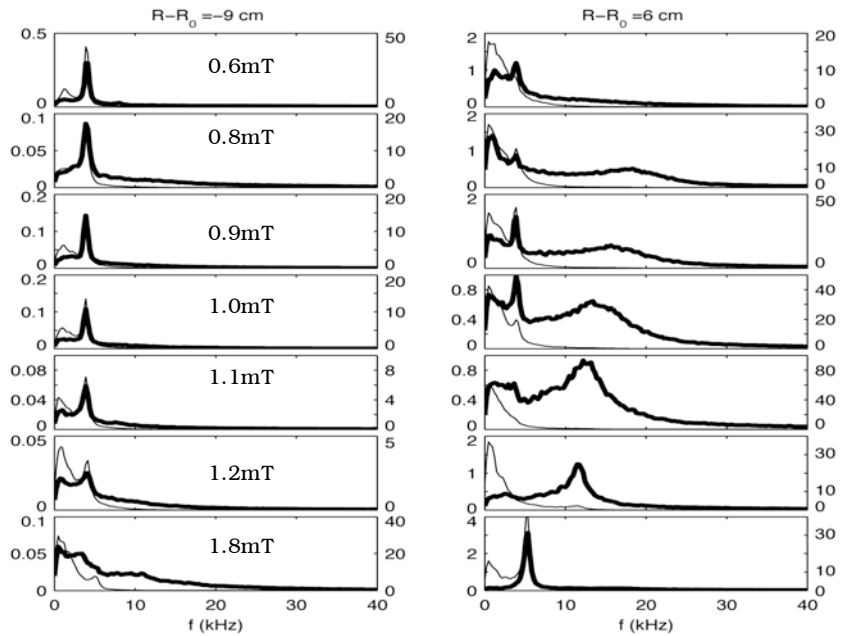


Fig. 2.3.1 Power spectrum of δn (thick line, left axis) and $\delta\phi_p$ (thin line, right axis) measured on the high field side (left) and on the low field side (right), for different values of B_z , increasing from top to bottom Units are V^2/kHz .

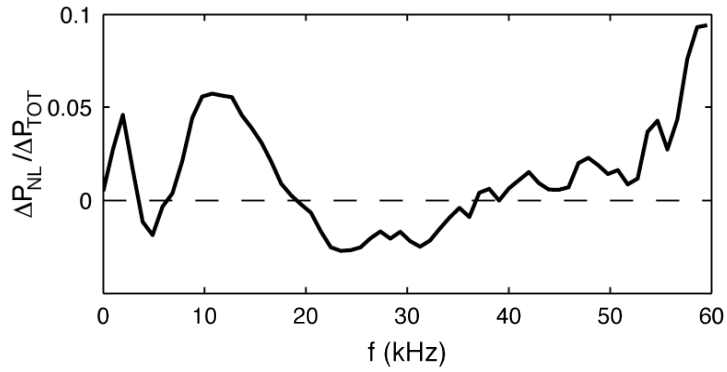


Fig. 2.3.2 *Relative variation of spectral power due to nonlinear interactions with respect to the total variation of spectral power. Negative values indicate a loss of energy, while positive values denote an energy gain.*

2.3.2 Drift wave antenna excitation in TORPEX

An electrostatic antenna tunable in vertical wave number is used to excite density perturbations in TORPEX plasmas. The antenna is positioned at the maximum density gradient, the source of free energy for drift waves. By applying a coherent detection technique to Langmuir probe signals, we can directly determine the antenna induced density response. Figure 2.3.3 shows an example of the density response for three different tuned antenna frequencies in the plasma frame, measured using the HEXTIP probe array.

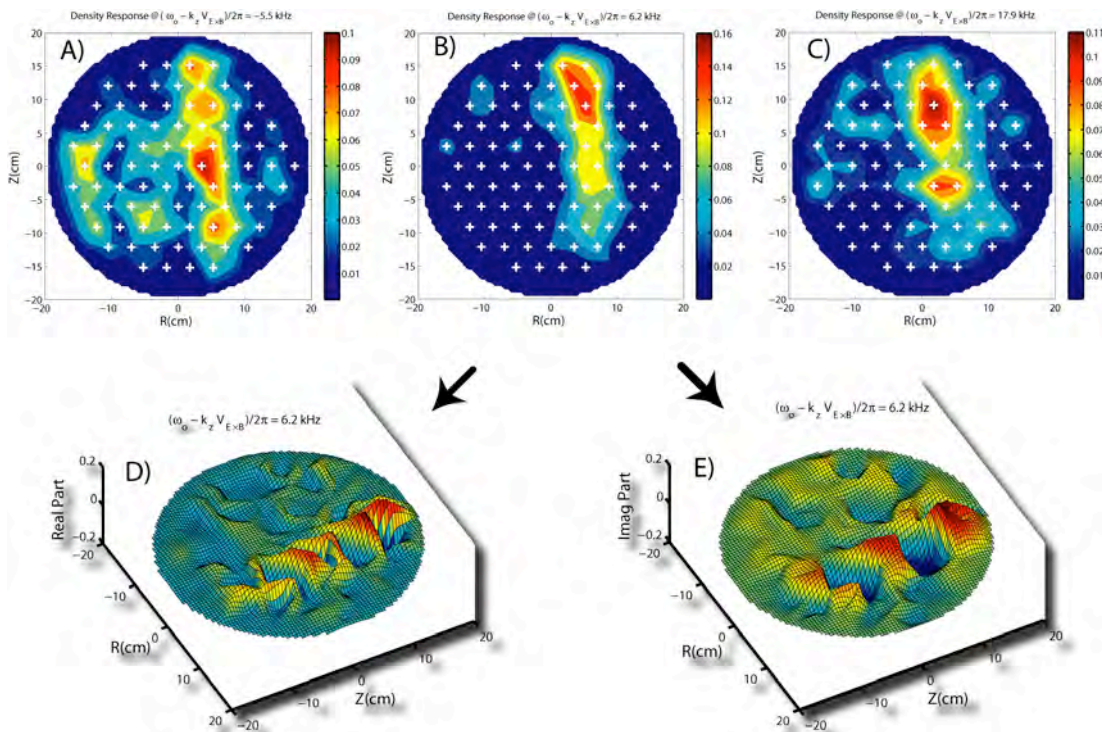


Fig. 2.3.3 *The plots A-through C represent the density response for three different frequencies measured with HEXTIP (white crosses). Shown in D is the real part of the response function when the antenna is tuned at 6kHz where a clear wave-like pattern is observed. Similarly, E represents the imaginary part of this density response.*

The density response induced by the antenna is described using a generalized Hasegawa-Wakatani fluid model, with $T_i=0$ and T_e constant, and taking into account magnetic field curvature and the experimental density gradients and antenna k-spectrum. Figure 2.3.4 shows dependence upon the tuned antenna frequency of the measured density response and of that calculated using the generalized Hasegawa-Wakatani fluid model. One peak can be clearly identified as due to the drift wave. The other peaks remain unexplained with the current linear model and suggest nonlinear wave-wave coupling.

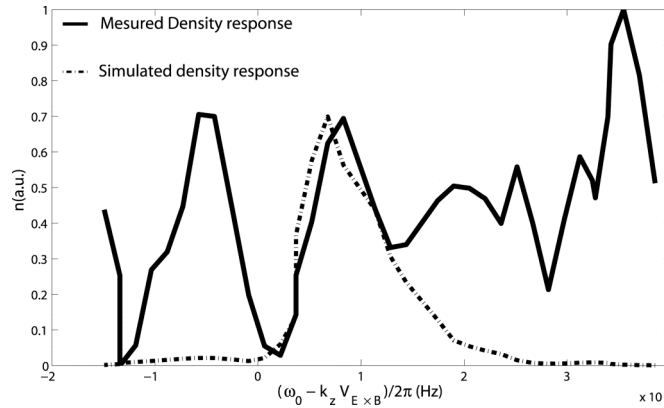


Fig. 2.3.4 The solid line represents the measured density response and the dashed-dot line is the calculated linear response.

2.3.5 Blob physics: Scenario and mechanism for blob formation

At the edge of magnetic confinement devices, such as tokamaks, stellarators, reversed field pinches and linear devices, a large fraction of the anomalous particle and heat transport is attributed to the presence of *blobs*. These are intermittent isolated structures with increased density and temperature with respect to the surrounding plasma which extend along the field lines and propagate away from the plasma core.

Recently, we have identified a scenario in which blobs with properties similar to tokamak observations are observed to originate at the crest of a coherent interchange wave. We use a low level of EC power $P_{EC}=400W$ with standard $B_T=76mT$ and relatively large $B_z=2.3mT$. This experimental setup results in a separation of the plasma in two regions with different dynamics: a main plasma region for $-5 < r < 5cm$, dominated by a coherent interchange wave, and a region on the low-field side for $r > 5cm$ with negligible plasma production, dubbed source-free region. The source-free region is characterized by the propagation of plasma blobs, resulting in intermittent transport events.

In Fig. 2.3.5(a,b), we illustrate the nature of the fluctuations in the two regions using 2D profiles of skewness S and kurtosis K of ion-saturation signals. In the main plasma region for $-5 < r < 5cm$, fluctuations are characterized by coherent oscillations at a frequency of $3.9kHz$. In Fig. 2.3.5(a), the 2D profile of the spectral power in the range $f=3.9 \pm 1kHz$ peaks around the position of maximum $\nabla p/p$, where such range represents approximately 50% of the total spectral power of the fluctuating signal. At this position, $S \sim 0$ and $K \sim 2$, consistently with the presence of coherent oscillations. The wave propagates upwards with a velocity of $V_z \sim 1200ms^{-1}$, consistent with the time averaged v_{ExB} profile in Fig. 2.3.5(c). The wave is identified

as a drift-interchange mode with a vertical wave number $k_z \sim 30 \text{m}^{-1}$ and an upper bound for the parallel wave number $k_{\text{max}} = 0.046 \text{m}^{-1}$.

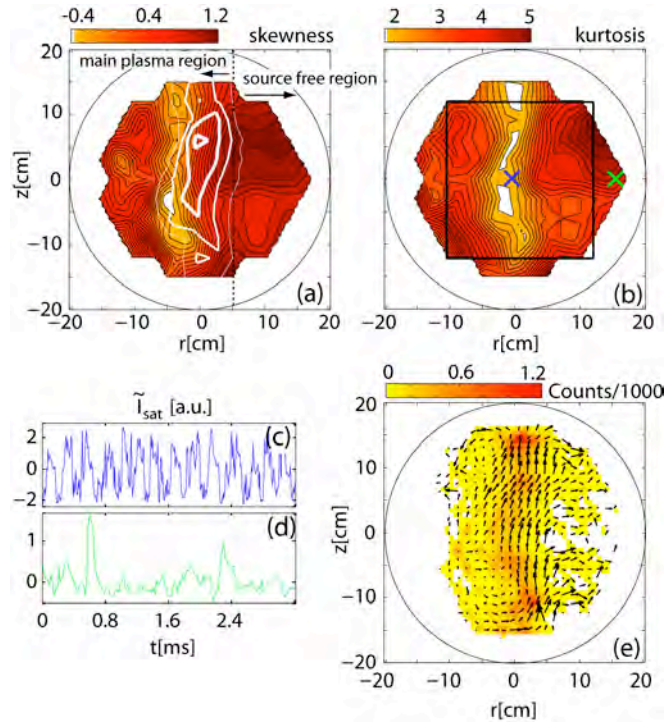


Fig. 2.3.5 Poloidal profiles of (a) skewness and (b) kurtosis of ion saturation signals. In (a) the profile of spectral power in the frequency range $3.9 \pm 1 \text{kHz}$ is shown in white and localizes the drift-interchange wave. Contours correspond to 90%; 60%; 30% and 10% of the maximum spectral power. (c,d) Ion-saturation signals at the two locations indicated in (b) show coherent fluctuations in the main plasma region (blue cross) and intermittent bursts at the edge (green cross). (e) Mean velocity field of positive structures and histogram (in colour) of trajectory counts. The generation mechanism is investigated using the modified CS method

In the source-free region, the fluctuation spectrum is broad and exempt from coherent modes. The skewness is positive ($S \sim 1$) indicating the occurrence of intermittent bursts as shown in Fig. 2.3.5(d). Figure 2.3.5(e) shows the mean velocity field of positive structures lasting between $40 \mu\text{s}$ and $200 \mu\text{s}$, as evaluated by a spatio-temporal pattern recognition method. The pattern suggests that the bursts are associated with the presence of blobs that originate in the main plasma region and propagate outwards into the source-free region as individual coherent structures over distances of the order of the minor radius.

To investigate the mechanism for blob generation, time-resolved 2D profiles of n_e , T_e , V_{pl} and velocity fields are required. These are obtained by performing a conditional sampling over many blob events of the I-V characteristic of a Langmuir probe in a time window centered on the blob detection. Figure 2.3.6 illustrates the results of the conditional sampling. Figure 2.3.6(a) shows the time evolution of n_e in the mode region (red) and in the source free region (black). Figure 2.3.6(b-e) shows 2D profiles of n_e at four different times during the ejection of the blob together with the total ExB velocity field. The dynamics of blob formation and ejection from the interchange wave is captured by frames (c-e). A radially elongated density structure forms from the positive cell of the wave, Fig. 2.3.6(c), and a relative displacement between them is obtained, Fig. 2.3.6(d). Finally, the original density structure is is

sheared off by the ExB flow and breaks into two parts, Fig. 2.3.6(e). The new structure on the low field side forms a plasma blob.

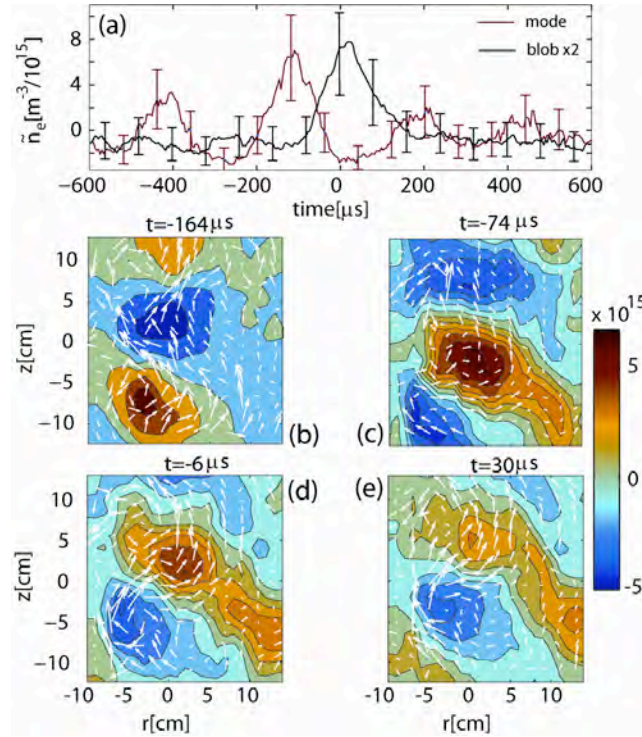


Fig. 2.3.6 Plasma dynamics from the conditional sampling technique: (a) time history of n_e , including uncertainties, in the mode region (red) at $r=1$ cm, $z=5$ cm and in the source free region (black) at $r=13$ cm, $z=5$ cm. Note that this later is multiplied by two for clarity. (b-e) 2D profiles of n_e at different times during blob ejection. Arrows show the instantaneous V_{ExB} profile.

In Fig. 2.3.7, we illustrate the mechanism driving the elongation of the density wave crest. The instantaneous pattern of the fluctuating v_{ExB} in Fig. 2.3.7(a) clearly shows that the interchange mechanism exchanging a zone of high plasma pressure with a zone of low plasma pressure is at play. The interchange drive (inverse of the local radial pressure scale length) is maximum in the region where the pressure negative wave crest is localized, Fig. 2.3.7(a). The time evolution of the interchange drive is shown in Fig. 2.3.7(b) and shows that the elongation of the density cell (at $t \sim 200 \mu s$) follows a sudden increase of the interchange drive.

In order to investigate the link between the blob amplitude and the pressure scale length, we perform the conditional sampling analysis over eight different classes of blob amplitudes. In Fig. 2.3.7(c), we show the dependence upon the blob amplitude of the maximum interchange drive. A monotonic and faster than linear dependence upon the interchange drive is found, showing that the ejection of blobs is preceded by an increase of the pressure gradient that leads to blobs with larger amplitude for larger drives.

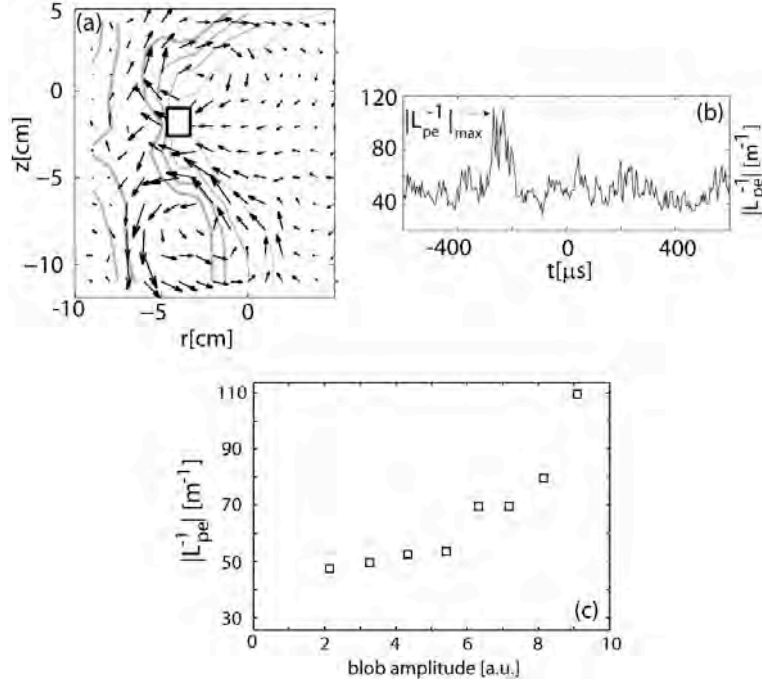


Fig. 2.3.7 A zoomed view of the instantaneous fluctuating v_{ExB} velocity field at $t=-184\mu s$ shows the convective cells interchanging zones of high and low plasma pressure. (b) Time evolution of the interchange drive. (c) Dependence of blob amplitude upon the interchange drive.

A complementary investigation of the blob dynamics in k -space was carried out using the HEX TIP density fluctuations measurements. Figure 2.3.8 shows the k -spectrum for each time frame related to the blob event. This figure reveals a tilting process at play in k -space, which is intrinsically associated with the shearing effect discussed above and results in a channelling of the density fluctuation energy to larger radial wave numbers, leading to an enhanced dissipation.

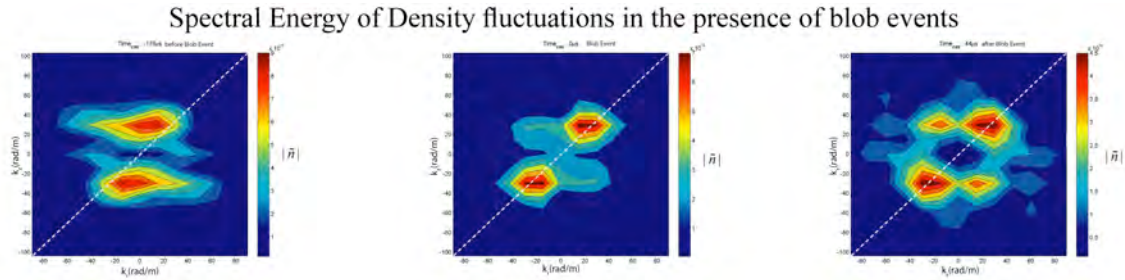


Fig. 2.3.8 Three time frames of the k -spectrum of the density fluctuation energy. These plots emphasize the tilting effect in k -space.

The tilting in k -space is found to precede the blob ejection. It is expected to be associated with generation of Reynolds stress, as $\langle \tilde{V}_z \tilde{V}_r \rangle \propto k_r k_z |\tilde{\Phi}|^2 \sim k_r k_z |\tilde{n}|^2$. The results of the two types of analysis underline the importance of fluctuation-induced vertical flows prior to the blob ejection. These observations also highlight the potential of TORPEX for further detailed investigations of the Reynolds stress generation in electrostatic turbulence.

In general, these results detail a fundamental phenomenon in plasmas and can be used to validate theories and numerical simulations of blob dynamics. Similarly to

the tokamak SOL, the magnetic configuration features open field lines, and a B and magnetic field curvature. Blobs in TORPEX exhibit universal statistical properties with strong similarities with observations in the tokamak SOL. Thus the observed dynamics may shed light on the blob ejection mechanism in tokamaks, where there are strong indications that blobs result from interchange instabilities in the SOL.

2.3.6 *Blob physics: Role of pressure gradients on the formation of blobs and turbulent structures*

The cause of the radial elongation of an interchange mode that is found to be at the origin of the formation of blobs has been studied using measurements of the Langmuir probe array HEXTIP, which covers most of the plasma cross-section. Two different scenarios are identified. In one case, the mode grows from a steep density profile. A statistical analysis reveals a monotonic dependence of the probability for the radial elongation of the mode upon the preceding maximum value of the vertically averaged inverse radial density scale length.

In the other scenario, the mode is found to be in a saturated stage before it radially elongates. The events when the latter happens are compared with the average evolution of the mode. The result is illustrated in Figure 2.3.9. The difference in density between the events where an elongation of the mode takes place and the average mode evolution is shown. Also shown are the contours of the positive (solid lines) and negative (dashed lines) wave crests. While the difference is small at the beginning, a clear trend is seen in the second and third frames. Positive values at the left of negative wave crests as well as negative values at the right of positive wave crests indicate an overall steepening of the density profile preceding the mode radial elongation.

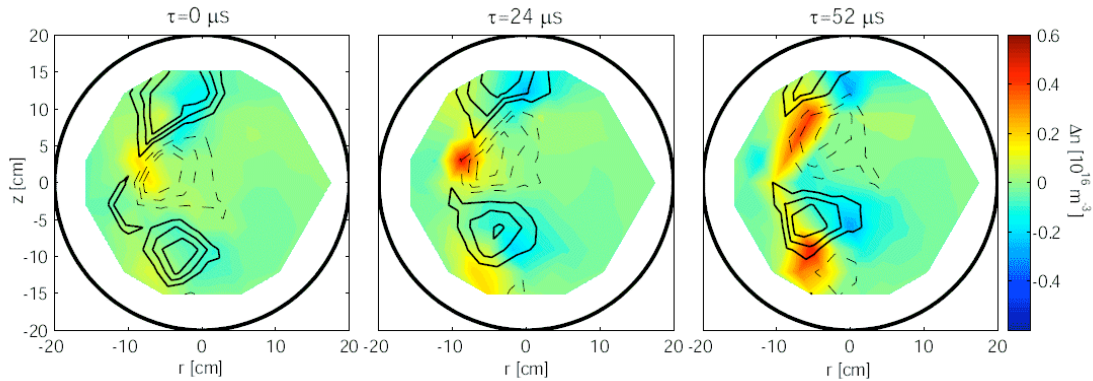


Fig. 2.3.9 *Variation in density during blob ejection for the cases where an elongation of the mode takes place with respect to the average evolution of the mode. The three time frames show the result before the radial elongation of the mode and indicate a steepening of the density profile. Also shown are the contours of the positive (solid lines) and negative (dashed lines) wave crests.*

2.3.7 *Characterisation of transport in the scenario with turbulence and blobs*

A complete characterisation of the transport across the magnetic field was made for the blob scenario described in the previous Sections. The contributions to the transport associated with plasma waves and blobs are identified and quantified. Either mechanism can dominate in a different plasma region. The fluctuation-

induced flux, Γ , is maximum in the main plasma region (Fig. 2.3.10a), where an interchange mode is destabilised by the pressure gradient and by the curvature of the magnetic field. The heat flux, Q , is convective, with $Q \propto \Gamma$ (see inset in Fig. 2.3.10a). The results obtained from time-space and Fourier analyses are compared for the radial component at midplane. In the main plasma the results from the two methods are in qualitative agreement. A quantitative discrepancy by a factor ~ 5 is ascribed to the averages implied by the time-space method. In addition, the Fourier analysis reveals that the coherence between density and potential fluctuations drops to zero in the source-free region, making the measurement of Γ and Q meaningless.

In the source-free region the cross-field transport is mostly due to macroscopic structures, characterised by an excess of density with respect to the background plasma (Fig. 2.3.10b). These structures are identified as blobs, propagating radially outward (Fig. 2.3.10c). The blob-related transport rate is comparable with that measured in the main plasma, indicating that blob ejection represents an efficient channel for cross-field losses. The blob propagation is tightly correlated with the instantaneous $E \times B$ velocity, to which two terms contribute. The first term, $v_{0,E \times B}$, comes from the background time-averaged electric field and has a dominant vertical component for the scenario described herein. According to the theory, the second term, $v_{p,E \times B}$, is due to a ∇B -induced polarization of the blob, producing a vertical electric field, hence a $E \times B$ velocity component along the major radius direction. We find the two to be comparable in magnitude, $|v_{0,E \times B}| \sim |v_{p,E \times B}|$, in the source-free region, consistently with the observed blob trajectories (see inset in Fig. 2.3.10c).

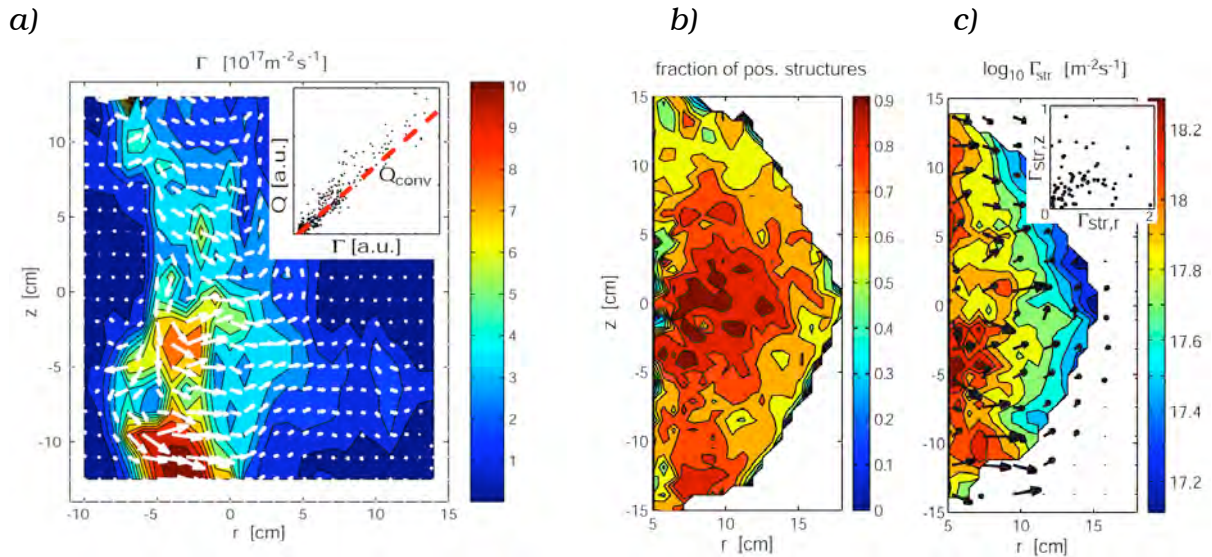


Fig. 2.3.10 (a) Fluctuation-induced flux measured through time-space analysis. The inset shows the dependence of the heat flux upon the particle flux, revealing the convective character of Q . (b) Fraction of positive structures measured in the source-free region. Positive structures, identified as blobs, are mostly observed. (c) Time-averaged particle flux associated with blobs in the source-free region.

2.3.8 Measurement of plasma flows with turbulence and blobs

A Mach probe that can measure simultaneously the plasma flow in the vertical and toroidal directions over the 2D poloidal cross-section was installed on TORPEX. For similar imposed parameters, the flows in the four magnetic configurations given by the different combinations of sign of the magnetic fields have been measured. The

time averaged radial profiles appear consistent with the equilibrium ExB drift, but the amplitude of the measured toroidal velocity is largely underestimated by this drift.

In the absence of drifts, it is expected that the plasma should enter in the sheath with the ion sound speed and the flow being symmetric along the field line. This is not the case in TORPEX plasmas. The large drifts strongly affect the toroidal flow along the same magnetic field line: the plasma flows with the ion sound speed at one end of the field line but with almost zero flow at the opposite end. To understand these discrepancies, the role of parallel currents will need to be assessed.

We have also investigated the question of whether or not a density blob carries momentum when it moves radially. For the well established experimental scenario on TORPEX in which blobs are generated, we have measured the 2D profile of the toroidal velocity. Using the conditional sampling technique, we reconstructed the time evolution over the cross-section of the toroidal velocity correlated with a blob detected at the plasma edge. Figure 2.3.11 summarises our observations. Before the blob detection ($\tau=0$), the normalised pressure gradient increases. This accelerates the plasma in the toroidal direction, and leads to an increase of the interchange mode amplitude. This “excess” of toroidal velocity is expelled and moves radially with the density blob. We have shown that there is a linear relationship between the increase of the interchange drive and the toroidal acceleration of the plasma.

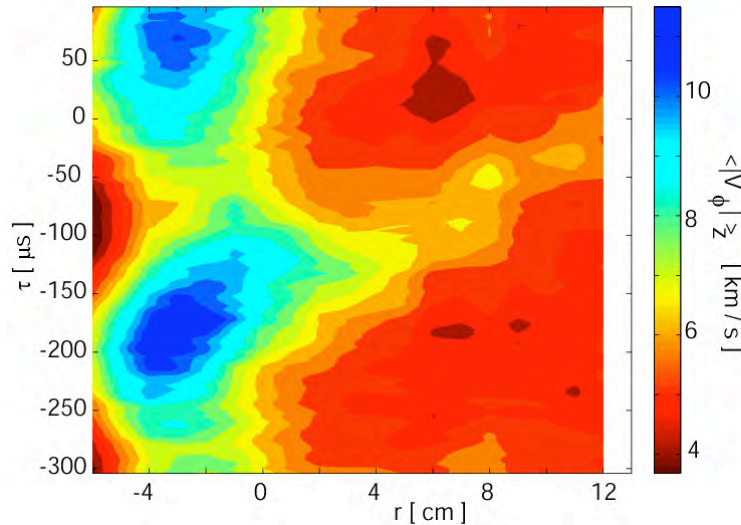


Fig. 2.3.11 Time evolution of the radial profile of the toroidal velocity amplitude, averaged over the vertical direction. The density blob carries momentum during its radial trajectory.

2.3.9 Universal aspects of fluctuations and turbulence

The effort on the characterisation of plasma fluctuations with their statistical properties continued. The method we proposed for revealing the universal character of the density fluctuations has been successfully applied to TCV data. The kurtosis and the skewness of a large number of density signals measured in the SOL of the tokamak are related by the same quadratic polynomial as the one found for TORPEX. This reinforces the prominent role played by interchange turbulence at the edge/SOL transition in tokamaks, already suggested by numerical simulations.

We have also evaluated the statistical properties of quantities other than the electron density. This has been done in the experimental scenario in which blobs are produced. The radial profile of the skewness of different quantities such as the fluctuating electron temperature, plasma potential, and the vertical and toroidal Mach numbers, was reconstructed. Even if these profiles are quite different, it will be interesting to determine if these fluctuations keep a universal character and in particular if the Beta distribution is still the PDF that provides the best fit with the experimental distributions.

2.3.10 Theory supporting basic plasma physics studies

Theoretical investigations of plasma dynamics in the TORPEX experiment have focused on the study of interchange-dominated turbulence. Owing to the flute character of the interchange mode, two-dimensional three-field fluid equations, valid in the typical TORPEX parameter regime (i.e., $\beta \ll 1$, negligible electromagnetic effects, $T_i \ll T_e$), have been derived from the drift-reduced Braginskii equations. A code has been developed to solve this system of fluid equations.

By exploring the character of turbulence when the vertical magnetic field and the plasma source intensity are varied, a theoretical framework has been built of turbulence in simple magnetized toroidal plasmas. The simulations have shown the surprising presence of two turbulent regimes. The increase of the importance of the $E \times B$ shear, leading to a lower perpendicular transport, and the steepening of the plasma profiles, with an associated increase of the peak density and temperature, closely recall the L-H regime transition observed in tokamaks. Typical snapshots of ϕ from a simulation in the first regime (that we have denoted as the L-mode) are shown in the upper panels of Fig. 2.3.12. In this regime, background shear flow effects are negligible, and the interchange instability shows an intermittent character with the emission of plasma blobs that transfer plasma from the source region to the low field region, where plasma is eventually lost due to parallel absorption. The time-averaged profiles of T_e , ϕ , and n show an exponential decay on the low field side where the interchange dynamics is active. We have evaluated analytically the properties of the low confinement regime, obtaining expressions for the plasma gradients and for density and heat transports that agree well with the simulation results.

By increasing the plasma source strength or reducing the vertical magnetic field, the character of turbulence changes, reaching a new regime (denoted as the H-mode) in which a strong $E \times B$ shear flow appears. This flow limits the perpendicular diffusion, thereby causing the peak density and temperature to increase and the plasma profiles to steepen. The lower panels in Fig. 2.3.12 show typical snapshots and profiles in the H-mode regime.

The intermittent character of turbulence reported from the experiments suggests locating TORPEX turbulence in the L-mode regime. The theory provides a recipe to explore the accessibility of the H-mode in a dedicated experimental campaign.

Theoretical studies of TORPEX turbulence follow two avenues. The first focuses on including the drift-wave dynamics into the fluid model. This will require the development of a fully 3D code able to take the parallel dynamics into account. The study of the linear theory has been undertaken, and initial results show the enhancement of the importance of the drift wave dynamics in the presence of a low vertical field, as confirmed by experimental results. The second concentrates on the use of the same diagnostic tools developed for the TORPEX experiment in the analysis of simulation results. This will lead to a direct comparison between

experimental and simulation results, and to the definition of a metric to assess the accuracy of a simulation.

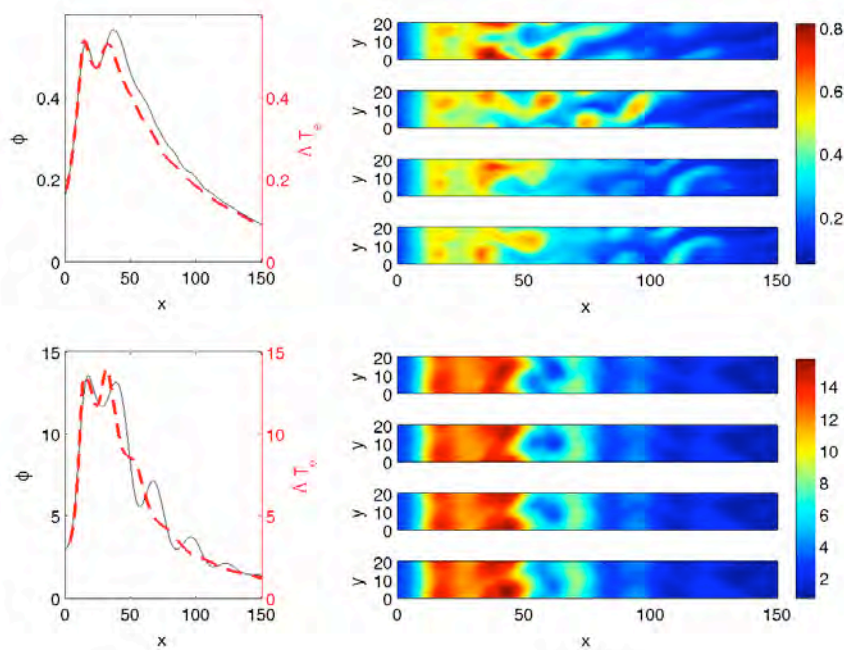


Fig. 2.3.12 Time-averaged profiles of potential and temperature, with typical potential snapshots, for L-mode (upper panels) and H-mode (lower panels) simulations

2.4 Materials research

The main objective of the Fusion Technology Materials (FTM) group is to investigate the effects of the damage produced by irradiation in a variety of materials, in particular candidate materials for structural components of future fusion reactors but also pure metals and model alloys. This group is located at the Paul Scherrer Institute (PSI) in Villigen.

In fusion reactors, the plasma facing (first wall, divertor) and breeding-blanket components will be exposed to plasma particles and electromagnetic radiation and will suffer from irradiation by 14MeV neutrons that are the product, together with energy and helium nuclei, of the fusion reactions between deuterium and tritium nuclei. The high-energy fusion neutrons will produce atomic displacement cascades and transmutation nuclear reactions inside the irradiated materials. From the point of view of materials science, atomic displacement cascades induce the formation of point structure defects, i.e. vacancies and interstitial atoms, while transmutation nuclear reactions yield the production of impurities, e.g. helium or hydrogen gas atoms.

Key parameters for the first wall in fusion power reactors with a fusion power of 3 to 4GW and in quasi-continuous operational mode include a total neutron flux of 10 to $15 \times 10^{14} \text{ n/cm}^2 \cdot \text{s}$, a neutron wall loading of 2 to 3 MW/m^2 , an integrated wall load of 10 to 15 MWy/m^2 , a surface heat load of 0.1 to 1 MW/m^2 and a volume power density of 20 to 30 W/cm^3 . The accumulated dose will amount to 20-30dpa/year in steels, while the gas produced by transmutation nuclear reactions will amount to 10-15appm He/dpa and 40-50appm H/dpa, also in steels.

The final microstructure of irradiated materials results from a balance between radiation damage and thermal annealing. It may be formed of small defect clusters, dislocation loops, precipitates, stacking-fault tetrahedra, voids and/or helium bubbles (Fig. 2.4.1, left). This microstructure has a strong impact on the physical and mechanical properties of the irradiated materials. It may engender important hardening (Fig. 2.4.1, right), loss of ductility, loss of fracture toughness and creep strength, as well as macroscopic swelling of the materials. These effects are the main factors limiting the choice of candidate materials. The residual radioactivity of a large amount of exposed materials is also a concern and will govern the handling methods, dictate the storage periods and the overall waste management and recycling scenarios. The development strategy that takes into account these limitations has led to the development of the so-called low or reduced activation materials.

From the technological point of view, the efficiency of fusion power reactors will be mainly limited by the temperature window for use of the structural materials, which will be mainly limited by their mechanical resistance under irradiation. Candidate structural materials for plasma facing and breeding-blanket components have a chemical composition that is based on low activation elements (Fe, Cr, V, Ti, W, Si, C). They include mainly reduced activation ferritic/martensitic (RAFM) steels, oxide dispersion strengthened (ODS) RAFM steels, ODS reduced activation ferritic (RAF) steels, vanadium-base alloys, tungsten-base materials, and fibre reinforced SiC/SiC_f ceramic composites. Each alternative alloy class exhibits specific problems arising from radiation damage. For the time being, the most promising class of alloys are the RAFM steels for which the greatest technology maturity has been achieved, i.e. qualified fabrication routes, welding technology and a general industrial experience are already available.

As no controlled intense source of 14MeV fusion neutrons is presently available on earth, it is necessary to simulate experimentally the effects of 14MeV neutrons, by using for instance fission neutrons. Until December 2003, the FTM group was using preferably the high-energy (590MeV) proton beam of the PSI accelerator, through the Proton Irradiation Experiment (PIREX) facility. Since April 2004, most irradiation experiments are being performed with a mixed spectrum of high-energy protons and spallation neutrons by using a combination of the PSI proton accelerator and the target of the Swiss Spallation Neutron Source (SINQ).

Like 14MeV neutrons, 590MeV protons produce atomic displacement cascades and transmutation nuclear reactions within the irradiated materials. One of the main advantages of the 590MeV protons is to generate high production rates of impurities, which cannot be achieved with any other currently available irradiation source. While proton irradiations in PIREX were producing about 130appm He/dpa and 800appm H/dpa (in steels), irradiations in SINQ produce about 50appm He/dpa and 450appm H/dpa (in steels). However, in order to investigate the material properties changes and degradation under different irradiation conditions, the FTM group is also involved in specific neutron irradiations performed in reactors in the U.S.A., the Netherlands, Belgium and Hungary.

The design of materials with properties adequate for use in an irradiation environment requires an understanding of the effects of irradiation on their physical and mechanical properties. The FTM group has been active in that field for several years within the framework of the European Fusion Development Agreement (EFDA) and collaborates with many research institutes and industries in Switzerland as well as abroad. The research activities of the FTM group include basic research on radiation damage in pure metals and alloys, development and characterisation of low and reduced activation materials for fusion power reactor applications, design activities and small specimen test technology in relationship with the future International Fusion Materials Irradiation Facility (IFMIF), an intense source of 14MeV neutrons, and characterisation of materials destined to

ITER. The scientific approach adopted by the FTM group to understand the fundamentals of radiation damage in metals and alloys is based on investigating the structure/mechanics relationships at different length scales (micro-, meso-, and macroscopic). A range of experimental and numerical tools is used to reach these objectives. The main experimental tools include mechanical testing of sub-sized and standard specimens, scanning and transmission electron microscopy (SEM, TEM) observations, small angle neutron scattering (SANS) measurements, and corrosion experiments. The main numerical tools include ab-initio calculations, molecular dynamics (MD), Monte-Carlo (MC) and dislocation dynamics (DD) simulations, as well as finite element modelling (FEM).

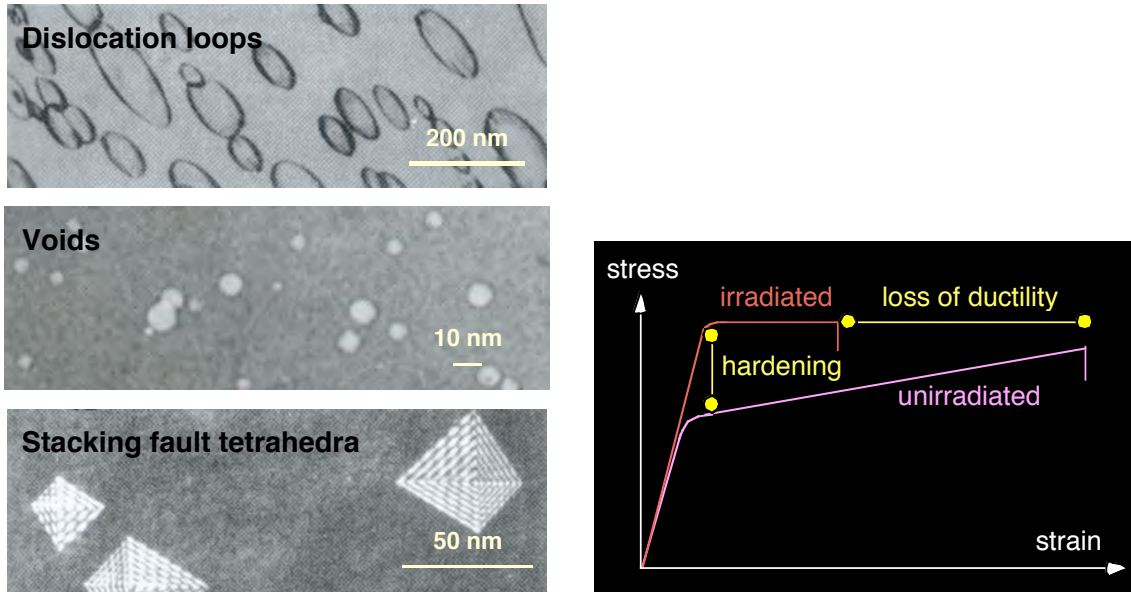


Fig. 2.4.1 Left: Examples of transmission electron microscopy images of irradiation-induced structure defects. Right: Schematic of irradiation-induced hardening and loss of ductility, as measured in tensile tests on irradiated specimens.

2.4.1 Irradiation Experiments

The definitive shutdown of the PIREX facility took place on December 22, 2003. Decommissioning of the PIREX facility was started in March 2004 and achieved in September 2006. A number of specimens of various materials have been irradiated in the Swiss Spallation Neutron Source (SINQ) for two years in 2004-2005. The cooling phase took place in 2006. Post-irradiation experiments started in 2007 and should be completed in 2008.

2.4.2 Underlying Technology Tasks

Contribution to the development of W-Cu composites for fusion applications in collaboration with Technical University in Warsaw

Three ingots of W-Cu composites, with the compositions of 50W-50Cu, 40W-60Cu and 25W-75Cu (in volume percent), as well as two ingots made of Cu, were manufactured at the Technical University in Warsaw. The small ingots (12mm in diameter, 30mm in height) were received in August 2007. One specimen for thermal

conductivity measurements (12mm in diameter, 1mm in thickness) and a series of tensile flat specimens were cut out from each ingot. Thermal conductivity measurements and tensile tests were started at the end of 2007 and will be completed in the first semester of 2008.

Study of the microstructures of the EUROFER 97 and F82H steels in relation to their fracture properties

The microstructures of the F82H and EUROFER 97 RAFM steels have been characterized with metallography, TEM, and SEM equipped with X-ray dispersion analysis system. This activity has been undertaken to pinpoint the microstructural features that control the respective fracture properties of both steels, which have already been shown to be different.

The prior austenite grain (PAG) size was found to be about 80 μm in F82H and 10 μm in EUROFER 97. This is likely to result from the large differences in Ta, Al and O contents between the two steels. In fact, the combination of high O content with low Al content in F82H leaves sufficient O free to combine with Ta. Thus, Ta forms oxides instead of forming small TaC carbides, which act as PAG grain refiners. On the contrary, in EUROFER 97 there is enough Al with respect to O content to form Al oxides, so that all Ta combines with C, resulting in a small dispersion of carbides. EUROFER 97 contains a smaller fraction of martensite laths and more equiaxed sub-grains than F82H. This difference is probably related to the tempering conditions: longer time and higher temperature result in a more tempered microstructure, i.e. in fewer martensite laths. The dislocation density was not measured, but a close inspection of TEM micrographs showed that it is likely to be lower in EUROFER 97, probably due to the longer tempering.

In EUROFER 97, there are at least two types of precipitates: fine ones, smaller than 40nm in diameter, which are more or less homogeneously distributed inside the grains (Fig. 2.4.2, left), and larger ones, typically about 100-200nm in diameter, which are found mainly at the grain boundaries or on the triple points. Chemical analysis proved the existence of two types of precipitates: complex Cr-W-Fe-V carbides and Ta carbides. The complex carbides are more frequent than the Ta ones. There are clearly more precipitates in EUROFER 97 (5vol.%) than in F82H (2vol.%). The size distributions of fine precipitates look similar in both materials. In F82H all precipitates are complex M_{23}C_6 carbides containing Cr, W, Fe and V. Large Al-Ta-O inclusions were also observed in F82H (Fig. 2.4.2, right), which was not the case in EUROFER 97. These large inclusions are expected to impact the fracture toughness properties by acting as possible nucleation sites for micro-cracks.

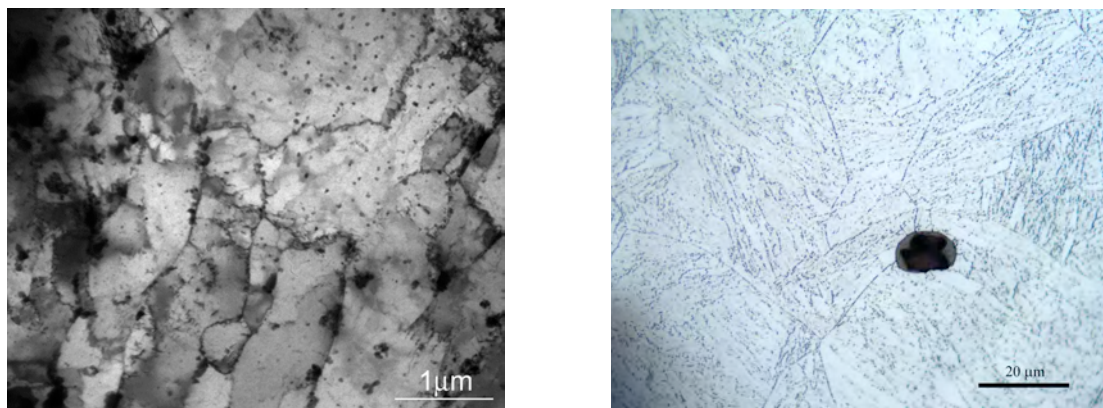


Fig. 2.4.2 *Left: TEM image of fine carbides inside grains of EUROFER 97. Right: Optical micrograph of a large inclusion in F82H.*

Supporting research

Small angle neutron scattering analysis of nano-sized irradiation-induced defects in pure metals and alloys

Nano-sized irradiation-induced defects are believed to significantly contribute to the hardening and/or embrittlement of metallic materials under irradiation, along with the microscopic defects. Transmission electron microscopy (TEM) allows direct observation of defects whose size is larger than about 1nm in weak beam imaging but other techniques have to be used to reveal ultra-fine scale microstructures. Small angle neutron scattering (SANS) is an effective technique to characterize nano-scale distributions of features in terms of number density, size distribution and chemical composition. Typical nano-sized irradiation-induced defects include small, unidentified defect clusters (of vacancy or interstitial type), voids, helium bubbles, small dislocation loops (of vacancy or interstitial type), carbides and/or precipitates.

In 2007 activities have been focused on simulation of the SANS signal for specimens containing a single nano-sized defect. The Electron Microscopy Software (EMS), originally developed by P.A. Stadelmann [Ultramicroscopy 21 (1987) p. 131] to simulate transmission electron microscopy (TEM) images, has been modified to account for the scattering length and wavelength of neutrons. This modified code was used to simulate the SANS signal of a specimens generated by MD. Figure 2.4.3 shows the simulated SANS signal of a 1 million atoms Fe specimen containing a void, 2nm in diameter, in the centre. The simulated SANS signal exhibits an excellent agreement with an analytical calculation of the SANS signal.

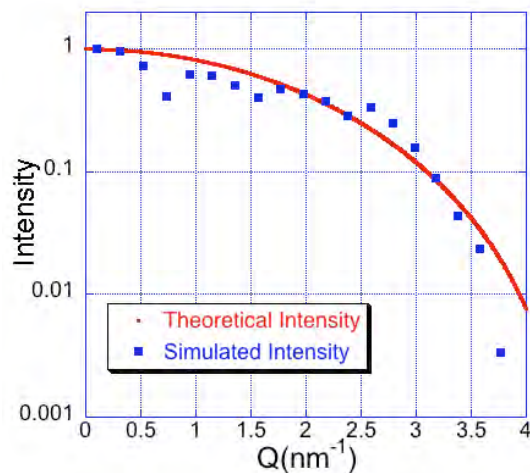


Fig. 2.4.3 Simulation (data points) and analytical calculation (solid line) of the SANS signal (scattering intensity versus scattering vector Q) of a MD specimen containing a 2nm void in the centre.

Modelling of the fracture toughness-temperature curve of the EUROFER 97 RAFM steel in the ductile-to-brittle transition region

Having produced a large fracture toughness database for the EUROFER 97 RAFM steel, based on 0.35T and 0.9T C(T) (compact tension) specimens, and having shown that the behaviour of the toughness in the transition region is somewhat

different from that defined in the ASTM E-1921 standard for “ferritic” steels, an attempt to better assess the overall shape of the median fracture toughness-temperature curve and associated bounds (1% and 99% failure bounds) was done. We just recall here a few ideas that are being used to analyze the temperature dependence of fracture toughness data in the transition region. First, at a given temperature, the scatter of the data is described by the three-parameter Weibull distribution:

$$P(K \leq K_{Jc}) = 1 - \exp\left(-\left(\frac{K - K_{\min}}{K_o(T) - K_{\min}}\right)^4\right)$$

Various models have been developed to account for the crack front length effect on toughness. They predict the following statistical size effect on the measured fracture toughness, B being the crack front length:

$$K_{B_2} = K_{\min} + [K_{B_1} - K_{\min}] \cdot \left(\frac{B_1}{B_2}\right)^{1/4}$$

where K_{\min} is a cut-off value. For structural steels, it was found that the median fracture toughness-temperature curve of 1T-thick specimens is well described by an equation of the type:

$$K_{Jc_median(1T)} = a + b \exp(c(T - T_o))$$

This equation is usually referred to as the Master-Curve that can be indexed on an absolute temperature scale by a reference temperature T_o at a reference fracture toughness of $100\text{MPa}\cdot\text{m}^{1/2}$. The ASTM E1921 standard gives $a=30$, $b=70$, and $c=0.019$ for “ferritic” steels. However, we already showed that the shape of the fracture toughness-temperature curve is somewhat different for EUROFER 97. Since our database contains more than 100 hundred data points, it was possible to make a reliable shape assessment by fitting the coefficients in the previous equation, namely a , b , c , and T_o . Note also that the parameters b and c are strongly correlated. Therefore, we arbitrarily kept the value of c equal to 70 (like in the ASTM E1921 standard) and adjusted the parameter b , which controls the shape of the curve more strongly than c . By combining the Weibull distribution with the Master-Curve equation and using the method of the maximum likelihood estimates, the parameters a , c and T_o were obtained by solving numerically and iteratively the three following equations, where $K_{J,i}$ are the experimental toughness values obtained at T_i :

$$\begin{aligned} \sum_{i=1}^n \ln(2) \frac{(K_{J,i} - K_{\min})^4}{(a - K_{\min} + 70 \exp(c(T_i - T_o)))^5} - \sum_{i=1}^n \frac{1}{(a - K_{\min} + 70 \exp(c(T_i - T_o)))} &= 0 \\ \sum_{i=1}^n \frac{\exp(c(T_i - T_o))}{K_o - K_{\min}} - \sum_{i=1}^n \frac{(K_{J,i} - K_{\min})^4 \exp(c(T_i - T_o))}{(K_o - K_{\min})^5} &= 0 \\ \sum_{i=1}^n \frac{\exp(c(T_i - T_o))(T_i - T_o)}{K_o - K_{\min}} - \sum_{i=1}^n \frac{(K_{J,i} - K_{\min})^4 \exp(c(T_i - T_o))(T_i - T_o)}{(K_o - K_{\min})^5} &= 0 \end{aligned}$$

with

$$(K_o - K_{\min}) = \frac{a - K_{\min}}{\ln(2)^{1/4}} + \frac{70 \exp(c(T - T_o))}{\ln(2)^{1/4}}$$

Note that a value of K_{min} equal to $10\text{MPa}\cdot\text{m}^{1/2}$ was chosen, based upon a fitting of the Weibull distribution on the dataset obtained at $-120\text{ }^{\circ}\text{C}$ (Fig. 2.4.4, left). The numerical solution of the equations yielded the following values: $a=19.5$, $c=0.02313$, and $T_0=-82^{\circ}\text{C}$. Thus, the Master-Curve equation for EUROFER 97 reads:

$$K_{Jc_median(1T)} = 19.5 + 70 \exp(0.02313(T - T_0)) \quad \text{with } T_0 = -82\text{ }^{\circ}\text{C}$$

The experimental fracture toughness data along with associated 1% and 99% failure bounds have been reported in Fig. 2.4.4 (right). The main differences between this Master-Curve and that of the ASTM E1921 standard are first a lower shelf value (19.5 against $30\text{MPa}\cdot\text{m}^{1/2}$) and the steepness of the transition, which appears more pronounced for EUROFER 97 ($c=0.02313$ against 0.019).

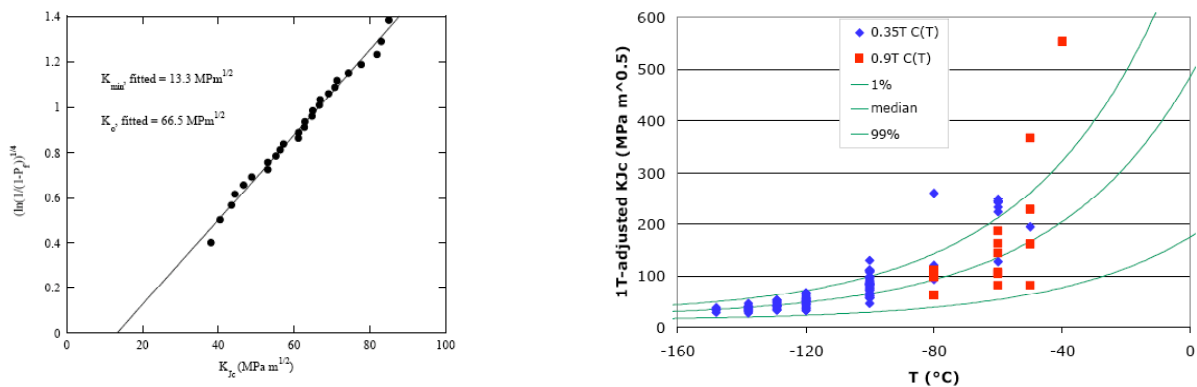


Fig. 2.4.4 Left: Failure probability diagram for 0.35T C(T) specimens tested at -120°C . K_{min} and K_0 are the fitted parameters of the Weibull distribution. Right: Fracture toughness data in the transition along with the Master-Curve for EUROFER 97.

EXTREMAT Integrated Project (IP) of the Sixth European Framework Programme

Activities within the EXTREMAT Project are aimed at:

- Modelling radiation damage and radiation effects on pure W.
- Developing reduced activation, radiation resistant, ODS ferritic steels for high-temperature application in the fusion power reactors.
- Developing reduced activation, radiation resistant, ductile, W-base materials for high-temperature application in the fusion power reactors.

Modelling of radiation damage and radiation effects on pure W

Until 2006 there were no reliable data on defect formation and migration energies in tungsten. Empirical potentials fitted to cohesive energy and compressibility curves predicted defect energies and configurations that did not agree with more recent electronic-structure based calculations. Therefore, a new many-body, semi-empirical potential of interaction between atoms in tungsten has been recently developed by UKAEA [D. Nguyen-Manh, A.P. Horsfield, S.L. Dudarev, Phys. Rev. B 73 (2006) 020101 (R); S. L. Dudarev, P. M. Derlet, C.-H. Woo, Nucl. Instr. and Meth. in Phys. B 256 (2007) 253-259]. Results obtained with this new long-range interatomic potential have been compared to those previously obtained with the former available long-range Embedded Atom Method (EAM) interatomic potential [G.J. Ackland, R. Thetford, Phil. Mag. A56 (1987) 15-30]. In particular, the melting

temperature at constant pressure of tungsten was found to be lower with the new interatomic potential than with the former available potential and therefore closer to the experimental melting point value. This discrepancy is responsible for the differences observed in collision cascade behaviour. The core of edge and screw dislocations appears more extended when calculated with the new interatomic potential than with the former available potential. Therefore, dislocations are less mobile in the case of the new interatomic potential.

Development of reduced activation, radiation resistant ODS ferritic steels

This work is complementary to the EFDA Long Term Technology Task TW6-TTMS-006/D5, in terms of manufacturing route and characterization of irradiation resistance. Powders of an ODS ferritic steel, with the composition Fe-14Cr-2W-0.3Ti-0.3Y₂O₃ (in weight percent), have been prepared by mechanically alloying elemental powders of Fe, Cr, W Ti (up to 10µm in diameter) with Y₂O₃ particles (about 20nm in diameter) in a planetary ball mill, in a hydrogen atmosphere. The numerous interfaces resulting from the presence of oxide particles are expected to act as sinks for the irradiation-induced defects. A batch of about 500 grams of milled powders has been sent to the CEA in Saclay, France. There, the batch of milled powders has been compacted by hot extrusion at 1150°C, using a maximal force of 462 tons, in the shape of a cylindrical bar (700mm in length, 11mm in diameter). Specimens for Charpy impact tests, tensile tests, small ball punch tests, TEM observations, SANS measurements and high heat flux tests, have been cut out from the hot extruded rod. They have been sent to NRG in Petten (The Netherlands), where they will be irradiated with neutrons in the High Flux Reactor (HFR) at about 600 and 900°C to a dose of 3 to 5dpa. A part of the hot extruded bar has been sent back to the CRPP for characterization of the mechanical properties. Tensile tests showed that the hot extruded material presents a tensile strength similar to that of materials compacted by Hot Isostatic pressing (HIPping), which were produced and tested under the Task TW6-TTMS-006/D5, at all test temperatures between room temperature and 900°C (Fig. 2.4.5, left).

Development of ductile, radiation resistant W-based materials

Three commercial materials have been selected and purchased from the Plansee company (Austria): pure W powder (99.99% purity), pure W rod (30mm in diameter, 200mm in length (99.97% purity), and W-1%La₂O₃ rod (40mm in diameter, 200mm in length). They have been sent to the Technical University in Warsaw (Poland). There, they have been submitted to high-speed hot extrusion (HSHE) at 1000°C, using a maximal force of 1.7GPa and a deformation speed of 10⁴s⁻¹, in order to reduce tentatively the size of the grains. Indeed, small grain size materials are expected to show improved ductility and better resistance to radiation damage, as the numerous grain boundaries should act as sinks for the irradiation-induced defects. Unfortunately, it was not possible to consolidate the pure W powder by means of HSHE. Without encapsulating, the rods of pure W and W-1%La₂O₃ broke in several pieces during HSHE and numerous cracks were observed inside the rods. With encapsulating the rods in stainless steel, very promising plastically deformed specimens, without any cracks, have been obtained (Fig. 2.4.5, right), and the ductile-to-brittle transition temperature of W-1%La₂O₃ was found to be significantly reduced by HSHE.

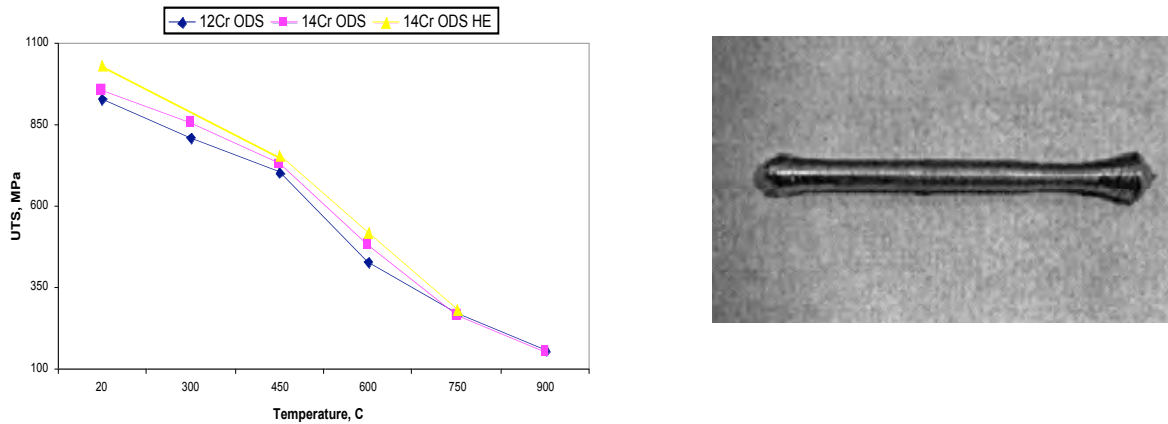


Fig. 2.4.5 Left: Ultimate tensile strength versus test temperature of the hot extruded (HE) 14Cr ODS ferritic steel, as compared to that of the 12Cr and 14Cr ODS ferritic steels compacted by HIPping under the Task TW6-TTMS-006/D5. Right: Specimen of W-1%La₂O₃ after HSHE.

PERFECT Integrated Project (IP) of the Sixth European Framework Programme

This project is aimed at investigating the possibility to identify by means of TEM observations nano-sized irradiation-induced defects and secondary phase precipitates in pressure vessel steels used in classical fission reactors. In 2007, TEM image simulations have been performed to find appropriate TEM imaging conditions for the identification of nano-sized dislocation loops in Fe-base materials. Specimens of pure Fe have been produced by MD simulations, which contain a nanometric dislocation loop in the centre. The first defects investigated consisted of dislocation loops with a size of 2nm and $a_0\langle 110 \rangle$, $\frac{1}{2}a_0\langle 111 \rangle$ and $a_0\langle 100 \rangle$ Burgers vectors (Fig. 2.4.6). MD simulations were performed using the EAM method and periodic boundary conditions. The relaxations were done using the conjugate gradient method. The atomic interactions were handled by the Finnis-Sinclair [M.W. Finnis, J.E. Sinclair, Phil. Mag. A50 (1984) 45-55] Ackland (1987) N-body type interatomic potentials for Fe-Fe interactions. TEM image simulations were performed using the EMS software and the multislice technique (Fig. 2.4.7). The selected imaging condition, a weak beam dark field condition $\mathbf{g}(4\mathbf{g})$ with $\mathbf{g}=(110)$, allows for better spatial resolution and improved contrast relatively to a bright field or a dark field condition.

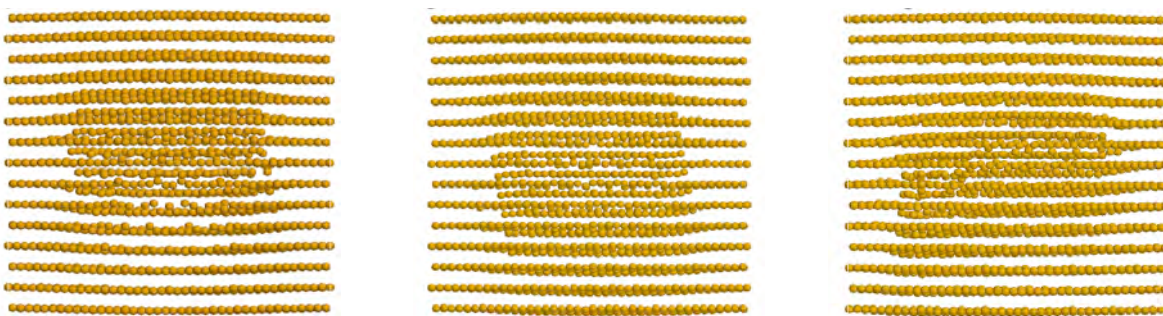


Fig. 2.4.6 View along the $[-115]$ direction of 0.8 million atoms MD specimens of Fe containing (left) a $\frac{1}{2}[110]$ interstitial loop in a (110) plane, (middle) a $\frac{1}{2}[111]$ interstitial loop in a (110) plane, and (right) a [100] interstitial loop in a (100) plane. All loops have a diameter of 2nm.

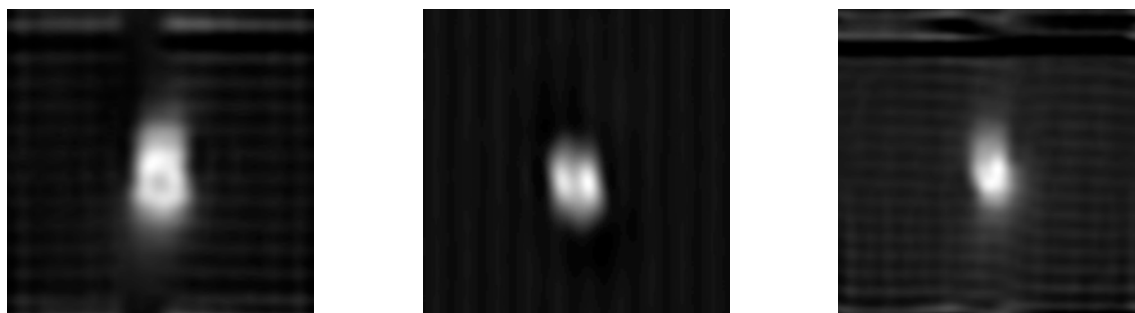


Fig. 2.4.7 Weak dark field TEM images, simulated with $\mathbf{g}(4\mathbf{g})$ and $\mathbf{g}=(110)$, of (left) $\frac{1}{2}a$ [110] interstitial loop in a (110) plane, (middle) a $\frac{1}{2}[111]$ interstitial loop in a (110) plane, and (right) a [100] interstitial loop in a (100) plane. All loops have a diameter of 2nm. The orientation of the diffraction vector \mathbf{g} is vertical and its sense is upwards.

2.4.3 EFDA Technology Tasks

Tasks Long Term

TW2-TTMS-004b deliverable 3: Development and testing of coatings to improve the corrosion resistance vs Pb17Li at T>450°C

Eighteen specimens of the EUROFER 97 RAFM steel have been sent to three different European companies for deposition of W and Cr coatings using three different techniques. Six specimens have been coated with a 10 μm -thick Cr coating using a galvanic technique. Six specimens have been coated with a 18-22 μm -thick W coating using a physical vapour deposition (PVD) technique. Six specimens have been coated with a 120 μm -thick W coating using a plasma spraying technique. All the coated specimens have been received in 2004. Construction of twelve small corrosion devices, which are destined to test the resistance of the three types of coatings as protection barriers for EUROFER 97 against corrosion in molten Pb-17Li, has been achieved at the beginning of 2005. In such a device a cylindrical specimen is screwed to the bottom part of a rod that is connected to a small motor. Features of the motor allow the specimen to rotate in a bath of molten Pb-17Li at a speed between 1mm/s and 5m/s and a bath temperature between 300°C and 800°C. Corrosion testing of reference specimens (uncoated EUROFER 97) and coated specimens has been started in summer 2005 at a specimen rotation speed of 1cm/s and a bath temperature of 550°C, for various corrosion times ranging between 500 and 5'000hrs. Corrosion experiments for corrosion times of 500 and 1'000hrs have been completed, while corrosion experiments for corrosion times of 2'500 and 5'000hrs are still on going. The corrosion attack of reference specimens of EUROFER 97 seems to present an incubation time of at least 1'000hrs. The galvanic Cr coating dissolved very rapidly in flowing Pb-17Li at 550°C. After the exposure time of 500hrs no remaining trace of the galvanic coating could be found, which indicates that such a coating does not provide any good corrosion barrier for EUROFER 97. An oxide layer was observed between the EUROFER 97 substrate specimen and the plasma sprayed W coating. The thickness of that layer increases with exposure time, while the plasma sprayed coating is gradually dissolved. This might be due to the porous nature of such a coating. The thickness of the PVD W coating was found constant up to the exposure time of 1'000hrs. No oxide layer was observed between the PVD coating and the EUROFER 97 substrate specimen. Therefore, PVD W coatings appear to be much more promising barriers against corrosion by flowing Pb-17Li at 550°C than galvanic Cr and plasma sprayed Wcoatings.

TW3-TTMS-005 deliverable 2: Investigation (tensile and Charpy testing) of PHT and PWHT to improve the design limits and to define the acceptable temperature range

In June 2007, FZK agreed to produce two electron beam welds, 40mm deep, for mechanical investigations to be performed by CRPP. The first weld tests have been carried out, for which the manufacturer used a broader beam and applied heating during welding. There are still some fine adjustments necessary to do prior the final weld production. Mechanical characterization of the welds will take place in 2008.

TW5-TTMS-001/D7: Assessment of irradiations performed on EUROFER97

A critical assessment of the existing databases for the F82H and EUROFER 97 RAFM steels has been finalized. The development of these two databases has been chronologically reviewed. For both steels, the data were analyzed for the unirradiated condition on the one hand and for different irradiation conditions on the other hand. The analysis was based on the Master-Curve method, as defined by the ASTM E1921 standard. However, it has to be mentioned that the large majority of the fracture data obtained so far for both steels result from the testing of sub-sized specimens, for which it is well known that the measured fracture toughness is not a material property but depends to some extent on the specimen size and geometry. This assessment has shown that the size effect on measured toughness is not sufficiently well known and taken into account in the literature and can lead to rather large uncertainty in the determination of the ductile-to-brittle transition temperature. It remains that the Master-Curve method describes rather well the unirradiated databases of both steels, provided that minor adjustments are made. Note that these adjustments have been made possible for the EUROFER 97 RAFM steel owing to the large fracture database obtained with big specimens for EUROFER 97. This database has been produced by the CRPP. The open issues regarding the behaviour in the transition of the fracture properties after irradiation have been discussed on the basis of the limited fracture tests that have been performed on irradiated specimens.

TW5-TTMS-005/D2: SSTT: Model the brittle transition region - continuation of TW2-TTMS-005b/D6

This work is aimed at modelling the temperature dependence of the fracture toughness of the EUROFER 97 RAFM steel in the ductile-to-brittle transition. We had previously shown that it is possible to reconstruct satisfactorily the fracture toughness-temperature curve, $K(T)$, of RAFM steels in the transition region by using a local critical condition for cleavage. This critical condition assumes that quasi-cleavage is triggered when a critical principal stress σ^* encompasses a critical area A^* around a crack tip, where the values of $\sigma^* \cdot A^*$ are calibrated by means of finite element simulations. The effect of the critical ($\sigma^* \cdot A^*$) values on the shape of the $K(T)$ curves are exemplified in Fig.2.4.8 (left), where two values of σ^* and two values of A^* have been selected, namely $\sigma^*=1950/2050\text{MPa}$ and $A^*=500/4250\text{m}^2$. With these values, four $K(T)$ curves have been reconstructed using all possible combinations of ($\sigma^* \cdot A^*$). The most salient observations relate to the curvature of the $K(T)$ curve and to the vertical position of the curve at the lower shelf. Indeed, a σ^* increase at a given A^* makes the curve rise much faster with increasing temperature. The effect of a change in σ^* at constant A^* can be seen by comparing the curves with the circle and square symbols. An increase in A^* yields a significant increase in fracture toughness, while the shape of the $K(T)$ curve remains little affected. It has also been found that several sets of ($\sigma^* \cdot A^*$) values can be used to satisfactorily reconstruct an

experimental $K(T)$ curve. All these “correct” pairs of critical values define a window that represents the uncertainty of the calibration process, as a consequence of the experimental and numerical uncertainties in addition to the intrinsic uncertainties of the model. The experimental data obtained with 0.35T CT fracture specimens are reported in Fig. 2.4.8 (right), as well as the experimental lower bound $K(T)$ curve (black curve) and five different pairs of (σ^*-A^*) values that were used to reconstruct rather well the lower bound curve. It has to be emphasized that the critical stress σ^* is practically constant for each pair, and equal to $2080 \pm 12 \text{ MPa}$, while the uncertainty in the critical area A^* , equal to $808 \pm 461 \mu\text{m}^2$, remains quite large. It is emphasized that the model predicts the very weak temperature dependence, observed experimentally, of the lower shelf of fracture toughness. This observation is remarkable, considering that the maximum rate of variation in the yield stress with temperature is actually observed in this temperature range.

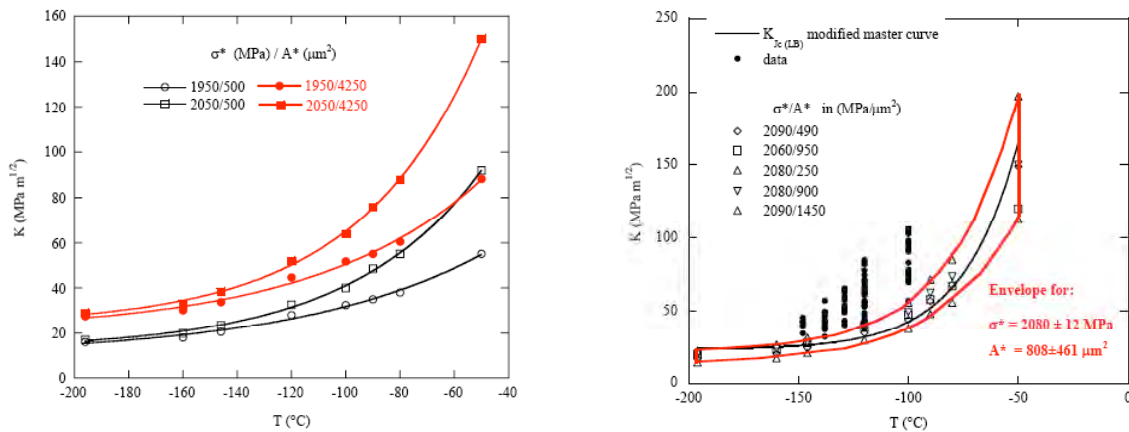


Fig. 2.4.8 Left: Illustration of the effect of the (σ^*-A^*) values on the shape of the $K(T)$ curve. Right: Reconstruction of the $K(T)$ lower bound, with different sets of (σ^*-A^*) values.

TW5-TTMS-005/D10 : Support in development of design rules for structural materials with low ductility

Eighteen compression specimens, 3mm in diameter and 5.5mm in height, have been irradiated with neutrons at 300°C up to 0.6dpa in the BR2 reactor located at SCK-CEN (Mol, Belgium). The specimen matrix consisted of six different materials including two 9Cr ferritic/martensitic steels, namely the T91 and EUROFER 97 steels, and four Fe-Cr model alloys with a Cr content equal respectively to 2.4wt.%, 4.6wt.%, 8.4wt.%, and 11.6wt.%. Compression testing of these six materials in the unirradiated and irradiated conditions was carried out at room temperature using a nominal strain-rate of $1.5 \times 10^{-3} \text{ s}^{-1}$. True stress-strain curves of unirradiated specimens of these six materials are reported in Fig. 2.4.9 (left). All the curves exhibit a parabolic shape with a rather moderate strain-hardening rate. The flow stress of unirradiated Fe-Cr model alloys increases with Cr content. The effect of irradiation on the deformation curves is illustrated in Fig. 2.4.9 (right). The transition from the elastic regime to the plastic one appears more abrupt for the irradiated specimens than for the unirradiated ones. Interestingly, the increase in flow stress resulting from irradiation (radiation hardening) appears strongly dependent on Cr content, in such a way that the flow stress of irradiated specimens does not simply increase with Cr content but a minimum in radiation hardening is actually measured for a Cr content of about 7wt.%.

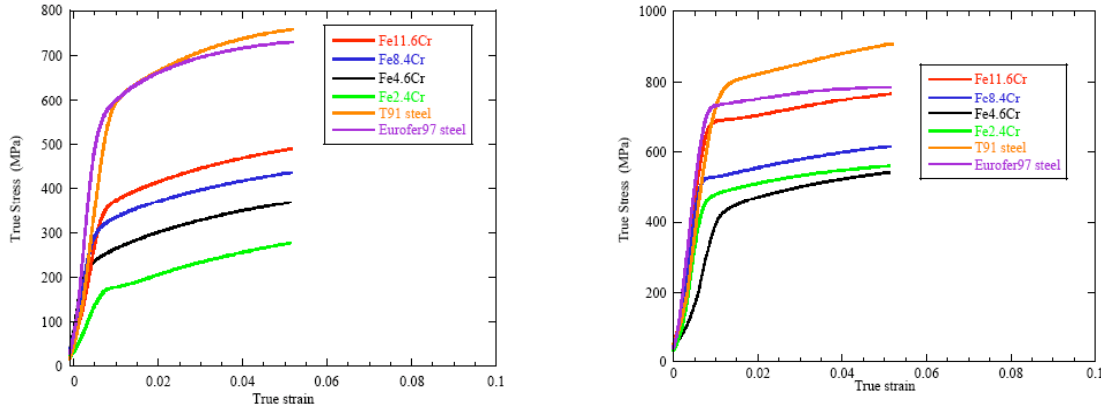


Fig. 2.4.9 Left: True stress-strain curves obtained for compression specimens, unirradiated condition. Right: True stress-strain curves obtained for compression specimens, irradiated condition: $T_{irr}=300^{\circ}\text{C}$, 0.6dpa .

TW5-TTMS-005/D11 : Experiments in support of TW5-TTMS-005/D2

A large fracture toughness database for 0.35T CT specimens of the EUROFER 97 RAFM steel has been developed in order to characterize the lower transition between the brittle fracture mode and the ductile one. The specimens were fatigue pre-cracked up to $a/w=0.5$ (a =crack length, w =specimen width). The main goal was to assess the shape of the median fracture toughness-temperature curve, $K_{Jc_med}(T)$, with specimens large enough to ensure enough constraint (or triaxiality) at the crack tip. In particular, it was intended to check whether it is possible to apply the ASTM-E1921 standard in the specific case of RAFM steels, in order to determine the reference temperature T_0 at which K_{Jc_med} is equal to $100\text{MPa}\cdot\text{m}^{1/2}$. According to the ASTM-E1921 standard, the shape of the $K_{Jc_med}(T)$ curve (median toughness value for 1T-thick specimens) is described by:

$$K_{Jc_med} = 30 + 70 \exp(0.019(T-T_0))$$

This equation has been shown to describe satisfactorily the $K_{Jc_med}(T)$ curve transition for a variety of reactor pressure vessel steels. Note also that if fracture specimens with a crack front length different from 1T (25.4mm) are used (xT), the data have to be statistically size-adjusted using the equation:

$$K_{Jc\ 1T} = 20 + (K_{Jc\ xT} - 20)(B_{xT} / B_{1T})^{1/4}$$

The analysis of data for 0.35T C(T) specimens in the lower transition suggested that the shape of the $K_{Jc_med}(T)$ curve might be steeper than the one of the Master Curve described by the ASTM-1921 standard. Thus, it was proposed to replace the previous equation by:

$$K_{Jc_med} = 30 + 70 \exp(0.04(T-T_0))$$

In order to verify this proposal, a series of fifteen large fracture specimens, namely 0.9T C(T) specimens, were tested in the middle part of the transition, in the temperature range $[-80;-40^{\circ}\text{C}]$, in collaboration with University California Santa Barbara. It turned out that many data for 0.9T C(T) specimens fall relatively low, i.e. systematically below the median curve (corresponding to a failure probability of 50%) of the suggested modified Master Curve. This is illustrated in Fig. 2.4.10, where the modified Master Curve, as obtained for 0.35T C(T) specimens, is shown along with the fracture toughness data obtained for 0.9T C(T) specimens.

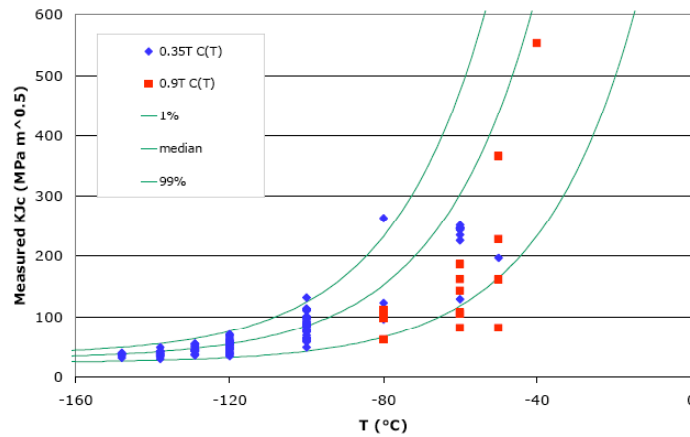


Fig. 2.4.10 Modified Master Curve for 0.35T C(T) specimens. This curve does not predict correctly the fracture toughness behaviour of 0.9T C(T) specimens.

TW5-TTMS-007/D11 : Ion irradiations for verification analyses on thin foils of Fe-Cr-C model alloys

This work is aimed at closing the gap between modelling of radiation damage in Fe-(Cr,C) model alloys and experimental observations of radiation damage in tempered martensitic (or ferritic/martensitic) and martensitic steels. Selected materials included Fe-9Cr-C and Fe-12Cr-C model alloys. Further heat treatments were applied to obtain the desired microstructure, either tempered martensitic or martensitic (Table 2.4.1). About 10 TEM disks, 3mm in diameter and 100µm in thickness, from each material were implanted with 350MeV Au ions at the Hahn Meitner Institute (HMI) in Berlin (Germany) at room temperature to a dose of 0.05dpa at 7µm below the surface.

TEM observations confirmed that the materials tempered at 760°C show a typical tempered martensitic structure, with carbides of the type Cr₂₃C₆, while the water quenched materials show a typical martensitic structure with sharp laths and high dislocation densities. The materials with a martensitic structure contain a lower defect density than the materials with a tempered martensitic structure (Table 2.4.1), due to the presence of a higher density of sinks for the irradiation induced defects, such as grain and lath boundaries, in martensitic materials. In the case of tempered martensitic materials, the number of boundaries decreases and the distance between boundaries increases upon tempering, leading to higher defect accumulation and leaving a lower sink density for the irradiation-induced defects. Small black dots with a size in the range of 2-4nm and dislocation loops with a size in the range of 5-8nm have been observed in materials with a tempered martensitic structure. Small black dots with a size in the range of 2-4nm have been observed in materials with a martensitic structure. The dislocation loops that could be identified have a Burgers vector of $\mathbf{b} = 1/2a_0\langle 111 \rangle$.

Material	Heat treatment	Structure	Defect density [x10 ²² m ⁻³]	Defect size [nm]
Fe-9Cr-0.1C	1h at 940°C, 1h at 760°C	tempered martensitic	4.2	2-8
Fe-9Cr-0.1C	1h at 940°C, WQ	martensitic	2.6	2-4
Fe-12Cr-0.1C	1h at 940°C, 1h at 760°C	tempered martensitic	4.5	2-8
Fe-12Cr-0.1C	1h at 940°C, WQ	martensitic	2.8	2-4

Table 2.4.1 Defect size and density measured in Fe-9Cr-0.1C and Fe-12Cr-0.1C model alloys ion irradiated at room temperature to 0.05dpa. WQ: water quench.

TW5-TTMS-007/D15 : Dislocation-defect interaction and the evolution of the deformed microstructure in Fe (development of dislocation dynamics methods)

This work is aimed at simulating the effects of irradiation-induced defects like dislocation loops and/or cavities, such as voids or helium bubbles, on the plasticity of Fe by dislocation dynamics simulations. The code microMegs from LEM-ONERA was successfully compiled and implemented in our computers. It is based on the so-called lattice model. In a first step, irradiation-induced defects were successfully simulated as a population of locked, short dislocation segments. It was observed that in the presence of obstacles in the matrix deformation occurs by junction formation and cross slip events at the beginning of deformation and then by increase in the dislocation density as a result from forest hardening.

The next step consisted in implementing defects that are closer to a proper description of irradiation-induced defects, such as cavities and dislocation loops. Rules for the dislocation dynamics simulations are deduced here from MD simulations of the interaction between a mobile dislocation and an irradiation-induced defect. In order to map the interaction between an edge dislocation and a cavity the stress state around the cavity has been assessed by MD simulations, in terms of hydrostatic stress and von Mises stress, given respectively by:

$$\sigma_h = \frac{\sigma_{11} + \sigma_{22} + \sigma_{33}}{3} \text{ and } \sigma_{vm} = \sqrt{\frac{(\sigma_1 - \sigma_2)^2 + (\sigma_2 - \sigma_3)^2 + (\sigma_1 - \sigma_3)^2}{2}},$$

and yz shear stresses.

Figure 2.4.11 shows the evolution of the hydrostatic stress and von Mises stresses in the cavity with increasing He content. It appears that, as expected, the pressure inside the cavity increases with He content. Note that already at 1 He atom per vacancy there is a pressure of about 3GPa. The Von Mises stress also increases with increasing He content, but beyond 3 He atom per vacancy it decreases. This coincides with the onset of the loop punching mechanism, with emission of interstitial atoms in the matrix.

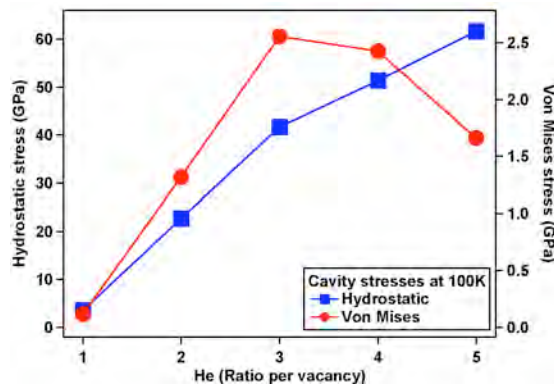


Fig. 2.4.11 Average hydrostatic and Von Mises stresses versus He content in the cavity.

In dislocation dynamics simulations the moving dislocation impinges the cavity at a certain random height relatively to the glide plane going through the centre of it. The necessary data for such simulations were obtained by performing MD simulations. Figure 2.4.12 shows the resulting release stress and strain in Fe for an edge dislocation escaping a 2nm cavity at 100K, as a function of He content in the

cavity and as function of dislocation-cavity interaction height. It appears that it is not monotonous. For example, at 1.5nm, where the dislocation is above the cavity and does not go through it, there is a significant release stress, while at 1.0nm the release stress is the lowest even though the dislocation touches the cavity surface. This reveals a strong relationship to the complex stress state around the cavity. These data can be readily used in dislocations dynamics simulations. Work is in progress to implement them in the microMegas code.

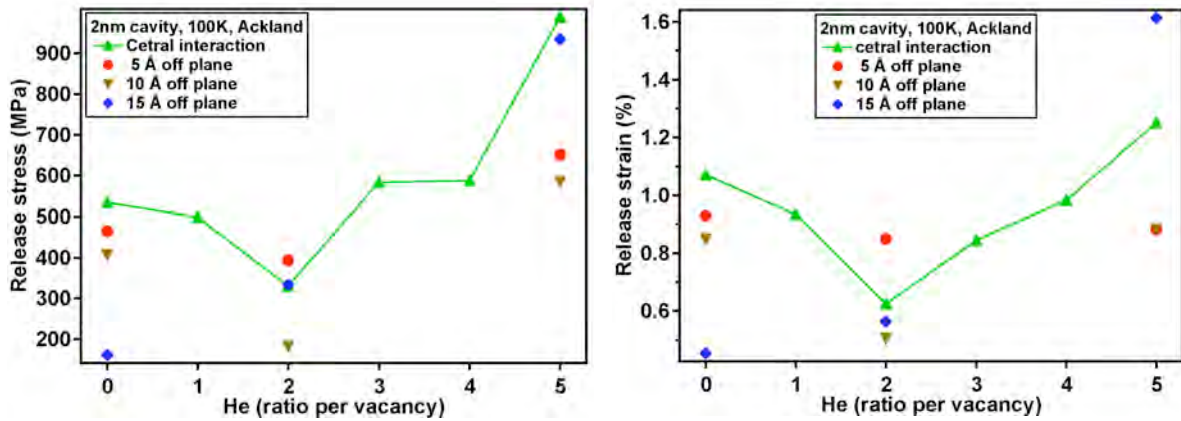


Fig. 2.4.12 (Left) Release stress and (right) release strain in Fe versus He content at 100K for an edge dislocation and a 2nm cavity and various dislocation heights over the glide plane going through the centre of the cavity.

TW5-TTMI-003/D7 : Development of the test rig technology for in situ creep-fatigue measurements in the MFTM

The IFMIF target facility and the irradiation modules will be located in a common volume called "test cell". The test cell will accommodate the lithium target, a lithium tank, and the two vertical test and irradiation assemblies VTA-1 and VTA-2, which will be all located inside a vacuum liner. The components will be surrounded by a massive gas-cooled shielding system. This project is aimed at presenting a concept for the realization of in situ creep-fatigue experiments in the medium flux test module (VTA-2) of IFMIF and also at making a first design step in producing a miniaturized actuator for axial loading of specimens. This mechanical actuator will be one of the main components of this new experiment. It will incorporate the latest developments in high quality mechanical components such as ball screw spindles, harmonic drives and electro-servo motors. One of the main difficulties relates to the very limited size of the IFMIF test modules and to the very high requirements in displacement accuracy and power.

A new actuator for IFMIF (Fig. 2.4.13, left) has been designed, manufactured and successfully tested using an available facility. Compared to conventional actuators used in testing machines, this new actuator presents a strong reduction in weight and volume, which will be a great advantage in the hostile environment of IFMIF. The actuator will be mounted in the future in a new fatigue set up and the system will be used for the testing of a typical IFMIF specimen. Calculations of neutron and gamma fluxes (Fig. 2.4.13, right) showed that fluxes for creep-fatigue devices in the IFMIF environment will be at least two orders of magnitude larger than for the *in situ* creep-fatigue system previously used in the PIREX facility at the PSI. Therefore, special measures will be needed to ensure survival of the components during a single irradiation period. A new concept for creep-fatigue experiments to be performed inside the medium flux test module of IFMIF was developed. The new concept consists in a vertical test assembly carrying three test modules, a creep

fatigue test module, a spectral neutron plate and a tritium release module. The main role of the vertical assembly will be to insert the three modules into the target and shield them from irradiation. The vertical assembly will also extract the test modules and bring them into the test cell room where they will be separated and transported to the service hot cells. This concept requires two interfaces with automatic couplings: one at the top of the vertical assembly and another one in the middle of it, for separation of the modules. The modules need also to be disconnected independently. The creep-fatigue test module will be composed of three independent testing machines. Each testing machine will include a mechanical actuator, a gripping system to hold the specimen and a measuring system. Due to the hostile environment, the testing machine will be used only once and replaced by a new fully instrumented and inactive system after each testing cycle. This should drastically reduce the efforts in the hot cells and improve the reliability of the experiments.

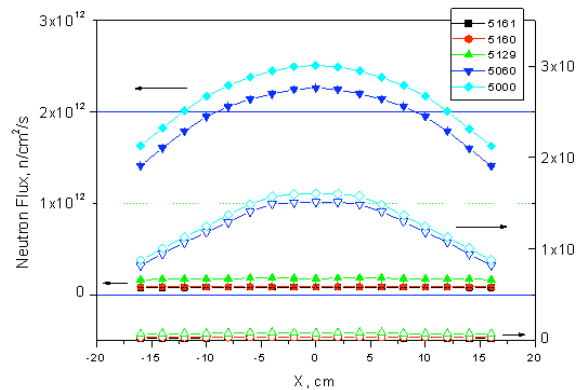
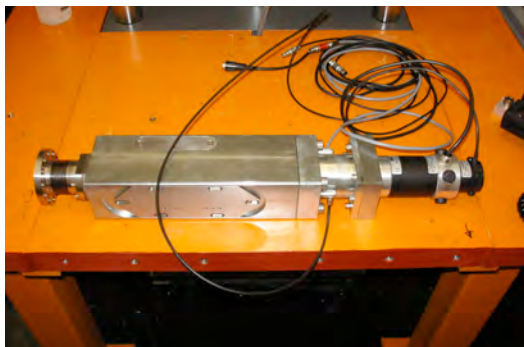


Fig. 2.4.13 Left: The actuator for IMIF. Right: Neutron and gamma fluxes versus lateral dimension at different vertical locations along the creep-fatigue system.

TW6-TTMS-007/D9a: Molecular dynamics simulation of the dislocation-defect interaction in Fe and its dependence on the Fe empirical potential

The interaction of a mobile edge dislocation in Fe with a cavity, as a void or a He bubble, 2nm in size, has been investigated by means of MD simulations, as a function of temperature and empirical potentials. The empirical potentials derived for Fe by Ackland et al. (1997), Mendeleev et al. (2003) and Dudarev and Derlet (2005) have been used. To deal with the presence of He in the sample, the interatomic potentials of Fe-He and He-He, developed by Wilson-Johnson (1975) and Beck (1968), respectively, have been used.

Fig. 2.4.14 shows the release stress and strain for a 2nm cavity, as a function of the He content, which is given as the number of He atoms per vacancy, as calculated at 100K using the Ackland potential. It appears that the void, with a strength of 550MPa, is a stronger obstacle than the He bubble at low He contents. The bubble strength decreases with increasing He content up to 2 He atoms per vacancy, where it reaches its weakest value of about 350MPa. The release strain is also reduced to about half the value needed for the void. For more than 2 He atoms per vacancy, the bubble strength and release strain increase with further increase in He content. At 5 He atoms per vacancy, the obstacle strength of the bubble, equal to 1GPa, overcomes the one of the void.

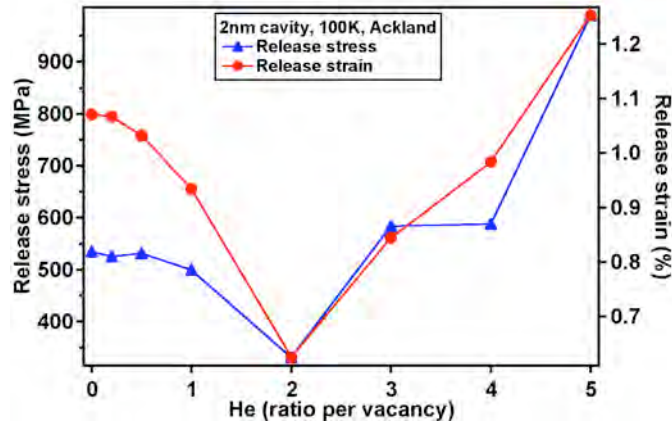


Fig. 2.4.14 Release stress and release strain at 100K for a 2nm cavity with various He contents, as calculated using the Ackland interatomic potential.

Fig. 2.4.15 presents cross sections at 10K of a 2nm cavity after the passage of an edge dislocation, for different He contents, which were simulated using the Ackland potential. The dislocation shears the cavity from left to right in the pictures. For 3 He atoms per vacancy and more, the pictures show that the cavity expands and generates interstitial atoms in the matrix (“loop punching” mechanism). Shearing of a void by an edge dislocation is made more complex by the He content. A clear shearing step can be seen on the entry surface of the cavity for 2 and 4 He atoms per vacancy, the former case corresponding to the drop point in the release stress and strain depicted in Fig. 2.4.14. This may be an evidence of shearing of the cavity by the edge dislocation rather than interaction with punched loop segments around the cavity or climb.

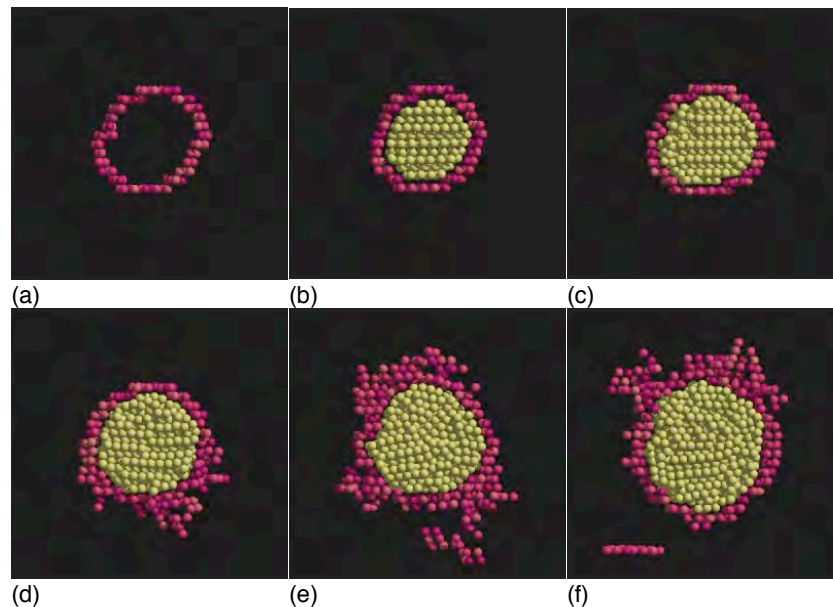


Fig. 2.4.15 Sheared shape of a 2nm cavity after interaction with an edge dislocation at 10K for He contents of (a) 0He:1V, (b) 1He:1V, (c) 2He:1V, (d) 3He:1V, (e) 4He:1V, and (f) 5He:1V.

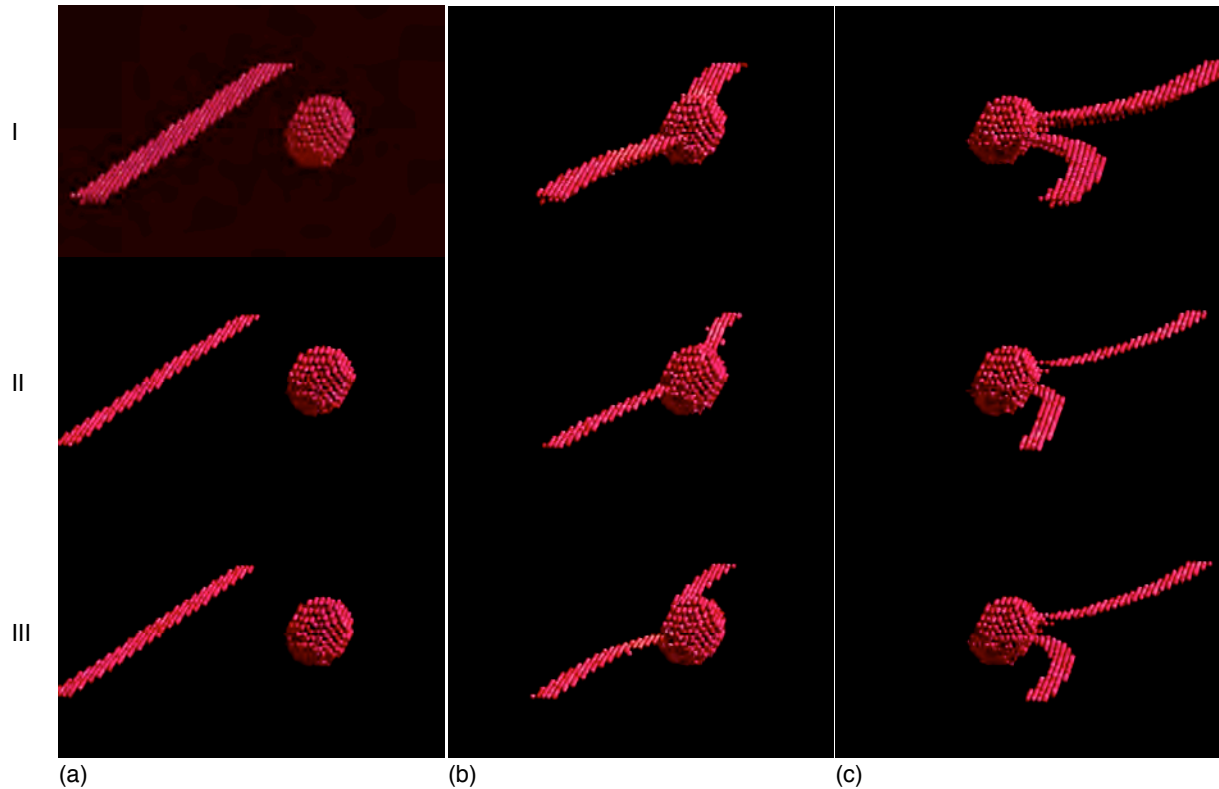


Fig. 2.4.16 *Interaction of an edge dislocation with a 2nm void in Fe under imposed strain rate at 10K using the (I) Ackland et al., (II) Mendeleev et al., and (III) Dudarev-Derlet interatomic potentials. (a) Dislocation glide, (b) dislocation attraction by the void, and (c) dislocation bowing before release.*

The effect of the interatomic potential on the morphology of the interaction at 10K of a moving edge dislocation with a 2nm cavity in Fe is shown in Fig. 2.4.16. In all cases the dislocation glides towards the cavity. Then, the dislocation is attracted to the void when a critical distance to the void is reached. The dislocation bows at the defect, and it escapes finally the cavity when a critical release angle is reached. Shearing of the void by the dislocation is clear in these images. However, the shape of the dislocation at the release point appears dependent on the interatomic potential. Images simulated with the Ackland et al. and Dudarev-Derlet potentials show a smooth curvature of the bowed mixed segments of the dislocation, whereas with the Mendeleev et al. potential there is a straight segment linking the screw arms of the dislocation to the edge part of it.

TW6-TTMS-007/D12: Selection of experimental methods in JANNUS for 2007

This work is aimed at preparing a detailed scientific programme of ion implantation of ferritic/martensitic materials, in collaboration with a number of other European partners, in view of validating the European effort of modelling radiation damage and radiation damage effects on fusion materials using the future JANNUS facility at the CEA (France). In order to ground and frame more precisely the scientific programme sketched in a common document prepared in 2005, preliminary investigations are in progress. In particular, Infra-Red (IR) spectroscopy is being assessed as a tool to probe irradiation-induced damage in ferritic/martensitic materials, in collaboration with Prof. J. Humlicek from Masaryk University in Brno (Czech Republic). The advantage of IR spectroscopy is that it is a non-destructive technique. It consists of measurements of the optical response (reflectivity or

ellipsometric angles) of a probe at different wavelengths. The optical response gives a conductivity corresponding to the applied light frequency. Then, an extrapolation towards zero frequency can be done, and the classical DC conductivity, or electrical resistivity, is obtained.

Fe-0.13Cu, Fe-0.33Cu and Fe-1.52Cu alloys (in weight percent) have been selected in order to investigate the well-known Cu precipitation and to calibrate and evaluate the precision of IR spectroscopy measurements relatively to electrical resistivity measurements performed on the same materials by Dr A. Barbu at the CEA. The surface of the specimens was electro-chemically polished, as the state of surface influences optical measurements. As the reflectivity is close to 1 for highly conducting samples, problems may arise with reflectance standards. On the contrary, ellipsometric measurements do not suffer the same problem, as the intensity of the reflected light is not relevant for this type of measurements. Ellipsometric measurements of the light penetration depth, using a middle infrared ellipsometer ($400\text{-}5000\text{cm}^{-1}$) showed that it ranges between 25 and 35nm for different wavelengths. This implies that the method is very sensitive to surface roughness and contamination. Four-point probe resistivity values of Fe-0.13Cu, Fe-0.33Cu and Fe-1.52Cu alloys were found equal to $10.6\pm 0.1\mu\Omega\cdot\text{cm}$, $11.9\pm 0.2\mu\Omega\cdot\text{cm}$, and $15.4\pm 0.2\mu\Omega\cdot\text{cm}$, respectively.

TW6-TTMS-001/D4: PIE SING irradiation

The irradiation rig containing specimens of EUROFER 97 RAFM steel and ODS EUROFER, which have been irradiated in the SING facility in 2004/2005, has been transported to the Hot Laboratory of the PSI in Spring 2007. Unfortunately, due to a lack of technical manpower at the PSI, the irradiated specimens have been extracted from the rig only in Autumn 2007. Therefore, Charpy impact testing, tensile testing and TEM observations of irradiated specimens will be performed in 2008.

TW6-TTMS-005/D11: SSTT: Continuation of modelling the brittle transition region

A series of notched tensile specimens of the EUROFER 97 RAFM steel have been tested in the lower part of the ductile-to-brittle transition region, using a machine crosshead velocity equal to 0.1mm/min. The notched specimens were 6mm in diameter, with a 1.5mm deep notch in the middle of the gage length (Fig. 2.4.17, left). The notch root radius was 0.4mm. In load-displacement curves the displacement corresponds to the opening of the notch measured with a clip gage whose knives were symmetrically positioned on each side of the notch plane. Finite element simulations have been undertaken for both CT and notched tensile specimens, in order to calculate the stress/strain fields ahead of the crack tip and notch root, respectively. They were performed using the ABAQUSTM 6.6 code. Linear reduced integration elements have been used for both types of specimens. The calculated curves for the notched specimens were obtained by extracting the force required for achieving the imposed displacement. Examples of load-displacement curves for notched tensile specimens tested at 20°C, -50°C, -100°C, and -155°C, are shown in Fig. 2.4.17 (right). The calculated curves are reported along with the experimental ones. An excellent agreement between them was found. It was also observed that at failure the stress distribution is always such that the maximum stress is located along the specimen axis. The critical fracture stress σ^* for the notched specimens was then defined as the maximum stress in the crack plane. The ability of the calibrated ($\sigma^*\text{-}A^*$) criterion to predict the failure load for notched specimens over a range of temperatures was checked by running finite element simulations up to the displacement level for which σ^* is attained. At this

displacement it was found that both the failure load and the failure displacement match very well those of the experimental curves.

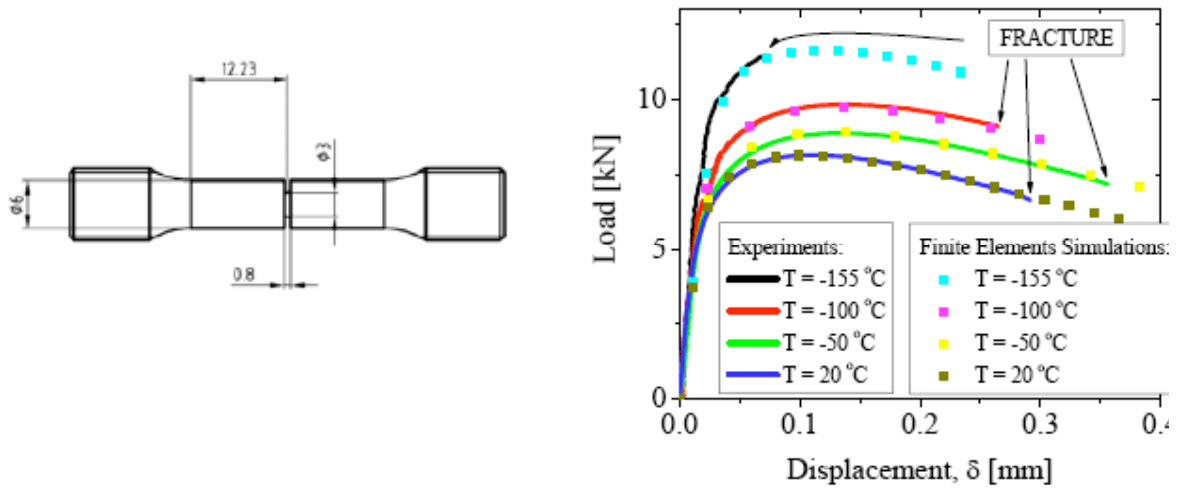


Fig. 2.4.17 Left: Schematic of a notched tensile specimen. Right: Load-displacement curves for notched tensile specimens.

TW6-TTMS-006/D5: Nanocomposited ferritic steels for HT application (continuation of TW5 deliverable)

This work is aimed at developing reduced activation, radiation resistant ODS ferritic steels, by mechanical alloying followed by Hot Isostatic Pressing (HIPping), for high-temperature application in the fusion power reactors. The numerous interfaces resulting from the presence of oxide particles are expected to act as sinks for the irradiation-induced defects. As the result of previous R&D activities, 2007 activities were focused on the two following compositions: Fe-12Cr-2W-0.3Ti-0.3Y₂O₃ and Fe-14Cr-2W-0.3Ti-0.3Y₂O₃, in weight percent. In order to reduce the oxygen content in the materials, mechanical alloying was performed in a hydrogen atmosphere instead of an argon atmosphere. The microstructure was found not affected by the new atmosphere. Both types of materials appear composed of a bimodal microstructure composed of coarse grains, a few micrometres in size, and smaller grains, about 500nm in diameter. The coarse grains are almost dislocation-free, while the smaller grains are surrounded by tangles of dislocations. Both types of materials contain a high density of Fe-base nanoclusters, enriched with Y, Ti and O, with a mean size ranging between 5 and 6nm (Fig. 2.4.18). However, the fast fracture behaviour of both types of materials, as measured by means of Charpy impact tests, was found strongly improved by the use of the new atmosphere, in the sense that the ductile-to-brittle temperature (DBTT) was strongly reduced and the upper shelf energy (USE) was strongly increased (Fig. 2.4.19). High strength and elongation values were measured for both materials by means of tensile tests. However, the 14Cr material was found slightly stronger and less ductile than the 12Cr material, at all test temperature between room temperature and 900°C.

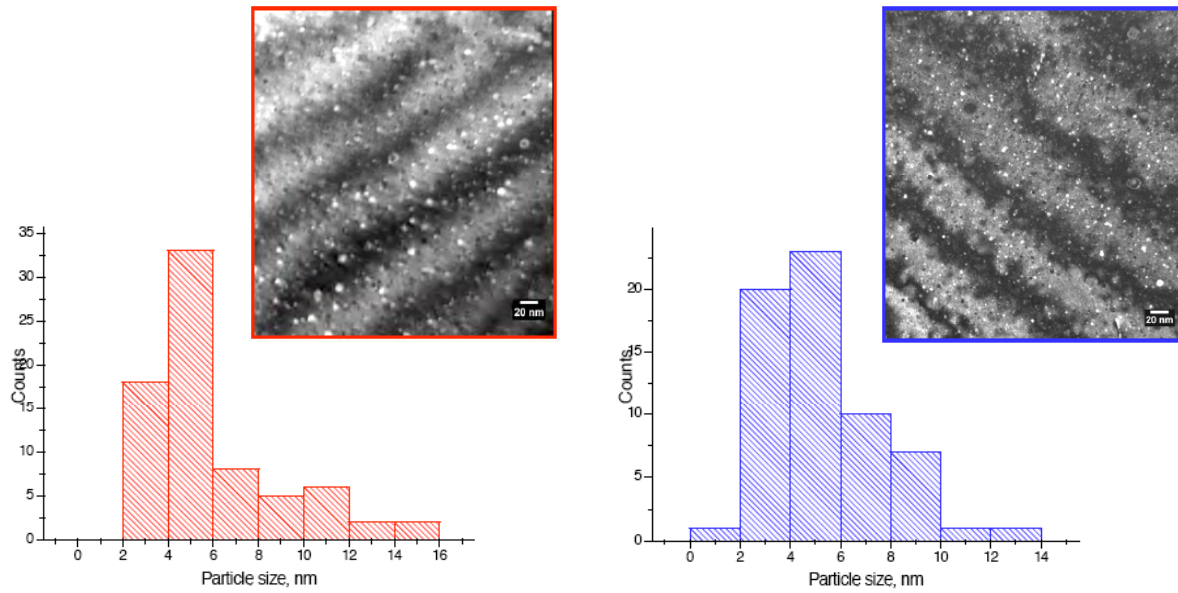


Fig. 2.4.18 Size distributions and TEM weak beam images of Y-Ti-O nanoclusters in (left) the 12Cr ODS ferritic steel, and (right) the 14Cr ODS ferritic steel. The mean grain size of nanoclusters is ranging between 5 and 6nm.

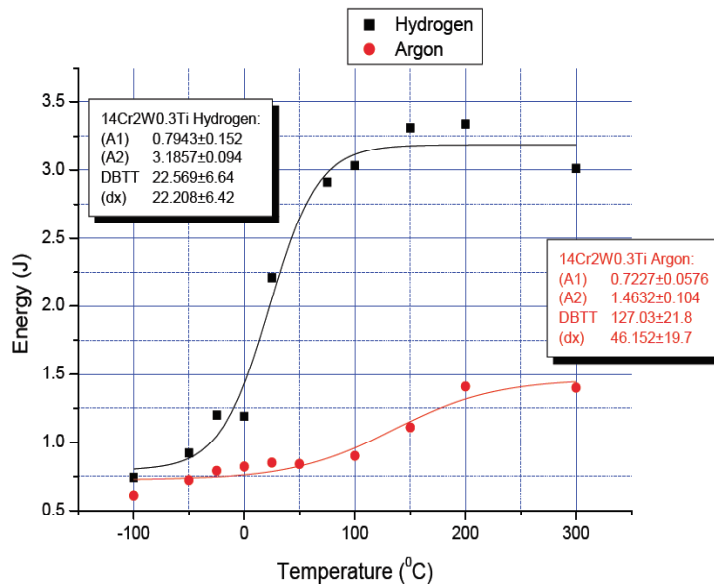


Fig. 2.4.19 Effect of the mechanical alloying atmosphere on the fast fracture behaviour of the 14Cr ODS ferritic steel. The DBTT has been reduced from about 127°C to 23°C and the USE has been increased from about 1.5J to 3.2J by the use of a hydrogen atmosphere.

TW6-TTMA-002/D10: Development of W-TiC and W-Y₂O₃ alloys

Recent activities have been focused on the W-Y₂O₃ material. W-0.3Y₂O₃ powders (in weight percent) was prepared by mechanically alloying pure W powder particles (up to 4-6µm in diameter) with Y₂O₃ oxide particles (about 20nm in diameter) in a planetary ball mill, in an argon or a hydrogen atmosphere. The evolution of particle size and crystallite size with milling time (Fig. 2.4.20), as well as X-ray diffractometry, showed that the milling time should not exceed 10hrs, in order to obtain small and stabilized particle sizes and crystallite sizes and to avoid

important formation of W-C particles, due to contamination of the powder by the balls and walls of the milling system, which could lead to strong embrittlement of the material. No significant effect of the atmosphere on the particle size and morphology was evidenced. However, the W-0.3Y₂O₃ powders mechanically alloyed in hydrogen exhibit larger microhardness values than the W-0.3Y₂O₃ powders mechanically alloyed in argon (Fig. 2.4.21). Possible compaction methods of the milled powders (e.g. sintering, HIPping) are now under evaluation.

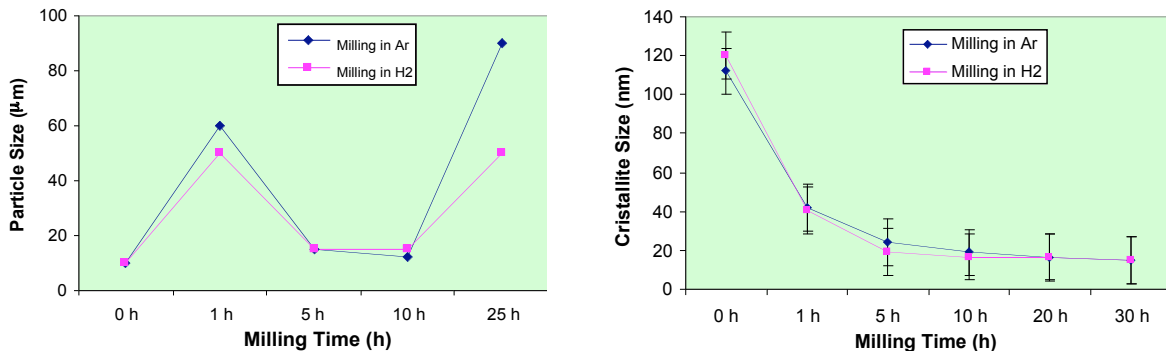


Fig. 2.4.20 Left: Particle size versus milling time. Right: Crystallite size versus milling time. The optimal milling time is 10hrs.

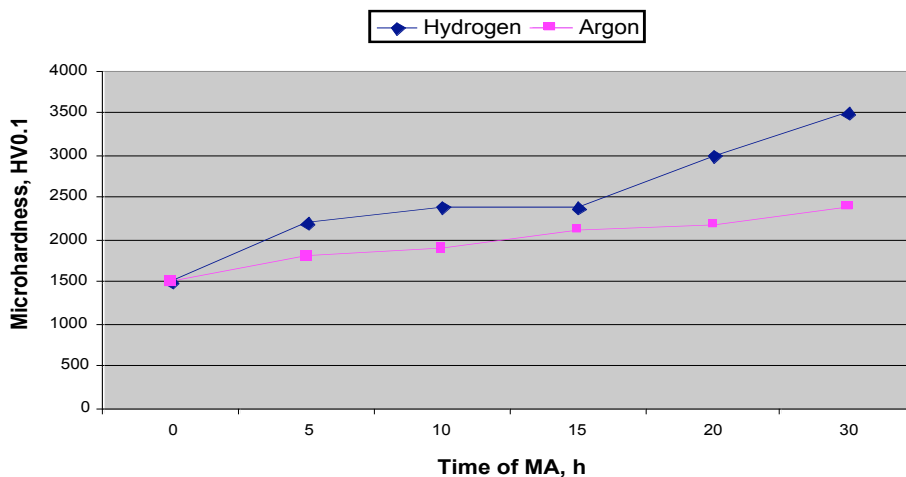


Fig. 2.4.21 Vickers microhardness versus milling time for two different mechanical alloying atmospheres: argon and hydrogen.

Tasks Next Step

TW4-TVM-CUSSPIT : Testing of irradiated CuCrZr/SS joints produced under different blanket manufacturing conditions

CuCrZr/SS joints, where CuCrZr refers to a precipitation strengthened Cu-base alloy and SS to the 316LN austenitic stainless steel, are part of the current ITER design. Their final applicability in ITER will depend on their mechanical properties before and after neutron irradiation, with respect to those of the base materials. This project is aimed at investigating the effects of two different heat treatments on the mechanical properties (joint strength, fracture toughness) of unirradiated and neutron-irradiated CuCrZr/SS joints and base materials. The work is being performed by three fusion Associations: SCK-CEN (Belgium) is responsible for the

neutron irradiations, VTT Manufacturing Technology (Finland) is in charge of testing the joints, and CRPP is in charge of measuring the fracture toughness of the CuCrZr base material.

Two series of six specimens of the CuCrZr base material, having withstood two different heat treatments, have been irradiated with neutrons at SCK/CEN to three different doses of 0.001, 0.01 and 0.1dpa. The specimens have been then delivered to Risoe National Laboratory (Denmark), in accordance with the usual procedure between these two institutions. After that, the specimens were shipped to the VTT laboratories. The specimens are being stored in a hot cell at VTT. They will be extracted from their capsules, sorted, re-packed and sent to the PSI, together with unirradiated specimens having withstood the same heat treatments, at the beginning of 2008. The fracture toughness of the specimens will be measured in summer 2008, via three point bend fracture experiments and according to the J1C procedure.

TW5-TVM-COMADA: Investigation of the effect of creep fatigue interaction on the mechanical performance and lifetime of CuCrZr

The CuCrZr alloy is a candidate heat sink material for the first wall of ITER. Therefore, extensive research was conducted in the past on the fatigue properties of the CuCrZr alloy, under ITER-relevant operating conditions. Unfortunately, only few data exist concerning its creep-fatigue behaviour, mainly due to the very costly testing involved, as the tests may run for months. This work is aimed at checking if a prediction method based on pure fatigue and creep tests only can be found or eventually modified to fit the results. The work consists of two different parts: (1) a literature survey with an analysis of the existing data, (2) an experimental part in which selected data points will be obtained in order to verify the suitability of life time prediction for creep-fatigue tests.

The first part of this work has been completed in 2006. Within the second part of this work, an experimental testing program was prepared with the aim of producing the additional data points needed to make reliable predictions for the first wall of ITER. The material necessary for the experimental part of this work has been ordered by CEA (Grenoble) from the KME company and heat treated to reproduce the manufacturing route for the first wall sections of ITER. Unfortunately, the resulting grain size was up to 20mm and, therefore, of the order of the size of the test specimens. As a consequence, a new material was prepared by using another heat treatment: solutioning at 980°C for 30min, air-cooling at a rate of 50-60°C/min, ageing at 580°C for 2hrs. The new material was found to have the right microstructure with grain sizes ranging between 200 and 400µm. Therefore, 40 fatigue specimens and 12 creep specimens have been manufactured from that material. Preliminary creep experiments have been performed at 300°C and 350°C using a constant stress creep machine and applied stresses ranging between 190 and 200MPa. The creep times to rupture have been found to range between 334 and 526hrs. Further creep experiments will explore the effects of lower and larger applied stresses. Fatigue tests will be performed in 2008.

TW6-TVM-LIP3: Modification of ITER materials documents

Over the past few years a number of ITER Materials Properties Handbook (MPH) files have been created. Some of the existing files on the mechanical properties (fatigue, creep, creep-fatigue) of unirradiated CuCrZr have been produced by the FTM group of the CRPP. ITER MPH files need to be constantly updated. The available data have to be reduced to data produced under well-accepted standards and for which a good traceability exists. The new produced data, when available, will have to be introduced into the datasets, the figures of the MPH files will have to

be updated, mean curves and data equations will have to be re-calculated, and new recommendations for the designers will have to be proposed. This task will consist in particular in revising the documentation available on the production of joints of the following types: SS to SS (stainless steel), SS to CuCrZr and Be to CuCrZr. New MPH files will be written, focused on the main properties of interest: fracture toughness, tensile and fatigue properties. The results being produced under the tasks TW4-TVM-CUSSPIT and TW5-TVM-COMADA will be introduced into the corresponding MPH files. As a consequence, this work is presently on hold and will start at the completion of the CUSSPIT and COMADA tasks.

2.5 Superconductivity

In 2007, a first series of large size Nb₃Sn Cable-in-Conduit-Conductors were tested in SULTAN as *Qualification Samples* for the ITER toroidal field conductor. Three out of seven samples were tested under bilateral agreements between CRPP and the ITER parties, i.e. outside the scope of the EFDA contracts. The results of these tests, which are the basis to start the procurement of the ITER conductors, received high attention from the fusion community.

The preparation work the Dipole test facility at CRPP (nickname EDIPO) has progressed in 2007 with the test in SULTAN of three prototype conductors and the detailed design of the cryogenic components. The superconducting NbTi strand for the windings of the transformer has been procured and the windings are being manufactured. Calls for tender of critical items (HTS for current leads and large power supplies) have been completed.

The studies on high temperature superconductors (HTS) are completed. Studies and analysis activities are carried out on an alternative TF winding pack, ac losses for control actions, friction factor on porous media, assessment of SULTAN results, current leads for ITER, Poloidal Field winding design and inter-strand resistance.

2.5.1 Underlying Technology

Assessment of friction factor coefficient in CICC vs. void fraction

The assessment of the pressure drop along a CICC is crucial in determination of the pumping costs, particularly dealing with huge hydraulic lengths of several hundred meters typical of a coil. This assessment requires the knowledge of reliable correlations for the friction factors in each flow region of a CICC. Here we performed an experiment whose goals are: to determine the longitudinal bundle friction factor as a function of the void fraction and Reynolds number and to check the possible dependency of the friction factor on the cable pattern. The experimental device at CRPP uses pressurized water at room temperature.

Two single channel CONDOPT CICC's with different cabling patterns were used in the experiment. The ~3m long samples underwent a series of compaction steps to bring their outer diameter from the nominal size (~18.5mm) to ~17.6mm in three different steps of ~0.3mm. The longitudinal friction factor is deduced from measurements of pressure drop (Δp) and mass flow rate (\dot{m}). In the measurements the water flow was increased from 0 to the maximum achievable in approximately equal increment steps.

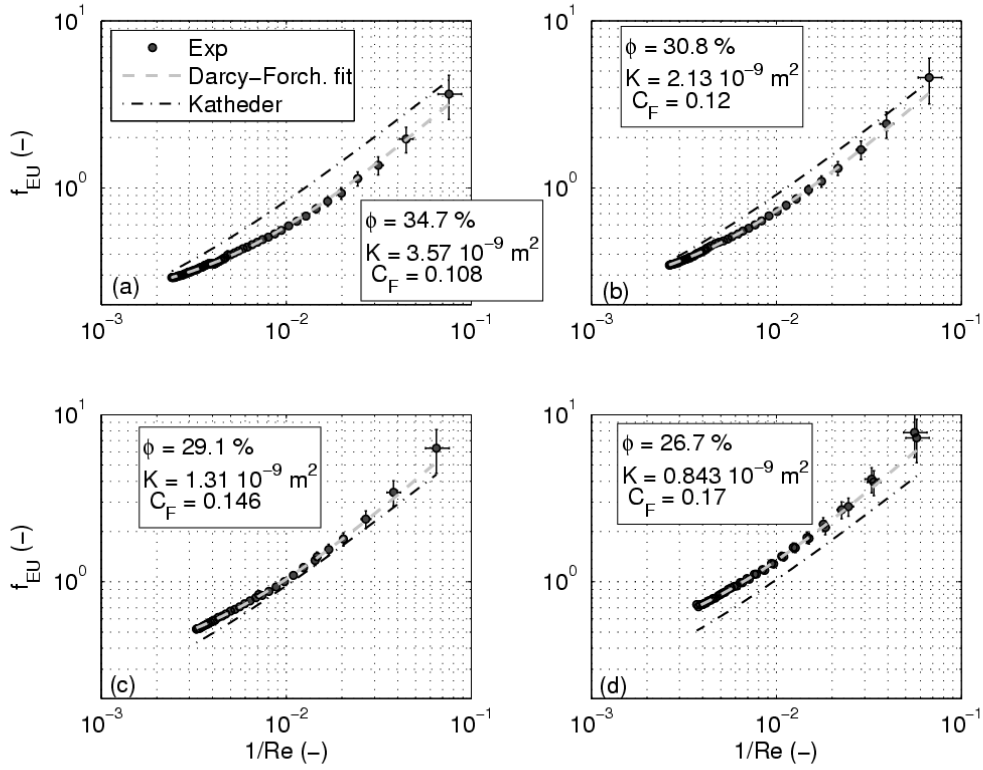


Fig. 2.5.1 Friction factor as a function of the inverse of the Reynolds number in for CONDOPT1 sample in initial state (a), after the first (b), second (c) and third (d) compaction. The best-fitting Darcy-Forchheimer (porous medium) and the Katheder correlations are also shown.

Two additional lengths (~2m) of the same original conductors underwent the same swaging process as the measured samples. Eventually the void fraction of a short sample of each reduction step ($l \approx 200\text{mm}$) was measured by vacuum ultrasonic water filling. The difference in weight between the empty and filled conductor gave the mass of water contained in the voids ($V_{voids} = V_{water}$) and hence the experimental void fraction is calculated as

$$\varphi_m = \frac{V_{void}}{V_{CS}} = \frac{m_{water}}{\rho_{water} V_{CS}}$$

where $V_{CS} = A_{total}l$ is the volume of the cable space inside the sample length l .

The dimensionless analysis is then performed in terms of Reynolds number Re and longitudinal friction factor f_{EU} . The Reynolds number is defined as a function of the hydraulic diameter $D_h = 4A_{fluid} / p_w$

$$Re = \frac{\dot{m}D_h}{\mu A_{fluid}}$$

and the Darcy friction factor defined as

$$f_{EU} = \frac{2D_h \rho A_{fluid}^2 \Delta p}{\dot{m}^2 L}$$

The results of f_{EU} as a function of the inverse of Re are reported for CONDOPT1 in Fig. 2.5.1, with the error bars computed as a combined standard uncertainty. The experimental f_{EU} (Re) are compared with the correlation for CICC proposed by Katheder and with another, more fundamental, porous-media (PM) analogy approach according to which the bundle friction factor is linearly dependent from the inverse of the Reynolds number $f_{EU,PM} = \frac{a}{Re} + b$. The Katheder correlation confirmed its predictive capabilities in the range $25\% < \varphi < 30\%$ but the relative errors can be as high as 100 %. The porous media analogy gives a much better agreement with fitting parameters comparable with previous works and surveys.

Interstrand resistance measurement on ITER size electrical termination

In large, cabled superconductors, a non-negligible level of current unbalance among the strands is unavoidable in DC operation due to non-homogeneous contact resistance distribution at the electrical connections. When the overloaded strands saturate their current carrying capability, a current sharing voltage is sensed at the high field region, driving the redistribution of the current to the less loaded strands. In large CICC's, the current redistribution takes place preferably in the cable terminations, where the resistance is lower. The crucial parameter that governs this phenomenon is the contact resistance between the strands of the cable at the joint. In fact, the lowest the inter-strands resistance, the lowest the voltage required for an effective current redistribution process.

In order to evaluate the interstrand resistance in the termination and therefore assess the effectiveness of the current redistribution, a CICC Nb₃Sn sample, already tested for resistance distribution in the JORDI test facility, is rearranged to measure the interstrand resistance. Just after the termination, the cable is opened down to the first cable stage and only two elements (strand or braid) are connected at the time to the current lead. The voltage between the two elements is sensed just below the connection. The aim of the experiment is to investigate the resistance between two current carrying elements, which could be strands and/or braids, by considering different configurations (i.e. adjacent or non-adjacent elements, element in adjacent or non-adjacent sub-cables). The particular structure of the termination is neglected, it is treated as a 'black box', and the equivalent resistance viewed from two external terminals is measured. To this purpose, a representative number of connections is selected. In particular, 16 current leads and 22 pairs of voltage taps, corresponding to 22 survey channels, are connected to a defined number of strands and/or braids. In Fig. 2.5.2, a picture of the sample before the cool down is shown together with a cross section of the cable with identification of the first cable stage.

A switch board at room temperature selects the connection according to the test program without warming up the sample. The measurements are carried out by ramping up the current to around 50A, waiting few minutes until the steady state has been reached, and then ramping down the current to zero. The amplitude of the current is of the same order as the average current per strand in a ITER TF conductor, which is about 75A. The results are summarized at the bottom of Fig. 2.5.2.

Starting from these results, the voltage that can drive the current redistribution and that could therefore be ascribed to this phenomenon can be calculated as the product between the interstrand resistance and the excess of current circulating in a strand or in a group of strands. Since the measured resistances are very low, in the range of few nΩ, an effective current re-distribution at the termination is driven by voltage as low as 0.1μV, corresponding to very low electric field in the high magnetic field section of a SULTAN sample. If in the high field region a voltage

higher than $1 \mu\text{V}$ is detected, this can not be ascribed to a current unbalance and current re-distribution at the joint, because that kind of current redistribution is driven by much lower voltage levels.

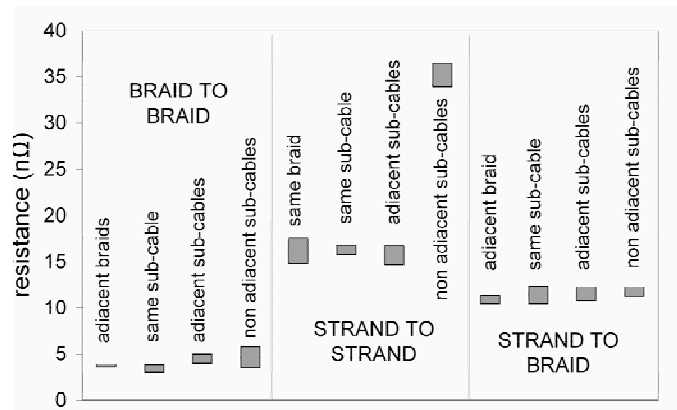
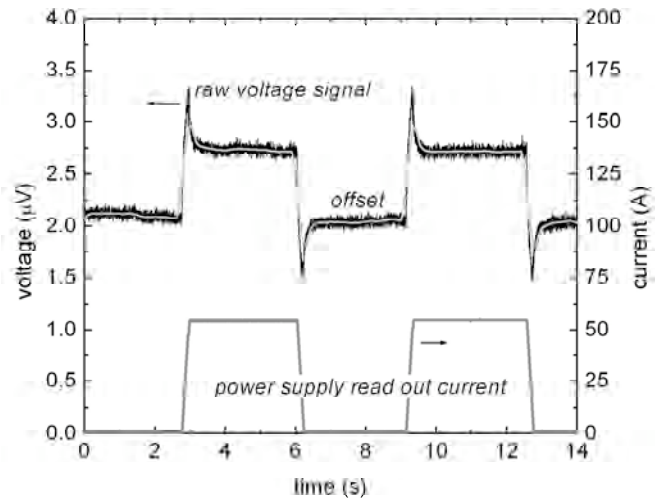
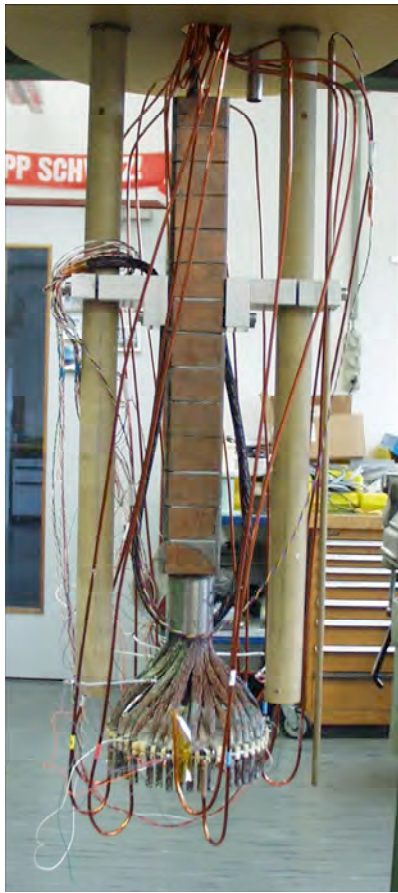


Fig. 2.5.2 Left, the termination (upside-down) with connections and wiring. Right, current / voltage for a strand-to-adjacent-braid connection and summary of interstrand resistance results

Design of a ITER TF winding pack using a react-and-wind conductor

Following the successful development and test of a 48kA react & wind conductor for the TF coil of ITER, a TF winding pack option is designed and analyzed at CRPP, based on a 68kA conductor designed to the same principles as the 48kA prototype, except that the low melting alloy impregnation was eliminated, see Table 2.5.1.

The conductor insulation is a 1.25mm pre-preg glass-epoxy with interleaved Kapton foil. It is applied after jacketing and is designed to withstand the voltage of a whole, single pancake (398V). At the coil winding, a straight length of conductor (50 m – 80 m long) is wrapped by the pre-preg insulation, cured overnight and inserted into a length of pre-assembled U-profiles. The profiles are closed and laser welded. An adhesive, 0.5mm thin glass-epoxy sheet is applied on the inner side of the outer jacket in order to eliminate large eddy currents loops during a current dump, as happen with the ITER radial plates. The completed section of conductor is wound on the D-shape and another straight conductor section is assembled. A full single pancake is wound within 20 working days. With two assembly/winding lines in parallel, the production rate is of the order of 4 TF coils/year.

The size of the double-jacketed conductor is 40.1x76.5mm. At one end of the single pancake, the outer jacket is electrical connected to the conductor. The winding pack consists of 8 full single pancakes (each 511m long) and two smaller side pancakes (≈ 200 m long). The AmpereTurn are the same. The inter-pancake insulation is 2mm thick. The ground insulation and case are the same as in ITER. The fillers to adjust the winding pack to the case size are made of insulated stainless steel profiles.

Diameter / Number of Cr plated Nb ₃ Sn strands	1.8mm/126	
Cu : non-Cu / twist pitch in Nb ₃ Sn strands	1/25mm	
Cable pattern, 2 stages	(1+6) x 18	
Cable pitches, right hand	65/350mm	
Ti strip as cable core	0.2mm x 30mm	
Void fraction in the flat cable	$\approx 20\%$	
Dimension of superconducting flat cable	10.2mm x 41.3mm	
Bending strain during manufacture (bonded model)	$< 0.11\%$	
Diameter / Number of Cr plated copper wires	4.0mm/28	
Pitch of copper layer, left hand	380mm	
Dimension of the stabilized flat cable	18mm x 49mm	
Thickness of steel jacket / Outer corner radius	2mm/8mm	
Dimension of the jacketed conductor	22mm x 59mm	
Total non-copper cross section	160mm ²	
Copper cross section, in strand / total	160/512mm ²	
Spacer cross section	20mm ²	
Helium cross section, channel / total	75/250mm ²	
Current sharing temperature in operation	> 6.3 K	
Non-copper current density @ 68 kA	425A/mm ²	

Table 2.5.1 Layout of 68kA conductor for ITER TF coils

The electromagnetic and mechanical performance of the TF winding pack has been assessed by means of 2D Finite Element (FE) analyses, carried out with the commercial code ANSYS. The results of the electromagnetic analysis have shown that the maximum value of the field is 11.6T. The Lorentz forces acting on the structure have been computed in order to apply them to the subsequent mechanical analysis. There is very good agreement between the results of the two models, being the field value in the conductors and the Lorentz forces essentially the same.

The mechanical model is essentially the same as the electromagnetic one. Moreover, “contact” elements have been inserted between the winding pack and the steel case in order to allow the sliding and the contact between the two surfaces. In order to implement the so called “generalized plane strain” option and consider the impact of forces perpendicular to the section, the 2D model has been extruded in a thin slice 10 mm thick. Those forces have been calculated by means of 3D analyses, where the winding pack has been modelled with smeared and homogeneous material properties. The in-plane Lorentz forces have been applied as pressure loads on the internal surface of the steel jacket. The winding pack has been constrained in the vertical direction in both edges.

The results that have been obtained for global displacement are in perfect agreement with those of ITER layout. The maxima are 13.1mm and 14.46mm for the proposed winding and for ITER respectively. The Lorentz forces push the winding pack against the steel case toward the centre of the ITER magnet system

(left direction in the model), by opening a gap between the winding and the steel case in the opposite side of the assembly. This gap is about 2.2mm in both cases.

In a first design iteration, the maximum stress intensity in the jacket was 675MPa and the shear stress in the turn insulation was 51MPa. Increasing the jacket outer radius from the original 6mm to 8mm, the values have been reduced down to 564MPa (jacket) and 42MPa (insulation), see Fig. 2.5.3. Actually, the proposed manufacturing process foresees that the conductor insulation is bonded to the conductor jacket, but not to the outer jacket. In this case, more complex to analyze, the insulation shear stress would disappear and the jacket stress would also be further reduced.

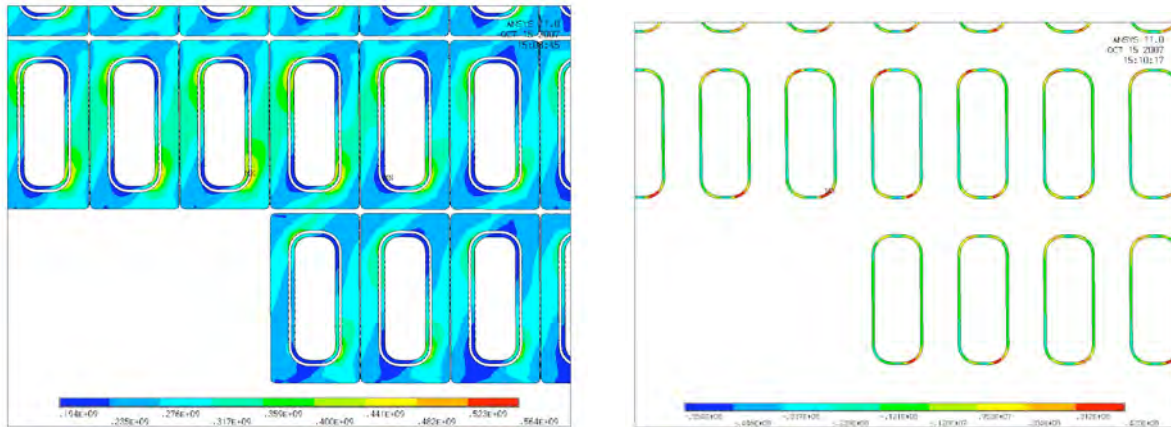


Fig. 2.5.3 FE Analyses for jacket and turn insulation stress of the proposed TF winding pack

Thermal-hydraulic analyses have also been carried out to assess the mass flow rate/pumping work and the heat removal capability, from the inlet temperature of 4.5K (same as ITER) to the T_{cs} . At the same pressure drop as in ITER (0.1MPa) the pumping work is lower and the heat extraction twice as much compared to ITER.

For the joints and connections, each conductor end is dismantled from the jacket and soldered into a steel/copper, vacuum brazed termination box. At the winding pack assembly, the individual pancakes are series connected by soldering two termination boxes. The layout of the connection is similar to what is used for the SULTAN sample. Each coil has five joints at the inner perimeter and four at the outer perimeter. The helium inlet is at the inner joints, the outlets at the outer joints and coil termination. The joint location is supposed to be at the same place where the terminations are, i.e. at the bottom part of the outboard leg, the same location as in present ITER TF coil design. The inter-pancake connections are overlap joints with minimum protrusion from the winding pack envelope. The coil terminations are sticking out of the coil envelope, as in present ITER TF coil design with a bending radius $\geq 1m$. The inter-pancake insulation and the ground insulation are vacuum impregnated in a single pass.

Beside the saving in Nb_3Sn strand due to the retention of strand properties in the conductor (140t Nb_3Sn strand = over 100M\$), other substantial advantages offered by the react & wind option are the simplification of the heat treatment procedure (no issue of conductor elongation and no welds in the heat treatment), the elimination of the expensive radial plates (the coil withstands a current dump without quench), and easier tooling for winding (no double pancake, no “transfer” procedure).

2.5.2 Technology Tasks

SULTAN Operation 2007 (TW6-TMSC-SULTAN07)

The operation of the SULTAN facility in 2007 is covered by an EFDA technology task. Besides European conductors, three samples from other ITER parties (KO and JA) have been tested under bilateral agreements in May-July. The time used for these “non-EU” tests will be recovered in 2008 by extending the EFDA contract at zero cost for the corresponding time. In the testing period reported here (November 2006 – November 2007), following test campaigns have been carried out on European samples:

- PITSAM1, high field prototype conductor for EDIPO (November 2006)
- TFAS1, bench mark test before solder filling the termination (November 2006)
- TFAS1, test after solder filling the termination (January-February 2007)
- TFPRO1, ITER TF sample with EAS strands (March 2007)
- TFPRO2, ITER TF sample with OST strands (April 2007)
- PITSAM2, square, medium field prototype conductor for EDIPO (July 2007)
- RFTF1 (NEFSS), ITER TF sample with Russian strands (July-August 2007)
- PITSAM3, rectangular, medium field prototype conductor for EDIPO (August-September 2007)
- TFPRO2, re-test with enhanced instrumentation (October 2007)
- PITSAM4, low field prototype conductor for EDIPO with LUVATA strands (October 2007)

Operation of SULTAN was discontinued in December 2006 for maintenance of the cryo-plant. The current year maintenance is in November 2007.

The tests of TFAS1 and PITSAM samples are reported below. The results of TFPRO1, TFPRO2 and RFTF1 are discussed in the scope of FSTEST task.

TFAS1 with solder filled termination and joint

The TFAS1 sample is composed of two CIC conductors made of EAS bronze route strands ($J_c=780\text{A}/\text{mm}^2$) and OST internal tin strands ($J_c=1100\text{A}/\text{mm}^2$). The TFAS1 sample was tested four times before solder filling of its extremities. A reference test was done before solder filling in November 2006. After solder filling the test was repeated at the same test conditions in January 2007.

In contrast to expectation, a significant increase of resistance up to $20\text{n}\Omega$ in solder filled joint is found compared to reference tests. The higher resistance is due to the mismatch of the surfaces of the termination boxes, slightly deformed during the thermal cycle to solder fill.

The voltage traces at different test campaigns are presented in Fig. 2.5.4 left. The current sharing temperature tests at 11T background field show a slight improvement in EAS conductor in reference test before solder filling, and further degradation is observed in OST conductor before and after solder filling while degradation in EAS conductor is found after soldering process only, Fig. 2.5.4 right. The solder filling of the termination was driven by a speculation about a high inter-strand resistance preventing current re-distribution at the joint. However, solder filling of the termination failed to cure the voltage drift observed in the former campaigns and the T_{cs} performance is not improved.

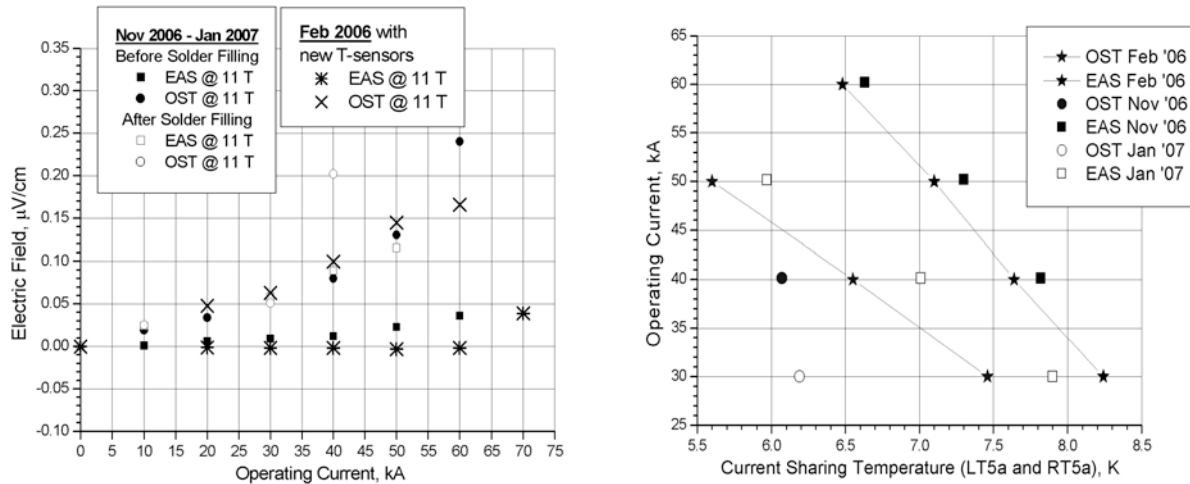


Fig. 2.5.4 Left, evolution of the voltage growth with current through the last three test campaigns. Right, T_{cs} results at 11T background field through the last three test campaigns.

PITSAM samples

A first version of the high field conductor for the EDIPO (European Dipole) was tested in 2006 with disappointingly low dc performance. The observed degradation of the dc performance with cyclic load has been attributed to the damage of the Nb_3Sn filaments in the strands. In the case of a relatively large void fraction the mutual support of the strands seems to be not sufficient to avoid transverse load degradation of the Nb_3Sn strands. The void fraction has been reduced to 30% in the PITSAM high and low field conductors. In addition, a rectangular shape has been selected for the conductors PITSAM1 and 3. The main characteristics of the PITSAM CIC conductors are listed in the Table 2.5.2.

In Fig. 2.5.5 left, the evolution of the current sharing temperature of the PITSAM1, 2, 3 and 4 samples during cyclic loading is compared. PITSAM2 shows a pronounced reduction of the current sharing temperature with increasing number of load cycles, whereas for the other three conductors no cyclic load degradation has been observed. In the case of the PITSAM3 sample, a reduction of the current sharing temperature has been found after a first warm-up and cool down cycle ($T_{cs}=6.81\text{K}$ at 8T, 17kA). A second thermal cycle leads to a further decrease of the current sharing temperature ($T_{cs}=6.63\text{K}$).

The exact value of the strain experienced by the Nb_3Sn strands in a cable-in-conduit conductor is not exactly known. Due the brittle nature of the Nb_3Sn superconductor the large transverse loads, which originate from the large Lorentz forces, may lead to a damage of the strands. Below the strain leading to micro-crack formation in the Nb_3Sn filaments, the critical temperature, the upper critical field and the critical current depend reversibly on the strain state of the superconductor, as described by the scaling relations for a longitudinal strain. Least squares fits have been used to determine the strain value providing the best agreement of measured and calculated T_{cs} data. A reduction of the performance with respect to the expectations from the strand data has been taken into account by a reduced filament area ($C_1^{cable}/C_1^{strand} \leq 1$), used to fit the data. For each conductor, both fitting parameters are optimized applying the minimum square sum criterion to the set of results.

Sample	PITSAM1	PITSAM2	PITSAM3	PITSAM4
Comments	High field	Low field	Low field	Low field
Cable pattern	(3×3)×4×4	(3×3)×3×4	(3×3)×3×4	(3×3)×3×4
Cu/non Cu strands	(0/9)×4×4	(5/4)×3×4*	(5/4)×3×4*	(4/5)×3×4**
Number of Nb ₃ Sn strands	144	48	48	60
Strand type	OST Nb ₃ Sn	OST Nb ₃ Sn	OST Nb ₃ Sn	Pori Nb ₃ Sn
Strand diameter (mm)	0.81	0.81	0.81	0.813
Number of Cu strands	0	60	60	48
Cu strand diameter (mm)	0.81	0.81	0.81	0.81
Twist pitch (mm)	58/95/139/213			
Jacket thickness (mm)	1.6	1.75		
Outer conductor dimensions (mm)	21.1 × 9.5	12.6 × 12.6	15.4 × 10.5	12.6 × 12.6
Void fraction (%)	30	30	30	30
Peak field factor k_p (T/kA)	0.032	0.042	0.040	0.042

* First triplet 1 Cu + 2 Nb₃Sn, second and third triplet 2 Cu + 1 Nb₃Sn

** First and second triplet 1 Cu + 2 Nb₃Sn, third triplet 2 Cu + 1 Nb₃Sn

Table 2.5.2 Layout of 68kA conductor for ITER TF coils (data provided by EFDA)

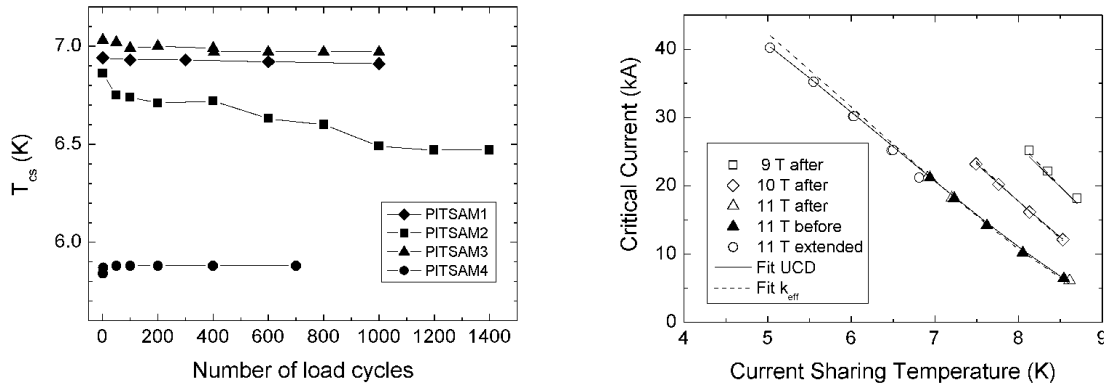


Fig. 2.5.5 Left, evolution of (T_{cs}) with increasing number of load cycles at 11T, 21.2kA (#1), 8T, 17kA (#2, #3) and 5.5T, 17kA (#4). Right, T_{cs} results for the PITSAM1 conductor before and after cycling loading. The solid lines have been obtained from a least squares fit to the T_{cs} values found after 1000 load cycles at 11T and 21kA (-0.65% strain, $C_1^{cable}=C_1^{strand}$). The T_{cs} values from the extended tests have not been used for the fit. The dotted line is calculated from an effective self-field factor of 0.0186T/kA and a strain of -0.65% .

In Fig. 2.5.5 right, the T_{cs} values of the PITSAM1 high field conductor, measured before and after cyclic loading, are compared. The current sharing temperature of the PITSAM1 conductor is insensitive to cyclic loading (however, no thermal cycle war carried out on PITSAM1). Even after the extended tests at higher currents the performance of PITSAM1 is nearly unchanged. The performance of PITSAM1 is close to the expectations for not degraded strands and a strain of -0.65% provided by a least squares fit procedure.

For a comparison of the performances of PITSAM1, 2 and 3 conductors, we retain a common strain value of -0.65%. The degradation factors are gathered in the Table 2.5.3.

CIC conductor	$A_r = C_1^{cable} / C_1^{strand}$	Comments
PITSAM1	1.00	After 1000 load cycles
PITSAM2	0.76	Initial performance
PITSAM3	0.79	Initial performance
PITSAM3	0.72	After first warm-up cycle

Table 2.5.3 Degradation, expressed as area reduction ratio, for PITSAM 1, 2 and 3, made of the same strand

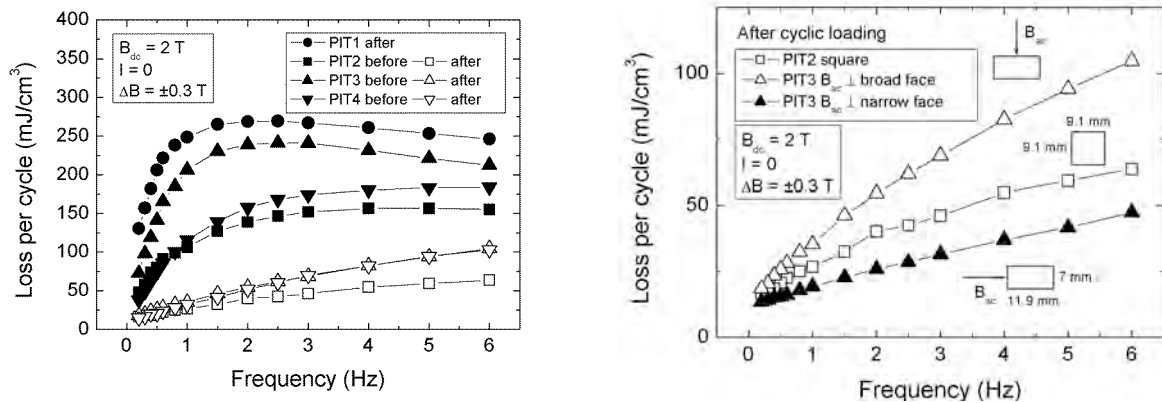


Fig. 2.5.6 Left, total loss per cycle normalized to the cable volume versus frequency. Right, ac loss for the same strand rope (PITSAM 2 and 3) after cyclic loading at different aspect ratio – square, thin rectangular and broad rectangular

The results of the ac loss measurements by gas flow calorimetry are presented in Fig. 2.5.6 left, normalized to the cable volume, including segregated copper. As usual, the ac loss is considerably reduced after cyclic loading. In the case of the rectangular conductors PITSAM1 and 3, the ac field is applied perpendicular to the broad face of the conductors. The total loss for fields, applied parallel to the broad face, has been also measured for the conductor PITSAM3, Fig. 2.5.6 right, highlighting the role of the aspect ratio (demagnetization factor) in both amplitude and slope of the loss curve. At frequencies of 1Hz or above the loss is at least by a factor of two smaller than for the unfavorable field direction.

Preparation of SULTAN Samples from ITER TF Conductors (TW6-TMC- TFPRO, TW6-TMSC-LTPSAM, TW5 – TMSC - NEFSS)

In the scope of three EFDA contracts, four SULTAN samples have been prepared between January and July 2007. For the NEFSS task, two short ITER TF conductor sections, based on Internal Sn strand developed at Bochvar Institute (Moscow),

have been purchased by CRPP. For the TFPRO and LTPSAM tasks, EFDA supplied four short sections of ITER TF conductor – two sections made out of “bronze” technology strands (EAS) and the other two by Internal Sn strands (OST). The LTPSAM task also included the modification of an existing sample, TFAS1, by solder filling the four conductor terminations.

Solder filling of TFAS1 termination. The aim of the solder filling of the TFAS1 sample extremities is to reduce the inter-strand resistance and to obtain a better balanced current distribution in the hope to eliminate an extra voltage growth phenomena with current ramp. The extremities of the conductors were fabricated with use of explosion-bonding technique (Copper/stainless steel bonding). In order to minimize a risk to destroy the terminations, it was decided to perform the filling procedure without disassembly of terminations. The sample was first disassembled in two conductor sections and each section went through solder filling procedure for both ends.

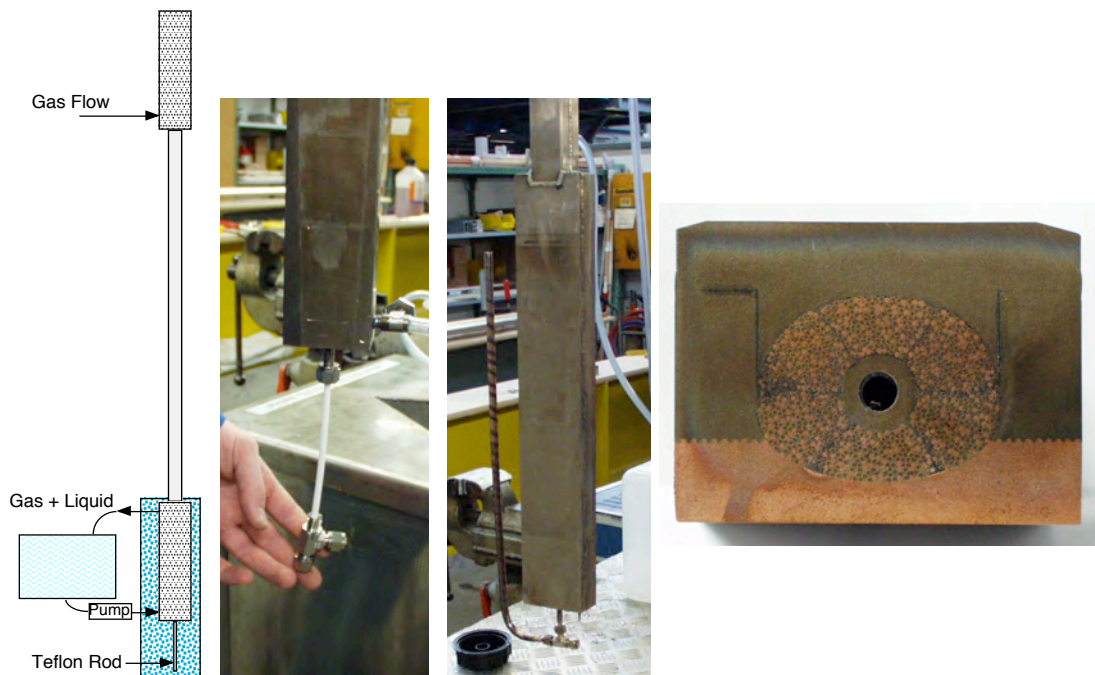


Fig. 2.5.7 From left to right: scheme of the Cr removal procedure by circulation of HCl, the copper siphon prepared for solder filling of the upper termination, a lower termination with the Teflon rod inserted to maintain free the central channel, cross section of a solder filled joint, destroyed after the test.

The solder filling procedure begins with Cr removal in upper termination. The existing Helium inlet pipe and the axial access of the termination are used to establish a flow of HCl solution through the cable for 10 minutes. Then, the same circuit is used to wash the cable with water and dry with compressed air. After Cr removal, the termination is filled from below with “Sodaflux K” in the ultrasonic bath; then, the flux is emptied, and the termination is removed from the ultrasonic bath. A copper siphon is brazed to the axial access of the termination and heated by heating wire; the termination is placed between two heating panels and heated to 290°C. Rods of SnAg5 alloy are fed into the siphon till the full length of the termination is filled by solder. After cool down of the filled termination, the siphon is cut. The conductor is washed with Acetone and dried overnight. In the upper termination, the central channel stays blocked by solder, as the coolant outlet is placed in the conductor before the termination. In the lower termination, the central channel must stay free for the coolant. To prevent the central channel to be

filled by solder, a 6mm Teflon rod is inserted from the axial access and removed once the solder solidifies. After completing the solder filling, the joint is re-assembled with an Indium foil interleaved between the bottom joint terminations. The original steel clamps and the instrumentation is applied to complete the sample assembly, see Fig 2.5.7.

The identification name for the three ITER TF samples is TFPRO1 (for task TFPRO), TFPRO2 (for task LTPSAM) and RFTF1 (for task NEFSS). A detailed description of the six conductor lengths building the three SULTAN samples is given in Table 2.5.4. The drawing of the three samples as well as the assembly procedure is identical. The main steps are highlighted below, see also Fig. 2.5.8. The detailed description of the assembly procedure is in the EFDA reports of TFPRO task.

After straightening and cutting the conductor lengths, the extremities are compacted to a lower void fraction without dismantling the jacket. To prevent any slippage between jacket and cable during the heat treatment and joint manufacture, two crimping rings are applied at the beginning of the compacted sections.

The heat treatment for the TFPRO1 and TFPRO2 conductor sections is carried out at once in the 4.5m long vacuum furnace at CRPP, with 8 barrels for strand witness samples. For RFTF1 a separate heat treatment with 2 barrels was done. The strand specimens (total of 10 barrels) have been tested for I_c in liquid helium in a background field of 10T to 14T.

After heat treatment, the strain gauges are applied on the jacket at the location of high field center. The change of strain measured on the jacket before and after dismantling the conductor ends is zero within the accuracy of the measurements. In a separate, destructive test, the conductor is cut immediately right and left of the strain gauge. The change of strain of the jacket in this case, i.e. when the crimping rings are no longer effective, was of the range of 800 ppm. On one section of RFTF1, two fiducial marks are welded on the jacket prior to the heat treatment to measure the average elongation / shrinkage. The elongation is 1.07mm, corresponding to 892ppm.

The cable surface is freed from the outer wrap and the sub-cable wrap and the Cr plating is chemically removed from the strand surface in a 16%-18% HCl solution. After Cr removal, the cable surface at the conductor ends is tinned.

The boxes for the upper termination are pre-fabricated by vacuum brazing of the copper plate and the steel half box. The pre-tinned termination is inserted into the box and soldered with an interleaved SnAg5 foil. Eventually, the steel lid and the collar of the termination box are welded to complete the upper termination.

The assembly of the bottom joint starts with the welding of the eye-glass piece to the conductor jackets. Then the steel plates of the joint box are pre-assembled around the pre-tinned cable ends, which are soldered to matching segmented copper elements. After completing the soldering, the steel plates are vacuum tight welded to complete the assembly of the joint box.

The two conductors are bolted into a steel clamp, segmented in three sections, which reacts the repulsive force in operation, estimated up to 1 MN/m. Electrical insulation between clamp and conductors is provided by glass-epoxy half shells matching the diameters of the two conductors.

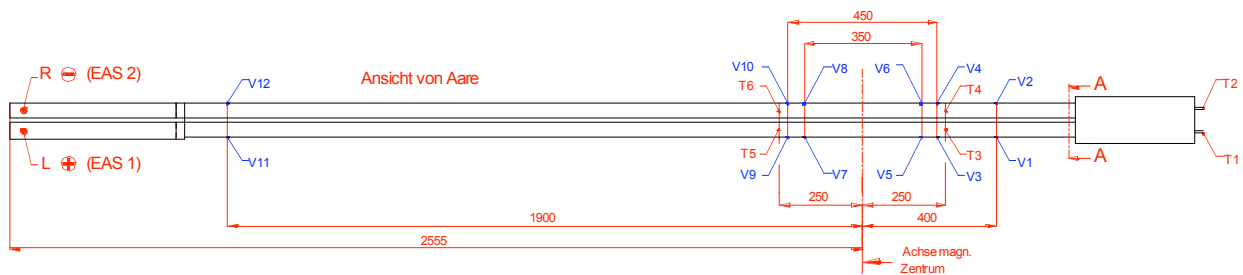
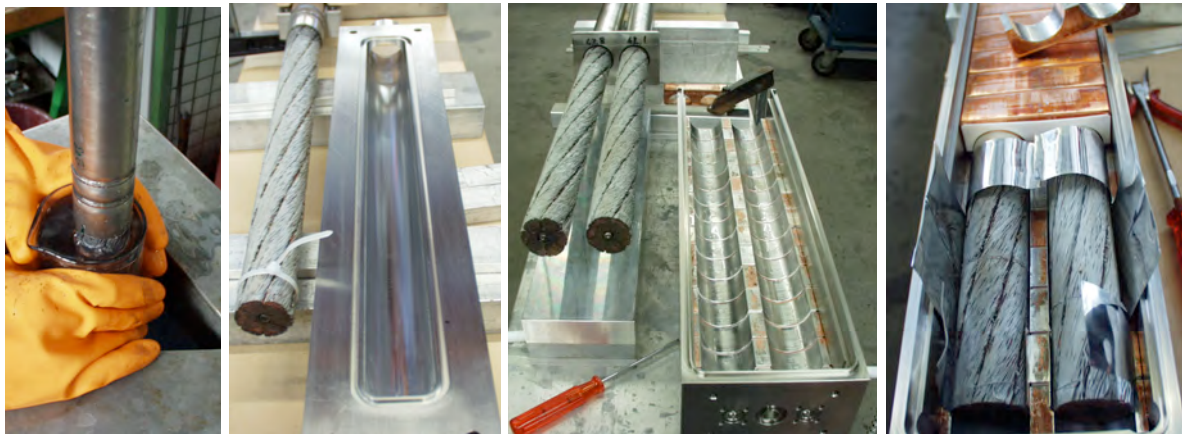
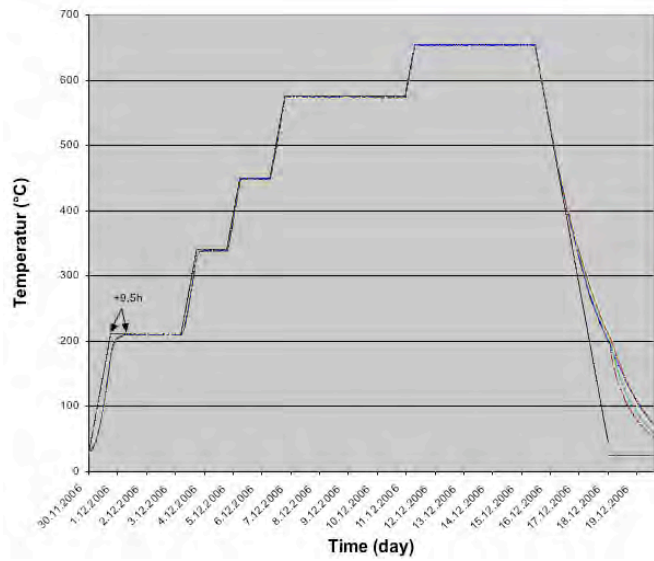


Fig. 2.5.8 Various phases of the sample preparation and assembly. From top to bottom, the conductor section at the entrance of the furnace, the temperature traces of the heat treatment, Cr removal in HCl solution, upper termination box before assembly, bottom joint before and during assembly, instrumentation scheme

The instrumentation includes voltage taps (14 signals by twisted pairs), two heaters and six temperature sensors, CERNOX, which have been applied with a novel method to improve the thermal coupling with the conductor jacket. On RFTF1 two additional CERNOX have been applied. The coolant flow, according to the ITER specification, is from bottom to top.

Participation in Conductor Tests and Evaluation of Test Results (TW6-TMSC-FSTEST)

The basis of the qualification of the cable-in-conduit (CIC) conductors for the toroidal field (TF) coils of ITER is the dc test of the conductor sample in the SULTAN facility. The ITER conductor requirements are fulfilled, when the current sharing temperature (T_{cs}), measured at the ITER operating conditions of 68 kA and 10.78 T background field, is 5.7K or above. Three samples TFPRO1, TFPRO2 and RFTF1 have been tested in the SULTAN facility in 2007. The task FSTEST, completed in September 2007, deals with the assessment of the test results. Both legs of TFPRO1 are manufactured of EAS strands, while two slightly different OST strands are used for the TFPRO2 sample. The conductors of the RFTF1 sample are manufactured of Nb₃Sn strands supplied by the Bochvar Institute (Russian Federation). The main features of the three SULTAN samples and the test results of the corresponding Nb₃Sn strands (witness samples) at 12T and 4.2K are listed in the Table 2.5.4.

Sample	TFPRO1		TFPRO2		RFTF1	
Conductor	EAS1 (L)	EAS2 (R)	OST2 (L)	OST1 (R)	RF33 (L)	RF30 (R)
Strand type	Bronze		Internal tin		Internal tin	
Strand identity	NSTT8305		7878	7567 ^a 7603 ^b 7730 ^c	BrP	
Cable pattern	((2 sc + 1 Cu) × 3 × 5 + core) × 6					
d _{strand} (mm)	0.813		0.815	0.815	0.82	
d _{Cu^{triplet}} (mm)	0.82		0.81	0.82	0.82	
Copper cores	3 × 4 (Pitches 45 mm / 87.5 mm)					
d _{Cu^{cores}} (mm)	0.81		0.81		0.82	
I _c at 12T, 4.2K (A) *	193.1		301.4 / 303.8	265.4	245.9	
J _c at 12T, 4.2K (A/mm ²) *	720		1160/ 1170	1020	930	
n at 12T, 4.2K *	39.1		25.1 / 20.8	32.4	36.2	
No of sc strands	900					
No of Cu wires	522					
Twist pitch (mm)	45 87 126 245 486*	45 87 126 245 492*	116 182 245 415 520*	45 87 126 245 520*	45 84 124 250 453	45 84 124 250 453
Petal void fraction (%)*	33.8	29.3	27.7	29.1	32.9	31.8
Central spiral id × od (mm)	6.9 × 9.0		7.0 × 9.1		7.0 × 9.0	
Cable space diameter (mm)	40.25	38.85	38.25	38.85	40.5	40.5
Jacket thickness (mm)	1.6	1.6	1.6	1.6	1.6	1.6
Conductor od (mm)	43.45	42.05	41.45	42.05	43.7	43.7
Distance of legs (mm)	51					

* measured at CRPP, ^a 496 strands, ^b 144 strands, ^c 260 strands

Table 2.5.4 Main Characteristics of strands and cable for the TFPRO1, TFPRO2 and RFTF1 samples

Originally it was intended to use the voltage signals without a current or temperature-dependent offset correction (raw data). In the raw data only the voltage offset at zero current is subtracted. However, for several ITER TF qualification samples non-negligible positive or negative current-dependent offsets have been observed. Fig. 2.5.9 illustrates this behaviour for the TFPRO1 sample. Above a current of 50kA the transition to the normal conducting state seems to begin leading to a more pronounced, non-linear increase of the voltage in the left leg. In the data with V-I correction, the linear fits shown in Fig. 2.5.9 have been used to

subtract the linearly increasing voltage in addition to the offset at zero current. In the considered example, this correction is very small for the right leg (EAS2) and provides a change of T_{cs} of the order of a few hundredths of a Kelvin. In the left leg (EAS1), the subtraction of the linearly increasing voltage leads to a correction of more than 0.1K

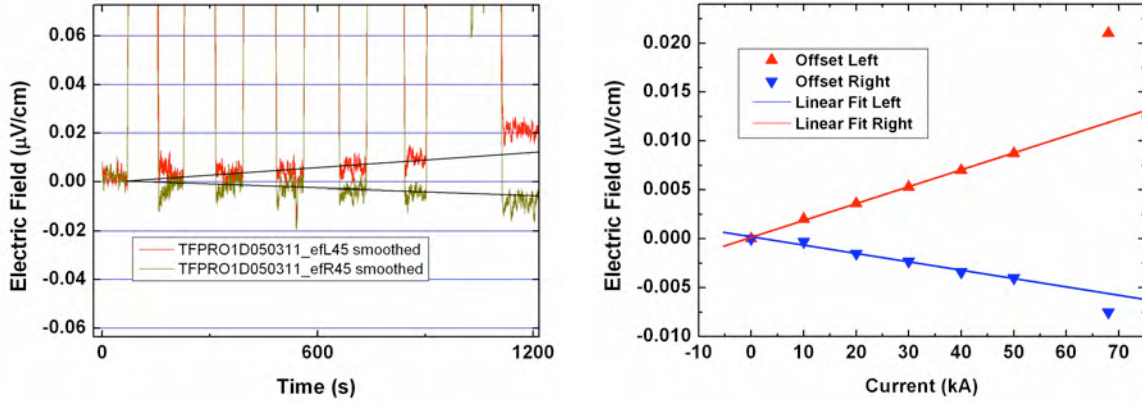


Fig. 2.5.9 Left, electric field vs. time during step-wise ramp-up from 0 to 68kA at $B_{SULTAN} = 10.78T$. The steps are at currents of 10, 20, 30, 40 and 50kA. Right, the same data are plotted as a function of current.

During the re-test of TFPRO2 with enhanced instrumentation in October 2007, it has been tried to determine T_{cs} from a calorimetric measurement of the current sharing power. The temperature of the conductor has been increased in steps in order to provide a quasi steady-state measurement of the current sharing power by means of gas flow calorimetry. The electric field deduced from the calorimetric measurement is

$$E_{cal} = \frac{P}{I_{op}l} = \frac{\dot{m}(T_{after}-T_{before})C_p}{I_{op}l}$$

where P is the generated power, l the length of the high field section (450mm), I_{op} the operating current, \dot{m} the mass flow rate, C_p the specific heat of helium at the temperatures T_{after} and T_{before} , which differ only by a few mK. In spite of the limited accuracy of the calorimetric measurements (e.g. non-homogenous temperature distribution and variations in the helium mass flow rate) they provide some evidence that the early voltages do not significantly contribute to the power generation in the cable. The non-equipotential cable cross-sections under the voltage taps seem to be the consequence of local current re-distribution effects.

In the case of the JATF2 sample, even the above described voltage correction linear in current seems to be not sufficient to provide a performance, which is in agreement with the calorimetric data. Therefore, an alternative voltage correction is proposed based on a fit of the V-T data by the following expression

$$E = E_{transverse} + E_{axial} = a \frac{T}{T_{cs}} + E_c \left(\frac{T}{T_{cs}} \right)^m$$

where E_{axial} is the longitudinal electric field related to the transition to the normal conducting state, $E_{transverse}$ an electric field related to current re-distribution effects, T the temperature, T_{cs} the current sharing temperature and a the offset at $T=T_{cs}$. We assume that the real transition can be described by a power law in temperature. An example of the fits to the measured data is shown in Fig. 2.5.10.

The qualification of all ITER TF conductors included a cyclic load test, performed in such a way that the current is ramped up from zero to the nominal value of 68kA and back to zero in a background field of 10.78T. Independent of the procedure used to assess the current sharing temperature (T_{cs}) no significant cyclic load degradation has been found for the conductors TFPRO1-EAS1 & EAS2, TFPRO2-OST2, RF33 (RFTF1) and RF30 (RFTF1). In the case of TFPRO2-OST1 the current sharing temperature after 1000 load cycles is about 0.4K smaller than the initial value. The current sharing temperatures of the conductors, found after 1000 load cycles, are listed in the Table 2.5.5.

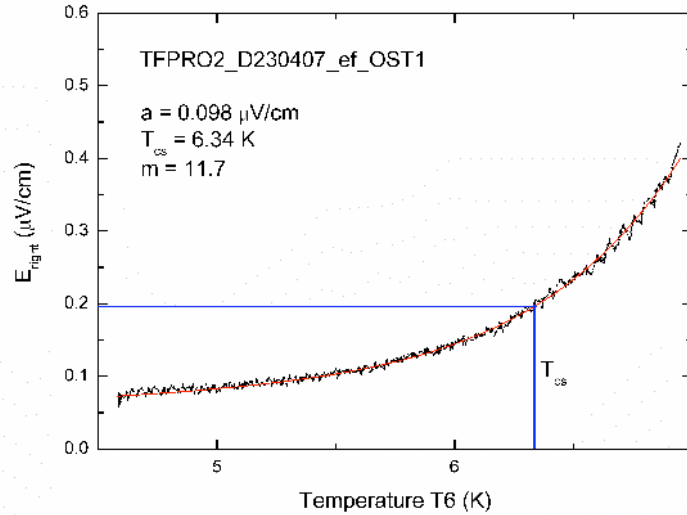


Fig. 2.5.10 Fit of the expression $E = a(T/T_{cs}) + Ec(T/T_{cs})m$ to the V-T curve measured for TFPRO2-OST1 leg.

Accurate values of the current sharing temperature have been obtained for the conductors TFPRO1-EAS2 and TFPRO2-OST2. In these two conductors the current-dependent offset is negligible, and hence all procedures to assess T_{cs} provide nearly identical values. The T_{cs} value of TFPRO1-EAS2 is well above the ITER specification of 5.7K at 10.78T and 68kA. TFPRO2-OST2 shows an extraordinarily high T_{cs} value of 7.35K, which seems to be related to the longer pitches in the first four stages. In the case of the TFPRO1-EAS1 conductor a subtraction of the offset linear in current (V-I correction) provides a T_{cs} value around 6.2K. In spite of the larger uncertainty, the measured T_{cs} value is clearly above the ITER specification. For the TFPRO2-OST1 conductor, the V-I correction leads to a T_{cs} value slightly above 6K, which is considerably smaller than the value of 6.5K provided by V-T fit procedure. Nevertheless, both values are well above 5.7K. In the left leg (RF33) of the RFTF1 conductor, a calorimetric assessment of T_{cs} leads to a value of ≈ 6.2 K, which is 0.3K larger than the T_{cs} found by a V-T fit. The results for the conductor RF30 show a large uncertainty. A V-I correction and the calorimetric assessment of T_{cs} provide a value close to 5.5K, which is below the ITER specification. On the other hand, a T_{cs} of 6.25K has been obtained from a V-T fit, which seems to overestimate the conductor performance.

Sample nickname	TFPRO1		TFPRO2		RFTF1	
Conductor nickname	EAS1	EAS2	OST2	OST1	RF33	RF30
Joint resistance at 0T (nΩ)	0.5		0.5		0.5	
Termination resistance (nΩ)	7.0	5.0	7.5	3.5	2.0	1.4
Electric field (68kA, 4.5K) (μV/m)	2.2	-0.8	-1.1	8.8	-3.0	28.1
Electric field (20kA, 4.5K) (μV/m)	0.4	-0.2	-0.3	2.0	-1.1	11.1
T _{cs} from raw data (K)	5.95	6.32	7.39	5.38	6.16	<4.5
m (fit to $E = a(T/T_{cs}) + E_c(T/T_{cs})^m$)	23.4	12.1	52.4	13.6	13.9	19.0
T _{cs} (fit to $E = a(T/T_{cs}) + E_c(T/T_{cs})^m$)	6.35	6.35	7.35	6.50	5.90	6.25

Table 2.5.5 Summary of T_{cs} results

The results of the ac loss measurements for TFPRO1, TFPRO2 and RFTF1 are presented in Fig. 2.5.11. The losses measured after cyclic loading are much smaller than those found before the dc test. Furthermore, the ac losses were found to depend on the void fraction. The higher loss is found in the conductors with the lower void fractions (EAS2, OST2, RF30). In the TFPRO2-OST2 the longer pitches of the first four cable stages may also contribute to the enhanced ac loss. The dashed lines in Fig. 2.5.11 show the initial slope of loss curves at the given, constant, nr, and are meant as an indication of the likely, low frequency loss range. The coupling loss constants are based on a normalization of the loss to the Nb₃Sn strand volume.

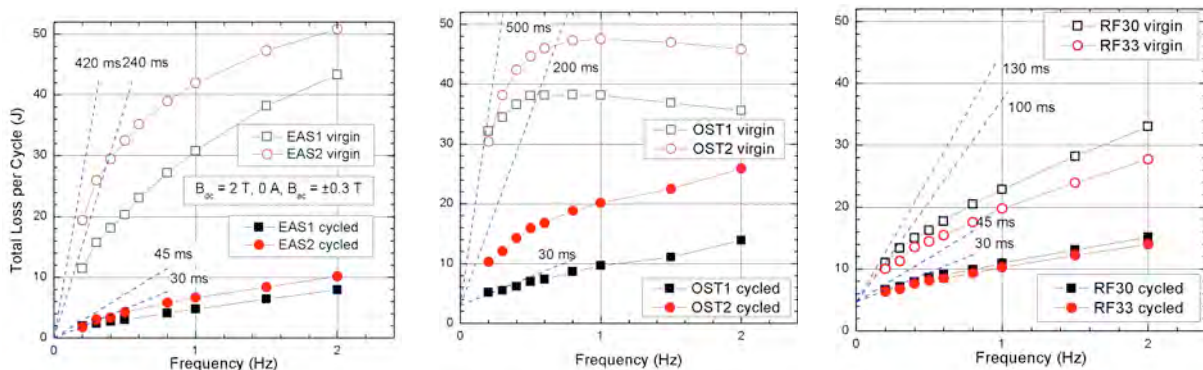


Fig. 2.5.11 AC loss measured in the two legs of TFPRO1 (top), TFPRO2 (centre) and RFTF1 (bottom) before the dc tests and after cyclic loading - the loss in the conductor legs with the lower void fractions is larger.

Manufacturing of Subsize Cable-in-Conduit Conductors (TW6 - TMSC - PITSAM)

The PITSAM series of four SULTAN samples builds the second generation of EDIPO prototype conductors, after the disappointing series named SUBSAM, tested in 2006. The characteristics of the four PITSAM conductors are listed in Table 2.5.2. The conductor sections were delivered by ENEA to CRPP under contract with EFDA.

The conductor for PITSAM1 arrived at CRPP on September 12th 2006, was heat treated in October 2006 and tested in SULTAN in November 2006. The conductor sections for PITSAM2, 3 and 4 were delivered on January 15th 2007 but ENEA asked to ship them back to LUVATA to adjust the outer size (void fraction). The final

delivery of the conductor section was in February 2007. The sample preparation was partly delayed as the heat treatment furnace was permanently used for the ITER TF qualification samples till May 2007. The test of PITSAM2, 3 and 4 was carried out from July 2007 to October 2007. The task is completed.



Fig. 2.5.12 Preparation of the PITSAM samples. From top to bottom: the dismantled conductor ends after removal of Cr coating (left the steel/copper sleeves), PITSAM2, 3 and 4 prepared for heat treatment (termination side), detail of the helium outlet next to the termination, penetration for the helium inlet at the U-bend, soldering of the termination into the thick copper plate, sample in the clamp with piping and sensors.

The procedure for preparation of sub-size CICC samples is identical as in the SUBSAM task (2006) and is not described here in detail. At large, it goes through the following steps, see also Fig. 2.5.12:

- The conductor, delivered as a 7m long section with both ends dismantled, is first straightened and bent to a hairpin shape. The Cr plating is chemically removed from the strand surface at the dismantled ends in a 16%-18% HCl solution. The bare conductor ends are slid into a prefabricated steel/copper sleeve (EB welded) and compacted by swaging to the design void fraction. The steel part of the sleeve is vacuum tight welded to the conductor jacket.
- The heat treatment is carried out in the 4.5m long vacuum furnace at CRPP, with 2 barrels for strand witness samples. The same treatment schedule as for the SUBSAM series is applied.
- After heat treatment, the terminations are solder filled (SnAg5) by the siphon method. The helium inlet is drilled and welded in the middle of the U-bend. The helium outlet are placed in both termination, before the copper sleeve. The termination are soldered into thick copper plates, to obtain the required sample cross section and contact surface at the transformer interface.
- The hairpin sample is bolted into a glass-epoxy clamp, which reacts the repulsive force in operation, estimated up to 300kN/m. The instrumentation is

the same as for SUBSAM and includes four voltage pairs in high field, and two pairs to monitor the termination voltage drop, five temperature sensors and two pressure taps to sense the pressure drop over two meters of straight conductor.

European Dipole Facility (TW5 – TMS – EDFAC)

The original schedule for completion of the preparatory work for the European Dipole Facility (EDIPO) has been moved from end of 2007 to the end of 2009 due to the delay in the supply of the superconducting winding from EFDA. The final design of the winding is being finalized by EFDA in the end of 2007. The interface document drafted in 2006 is still maintained as reference.

In 2007, most of the work for EDFAC task is focused on the superconducting transformer / sample holder (which is a component fully independent on the main winding). The design of the transformer is very similar to the SULTAN transformer, see Fig. 2.5.13. The main improvements are listed below:

- The operating current of the primary coil is increased from 200A to 300A, to extend the maximum magnetic flux (i.e. the ability to sustain high current in the sample for longer time). The number of turn is maintained but the size of the strand is slightly increased, mostly to provide the necessary copper cross section for quench protection.
- The primary coil, previously indirectly cooled with a force flow helium circuit, is now in thermal contact with a helium bath at 4.2K. This change is intended to slightly lower the operating temperature (from 4.5K to 4.2K) and improve the heat transfer during operation with fast cyclic current loading.
- The CICC conductor of the secondary, even if very similar to the existing one, has also been changed to avoid segregated copper strands. For this reason the copper to non-copper ratio of the superconducting strands has been increased from 2 to 3. This design minimizes the risk of the self-field instabilities observed in NbTi conductors. Moreover SnAg coating on the strands has been introduced to avoid aging effect on the inter-strand resistance.

The NbTi strand for the primary coil has been procured at LUVATA-Italy and the winding is in progress at MARTI Supratec, Zurich. For the secondary coil, contracts have been placed for the NbTi strand (VNIINM, Moscow), conductor cabling / jacketing (LUVATA-Italy) and winding (Meyer, Zurich). The detailed drawings of all the parts for the transformer/sample holder have been completed and the procurement orders are placed. The assembly work will be carried out in the CRPP workshop.

The design of the HTS current leads has been finalized according to the same concept discussed in the CLDES task for the ITER current leads (Bi-2223 tapes). The warm end temperature is dictated by the thermal shield circuit (80K) and is higher than the optimum one (60K – 70K), what calls for a larger HTS cross-section and high procurement cost. The stray field at the warm end of the HTS current leads has been calculated about 51mT (perpendicular direction). The call for tender for the stacks of soldered Bi-2223 tapes has been completed and the procurement order is being placed.

The specification for the main power supply has been completed and the call for tender has been completed. The procurement order for the 18kA, $\pm 10V$, thyristor power converter is being placed with the company Danfysik. The four-quadrant power supply for the primary coil of the new transformer, based on IGBT switching, is also being ordered.

During 2007, CRPP assisted EFDA in the assessment of the various updated versions of the EDIPO windings with thermal-hydraulic analysis (heat removal, flow pattern) and electro-magnetic calculation (field amps, ac loss).

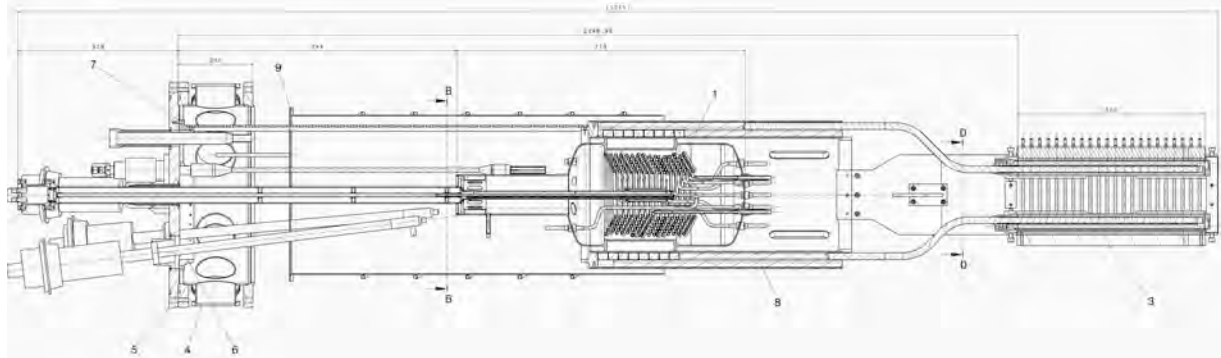


Fig. 2.5.13 The transformer / sample holder for the EDIPO test facility

Use of High Temperature Superconductors for Fusion Applications

The ITER Organization has decided to use HTS current leads for the magnet system of ITER (TF, CS and PF coils). The main advantage provided by HTS current leads is a considerable reduction of the refrigeration operation costs, as demonstrated by the European 70kA HTS current lead demonstrator. In collaboration with the Forschungszentrum Karlsruhe the final design of HTS current leads for ITER has been elaborated (Task TW4-TDS-CLDES). In the task TW5-TMS-HTSMAG, the possibility to use Bi-based HTS (Bi-2223, Bi-2212) in future fusion reactors beyond ITER has been studied. Moreover, the performance of industrially fabricated Bi-based HTS has been investigated as a part of the task TW5-TMSC-HTSPER. The last two tasks, HTSMAG and HTSPER are completed at the end of 2007.

Final Design of HTS Current Leads for ITER (TW4-TDS-CLDES)

In the task TW4-TDS-CLDES, a thermodynamic optimization study for ITER HTS current leads, consisting of a conduction-cooled HTS part and a heat exchanger cooled by helium gas, has been performed. For this study the case of the 68kA dc current leads of the toroidal field (TF) magnet system has been selected. The main results of this study are:

1. The optimum warm end temperature of the HTS part is in the range of 65 to 75K with respect to the required refrigerator input power. Taking into account the amount of HTS needed for the construction of the current lead it is preferable to use a warm end temperature of 65K.
2. The optimum helium inlet temperature is in the 50 to 60K range. The optimum difference of the helium inlet temperature and the metal temperature at the cold end of the heat exchanger is between 15 and 20K.

The 45kA current leads for the ITER central solenoid (CS) and poloidal field (PF) magnet systems have to be operated in pulsed mode. The outline design of a pulsed 45kA current lead is presented in the Table 2.5.6.

Parameter	68kA (reference)	27kA option	45kA option
Total length of the current lead including cold contact of 500mm	2.33m	2.28m	2.28m
HTS tape cross section	8.96cm ²	5.82cm ²	5.82cm ²
HTS engineering critical current density	12kA/cm ²		
Temperature at HTS cold end	4.5K		
Temperature at HTS warm end	65K	65 – 76K	63 – 65K
Stainless steel cross section	49.55cm ²	35.4cm ²	35.4cm ²
L _{HTS} including Cu end caps	650mm	410mm	410mm
Conduction heat load at 4.5K	5.6W	5.5 – 6.6W	5.4 – 5.7W
Heat exchanger Cu cross-section	62.83cm ²	31.17cm ²	41.58cm ²
RRR	75*		
Optimized current	68kA	27kA	45kA
Length of heat exchanger	715mm*	1100mm	890mm
Temperature at heat exchanger cold end	65K	65 – 76K	63 – 65K
Temperature at heat exchanger warm end	290 K		
Helium mass flow rate at nominal current (TF) and during plasma cycle (CS)	4.6g/s	1.639g/s	1.639g/s
Helium mass flow rate at maximum current (optimized lead ^o)	4.6g/s (4.3g/s)	3.6g/s	2.8g/s
Helium mass flow rate (stand-by T _{HTS,top} = 105K)	1.0g/s	0.25g/s	0.53g/s
Helium inlet temperature	50K		
Helium inlet pressure	6bar		

^o without contact resistance of interface between HTS module and heat exchanger

* In the design calculations for the 70kA HTS current lead (nominal current 68kA) a RRR of 50 has been used. Moreover, the realised length is slightly shorter than the optimum length.

Table 2.5.6 Parameters for ITER current leads

Due to the pulsed operation of the current leads for the PF and CS magnet systems it is possible to design the cross-section of the copper part for a current, which is smaller than the maximum current of 45kA. In the 27kA option (see Table), the ratio of length and cross-section is optimized for a current of 27kA. However, the mass flow rate in the copper part has to be adjusted to the actual value of the current to avoid an overheating of the current lead. Because of a fixed value of the helium inlet temperature the superconductor cross-section must be sufficient to carry the maximum current of 45kA.

The results of this first optimization study suggest that for a 45kA HTS current lead for pulsed operation the cross-section of the heat exchanger part should be designed for the maximum operating current. This option provides the largest safety margin and the lowest warm end temperature of the HTS part. The mass flow rate required for a current lead with a reduced heat exchanger cross-section is at the maximum current considerably higher than that necessary for the 45kA option. The main disadvantage of the 45kA option is the higher mass flow rate necessary for stand-by operation.

For the reference operating scenario, the AC loss in the HTS part (60 cm long) of a pulsed CS current lead has been estimated as 4.76mW, which has to be compared with the heat flow of 4.52W due to heat conduction. The AC loss will not provide a significant contribution to the heat load at the 4.5K level.

Scoping Study of HTS Fusion Magnets (TW5-TMS-HTSMAG)

In the framework of the task TW5-TMS-HTSMAG the possibility to use high temperature superconductors (HTS) for the magnets of future fusion reactors beyond ITER has been studied. High temperature superconductors are characterised by critical temperatures above the boiling point of liquid nitrogen, extremely high upper critical fields and a remarkable anisotropy of the physical properties. The first generation HTS (Bi-2223, Bi-2212) are now commercially available in kilometre length. In second generation HTS (Y-123 coated conductors) an impressive progress has been achieved regarding the conductor length. The first generation Bi-2223 HTS and the coated conductors are available only in tape geometry. In the case of Bi-2212, high critical current densities have been achieved also in round wires. The advantage of the round Bi-2212 wires is the fact that it is easily possible to fabricate a cable-in-conduit conductor or a Rutherford cable. The round Bi-2212 wire reached at 4.2K and 12T an extremely high engineering critical current density well above 50kA/cm². However, the critical current density declines rapidly with increasing operating temperature. At a temperature of ~18K the engineering critical current density is as low as ~10kA/cm². In developmental Bi-2212 round wires of lower performance at 4.2K, prepared at CRPP, the decline of the engineering critical current density with increasing temperature was much less pronounced. The Bi-2212 wires are a conductor candidate for a high field option, i.e. magnetic fields well above the present ITER design values and an operation temperature close to 4.5K. Even in the case of intermediate fields comparable to the present ITER design values the use of Bi-2212 wires seems to be limited to operating temperatures of 20K. The processing of the OST Bi-2212 wires seems to be optimized for 4K operation at extremely high fields. There may exist the possibility to optimize the preparation of Bi-2212 round wires for 20K operation.

For tape conductors, characterized by a strong anisotropy, it is not sufficient to consider only the absolute value of the magnetic field. In the case of the ITER toroidal field coils, the maximum field parallel to the winding pack is nearly 12T, while the perpendicular field reaches a value of 3.5T. For these field values, the maximum operation temperature of Bi-2223 tapes is limited by the field of 3.5T perpendicular to the broad face of the Bi-2223 tapes. Reasonable values of the operation temperature are between 20 and 30K. As in the case of the coated conductors new cable designs need to be developed. One possibility to bundle tapes to a high current conductor is a Roebel cable.

In general, HTS provide larger temperature margins than Nb₃Sn. These larger margins may provide some benefits with respect to the distribution of the coolant and may relax the thermal shielding requirements. Operation temperatures of 20K or above provide considerably improved superconductor stability because of the much larger metal specific heat at elevated temperatures. On the other hand, the detection of a quench may be more difficult. In addition, the refrigeration operation costs for the cooling of the magnet system can be reduced. However, considering the total cryogenic power (cryogenic circulation pumps, thermal shields at 80K level, other users of 4K helium (e.g. cryo-pumps, tritium pellet injection)) needed to cool a fusion reactor this saving is not very large.

HTS Materials for Fusion Magnets (TW5-TMSC-HTSPER)

The performance of currently available commercial High-T_c wires and tapes is evaluated in view of their suitability for magnet coils in future fusion reactors. We measured the critical current of Bi-2212 round wire and Bi-2223 tapes from two different manufacturers at temperatures up to 77K. Magnetic fields up to 12T were

applied parallel as well as normal to the plane of the tapes (always normal to the current direction) to investigate the materials' anisotropy.

Heat treatment of Bi-2212. Since the 10m sample of round Bi2212 wire came directly from the last stage of drawing, it was necessary to heat treat sections in pure oxygen gas, following the supplied temperature schedule precisely. To guarantee the temperature homogeneity in the furnace by less than 0.5°C from the set point of the controller during the critical phase above 800°C, a quartz-glass insert was designed and installed with new flanges. Samples up to 300mm long can be treated in oxygen, or any other gas, injected continuously into the quartz tube at the closed end through a capillary. The heat-treatment of the Bi-2212 samples lasted about 100h, most at temperatures above 75°C. The nearly identical I_c performance of samples heat treated in different runs shows that the process is controlled correctly and highly reproducible.

Type / Sample	A	B high I_c^b	C high strength ^b	D
HTS Material	Bi2223	Bi2223	Bi2223	Bi2212
Shape	tape	tape	tape	round wire
Width (mm)	4.07	4.46	4.20	
Thickness / Diameter (mm)	0.22	0.25	0.23	0.81 Ø
Matrix	AgMg ^a	high-strength silver alloy	high-strength silver alloy	AgMg ^a
No of filaments	121	multifilament	multifilament	595
I_c (77 K, self field, 1 μ V/cm) ^c (A)	95	133	115	resistive
I_c (4.2 K, 12 T, 1 μ V/cm) ^c (A)	210 ($B \parallel ab$) 145.5 ($B \perp ab$)	427 ($B \parallel ab$) 279 ($B \perp ab$)	332 ($B \parallel ab$) 221 ($B \perp ab$)	272 (isotropic)
Critical bending diameter (mm)	> 50	70	50	
Critical tensile strength at RT (MPa)	> 100	100	170	
Critical tensile strength at 77 K (MPa)		135	210	

^a Filaments embedded in pure silver

^b Type B and C are only distinguished by the Ag:Bi-2223 ratio

^c Measured at CRPP

Table 2.5.7 Main characteristics of the investigated HTS wires and tapes.

Table 2.5.7 lists essential parameters of the investigated first generation wires, which are fabricated in kilometre lengths. Bi-2223 tapes are commercially available from several companies. A disadvantage of the Bi-2223 tapes is the relatively high AC loss for a time-varying field perpendicular to the broad face of the tapes. The critical temperature of Bi2212 (80-90K) is considerably smaller than that of Bi2223 (\approx 110K).

Figure 2.5.14 shows a sequence (indicated by arrows) of I_c measurements, where the field was first increased (0→1→2→4→6 T) and then decreased. At each field-step the current was ramped to I_c five times. The observation that the I_c values are smaller for increasing than for decreasing field can be explained by a superposition of the applied field with the one generated by intergranular shielding currents at the location of grain boundaries, which determine the transport I_c . In increasing applied field the local field there is enhanced, while it is reduced in decreasing field. Subsequent ramps of the sample current to I_c appear to reduce the intra-grain currents, resulting in a 'closing' of the hysteresis loop. The hysteresis effect disappears at about 27K for $B \perp ab$ and at 40K for $B \parallel ab$.

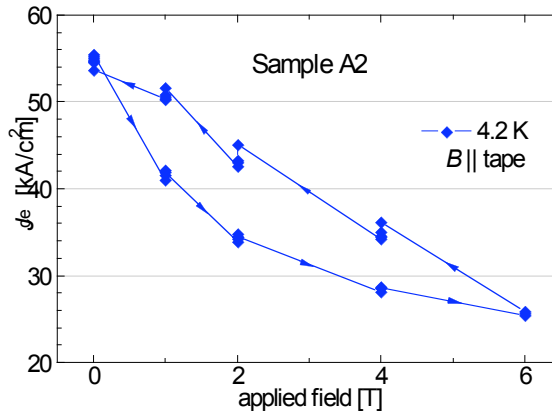


Fig. 2.5.14 Hysteresis: J_{ce} depends on the history of the applied field and of the conductor current.

To describe the I_c dependence on B and T in as large a range as possible, empirical scaling laws are useful. The data above 4T – the region interesting for applications – are fitted with the formula below within 10%, if the data for $B \perp ab$ and $B // ab$ were treated separately.

$$I_c = I_{sc} \cdot \left(1 - \left(\frac{T}{T_c} \right)^{\hat{a}} \right) \cdot \exp \left(-B \cdot \left(B_{sc} \exp \left(\frac{-T}{T_{sc}} \right) \right)^{-1} \right)$$

Figure 2.5.15 shows a typical fit result, while Table 2.5.8 summarizes the obtained fit parameters. The scaling current, field and temperature (I_{sc} , B_{sc} , and T_{sc}) are free parameters, T_c was estimated.

The exponent n , used to fit the I-V curve of the superconducting transition, is strongly correlated to the engineering critical current density J_{ce} in all investigated Bi-2223 samples, independent of T , B and even field direction (see figure 2.5.16). The index n increases linearly with J_{ce} until a near-plateau is reached at about 22 (observed for example at 15K with $4TB \perp ab$ and with $12TB // ab$). The fitting equation and the n - J_{ce} correlation provide full information of the superconducting transition in a wide range of T and B , useful e.g. for simulations of conductor behaviour in a coil.

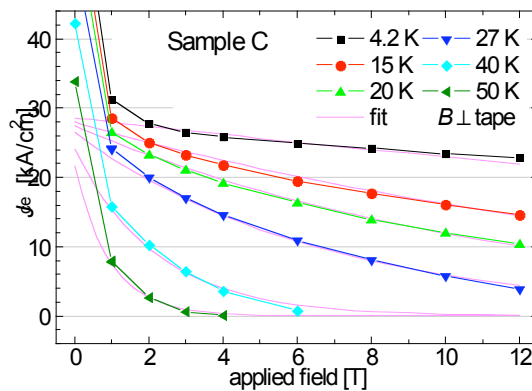


Fig. 2.5.15 Fit of the measured data above 2T.

The round Bi-2212 wire, heat treated at CRPP, reached very high current densities at 4.2K, but much smaller ones at temperatures as low as 15K. Figure 2.5.17

summarizes the temperature dependence of all samples investigated at 12T. Above 20K J_{ce} of the Bi-2212 Sample D is smaller than J_{ce} of the Bi-2223 samples with $B \perp ab$. Interestingly only a very small hysteresis effect appeared in the Bi2212 wire, even at 4.2K, indicating a better coupling at the grain boundaries.

		T_c	T_{sc}	I_{sc}	B_{sc}	β
A1	$B \parallel ab$	105	14.88	253.3	100.2	2.24
	$B \perp ab$	105	11.52	176.8	68.9	2.7
A2	$B \parallel ab$	105	16.8	247.3	86.4	1.91
B	$B \parallel ab$	105	15.24	494.6	111.8	1.79
	$B \perp ab$	105	11.6	344.4	65.7	1.9
C	$B \parallel ab$	105	15.35	396.5	121	1.75
	$B \perp ab$	105	11.84	276.8	64.9	1.9
D		80	8.28	622.2	59.45	0.33

Table 2.5.8 Fit parameters for all samples

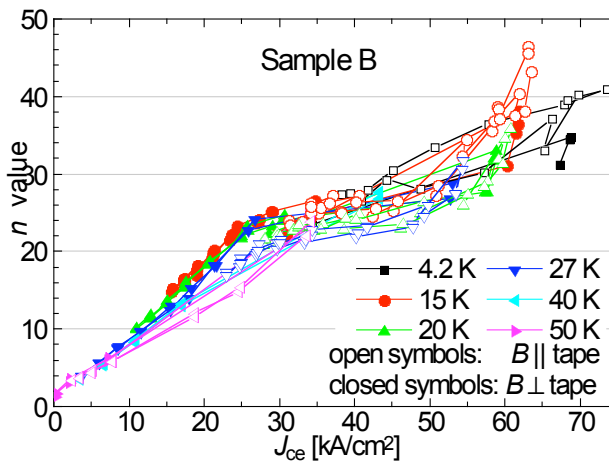


Fig. 2.5.16 Correlation between n values and J_{ce} .

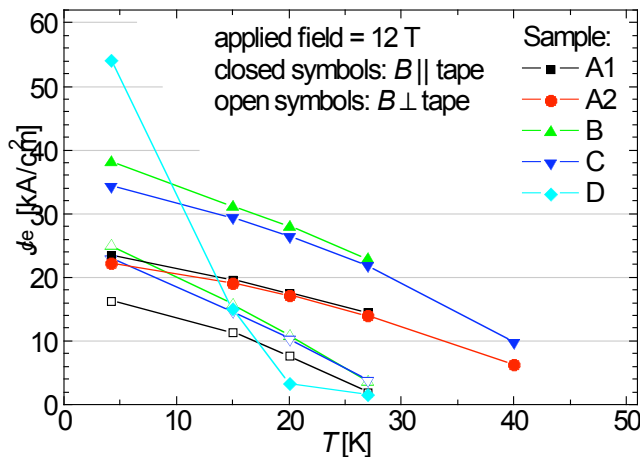


Fig. 2.5.17 Temperature dependence of J_{ce} at 12T applied field for all samples and both orientations. Sample D, the round wire, is isotropic.

ITER Thermo-siphon effect and CSMC Analysis (TW6-TMSC-ASTSPH)

The analysis on thermo-siphon effect (buoyancy of coolant in the bundle region of ITER CICC), was reported in 2006. In 2007, CRPP assessed the relevance of short sample measurements in SULTAN for the prediction of the performance of ITER coils using the case of the Nb₃Sn high field Central Solenoid Model Coil (CSMC) conductor, for which both coil performance and short sample SULTAN results (Good-Joint (GJ) sample) are available. As the different operating conditions during the GJ and the CSMC tests prevented a direct comparison of the measured data, it was necessary to scale the results to comparable conditions. A least-squares fit procedure, based on a uniform current distribution among the strands and the Durham scaling relations for the field, temperature and strain dependencies of the strand J_c, provided a suitable parameterisation. Relative to the measured J_c of the witness strand, the experimental data of the GJ sample could be best described with a thermal strain of -0.294% and a degradation factor of approximately 60% (see Fig. 2.5.18).

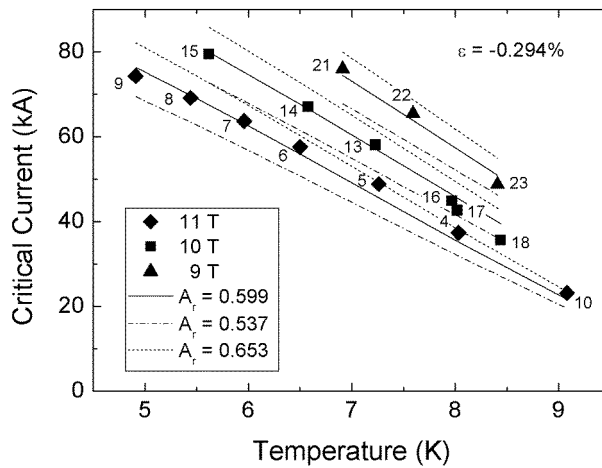


Fig. 2.5.18 Measured and calculated critical currents of leg A of the GJ sample. The numbers at the data points provide the sequence of the measurements. For the 4th and 5th runs, the I_c is close to the expectations for a degradation factor A_r=0.653, whereas an A_r value of 0.537 is appropriate for the 17th, 18th and 23rd runs.

The modelling of the electric field along Layer 1A of the CSMC required the consideration of the hoop strain and the temperature, both varying along the conductor, and of the magnetic field, which changes along as well as across the conductor. The temperature profiles used in the calculations were based on published temperature profiles and empirical relations between helium in- and outlet temperatures. The simulation of the Layer 1A terminal voltage showed that different sets of n- A_r- and ε-values are able to describe the recorded voltages, leading to an uncertainty in these values (see Fig. 2.5.19). However, the current sharing temperature, determined at the location along the conductor where the local electric field first reaches E_c, was nearly independent of the parameter sets, as long as they reasonably reproduced the observed overall voltage.

Scaling the GJ results (plotted in Fig. 2.5.18) to the operating conditions of CSMC Layer 1A (i.e. correcting primarily for the hoop stress in the centre of the CSMC coil), it is possible to compare the performance of the conductors in the two test settings (see Fig. 2.5.20).

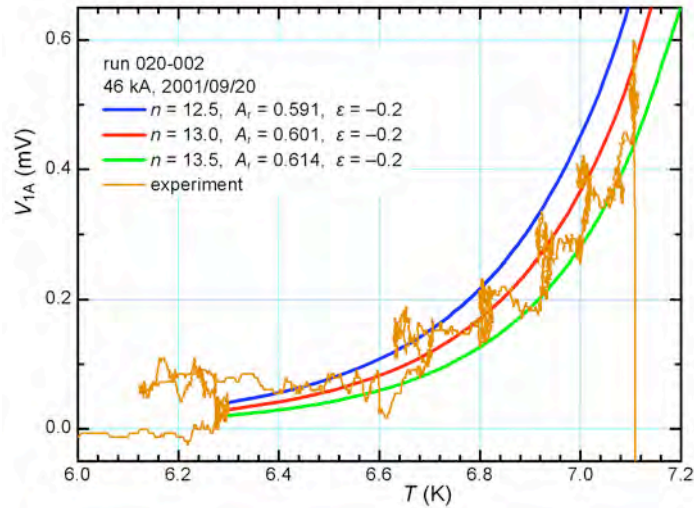


Fig. 2.5.19 Comparison of measured and calculated voltage-temperature curves for the 46kA run 020 002. The center, the upper and lower boundaries of the measured V-T curve is approximated by three different combinations of the degradation factor A_r and the n factor for $\epsilon = -0.2\%$.

In conclusions, the GJ performance can be well represented by a degraded strand model. The value of the thermal strain of approximately -0.29% , obtained from a fit based on a uniform current distribution, is close to the expectations for a Nb_3Sn CIC conductor with an Incoloy jacket. To avoid the problems related to the not exactly known degradation factor and strain state of the Nb_3Sn strands in the CSMC, the T_{cs} estimated for the CSMC have been directly compared to the performance of the GJ conductor at the CSMC operation conditions. The SULTAN results slightly underestimate the CSMC performance, and hence provide a conservative prediction of the coil performance.

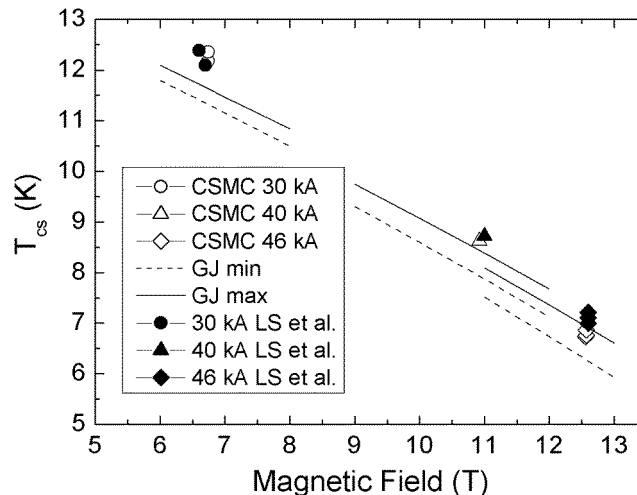


Fig. 2.5.20 Performances comparison of GJ and CSMC, taking into account the expected improvement of the GJ conductor due to the maximum hoop strain in the central part of the CSMC winding. For comparison, the T_{cs} values published by L. Savoldi Richard et al. are also shown.

Computation of AC Losses Associated with Plasma Control in ITER Magnets (TW6-TPO-ACCOMP)

The task TW5-TPO-ACLOS on AC loss calculation in different operating regimes of relevance for ITER plasma control has shown in 2006 that AC loss calculations can be performed on a model with a level of complexity and completeness not achieved so far. The model developed is however too large and computationally expensive for the inclusion in a fast control optimization procedure. The scope of the new task TW6-TPO-ACCOMP, started in late 2007 in collaboration with the company HORIZON, is to provide an optimized tool for fast AC loss estimate to a suitably approximate level. The work defines the simplified AC loss model based on a parametric representation of the ITER coils. The input to the simplified model shall be a set of current and plasma position excitations in a form that is compatible with the controller design. The proposed form is a frequency spectrum, as a set of amplitudes vs. frequency for each coil current and the plasma current and position, as can be obtained from a Fourier analysis. The parametric model is programmed in a Matlab procedure that is an integral part of the deliverables of this work.

Review of PF2-PF5 Winding Design (ITA 11-88) (TW6-TMSP-PFWDES1)

CRPP carried out a design review of the PF2-PF5 coils in close accord with the ITER International Team (IT), focusing on a number of winding-pack elements for which alternative design choices were considered in recent years.

Turn insulation of the P2 – P5 conductors. The turn insulation of the ITER PF conductors was foreseen to consist of two insulation layers, separated by a metallic screen, which was intended to enable the detection of developing insulation faults. One of the criteria to compare the design with screen to the one without is the maximum electric field created in the insulation. A 2D finite element analysis of the conductors in a double pancake with maximal voltages applied led to the field plot in Fig. 2.5.21 and the maximum values listed in Table 2.5.9.

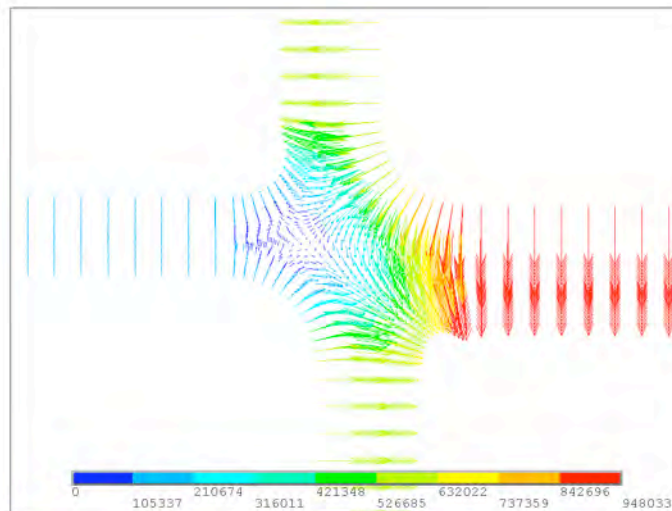


Fig. 2.5.21 Vector plot of the electric field for the design with screen and 18.7kV coil terminal voltage.

	Design with screens	Design without screens
Conductor spacing horizontal/vertical [mm]	6.9 / 7.4	6.4 / 6.4
Screen spacing horizontal/vertical [mm]	3.5 / 4	–
E_{\max} ($V_{\max} = 18.7$ kV) [kV/mm]	0.980	0.706
E_{\max} ($V_{\max} = 25.7$ kV) [kV/mm]	1.347	0.971
Design margin ($V_{\max} = 18.7$ kV)	3.1	4.2
Design margin ($V_{\max} = 25.7$ kV)	2.2	3.1

Table 2.5.9 Maximum electric fields in conductor insulation of PF2

Plates separating double pancakes. Because the PF3 and PF4 coils are particularly inaccessible and potentially required repairs therefore extremely difficult, the eight double pancakes are individually wrapped with ground insulation and separated by separation plates. The simulation of the temperature evolution after a turn-to-turn short in a double pancake helped to assess the effectiveness of the separation plates in preventing heat spreading to neighboring double pancakes and damaging them. Fig. 2.5.22 shows a snapshot of the evolution. Separation plates of thermally insulating material are better in containing the large amount of heat within the affected double pancake than metallic plates are able to spread the heat. Insulating separation plates are thus better in keeping the maximum temperature in neighboring double pancakes to a minimum.

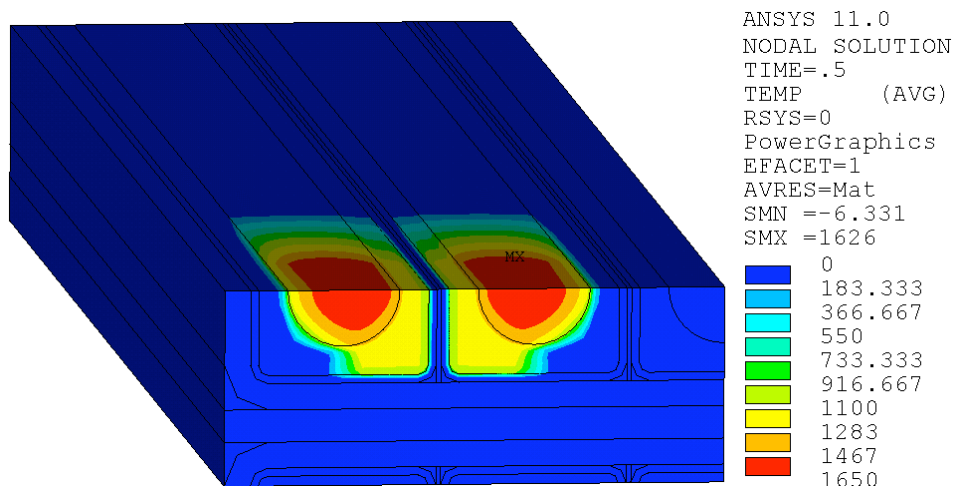


Fig. 2.5.22 Temperature distribution after 0.5s in the lower part of the simulation volume with a separator plate made of steel. Temperatures in K.

Jumpers to bridge double pancakes in case of a fault. If a double pancake in a PF coil fails it is possible to bridge it with a pre-installed jumper and continue operation of ITER in the so-called backup mode with the affected coil operating at higher current to reach the same field as in standard mode. Closely inspecting existing ITER drawings CRPP proposed a layout for these jumpers, which may reduce the number of access points and reduce the number of necessary jumpers while enabling to bridge every double pancake in all PF coils. For the jumper joints CRPP suggested a layout including insulation and associated joining procedure to allow fast, clean and reliable joint openings as well as reassembly. Figure 2.5.23 shows the cross sections of the proposed joints.

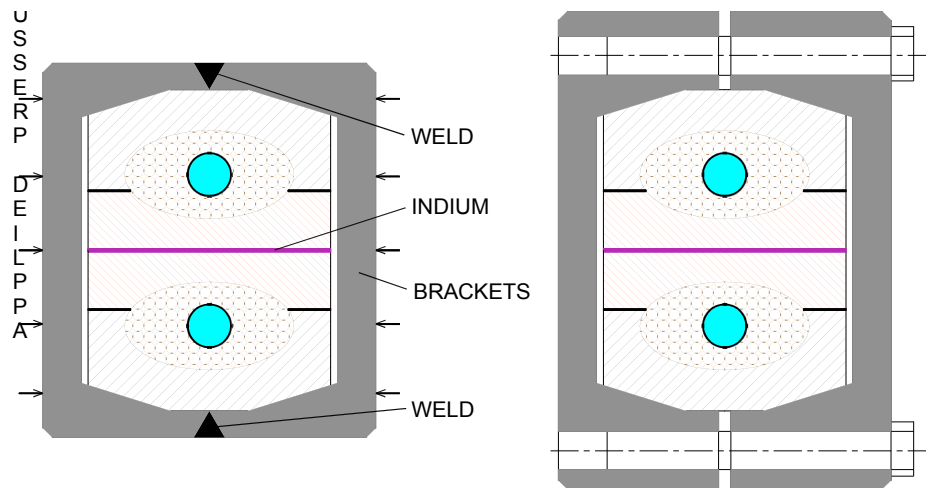


Fig. 2.5.23 Cross section of CRPP-proposed PF double-pancake joints with either a welded bracket (left) or a bolted one (right).

Conclusion of the Review. CRPP proposed several improvements to the existing PF design and reached conclusions on the questions agreed upon with ITER IT and EFDA. A comprehensive report was sent to ITER IT and EFDA.

2.6 Industrial process plasmas¹

The economic situation and changes in industry and academia have led to a substantial reduction of the R&D activities of the industrial plasma group. The number of projects and the manpower have decreased adapting to the present situation which will also influence the R&D activities of the group for 2008. Research topics such as industrial silicon thin film deposition for solar cells and thin film barrier coating for packaging continued during 2007. Most of the R&D concerning silicon thin film deposition for solar cell applications has been made under mandate. Projects such as investigating applications of the plasma torch to thin film deposition finished and a continuation CTI project is planned for 2008.

The design of large plasma reactors and up-scaling of plasma processes are the biggest challenges in the industrialisation of various plasma applications and their successful introduction into production. The up-scaling of small plasma reactors to industrial reactors implies, in most cases, a considerable increase in electrical power. One of the main problems in industrial reactors is the occurrence of arcing and parasitic discharges, which can hinder a successful introduction into industrial production lines. Arcing starts to be the limiting factor in several applications using plasmas, thus triggering intense research and development on this topic.

The study of arc phenomena is one of the oldest topics in plasma physics. In our opinion arcing is at present a key issue in the application of plasma in industry for the coming years. Arcing is also important in the space environment and space equipment, underlined by the mandate from Mecanex SA in Nyon undertaken on demand of the European Space Agency (ESA). It is intended to follow up this topic in the future. In addition, activities concerning the understanding of the basic

¹ Work not belonging to the EURATOM Association's work programme.

behaviour of the plasma during electrical discharge machining continued in collaboration with Charmilles SA.

The diversification of the R&D activities has continued and long-term topics have been initiated. One of the most interesting topics is the development of future high deposition plasma sources and their integration into a future industrial high deposition plasma reactor. Particular importance will be given to electrical discharge machining and arcing under various conditions.

During the year meetings and discussions with various industries on other new plasma processing issues have taken place and will generate new R&D topics and interesting science for the industrial plasma group of the CRPP in the future.

2.6.1 Microcrystalline silicon for thin film photovoltaic solar cell application

Microcrystalline silicon is used in a tandem structure with amorphous silicon to obtain low cost photovoltaic (PV) solar cells with light conversion efficiencies in the 10–15% range. This type of solar cell not only has a cost advantage with respect to silicon based wafer solar cells, but it is also much more environmentally friendly to produce. In order to compete with well-established fossil energy sources (oil, coal), the deposition process of silicon thin films still has to be optimized, as well as the deposition reactors used to mass produce large area PV solar cells. The aim of this project is to understand the inter-relation between $\text{SiH}_4\text{-H}_2$ plasmas and deposited film properties to be able to perform an efficient optimization of microcrystalline silicon deposition as opposed to the empirical approach used since the first use in PV solar cells in 1992. This is a key turning point to permit microcrystalline/amorphous silicon tandem solar cells to enter successfully in the fast growing (40–50% per year) PV world market.

Previous experimental and theoretical studies have shown that the plasma composition, i.e. the silane concentration *in the plasma*, is a relevant parameter to determine the deposited film crystallinity. Moreover, it has been demonstrated that it accounts for all process parameters such as the input RF power or the pressure. Nevertheless, these studies were only referring to steady-state plasmas, without considering the dynamic behavior from plasma ignition to chemical equilibrium. Time-resolved optical emission spectroscopy has been performed to measure the time needed to reach steady-state equilibrium as well as the behavior of the plasma composition during the transient phase, Fig. 2.6.1. Results have shown that less than 1 second was needed to reach equilibrium, which is significantly different from times of about 1 minute reported in the literature. Analytical (zero and one-dimensional) and numerical (two-dimensional) modeling have demonstrated that this difference is due to the particular geometry of the deposition reactor used for this study compared to usual laboratory reactors, Fig. 2.6.2. Laboratory reactors generally have a small plasma volume ($\sim 800\text{cm}^3$) connected to a large vacuum chamber where the pumps are connected. In our case, the plasma fills the entire reactor volume and the pumping is direct, i.e. without a large dead volume between the plasma and the pumping port. This configuration avoids the back-diffusion of SiH_4 to the plasma zone from the dead volume, hence reducing the time necessary to reach equilibrium to its theoretical minimum. Moreover, this is valid even if the plasma volume is much larger, as is the case of large area production reactors ($6700 - 35000\text{cm}^3$) such as the one used in this study. This difference favors closed and directly pumped design because it eliminates the plasma-induced amorphous silicon incubation layer which deteriorates the final solar cell performance.

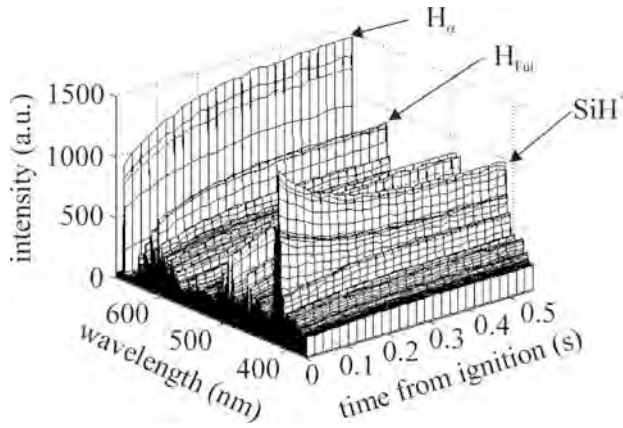


Fig. 2.6.1 Time resolved OES measurement in a closed reactor.

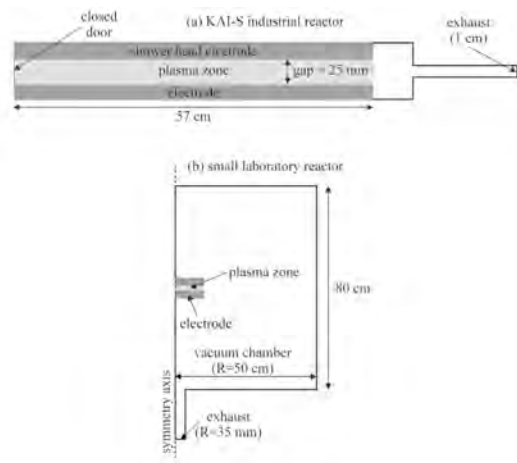


Fig. 2.6.2 (a) industrial closed and (b) laboratory reactor geometries.

Another crucial aspect for the production of solar cells is the layer uniformity of large areas (up to 1.4m^2). This includes the thickness uniformity as well as the uniformity of the crystallinity which should ideally be between 40 and 60%. It has been demonstrated that depending on the input silane concentration, the effect of a nonuniform power distribution may vary, as shown in Fig. 2.6.3. Hence, the higher the input silane concentration, the more the crystallinity is sensitive to a given power perturbation. Therefore, if we want to benefit from high deposition performances associated with high silane concentrations, we have to pay attention to design and build reactors with a geometry which perfectly compensates the standing-wave effect, i.e. also taking into account the plasma and thick dielectric substrate. This may lead to two categories of commercial reactors: on the one hand a simple reactor with approximate design for low performance plasma at low input silane concentration, and on the other hand, a perfectly designed reactor for high deposition rate and performance at high input silane concentration.

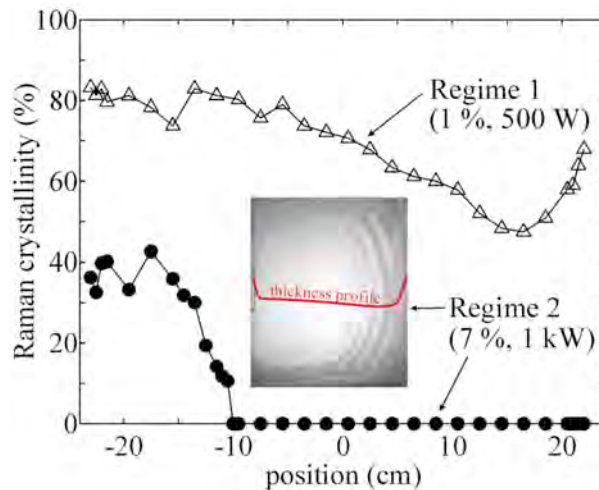


Fig. 2.6.3 Crystallinity uniformity sensitivity to a nonuniform power distribution: the higher the input silane concentration, the higher the sensitivity.

Despite the important improvement in overall understanding, process optimization procedures and reactor design, this project is still ongoing to push the limit further in order to increase the competitiveness of microcrystalline/amorphous tandem solar cells in the promising PV market. Attention is now paid to powder formation in $\text{SiH}_4\text{-H}_2$ discharges at high silane concentration and pressure, as well as to new plasma sources to enhance the deposition rate and material quality.

2.6.2 Problems in industrial thin-film silicon deposition by plasma processes

In large area reactors such as those used for the deposition of amorphous and microcrystalline silicon for thin film solar cells, the necessary RF power goes above several kW. This high RF power strongly increases the risk of parasitic discharges, which can happen anywhere in the large area reactor. Due to the high available electrical power, a large part of it can go directly into parasitic discharges instead of into the process plasma, thus leading to contamination of the coating or it can even seriously damage the reactor. Therefore, for industrial applications, the detection of parasitic discharges and a design of the reactor which avoids, or at least reduces, parasitic discharges is of prime importance. In order to reduce arc and parasitic plasmas, the origin of these discharges has to be evaluated.

Therefore development of optical and electrical diagnostic methods to detect and characterise the parasitic processes in large area PECVD reactors must be made. Furthermore, to have the necessary industrial relevance, the experiments must be undertaken in a (near) commercial plasma reactor. The most simple but also most powerful diagnostic method for parasitic discharges is the measurement of RF current and voltage. Since several types of parasitic discharge are possible, the fingerprints of these different discharges must be found. These fingerprints are necessary to distinguish and to localize the different parasitic discharges and to estimate later in the project the efficiency and validity of the counter measure.

Several types of parasitic discharges are thought to play an important role in these processing plasmas. Hollow cathode discharges, unipolar arcs and arcs are suspected to be the major contributors to parasitic discharges. These discharges also lead in most cases at high RF power to heavy damage and must therefore be suppressed. The various possible parasitic processes occurring under these particular conditions have been identified and classified. Counter measure have to be developed in order to avoid damage of the PECVD reactor due to parasitic processes. One of the most efficient counter measures is to change the mechanical and electrical design of the reactor and its accessories such as strip line and RF feedthroughs. Therefore this task leads to a redesign of important parts of the RF reactor. The effectiveness of the counter measures must be tested and the design changes included in the future design of large area RF reactors for the deposition of thin film silicon solar cells. Reduction or elimination of parasitic processes will also considerably contribute to a reliable process for the production of thin film solar cells and to their cost reduction. The technological challenge is to transfer this knowledge for the design of new high-performance reactors taking into account the previous results.

This should result in the availability of new production equipment at the industrial level achieving high-quality modules with high efficiencies at cost effective deposition rates. The long-term commercial objective is the commercialization and commissioning of production lines, allowing the fabrication of high-quality modules at low cost.

The project started during 2007 has been funded for one year by a mandate from industry. In future the project will be funded by SwissElectric which kindly took over the funding from CCEM.



Fig. 2.6.4 *Example of an unstable RF discharge*

First experiments showed that parasitic discharges, similar to those observed in the industrial reactor, can be reproduced in a simple test bed reactor. Various kinds of parasitic discharge and unstable discharge conditions could be reproduced under various plasmas conditions in different electropositive and electronegative gases. Figure 2.6.4 shows a spectacular photo of an unstable discharge in the modified RF reactor. A new design of a test bed reactor using an existing RF plasma reactor has been undertaken and the construction of the new device is expected to be finished towards the end of 2008.

2.6.3 From conventional plasma spraying to reactive thermal plasma CVD

The plasma torch is one of the most elementary plasma sources used in industrial applications. Many daily applications would not be possible without this widespread industrial process. However the applications are limited to relatively porous and thick coatings with respect to vapour deposition techniques, and the spray materials are restricted to substances with a convenient melting point.

The plasma torch up till now is the only plasma source which successfully allows the use of solid, liquid and gaseous precursors. Thermal plasmas are commonly used to deposit thick layers by spraying technique: some powder of the desired coating material is injected and melted into an expanding thermal plasma jet and then deposits on the substrate. The coatings obtained are thick but very rough and porous. All those spraying processes are performed at high pressure (above 500mbar).

A very different approach of the use of thermal plasma for coating can be obtained when the operating pressure is lowered down to typically 1mbar. In this case the purpose is not to melt a predefined material in order to deposit it, but to make plasma assisted chemistry, as in "classical" low pressure discharges. In this case gaseous or liquid precursors are injected into the plasma jet, possibly with the addition of other gaseous reactants, and are dissociated. The dissociation products will chemically react together, within the plasma itself and at the substrate surface,

in such a way that thin films can be deposited. A major advantage of low pressure thermal plasmas for thin film deposition is that very large surfaces can be rapidly treated, firstly because large amounts of precursor can be injected and converted in the thermal plasma, but also due to the large spatial extent of the jet at low operation pressures. The commercial plasma torch F4 is the basis for a new technology of reactive thermal plasma CVD which has been developed at the CRPP in collaboration with Sulzer Metco.

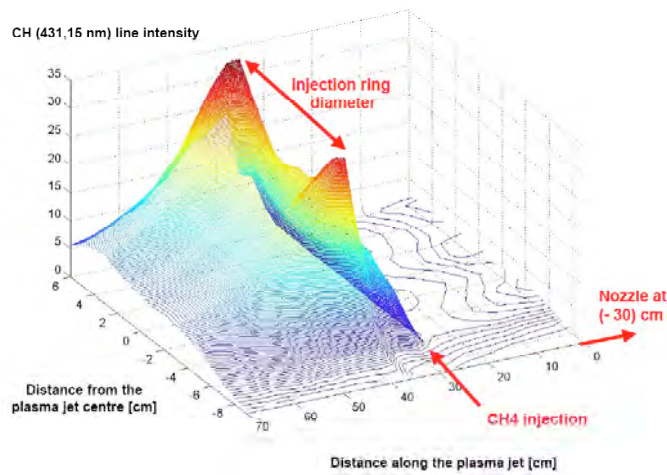
In preliminary experiments we mainly used hydrocarbonated precursors, such as CH_4 and C_2H_6 , to investigate the deposition of thin films by a plasma torch. Different kinds of carbon-containing materials, from diamond to polymers, depending on the plasma parameters (power, flows, pressure) and the substrate temperature were successfully deposited. One of the crucial features relies on the way how and where the precursor is injected. In fact we are able to inject the gas directly either into the torch nozzle or by means of a gas injection ring through which the plasma jet passes (see Fig. 2.6.5). Optical emission spectroscopy was used to investigate the chemical composition and the dynamics of precursor injection by mapping measurements, which show where dissociation and the different chemical reactions take place (see Fig. 2.6.6.a and b). A laser interferometer was used for the in-situ measurement of the deposition rate while FTIR spectroscopy gave first results on the composition of the films obtained and the film structure was investigated using SEM.

Extensive experiments have been performed to investigate the behaviour of the plasma and of the plasma chemistry on the different injection locations of gaseous monomers. To begin with, methane and ethylene gases were used. These measurements and their characterisation were used for a proof of principle for fast development of various carbon-containing films. The first experiments showed clearly that reactive thermal plasma CVD has a very large application potential. In the case of carbon-containing monomers, hard layers (diamond and diamond-like) and soft layers (polymers and amorphous carbon) can be obtained at high deposition rates. This first investigation clearly demonstrated the large potential of reactive thermal plasma CVD using the commercial F4 plasma torch.



Fig. 2.6.5 *Methane injection into a plasma torch jet*

a)



b)

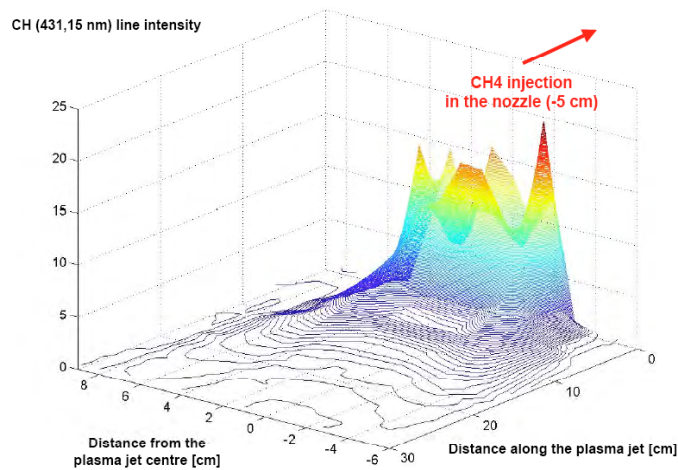


Fig. 2.6.6 a) Spatially resolved measurements of the 431.15nm CH line for gas ring injection
b) Spatially resolved measurements of the 431.15nm CH line for in-plasma torch gas injection

2.6.4 Optimisation of the plasma enhanced chemical vapour deposition (PECVD) process for the deposition of SiO_x barrier coatings on polymers.

The main technologies for the deposition of oxide barrier such as SiO_x, on polymer films are based on vacuum web coating methods. Reactive evaporation uses resistance heated sources to evaporate silicon in a controlled oxygen pressure. This results in an oxidation of the metal vapour in the gas phase and on the polymer films. The second technique applies electron beam bombardment (EB) to heat and evaporate material from a crucible. Silicon vapour enters the reactive zone as for reactive evaporation. It differs from the former technique in that it can be used in a non-reactive mode (PVD). In this case evaporation takes place from stoichiometrically controlled material to match the required chemical composition of coatings. A third technique is PECVD, plasma enhanced chemical vapour deposition. The organosilane is decomposed in the plasma phase, fragments

attached at the polymer film surface which then react with oxygen atoms to form SiO_x layers.

During SiO_x deposition, production of fine sized (micrometer or even nanometer sized) powder is a great disadvantage to the process. First the powder damages equipment such as vacuum pumps, leading to costly maintenance and repairs. Furthermore powder might be a potential health risk and should therefore be reduced or completely avoided. Strong powder production is also a sign that the process could have a much higher deposition rate since much of the available monomer is transformed into fine-sized SiO_x powder instead of being used for the coating. The mechanism of this powder formation in deposition plasma with HMDSO, oxygen and noble gases is completely unknown. In a current CTI project in collaboration with TetraPak the basics of SiO_x powder formation is investigated and ways are studied to strongly reduce the powder formation. In return, monomer conversion into coating and an increase of the deposition rate are the benefits, keeping a high oxygen barrier. The basic research is made in a small RF reactor at the CRPP whereas the test for high deposition rate/low powder formation shall be tested later in a semi-industrial reactor.

The main effort of this CTI project started in 2007 is to investigate the appearance of micrometer sized SiO_x particles in the plasmas used for the SiO_x deposition on polymers. For this reason various specific plasma diagnostics have been installed onto the existing small-sized capacitively-coupled RF reactor. In particular optical emission spectroscopy has been installed and tested. However difficulties arose due to the low light intensity of the HMDSO/ O_2 discharge. A light intensified CCD camera and an optimised light path must be used to have enough signal, especially for time resolved measurements. This is essential since time-resolved measurements are thought to be a key way to study the ongoing complex plasma chemistry and physics. First measurements show that optical emission spectroscopy coupled with other diagnostics could give important indications on the mechanism leading to powder formation. Therefore as many diagnostics as possible will be installed to elucidate the completely unknown mechanism of the powder formation in these industrially important processes. Simple diagnostics such as measurements of the laser extinction, electrical measurements such as detection of the floating potential and fast gas pressure measurements are installed. The installation and testing of the infrared absorption spectroscopy, using a Bruker FTIR equipped with an external IR detector, is underway. From this diagnostic method the plasma composition can be determined, in particular in combination with optical emission spectroscopy. Furthermore, additional information on the composition of the nano- and micro-particles and their development can be obtained since the size of the particles can be estimated from the absorption spectra.

2.6.5 Arc phenomena in space environment and equipment

In collaboration with RUAG (formerly Mecanex SA) in Nyon and ONERA in Toulouse mandated by the ESA (European Space Agency), the necessary fundamentals of small gap arcing have been established and applied to space equipment in order to reduce or suppress arcing in the space environment and space equipment.

In order to investigate arcing, a micro-plasma device has been mounted in a small UHV vacuum chamber in which a controlled atmosphere can be created. The distance between two wire electrodes is accurately controlled by a piezo-actuator allowing for distance control in the nanometre range. Contact openings under various conditions have been investigated at vacuum and atmospheric pressure.

At very small wire separation a liquid metal bridge is immediately formed. The liquid metal of the bridge, still heated, finally undergoes a transition to a supercritical fluid which expands explosively due to the high pressure gradient. This state is followed by a transition from a dense non-ideal plasma to an expanded ideal non-equilibrium plasma. At this moment a dense and cold and therefore strongly-coupled metal plasma must exist which develops rapidly into a dense metal plasma. In the first part of the discharge, pressure ionisation dominates due to a lowering of the energy for ionisation by the dense strongly-coupled plasma. Whereas in the second part the ionisation energy is supplied by particle collisions, mostly through electrons. In the first event of the experiment the voltage is around the minimum arc voltage necessary for classical ionization. The plasma in this case is limited to the non-ideal plasma phase. For later events the voltage can be higher than the minimum arc voltage and the plasma evolves up to the non-equilibrium plasma.

The transition mechanism is supported by electrical measurements. The contact ohmic resistance calculated from the instantaneous voltage and current measurements is of the order of 5 to 10 Ohms. Assuming, since at present no measurements of the discharge size are available, a discharge channel of about $10\mu\text{m}$ and a maximum separation of the wires of about $1\mu\text{m}$, an electrical conductivity of about $10^4\text{-}10^5 (\text{Ohm m})^{-1}$ is estimated. This value is very near to a calculation of the electrical conductivity of very dense metal plasma.

Spectroscopic measurements indicate that a metal plasma is formed. This metal plasma is very dense and accordingly non-ideal. The non-ideal behaviour of the micro-plasma might be deduced from electrical measurements and from an estimate of the electrical conductivity. The transport properties of non-ideal plasmas, in particular the electrical conductivity, are sensitive to the non-ideal behaviour of the plasma.

The different arc events at very small wire distance seem to be composed of several discharges with a duration less than a few tens of nanoseconds. In the first few nanoseconds of the discharge, an extremely dense plasma is formed, most probably a non-ideal plasma developing towards an ideal non-equilibrium plasma. The observation indicates that the arc melts sufficient material from the wires so that a bridge could be formed again re-establishing full contact. The physics of the micro-plasmas existing in the sub-micron gap is completely unknown and further work is necessary to understand the basics of this important class of plasmas and its role in contact opening.

If the contact gap is larger than a few micrometers the electron-neutral mean free path is shorter than the gap dimensions. In this case a self-sustained gas discharge can ignite. At first spiky light emission and oscillation on the voltage trace indicate the presence of individual plasma pulses accompanied by the oscillations of the circuit, which suddenly transit to a continuous light and a constant voltage with no noticeable voltage fluctuations; a stable metal vapour discharge is formed.

2.6.6 Influence of a weakly-ionised boundary layer on transonic and supersonic air flow

It is only during the last decade that Dielectric Barrier Discharges (DBD), which are found in applications in aerodynamics, airflow control and plasma assisted combustion, have started to be investigated. The present study focuses on the effects of high-speed airflows on dielectric barrier discharge characteristics. The DBD is being investigated in the common project between the CRPP and Laboratoire de Thermique Applique et de Turbomachines (LTT) and the Laboratoire d'Ingénierie Numérique (LIN) of the Energy Institute (ISE) from the Faculty of

Engineering (STI) consists of an alumina plate, on which two electrodes are printed. The frequency of the plasma excitation has been varied from 1 to 15kHz and rms voltages of 1 to 15kV have been applied. The use of appropriate materials enables a lifetime for the DBD plate in air of more than twenty hours.

The objective of the project is to investigate experimentally the interaction between a weakly ionized surface plasma and aerodynamic shocks that form in transonic and supersonic gas flows. After investigating the effects of a high speed airflow on a flat surface dielectric barrier discharge, attention has been focused on the inverse phenomenon.

First of all, a system has been developed in which a curved dielectric barrier discharge plate is mounted on a NACA3506 wing profile (patent pending), and a surface plasma can be maintained for over ten hours (Fig. 2.6.7). Different measurements have been performed in order to detect the effects of the plasma on the shock that appears on the suction side of the airfoil when the speed ranges between $M_{is}=0.6$ to $M_{is}=0.75$. Electrical and optical measurements (CCD, photomultiplier) have been performed on the plasma, and pressure measurements as well as Schlieren visualizations (Fig. 2.6.8) have been used to study the transonic flow.

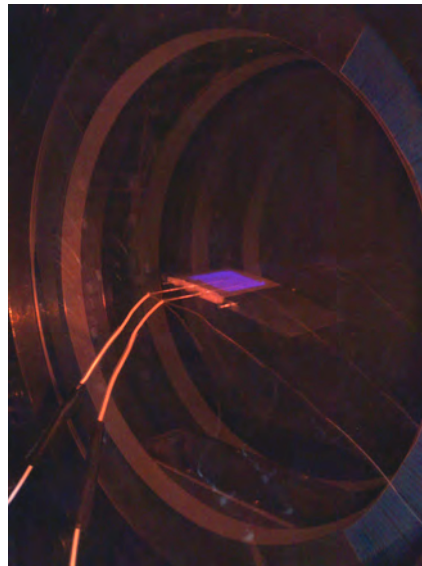


Fig. 2.6.7 *Surface dielectric barrier discharge generated on the suction side of a NACA3506 profile, and mounted in a Laval nozzle*

Several measurement campaigns have been conducted using different electrode geometries to generate the discharge. The basic idea is to generate a maximum of micro-filaments which are believed to interact in a more significant way with the airflow than the glow discharges. Moreover, the effect of the position of the surface discharge relative to the shock was also studied. In these experiments, the frequency was fixed at 10kHz, the voltage was varied from about 2.5kV to 4kV, the angle of incidence of the profile is fixed at 8° (giving strong shocks at different positions on the airfoil) and the airflow velocity is varied from $M_{is}=0$ to $M_{is}=0.75$.

Measurements have been carried out by first establishing the flow conditions, then switching the plasma on and off. Schlieren visualizations show that the shocks seem to be redistributed, forming several fainter shocks at $M_{is}=0.6$ or forming a lambda shock at $M_{is}=0.7$. However, the shocks formed on this specific profile are very unstable, making conclusions difficult to draw. Therefore numerical

simulations are being used to help understand the effects that can be expected and estimate the sensitivity of diagnostics needed in order to detect them.

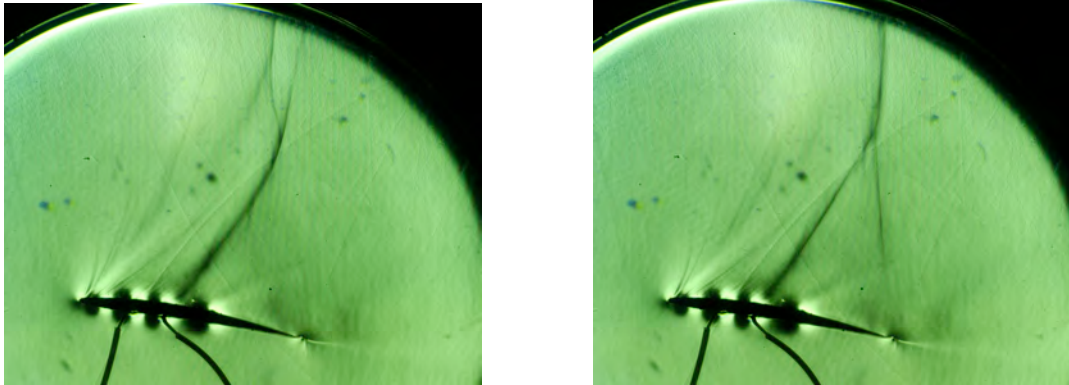


Fig. 2.6.8 Examples of Schlieren images at $M=0.7$, without plasma (left) and with plasma (right) at 10kHz and 2.3kV

2.6.7 Plasma diagnostics for electrical discharge machining (EDM)

Electrical Discharge Machining (EDM) is a widely-used machining technique. With this technology, numerous industries produce moulds, dies and finished parts with complex shapes. The process consists of successively removing small volumes of workpiece material, molten or vaporised during a discharge. The sparks are created in a flowing dielectric, generally water or oil. The liquid dielectric plays a crucial role for the electrode cooling and for the material removal: it increases the removing force on the molten metal when the plasma collapses, then it solidifies the molten metal into small particles, and finally it flushes them away.

During 2007 a new CTI project was started in collaboration with Charmilles Technologies SA, the Ecole d'Ingénieur de Genève and Micron SA. This project is dedicated to the development and investigation of EDM milling. In this case a rotating electrode is used to perform electrical discharge erosion.

Emission spectroscopy is at present the most suitable plasma diagnostic to investigate these interesting plasmas. Therefore optical emission spectroscopy has been applied to elucidate the high density plasma formed during EDM milling. Contrary to the traditional EDM, the plasma in EDM milling is rotating at very high speed. The interaction of the plasma with the dielectric at high rotation speeds of the electrode is of prime importance for the process and is presently being investigated. First dependencies of plasma parameters on different process parameters were established in the first months of the project.

Unfortunately the progress of this project has been delayed due to a breakdown of the existing EDM electrical generator. The generator has been replaced in the meantime by a new, more versatile generator, provided by the industrial partner Charmilles SA.

An additional important point for the future development of EDM with Charmilles SA is the development of advanced plasma diagnostic methods. Plasma diagnosis of the spark is a challenge since the discharge immersed in a dielectric is small, typically far below a millimetre, complicated by the poor reproducibility from spark to spark. New innovative plasma diagnostic methods are absolutely necessary if the EDM discharge or other micro-discharges are to be understood. Therefore the development of advanced plasma diagnostics is also a primary element in a planned future CTI project.

2.6.8 Other collaborations and industrial mandates

Design, characterisation and modelling of new advanced plasma sources

In the frame of a mandate, the possibility of the development and use of an advanced plasma reactor for high rate microcrystalline silicon deposition has been investigated. The aim of the proposed mandate is to establish a catalogue of advantages and problems related to new plasma sources in an advanced plasma reactor for the production of microcrystalline silicon at very high deposition rate. Since the CRPP is already equipped with the necessary infrastructure the mandate also includes preliminary experiments concerning the deposition of microcrystalline silicon by such an advanced plasma reactor.

Helyssen SARL, a start-up company at the CRPP

Helyssen SARL, a start-up company, uses a test bed in the laboratories of the industrial plasma group to evaluate the performance of an industrial Birdcage antenna as a Helicon source. The magnets and the necessary equipment for benchmarking and infrastructure have been lent to Helyssen SARL by the CRPP. This also includes equipment for plasma diagnostics and equipment and know-how to quantify the performance of high power RF plasma sources.

The results of the development and research of Helyssen SARL during the last year resulted in the design and test of a high RF power Birdcage antenna. Such high power tests are important for the future industrial application of the versatile Birdcage antenna.

Future projects

The success of OC Oerlikon in selling PV equipment to several large companies with a value of several hundreds of millions SFr also had an influence on the industrial plasma group. The strongly increased activities of OC Oerlikon led and still leads to scientifically very interesting future projects and mandates on silicon deposition and related topics. Intense collaboration with the IMT in the domain of equipment for the production of thin film solar cells in the frame of projects such as one supported by SwissElectric. Furthermore, a CTI proposal together with Sulzer Metco is being made at the end of 2007. It is hoped that such a project will lead to the final development of a new plasma tool capable of making thick and thin coatings at a competitive rate and cost. In addition, the successful collaboration with TetraPak in Romont shall be continued in the frame of the running CTI project. Furthermore it is intended to further increase the activities in EDM, where an intense collaboration with Charmilles is foreseen. Activities on arcing are in preparation with RUAG in collaboration with ESTEC.

New contacts with interested industries as well as with other university institutes have been established with the aim of diversifying the activities of the group. As an example it is intended to collaborate with the Ecole d'Ingenieur d'Yverdon (Swiss Welding Institute) on the development of a micro-torch for welding. The diversification towards new topics has started and new proposals were discussed between industry and the CRPP at the end of 2007.

3 TECHNICAL ACHIEVEMENTS OF THE CRPP IN 2007

3.1 TCV Operation

To anticipate a long shutdown starting in April 2007, the operation of TCV was intensified during the first quarter with 9 sessions per week without any break for maintenance. The shutdown is expected to end in January 2008. The work carried out during this period is listed below.

3.2 Shutdown activities and diagnostic upgrade

- Hard X-Ray tangential camera: assembly and installation on vacuum vessel
- Phase contrast interferometer: assembly and installation on vacuum vessel
- Infrared camera: update of optical system
- X-bolometer: upgrade of filters and diode detectors
- Langmuir probes: reparation and maintenance of probes; tile leveling around the probes to reduce shadow effects
- Vacuum vessel thermocouples: update with new design for 4 sensors
- Charge exchange spectroscopy: alignment and calibration
- X3 launcher: regular maintenance operations
- Lower hybrid parametric instability antenna: design, construction and installation
- SPRED: alignment
- Diagnostic neutral beam injector: installation and commissioning of arc source
- Polarimeter: installation of windows on vacuum vessel. Laser and waveguide assembly
- Hard-X ray camera
- Fast frame camera: replacement of detector; installation for test
- Glow antennae: new construction and installation on vacuum vessel
- Metal bolometers: repair of lower camera
- TCV pumping system: repair and maintenance operations
- Vertical ECE: construction and installation of viewing dump
- Fast gas injection valve: assembly and installation on vacuum vessel
- Thomson scattering: change of windows; observation window shutter maintenance; update of electronics and data acquisition for laser operation
- Magnetic probes: repair of connectors on one probe
- X-Ray tomography: replacement of detectors; replacement of data acquisition
- Carbon tiles: sanding, cleaning and conditioning of all tiles

Following the TCV vacuum opening early in 2007, most of this year's diagnostic activity has been in the installation of new diagnostics and in the continual upgrading and repair of existing diagnostics. Preference has been given to diagnostics requiring internal TCV access or those that require someone in the TCV vacuum vessel for measurement and/or alignment procedures.

This section is structured as follows. Diagnostics that have undergone major changes are accorded an extended description whereas only a short paragraph is presented for others.

3.2.1 Thomson Scattering

Aiming at higher spatial resolution in a selected zone of the plasma, part of the TCV Thomson scattering system has been modified. This change is motivated by the interest in more precise measurements of the gradients of electron temperature and density profiles associated with the formation of ITBs. The design of the TCV Thomson scattering diagnostic permits changes of the spatial resolution via changes in the configuration of the optical fibre bundles collecting the scattered light. After installation of a new set of fibre bundles, which comprises 8 individual large-core fibres ordered in 2 groups to feed 2 spectrometers, the spatial resolution in 20 channels will be improved significantly (vertical separation 36mm \rightarrow 16mm). Due to the number of spectrometers presently available, the coverage of the plasma in vertical direction has been reduced. Plasma configurations positioned in the lower TCV vessel region will no longer be accessible. This restriction is acceptable in view of the experiments envisaged for 2008.

3.2.2 X-Ray Tomography

The first calibration and upgrade of this system has been performed. The cameras have been continuously operated since 1999, the date of the last X-Ray calibration. The 9 cameras, containing 10 detectors each (totalling 200 channels), have been dismantled, and the arrays of photodiodes replaced with new arrays, manufactured by IRD (International Radiation Detectors inc.) in 1998. These arrays differ from the previous CENTRONIC models as they have no dead layer, and will thus provide a better signal to noise ratio without spectral regions of reduced sensitivity. The head amplifiers boards have been updated, using operational amplifiers with improved gain properties. A LED has been installed in each camera to provide a mean of testing and possibly calibrating the cameras during the campaign. The arrays and the head amplifiers have been tested and calibrated with a medical X-Ray source.

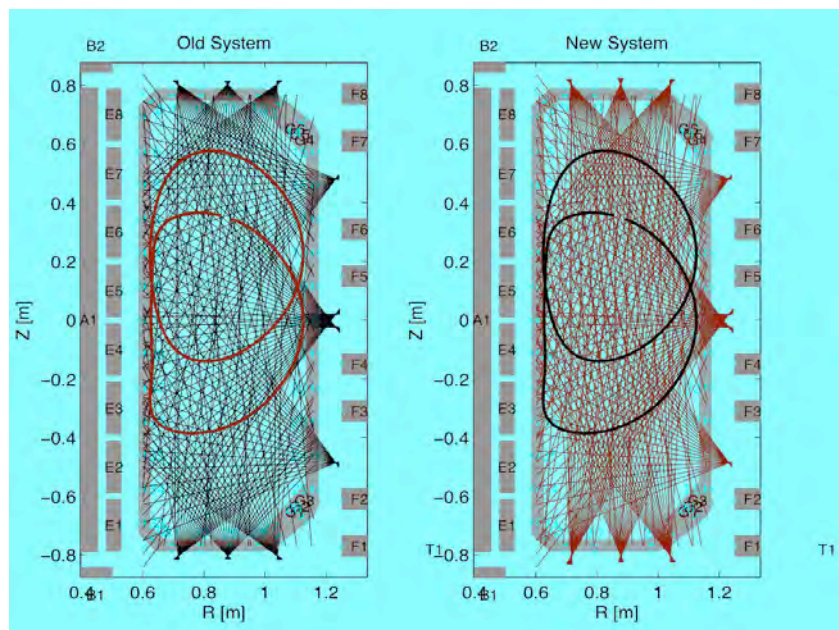


Fig. 3.2.1 Poloidal TCV cross section with the position of the chords until 2007 on the left and the modified chord disposition on the right. The chord density in the plasma core is considerably more evenly distributed.

The cameras on the machine top and bottom cameras have been modified to provide align more lines of sight within the typical plasma configurations (for $Z=0\text{cm}$ or $Z=21\text{cm}$) in order to improve the quality of tomographic reconstruction. This was implemented despite a slight loss of flexibility of the system, which was originally designed to cover the full extent of very elongated TCV configurations. Six supports were designed and manufactured to narrow the X-Ray acceptance cones covered by the cameras, and to reduce each channel cross-talk by making the diode array perpendicular to the central line of sight. A new acquisition system has been installed (D-TAQ, 500kHz acquisition frequency, 16 bit resolution, CPCI connectors), which will improve the dynamic range.

3.2.3 FIR polarimeter

A far-infrared (FIR) polarimeter diagnostic is implemented to measure the poloidal magnetic field and hence the current density profile in TCV plasmas. During the first part of 2007, most of the optical systems were optimised, designed and manufactured (polyethylene lenses, metallic meshes used as beam splitters, Pyrex waveguides, quartz wave plates, dichroic filters etc.). Figure 3.2.2 illustrates the drawing of the main beam splitter that divides the main laser beam into 5 equivalent beams.

The installation and implementation of the diagnostic onto TCV commenced in the second half of 2007. The CO₂-FIR laser system is now in its operational position and the waveguide transmission lines are installed. The diagnostic is expected to become fully operational during the first half of 2008.

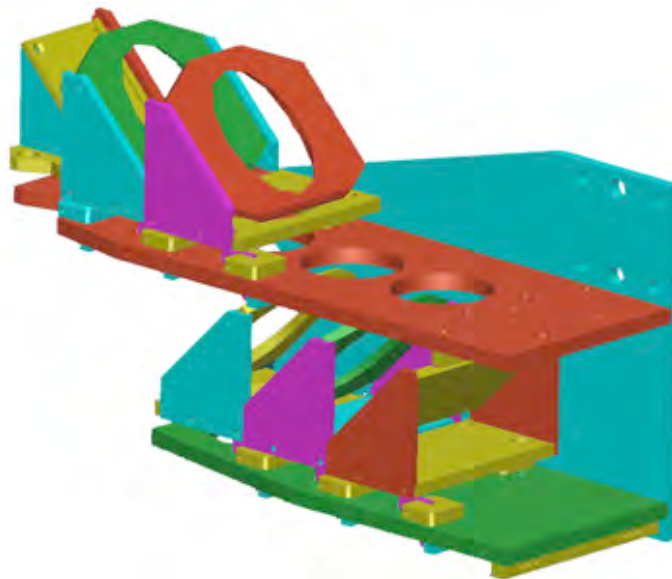


Fig. 3.2.2 *Details of the main beam splitter for the FIR polarimeter diagnostic. The main beam enters vertically from below and is split into five equivalent beams that will diagnose the plasma.*

3.2.4 Diagnostic Neutral Beam

To increase the beam purity and reduce divergence, the RF-plasma generator of DNBI was replaced by an arc-plasma source. The ion optical system (IOS) was then

re-optimised in September 2006 within a contract with the Budker Institute (Novosibirsk, Russia). The goal of upgrade was to increase the H^+ (primary energy) current fraction from ~50% to 85% and to reduce the beam size in the plasma from 8 to 5cm (beam radius on $1/e$ level). In the period of October 2006 to March 2007 the DNBI was operated with a nominal energy of 50.3keV, mean ion current of 2.5A and the primary energy fraction of ~82%; the beam was operated for 526 TCV discharges with a reliability of ~70%.

Following the ion-source upgrade, a significant reduction of the signal levels in the Charge eXchange Recombination Spectroscopy (CXRS) was observed, instead of the expected increase by a factor of 1.5-2. Measurements of the beam size and profile in the TCV vessel and in beam duct performed in the of November 2006 to May 2007 period, combined with beam shape modelling, indicated that the beam angular characteristics (divergence and position of the focal point) were far from the specifications. The source is presently at the Budker INP for repair and corrective modifications. A commercial camera, installed on the CXRS diagnostic port, measuring the visible light emission from the DNBI, was used to measure the beam profile in the TCV vacuum chamber.

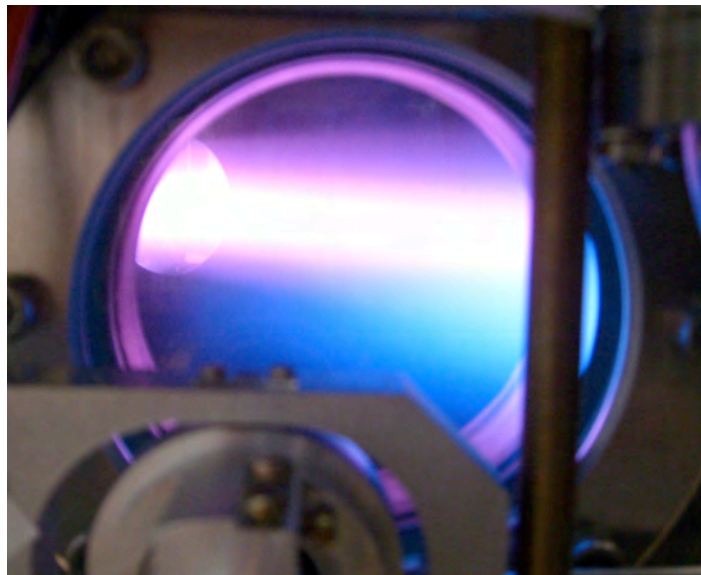


Fig. 3.2.3 *Image of the Neutral Beam with a WebCam from which the beam waist was estimated.*

Analysis of the operational beam reliability indicated that ~25% TCV discharges were lost by timing faults in the in the updated DNBI control system. To solve this and numerous other problems with the initial DNBI control system, it was decided to replace the existing CAMAC based DNBI LCS by the system based on the Data Acquisition Devices in the PCI standard of National Instruments Corporation. On the software side, the previous Java-based control program will be replaced by a control program written in LabVIEW which may now be directly maintained by CRPP staff.

Typical configurations will aim the camera at the $q=1$ (for sawteeth) or $q=2$ (for disruptions) surface in a direction nearly tangential to the magnetic field (see Fig. 3.2.6). This arrangement maximises the signal in the case of MHD phenomena or runaway generation, since electrons accelerated along the field lines emit radiation primarily in a forward cone; additionally, for spatially periodic structures on flux surfaces, such as in the case of MHD, tangential viewing minimises cancellation from line averaging over multiple periods and enhances the spatial localisation. The presence of multiple detectors provides some redundancy to aid in the estimation of the spatial extent of the emission region. The diagnostic is also expected to be useful for surveying suprathreshold electron generation during electron cyclotron heating, a phenomenon that was extensively studied in past years using a spectroscopic hard X-Ray camera that is no longer installed on TCV.



Fig. 3.2.5 View of the X-Ray diagnostic head from inside the vessel. The system is rotated to a typical near-tangential viewing direction. The outer set of Soller plates is visible.

The full design and construction of the instrument have been carried out in Moscow under contract to and in collaboration with the CRPP. The diagnostic was installed on TCV in October 2007 and its viewing orientations were calibrated against the motor encoder readings by means of a laser diode.

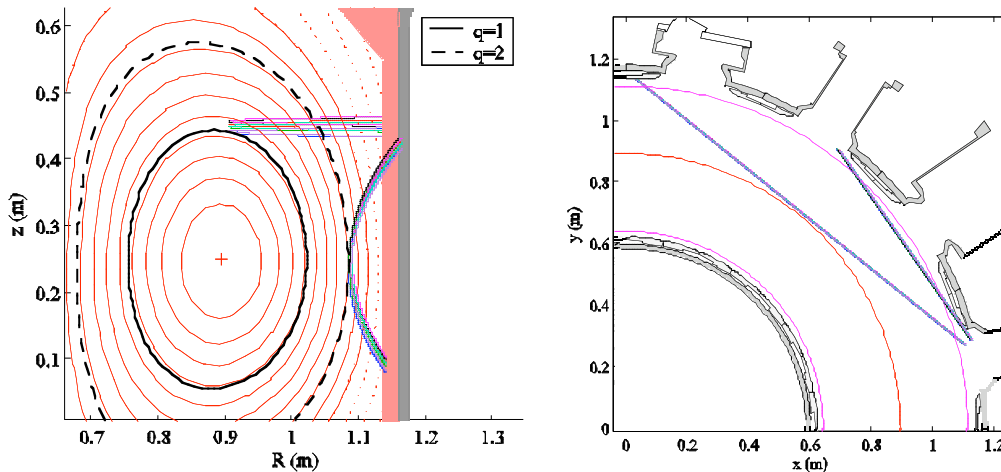


Fig. 3.2.6 Poloidal (left) and top (right) views of a typical TCV plasma configuration along with viewing chords from the X-Ray detectors in two orientations that provide approximately tangential views to the $q=1$ and $q=2$ surfaces, respectively. Flux surface contours are shown on the left.

3.2.6 Tangential phase contrast imaging

Until recently, fluctuation studies on TCV were limited to the scrape-off layer. We have now launched a multi-pronged programme of core turbulence diagnostics that includes the recently installed correlation ECE and reflectometer systems. The latest arrival is a laser imaging apparatus that employs the phase-contrast technique to project cross-field images of plasma density fluctuations with very high spatial localisation, thanks to a tangential viewing arrangement.

The motivation for this diagnostic is provided by the unique operating conditions of TCV, with a very powerful and flexible ECRH system that enables the exploration of a wide variety of scenarios in conditions of dominant electron heating. It is thus possible to isolate the physics of turbulence in the electron fluid, an important piece of the puzzle of anomalous transport that will play by necessity a strong role in a D-T reactor partly or wholly sustained by alpha heating of electrons.

The diagnostic is based on a 7cm wide, 10.6 μm wavelength CO₂ laser beam launched in a near-tangential direction (see Fig. 3.2.7) from a median port to an upper lateral port, to match closely the field-line pitch angle in the plasma core. The transmitted signal is phase-shifted by the density fluctuations, and this phase shift is transformed into a detectable amplitude variation by a phase contrast plate. The signal is detected by a 30-element photoconductive HgCdTe detector array with a bandwidth in excess of 1 MHz. The system is in essence an internal-reference interferometer, incapable of measuring *absolute* phase variations but extremely sensitive to *relative* phase shifts across the width of the beam. Line-integrated density fluctuations down to $1.5 \times 10^{15} \text{m}^{-2}$ can be detected in principle in the TCV setup. The tangential arrangement provides extremely high spatial resolution through spatial filtering. Since fluctuation wave vectors are known to be essentially perpendicular to the magnetic field and the line integration selects wave vectors perpendicular to the beam propagation direction, at any point along the beam only one specific wave-vector orientation (the cross-product of the magnetic field and beam direction) is selected by the measurement. By operating a similar post-processing wave-vector selection with a spatial filter, one can thus isolate signal originating from specific localised segments of the beam, effectively enhancing the spatial resolution. In addition, the near-tangential orientation intrinsically enhances the cross-field resolution, down to 1% of the minor radius in the innermost core region.

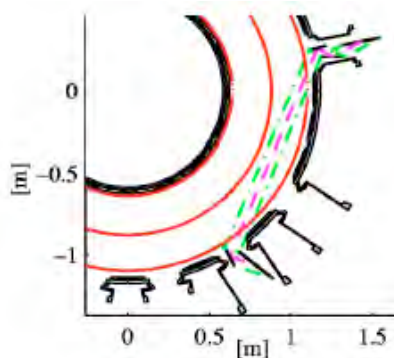


Fig. 3.2.7 Top view of the tangential laser beam path in the phase contrast imaging diagnostic.

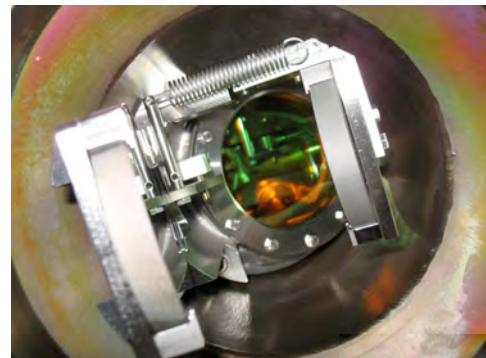


Fig. 3.2.8 View of the entry port assembly from inside the torus. The ZnSe window is visible, as well as the two mirrors located in the vacuum chamber.

The accessible wave-number range, from 0.1 to 7cm^{-1} , spans the spectrum of ion- to electron-dominated turbulence (ITG, TEM and ETG modes), opening for the first time the possibility of a thorough study of core turbulence in plasmas with very strong electron heating. In the first measurement campaign, particular emphasis will be placed on scenarios with electron internal transport barriers (eITB), which are routinely generated in TCV in conditions of fully or mostly non-inductive current drive with strong ECCD. The physics of the generation and sustainment of eITBs is still only partly understood, and it is believed that a key element in the formation of an eITB is a modification of the underlying turbulence characteristics.

In the absence of ports with intrinsically tangential views, the beam steering is provided by a complex system of 3 and 2 mirrors in the entry and exit ports, respectively. The plasma-facing mirrors are made of fused silica with a protected Mo coating; the metallic coating is electrically floating to minimise sputtering from glow discharge cleaning. The vacuum interfaces consist of ZnSe windows. The entire port assemblies can be translated radially, to give access to different plasma regions, and one mirror per port can be rotated through a manual actuator for fine adjustments of the beam alignment. The port assemblies were installed in October 2007 (see Fig. 3.2.8) and have been successfully aligned. The laser source and the detector array and related electronics are delivered, and the external optics and the data acquisition electronics are currently being procured. The diagnostic is expected to be operational at the restart of TCV operation in early 2008.

3.2.7 *Microwave reflectometer*

A single-frequency homodyne reflectometer was installed on TCV in 2006. The reflectometer is connected to a spare 2nd harmonic steerable ECRH launcher, which provides the possibility of orienting the launch wave vector in a wide variety of directions. The reflected wave is collected along the same path as the launched wave and is separated inside the instrument. A 70-GHz and a 78-GHz system are available but are not used simultaneously. The diagnostic was employed successfully on TCV from December 2006 to March 2007. A more extensive and systematic measurement campaign is planned for 2008. The system is used both for single-point density fluctuation measurements and for plasma flow measurements using the Doppler reflectometry method. In the latter case, the beam is injected at a non-normal angle to the flux surface and the signal detected is the first-order diffracted component, reflected from the plasma cut-off layer. This technique relies on turbulence as a tracer to detect the Doppler shift resulting from the poloidal component of the $E \times B$ fluid flow.

This diagnostic is the result of a collaboration with Dr. E. Holzhauer of the University of Stuttgart and Dr. M. Hirsch of the Max Planck Institut in Greifswald. The instrument had previously been used in the Wendelstein 7-AS stellarator.

3.2.8 *Lower-Hybrid Parametric Instability Probe*

A lower-hybrid parametric instability (LHPI) probe for the detection, spectrum analysis and monitoring of lower-hybrid waves (LHWs) is under construction. It consists of a rectangular loop-antenna connected to a coaxial conductor balanced by a sleeve. LHWs are generated by parametric decay at the extraordinary-to-Bernstein (X-B) mode conversion of externally launched electron cyclotron (EC) waves. This non-linear three-wave interaction is a potential loss channel for the O-X-B electron Bernstein wave heating (EBWH). The strongest LHPI signal would correspond to a maximum of EC power reaching the X-B conversion layer, that is

an optimised EC-EBW coupling with, in particular, optimum injection angles for the O-X conversion. The LHPI probe is also of interest for suprathreshold ions physics studies.

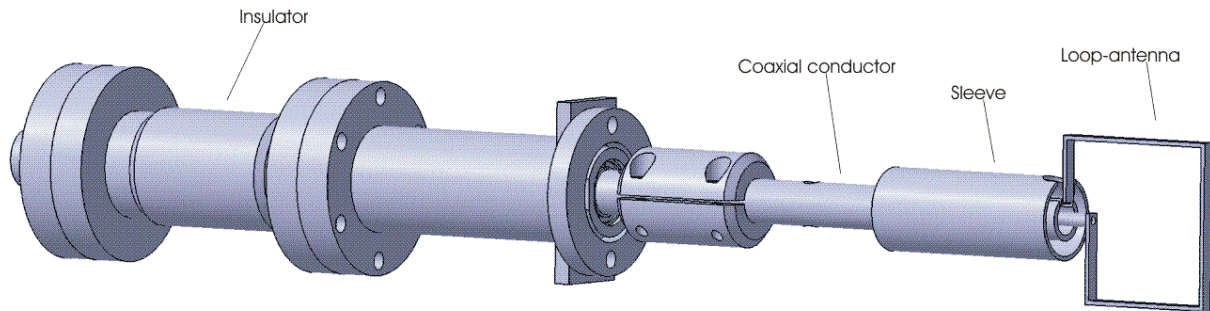


Fig. 3.2.9 LHPI-probe (rectangular loop) with its coaxial feed.

3.2.9 Oblique ECE receiver

The 7th launching antenna (identical to the X2 launchers) was installed in 2006 to be used as an orientable microwave receiver. A window is installed in place of the gate-valve (of the launchers). The receiver was used for EBW studies in 2006 and has been modified to permit oblique ECE and reflectometer measurements in 2007. An available 63.5mm-diameter HE₁₁- waveguide to WR12 mirror/scalar horn adapter was used in place of the simple open ended 25mm waveguide to connect the receiver to the low-field side (LFS) radiometer. This decreases the dimension of the beam transverse to the direction of propagation so that it rivals the LFS lens focusing. It can thus be used for correlation ECE measurements with good $k\theta$ -spectral resolution ($k\theta < 1.2\text{cm}^{-1}$). The adapter permits launching/reception with linear polarisation for reflectometry and nearly circular polarisation reception for oblique ECE at large angles. The latter was accomplished by inserting a spare grating mirror from the X2 MOUs in the free-space path of the beam as seen in Fig. 3.2.10. The grating is oriented for nearly-circular-to linear conversion. The handedness of the circular polarisation is changed by rotating the grating to the appropriate angle (this allows either quasi-O-mode or quasi-X-mode emission from the plasma to be received). The coupling from the quasi-X or quasi-O modes is calculated based on the plasma equilibrium, receiver angles and polariser grating angle, analogously to the launched X2 heating beams. An omni-directional antenna is used to shut off the gyrotrons if excess gyrotron radiation is detected. For reflectometry, the grating is removed and the adapter orientation is changed so that the HE₁₁ guide radiates directly to the mirror. The experiments using a temporary setup, using available equipment, were successfully tested and a more permanent setup will now be made using a recently ordered telescopic adapter.



Fig. 3.2.10 *Oblique ECE receiver: (a) motorised launcher, (b) HE11 waveguide, (c) adapter baseplate, (d) grating mirror, (e) focusing mirror, (f) scalar horn, (g) 25mm waveguide to LFS radiometer, (h) HE11 waveguide connection for adapter orientation when used for reflectometry, (i) reflectometer source/detector and (j) omni-directional detector for security against gyrotron radiation.*

3.2.10 Plasma edge diagnostics

The long 2007 shutdown has provided an opportunity to refurbish and upgrade some of the TCV edge diagnostics. All three in-vessel, tile embedded Langmuir probe arrays (comprising a total of 80 single probes) have been serviced, replacing defective components. In-vessel access has also allowed a part of the region of the vacuum vessel floor acting as outer divertor target area to be surveyed using a state-of-the art optical pose tracker. This permits an accurate mapping of the degree of floor tile misalignment, allowing improved interpretation of infra-red thermographic observations of the 22.5° toroidally wide field of view (FOV) covered by the vertically viewing fast IR camera. Relay optics for the latter have been upgraded to the final system foreseen when the camera was first purchased at the end of 2006, but which were not available for the preliminary tests of the system before the major TCV shutdown in 2007. A new set of 12 tile mounted thermocouples has also been installed within the camera FOV, replacing the old array used primarily for monitoring of in-vessel temperatures during machine vessel bakeout. The new array has been designed to provide fast response with higher spatial resolution in the vicinity of the outer strike zone and will be used to improve, via calorimetric energy balance, estimates of power fluxes obtained from IR surface temperature data. During the 2007 shutdown the entire first wall set of graphite protection tiles have been grit blasted to remove co-deposited layers after nearly 10 years of plasma operation (see Section 3.2.14). Only 3 tiles have been left untreated, all in the IR camera FOV. At least early on in the 2008 campaigns, this should allow the effect of deposited layers on the surface temperature response to transient heat loads (such as ELMs) to be approximately calibrated.

In late 2005 an array of 7 pinhole AXUV diode cameras was installed on TCV. In the original system, each camera was equipped with two, 20 channel detectors, one open to all photonic plasma radiation and the second filtered for $L\alpha$ radiation at 120nm. After more than a year of experience with this system, it became clear that the poor transmission of the VUV transmission filters and the relatively low $L\alpha$ emission from most TCV plasmas make the filtered part of the array difficult to use. It has also become evident that the unfiltered diodes age rapidly upon exposure to photon fluxes and are affected (though it is difficult to quantify the relative importance with respect to photonic exposure) by impurity deposition on the diodes during conditioning procedures (e.g. He glow and boronisation). During this year's shutdown, all 14 diode arrays have been replaced by new elements, comprising 7 AXUV20ELG radiation hardened arrays (to reduce the ageing effect) and 7 AXUV20EL arrays on which have been directly deposited a 1 μ m thick polyimide coating. Each camera thus consists of one of each type of array. The polyimide coating has been chosen to provide a crude degree of wavelength (or energy) selectivity: all photons with energies less than ~ 100 eV are blocked by this coating. By comparing the unfiltered (but radiation hardened) detectors, which are sensitive to all photon energies but with a non-linear spectral response at low energy (where much of the plasma radiation from the cooler edge is emitted), with their filtered counterparts, studies will be possible of the relative contributions of core and edge radiation.

Throughout 2007 a new fast gas injection valve system has been developed by collaborators from the Hungarian Association who work closely with the TCV group on a number of edge physics issues. This new system is destined for disruption mitigation and particle transport studies. It is based around the commercially available (Parker-Hannifin) solenoidal valve, capable of pulsed operation down to several 100 μ s. Dedicated nozzles and skimmers have been designed to shape the injected gas pulse and full laboratory tests performed in Budapest. All components have been manufactured and transported to CRPP and will be installed on TCV on an upper lateral vacuum vessel port for the beginning of 2008 plasma operations. A remotely controllable gas exchange system is being provided by CRPP. Initially, noble gases He, Ne and Ar will be tested (He is expected to be marginal on TCV for disruption mitigation) with the possibility to try different gases or gas mixtures once the system is commissioned.

3.2.11 Compact NPA

The CNPA was moved to another midplane sector where the diagnostic may be connected to the TCV vessel along a line of sight perpendicular (as before) or oblique ($\sim 60^\circ$) with respect to the toroidal direction. This new arrangement provides the possibility of diagnosing spatial suprathreshold temperature and neutral particle flux anisotropies or the fast ion dynamics in turbulent regimes with resonant wave-ion interactions observed in ECCD-driven plasmas or upon sawtooth crashes.

3.2.12 Charge Exchange Spectroscopy

Both toroidal fibre arrays of the CXRS spectrometer have been upgraded from 16 to 40 channels. These may be arranged as 40 separate chords or an array of 20 chords with two fibres per chord to increase the collected light. This system now covers a radial chord from 80% out to the high field side and up to the machine wall on the low field side.

3.2.13 SPRED UV-Spectrometer

Analysis of the SPRED-spectrometer performance during a TCV diverted discharge indicated that there is a non-negligible “defocusing” due to the magnetic field. A 5mm thick soft-iron cage has been designed that can be mount around the SPRED microchannel plate detector that will be installed early in 2008.

3.2.14 First wall tile cleaning

The majority of the ~1700 individual graphite tiles covering ~90% of the TCV in-vessel plasma facing surface have been in place since 1998, encompassing a period of some 15,000 tokamak discharges. Over this period 19 vessel boronisations have been performed, each depositing a thin film of ~100nm on the plasma-facing component (PFC) surfaces. During normal campaigns in 2006, evidence began to mount that under certain conditions (for example disruptive transient events leading to plasma impact on surfaces not generally wetted by plasma), excessive dust or flake accumulation was occurring in-vessel. This was almost certainly due to the degradation or delamination of layers built up over the years of plasma and conditioning discharges. A decision was taken to pursue an aggressive tile cleaning programme throughout the planned 2007 shutdown. Enquiries at other tokamak groups employing graphite PFCs revealed that grit or sand-blasting has been occasionally employed to remove the top few microns of tile surfaces. This technique has been adopted for the first time at CRPP with the purchase of a small industrial grit-blasting apparatus (AUER, model SG 1000 J) employing a centrifuge to recycle the blast material. For the latter, boron carbide (B_4C) powder with average grain size ~60 μ m was employed with an 8mm nozzle at typical blast pressure of a few bars. Blasting of all 1700 separate tiles was accomplished in ~2 months, requiring ~50kg of B_4C , followed by ultrasonic cleaning in alcohol, drying in air and brushing of all surfaces with a fine nylon brush to evacuate the thin layer of dust which settles on the tile surfaces immediately after the ultrasonic cleaning is terminated. No testing of surface composition before or after the treatment was performed, nor was the removed layer thickness determined. Before plasma operations begin in 2008 an extended vacuum vessel bake of several weeks and deuterium/helium discharge cleaning will be performed.

3.3 Preliminary studies in view of possible TCV upgrades

3.3.1 Neutral beam heating

The powerful ECH systems on TCV allow an exploration of electron heated regimes with T_e/T_i typically in the range 2-20, depending on plasma parameters and heating power. This is due to the fact confinement times in TCV, as in most small devices, are much smaller than electron-ion collision times. These regimes are at the opposite of the mainstream heating method in most tokamaks, especially those operating in H-mode, namely neutral beam heating, which mainly heats the ions. ITER and future reactors will lie in between. Although electron heated by high energy beams or radiofrequency waves and alpha particles, the better thermal equipartition between species in reactor plasmas will provide the ion heating required for fusion reactions to occur. In small devices, such strong equipartition is only possible at plasma densities achieved at extremely high field. In order to explore this regime, which is of direct reactor relevance, smaller devices with

modest magnetic fields, need to be able to provide a controlled mix of heating to both species directly. This has motivated the initiation of a feasibility study for neutral beam heating on TCV, as a possible option for a future upgrade.

The physics issues that may potentially be addressed with a combination of ECH/ECCD and neutral beam heating include transport in reactor-relevant mixed heating regimes, neoclassical tearing mode physics and stabilisation, resistive wall mode physics, the physics of edge localised modes and fast particle physics.

The geometry of the TCV device and vessel poses challenges to the implementation of neutral beam heating. The midplane port diameter (15cm) appears to be sufficient according to preliminary contacts with a potential manufacturer. The largest possible toroidal angle at the point of vessel entry is about 11 degrees, corresponding to the geometry of the existing diagnostic beam. In this geometry, particles deposited at the low field side are practically all trapped. Somewhat larger angles, would require re-machining and welding work on the vessel. For tangential injection, allowing best orbit confinement, the toroidal field coils would also need to be modified.

TCV is capable of a very wide range of operating conditions, from low density ($1-2 \times 10^{19} \text{m}^{-3}$), low current (100-200kA) plasmas for ECCD and eITB experiments, to H-mode plasmas with higher densities ($>5 \times 10^{19} \text{m}^{-3}$) and currents (300-500kA). The high elongation plasmas which were intensively studied in the past, were also obtained at high density and high current (up to 1MA) and have so far barely been investigated with auxiliary heating. At low density, NBI may be combined with ECH at the second harmonic, at central densities above $4 \times 10^{19} \text{m}^{-3}$, with third harmonic ECH.

The fairly low available plasma thickness and relatively low plasma currents favour the usage of deuterium beams of fairly low energy, typically in the range 20-40keV. Even in this case low density plasmas suffer significant shine-through except for tangential injection, limiting pulse durations to some 100ms. Orbit calculations show that for $I_p < 200 \text{kA}$ first orbit losses occur over an excessively large fraction of the plasma cross section, except for tangential co-injection.

The slowing down of injected ions was modelled using a Monte Carlo orbit code. Pitch angle scattering leads to larger losses than those affecting first orbits only. Satisfactory confinement during the entire slowing down process and hence satisfactory heating performance is obtained for the easiest injection geometry (11 degrees toroidal angle) for $I_p > 200 \text{kA}$. An example of slowing down orbits obtained in a 400kA plasma for 35keV injection energy is shown in Fig. 3.3.1. Power deposition profiles are obtained by summing the contributions of large numbers of slowing down orbit sequences over many launching positions, weighted consistently with the beam attenuation. An example of heat deposition profiles for a 400kA plasma with parameters of the X3 heated plasmas described in this report is shown in Fig. 3.3.2. In that example, globally 46% of the power is delivered to the ions, 16% to the electrons, 25% is lost due to unconfined orbits and 13% due to shine-through.

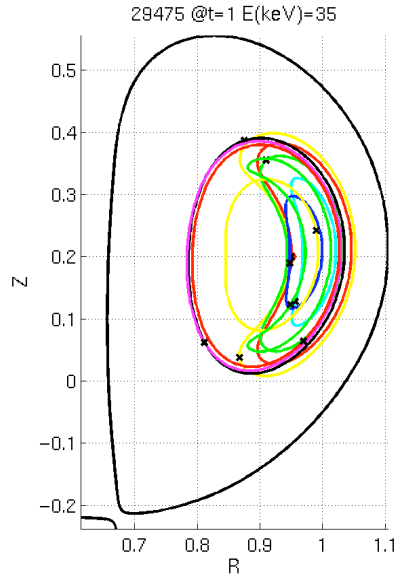


Fig. 3.3.1 *Examples of orbits from a slowing down sequence in a 400kA plasma. Beam energy: 35keV, injection angle 11.25 degrees at vessel entry, birth position R=0.95m, Z=0.2m, counter-injected. First orbit is red banana.*

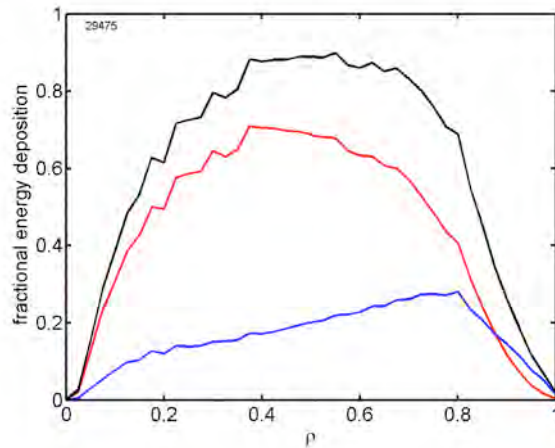


Fig. 3.3.2 *Normalised power deposition in a 400kA plasma for a 35keV heating beam. (Fractional power per interval of normalized poloidal radius). Injection angle 11.25 degrees at vessel entry, co-injection. Summed from 30 launching positions with 50 slowing down runs each. Blue curve: electron heating, red: ion heating, black: total.*

3.3.2 X3 Upgrade

A preliminary study for a substantial upgrade of the X3 system has been carried out. The main motivation of this study comes from the very encouraging results obtained using the present X3 top-launch system (118GHz/1.35MW) to heat ELMY H-mode plasmas. These high-confinement ($H \approx 1.6$) ELMY H-mode plasmas exhibit properties of the H-mode hybrid modes proposed for ITER and, in TCV, are dominated by electron heating.

Starting from the achieved plasma parameters for these H-modes ($B_0=1.42T$, $n_{e0}=8 \cdot 10^{19}m^{-3}$, $T_{e0}=3keV$, $I_p=0.4kA$, $\kappa_{95}=1.65$, $\delta_{95}=0.36$), the first criterium used to evaluate the additional X3 rf power was the need to reach the ideal β -limit. Considering a

confinement time scaling with, $\tau_E \sim P^{-0.69}$, to reach the β -limit on needs 2.7MW of additional X3-power in the plasma, bringing the total power in the plasma to 3.8MW. With these plasma parameters, it has been verified that the single-pass absorption for top-launch injection is in excess of 90%.

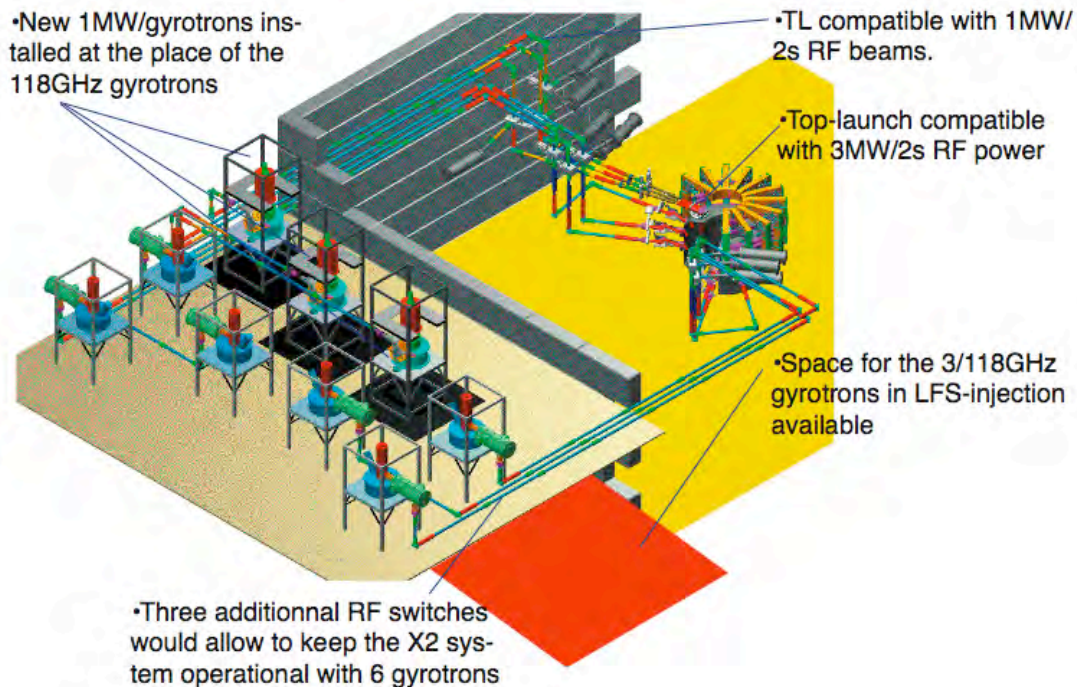


Fig. 3.3.3 *Layout of the TCV EC system including 3 new X3 1MW gyrotrons installed at the location of the present 118GHz gyrotrons.*

Based on these considerations, and on the space availability in the TCV experimental hall (see Fig. 3.3.3), 3 additional 1MW-gyrotrons could be installed and operated with the existing HVPS and rf transmission lines. One important advantage of this scenario is that the new gyrotrons would be installed where the present X3 gyrotrons are and the 3 old ones would be connected via microwave switches to the X2 transmission lines for an X3-LFS injection. The X3-LFS injection in H-mode plasmas allows a local deposition of rf power which is not the case in top-launch. The calculated single-pass absorption for the an X3-LFS is higher than 50% with a strong electron temperature dependence. The scheme proposed for X3-LFS via a microwave switch was already successfully used in preliminary studies of the X3 EC physics.

The 140GHz/1MW gyrotron developed by EU for W7-X is a possible choice. With the present TCV magnetic field of 1.42T, in order to optimise the absorption for the top-launch injection it would preferable to operate the gyrotron on a different mode ($TE_{26,7}$) oscillating at 126GHz. The operation on these modes has been experimentally verified during tests performed at FZK. From the hardware point of view, this upgrade preserves the entire flexibility with the two X2 and X3 systems, and is fully compatible with the existing EC systems. Practically only the 1MW gyrotrons with the respective superconducting magnets must be procured.

3.3.3 Ergodisation coils

Coils generating radial magnetic field at the plasma edge have been added to the DIII-D tokamak to ergodise the magnetic field structure. The magnetic field ergodisation induced a mitigation of the ELMs leading to a stationary H-mode without large ELMs with excellent confinement properties. Despite the clarity of the results, an understanding of this interesting regime is missing. This TCV can be an excellent candidate for such basic investigation of the mechanics behind ELM control.

Preliminary studies were performed, leading to the choice of a design with coils surrounding each upper-lateral and equatorial plane ports, external to the vacuum vessel. This approach, coupled with a well-thought connectics, will allow us to characterise the effect of different toroidal and poloidal modes on the ELM behaviour. Estimations of the ergodisation level as a function of the plasma radius are under way.

Such a system can be used to correct error fields as well. Misalignments in the poloidal coils set are responsible for these error fields, which, in turn, provoke instabilities in the plasma and can lead to disruptions. The ergodisation coils, with an appropriate current distribution, should correct these error fields. On the other hand, creating error fields by other coil combinations should have an effect on the plasma rotation, which is linked with different plasma properties such as the H-mode accessibility.

3.3.4 Fast ion physics tools

The interaction between fast ions, waves and turbulence is a major topic of current-day research aimed at the development of a reliable burning plasma regime. TCV has various technical and operational characteristics that make it an ideal candidate for the development of a trace fast ion physics program, where many central aspects of the wave-particle interaction mechanisms can be studied without most of the complications associated with larger devices operating closer to the burning plasma regime.

A technical and scientific proposal has been made to develop a set of trace fast ion physics tools for TCV, which involve one set of antennas for heating in the Ion Cyclotron range of frequencies (ICRF) and one set of antennas for the excitation of waves in the Alfvén frequency range (AW). For the ICRF antennas, a low-power system has been envisaged, capable of delivering around 100kW to the plasma. The basic concept considers two straps per antennas, with two (or three) antennas at different poloidal locations on the same machine sector, so as to improve the antenna-plasma coupling for the different TCV operating scenarios. For the AW antennas, a moderately high-power system has been envisaged, capable of delivering around 30kW to the plasma, so as to drive Alfvén Eigenmodes (AEs) at sufficiently high amplitude to affect the radial transport of ICRF-driven fast ions. The basic concept considers a multi-layer, coil antenna, located at different poloidal locations and on various machine sectors, for control of the mode number excitation spectrum.

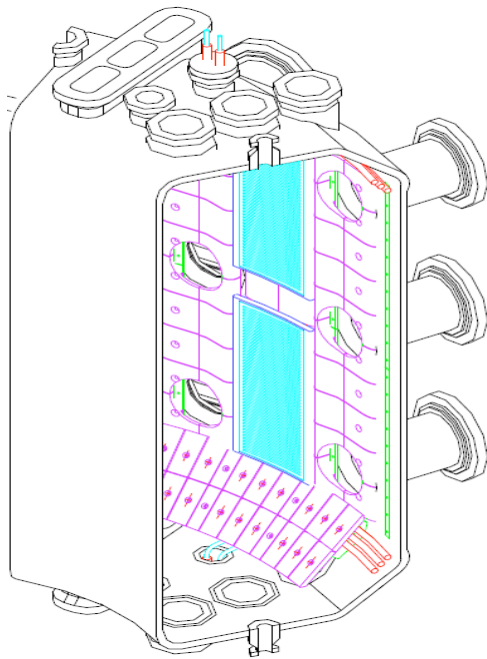


Fig. 3.3.4 Schematic layout design for the ICRF antenna at one poloidal location.

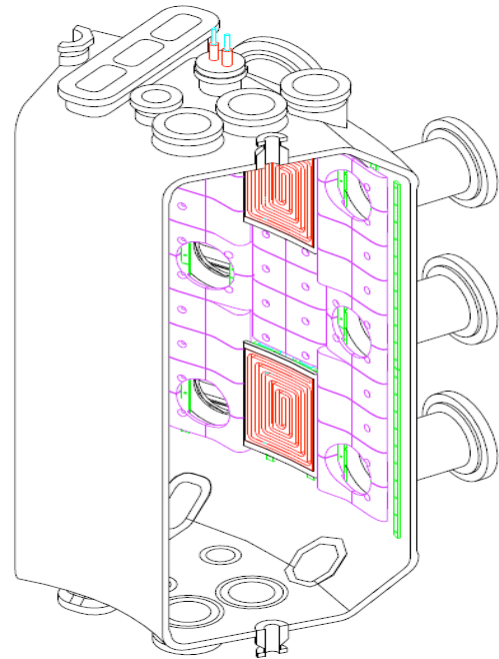


Fig. 3.3.5 Schematic layout design for the AW antennas at one poloidal location.

3.4 Control and acquisition

3.4.1 Plant control and data acquisition

300 shots were acquired in the first two months of 2007, preceding the long TCV opening.

The data acquisition system has been re-designed, to speed it up and decrease the total acquisition time for a single discharge from 15-20 minutes to 2-3 minutes. We plan to do it using a network of small dedicated PC's, and a fileservers with large storage (a few Terabytes). A constraint is that the passage to the new data acquisition system has to be completely transparent to the users. This upgrade is conceived as part of the migration from the OpenVMS operating system to Linux. The modification and testing of the software is under way, and a proof of principle was successfully done in November. We expect to complete the upgrade during the first half of 2008.

3.4.2 Plasma control system

The Advanced Plasma Control System (APCS), built in collaboration with IST Lisbon (Portugal) and based on digital signal processors (DSPs) to replace the current analogue control system kernel, underwent preliminary field tests on TCV in the short experimental campaign at the beginning of 2007. Successful plasma operation was achieved with the DSP set inserted in the logic flow of the current system and programmed to act as a simple PID controller. The APCS was fine-tuned in Portugal during 2007 and is expected to be fully compliant and ready for final integration by January 2008. New digital waveform generators, enhancing the time resolution for plasma control by up to a factor of 20, were successfully installed at

the same time and are now in routine use. This integration comprises the optimisation of the wave loading procedure, the interface with the TCV plant control and a fast automatic calibration procedure.

3.5 Heating Systems

3.5.1 X2 heating system

The full X2 system (2.7MW in the plasma) was operational at the start of campaigns in January and operated successfully until the end of operations. All 6 launcher angles were measured and cross-checked during the opening, as was the diagnostic launcher. The latter had undergone an in-situ laser calibration in 2006 and had never been verified using the standard method (requiring a worker in the torus). The laser calibration was found to be correct.

3.5.2 X3 heating system

X3 System-gyrotrons

The gyrotron with the broken cryogenically cooled sapphire window has been repaired by THALES and delivered to CRPP equipped with a CVD diamond window. The onsite acceptance tests took place during the summer 2007 and all the guaranteed specifications were met. With the CVD diamond window, the rf power is no more limited by the window and tests at rf power higher than 500kW have been carried out. As shown in Fig. 3.5.1, a maximum power level of 560kW has been measured in the rf load over a pulse length of 2s.

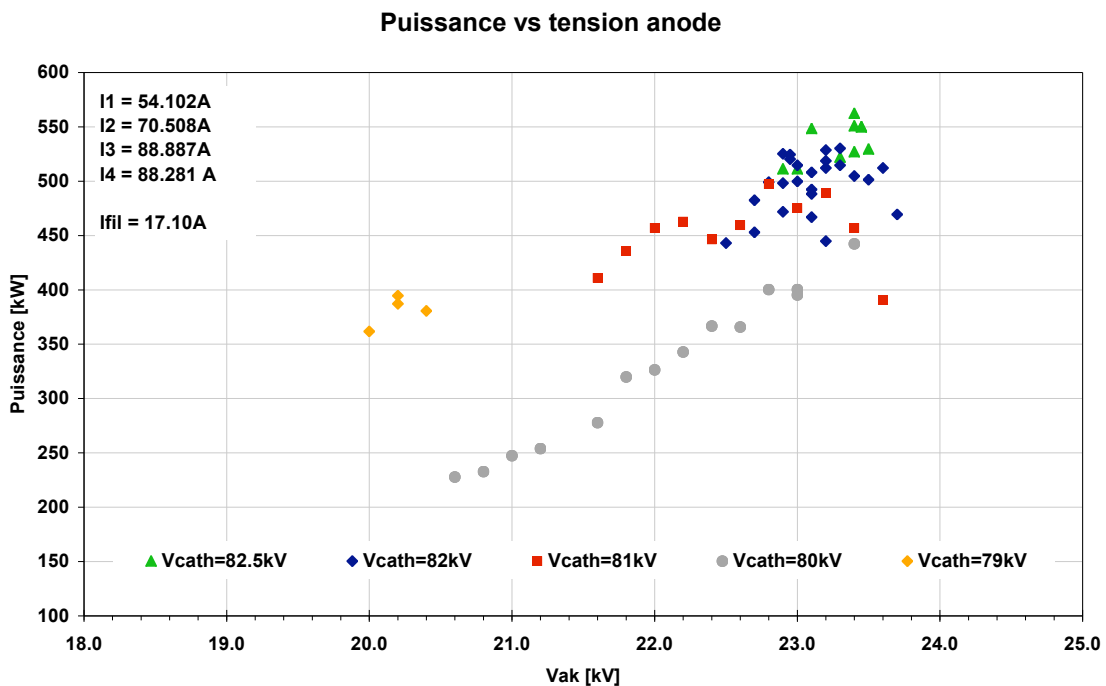


Fig. 3.5.1 RF power measured in the rf load versus anode voltage (V_{ak}) for different cathode voltages (V_{cath}). The rf pulse length is 2s.

Compared to the gyrotron with a cryogenically cooled window a power increase of approximately 20% has been obtained. Mainly based on financial arguments, this rf power increase does not justify the replacement of the cryogenically cooled window on the two other gyrotrons. The three X3 gyrotrons will be fully operational in the next experimental campaign.

X3 System-launcher

During the TCV opening, the top-launch system has been dismantled and the motorization of the top-launch mirror has been upgraded in order to improve its reliability.

3.6 TORPEX technical developments and diagnostic upgrades

3.6.1 New Magnetron

A magnetron with maximum output of 1200W (on loan from CNR-Milano) has been installed on TORPEX, as shown in Fig 3.6.1a, and is now routinely operating. This magnetron can inject very low power (<200W) with high stability of the source and can be operated in CW mode, thus allowing exploring regimes previously inaccessible with the original magnetron. The control of the new magnetron has been developed and is now fully integrated into the TORPEX discharge cycle.



Fig. 3.6.1 (a) The newly installed low power magnetron. (b) Faraday cage for the LIF system.

3.6.2 LIF

In view of the operation of the Laser Induced Fluorescence (LIF) diagnostics, a Faraday cage has been assembled in the TORPEX hall. This cage is used as an

optical laboratory, Fig. 3.6.1b, and is enclosing an optical bench, an Argon pump laser, and a dye ring cavity laser. To comply with EPFL safety rules, we still need to install all the necessary interlocks required when a class 4 and class 3B lasers are used. In addition, we need to align the dye cavity as well as the electronics that control the laser. Once this alignment will be successfully performed, the detection parts, which are ready to be installed, will be mounted on TORPEX.

3.6.3 Double Gridded Energy Analyzer for fast ion detection

For the fast ion physics studies on TORPEX, a double gridded energy analyzer was constructed in year 2006. During 2007, the detector (see Fig. 3.6.2) was installed and first measurements were done with a simplified version of the dedicated electronics. These preliminary experiments showed good signal-to-noise ratio, although an asymmetry of the measured amplitudes has been revealed between the two halves of the detector, and a strong dependence of the signal amplitude upon the angle between detector and magnetic field was found. Several additional upgrades of detector were performed to increase the signal to noise ratio and to decrease the asymmetry. Among those, the new dedicated electronic has been installed as close as possible to the detector. This new configuration is presently under test.

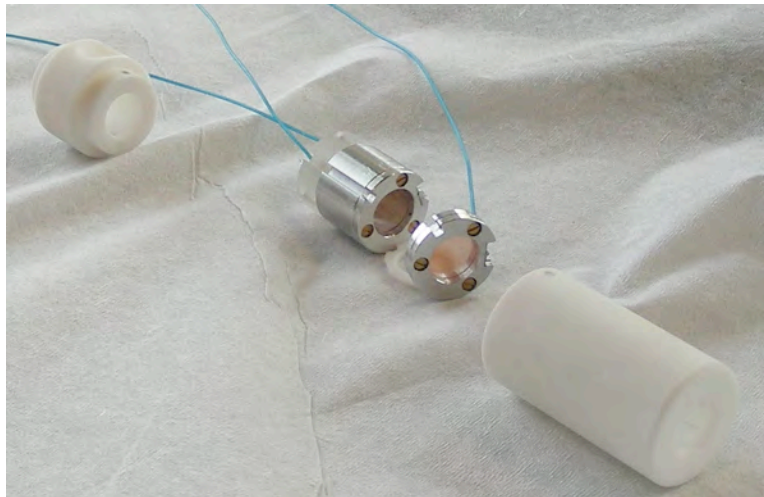


Fig. 3.6.2 *The double gridded energy analyzer for fast ion physics studies on TORPEX.*

3.6.4 Fast Camera

The Photron Ultima APS-RX framing camera, acquired last year, has been fully tested and integrated into the TORPEX cycle. This is done through a client-server technology which is based on the MDS+ database and TCL command language. To reduce the noise associated with the power network an isolation transformer is now used to power the camera. A cooling system has been built to avoid overheating of the camera after prolonged use. These have considerably increased the signal-to-noise ratio and also extended up to few hours the camera running period. Preliminary tests of the fast framing camera have been performed using different geometrical arrangements, including views which are radial and tangential to the toroidal direction of the device. First attempts to interpret the images using spectral analysis techniques have been done to extract information on the plasma dynamics and compare it with that from other diagnostics.

3.6.5 Ohmic system

A detailed study of the magnetic configuration for the Ohmic scenario in TORPEX has been conducted to improve the stability of the plasma during the Ohmic phase. A new configuration for the vertical and Ohmic systems has been found that may provide increased stability. A stack of five coils, identical to those used for the TORPEX toroidal field system, have been assembled to implement the new configuration, which is presently being tested.

3.6.6 Acquisition system

A new D-TAQ 196 PCI, which provides 96 channels for acquisition up to 250kHz, has been installed and is now available for routine operation.

3.7 Superconductivity

After the maintenance work in December 2006, re-cooling and operation of SULTAN started mid January 2007 and continued without major interruptions till next yearly maintenance in November 2007. The number of technical failures was smaller than past years, with fewer than 10 days of either shut-down or stand-by for the facility:

An upgrade of the data acquisition system (DAQ), planned in 2006, was implemented in early 2007. From January to April, both, old and new DAQ were operated in parallel. The main characteristics of the systems are gathered in Table 3.7.1

	Existing DAQ system	New DAQ system
DAQ computer	Vintage 2002 PC with PCI slots; located in SULTAN hall and controlled via a (blurry) screen-and-keyboard extender	Modern PSI PC located in the SULTAN hall and accessed via Remote Desktop from the SULTAN Control Room
DAQ programming language	Intelligent Instrumentation's Visual Designer, (not available and supported any more)	National Instrument's LabVIEW 8.0
DAQ hardware	Burr Brown PCI-20098C multifunction board (not supported any more)	CompactDAQ chassis with four 32-channel analog input modules.
Interface to computer	PCI slots	USB 2.0
Analog input resolution	12 bit	16 bit
Number of analog. input channels	80 single ended	128 single ended, extendable to 256
Max. analog input sample rate	1.25 ksamples per s and channel with 80 channels used	7.7 ksamples/sec with 128 channels used
Analog input range	Selectable with plugged 5B modules	±200mV, ±1V, ±5, ±10V software selectable

Table 3.7.1 Comparison of the existing and the new SULTAN DAQ systems

3.7.2 Commissioning of the new 15 T solenoid for small size experiments

The steadily increasing performance of Nb₃Sn superconducting wires required an upgrade of the wire test station at CRPP from a 12T to a 15T magnet to keep the capability of measuring the wire critical current at technically relevant conditions. Oxford Instruments designed and built the 15T superconducting solenoid and delivered it with auxiliary components in December 2006. Because the solenoid creates a substantial stray field and its support system in the cryostat is sensitive to lateral forces acting on the coil, ferromagnetic materials must not be closer than 1.8m from the coil's centre. This constraint required the construction of a new wooden platform raising the magnet above the metallic second floor in the SULTAN hall. In addition the steel floor panels had to be replaced by stainless steel ones; aluminium panels were not acceptable because of the strong eddy currents induced in these in case of a magnet quench.

With 103.4A the 70 Henry solenoid produces a magnetic field of 15T in a cold aperture of 80mm. To automate the test procedure and ramp the magnet with the highest permitted rate a new computer controlled power supply was installed, which delivers the required voltage and correctly manages the response to a quench. The time between required helium refills of the new cryostat in standby mode has increased from 2.5 to 3.5–4 days, thanks to the use of advanced cryo-superinsulation, which even supersedes the liquid nitrogen shield.

After some minor adaptations to accommodate CRPP's existing probes and sample holders, the 15T was successfully commissioned in April 2007 with measuring critical currents of ITER strands. Since then it has worked with high reliability and no quench. Fig. 3.7.1 shows a picture of the new 15T test station.

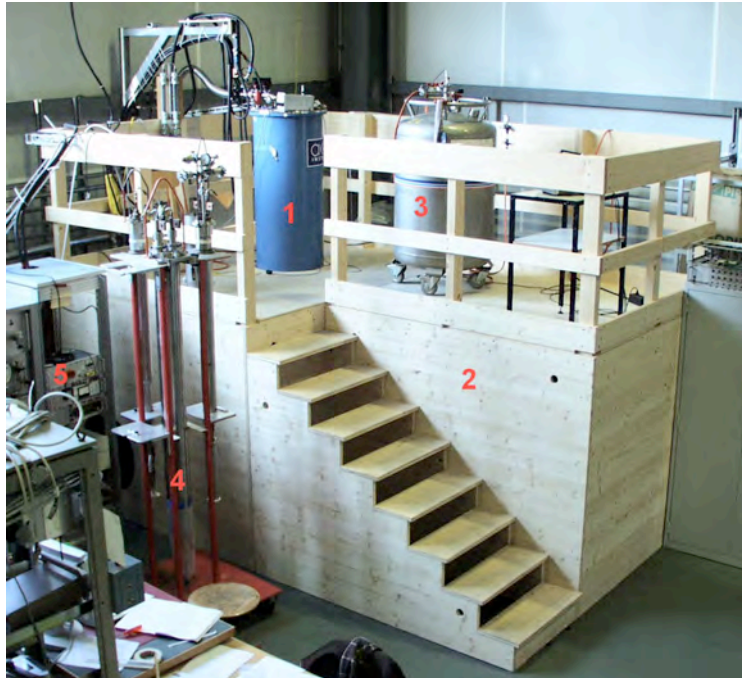


Fig. 3.7.1 The new 15T test station. 1: Cryostat with Nb₃Sn 15T solenoid. 2: Wooden support structure to permit convenient access for sample insertion. 3: He storage Dewar. 4: Rack with CRPP sample holders. 5: 19-inch rack with voltage amplifiers, a sample current source, a temperature controller etc.

3.8 ITER 170GHz gyrotron and its test facility

For the electron cyclotron wave system of ITER the European Party plans to deliver 2MW cw 170GHz sources. Compared with the reference design of ITER based on 1MW sources, a higher power source (2MW) allows a lower system cost. During 2007, CRPP members participated regularly in meetings with EFDA and other participating Associations (FZK, Karlsruhe, Germany, CNR, Milano, Italy) as well as the contract follow-up concerning all elements of the project.

The gyrotron prototype was delivered in December 2006. Initial tests of the gyrotron tube, not necessitating the presence of a magnetic field were successfully carried out in 2007.

The superconducting magnet delivery suffered from a significant delay and occurred in November 2007 only.

The contracts placed between EFDA and CRPP:

- a) for the operation of the ITER gyrotron test facility and
- b) for the scientific coordination of the experimental program on the prototype tube.

were extended in order to account for the delay in the program.

In order to optimize the chances of Europe to successfully deliver 8MW of ECH power to ITER, the preliminary design of a 1MW/170/CW tube is being considered as back-up solution.

3.8.1 Gyrotron components

Gyrotron first prototype and Superconducting 7T magnet

CRPP is the leading Association, responsible for the contract follow-up, as well as the organization of the regular bimonthly progress meetings. and will host the tests of the tube. The target performances of the first prototype are 2MW/1s, although the system, and in particular the cooling, has been designed to be compatible with CW operation.

The first prototype of the 170GHz/2MW/CW was delivered in December 2006. Since the Superconducting Magnet was delayed, the only tests that could be performed before November 2007 were related to the tube integrity, its voltage stand-off properties, and its capability to emit an electron beam.

Although not fulfilling the specifications, particularly in terms of Liquid Helium consumption, The Superconducting Magnet has been temporarily accepted, and delivered to CRPP in November 2007. The underlying idea is to be able to perform as many tests as possible with the gyrotron tube, then to send the SCM back to the supplier to correct for the non-conformities.

After a 9 month testing phase, it is foreseen to inspect carefully the first prototype, and to refurbish it to allow for an update of some of its critical internal components such as the mode converter. An initial version of those technical specifications has been written.



Fig. 3.8.1 *Picture of the 170GHz/2MW first prototype installed in the magnet after delivery to CRPP.*

3.8.2 C-GT170 test facility

Figure 3.8.1 shows the first prototype gyrotron tube and the Superconducting magnet installed in the C-GT170 test facility.

Due to a delay in the Main High Voltage Power Supply (MHVPS) delivery, an existing CRPP HV power supply (RHVPS) used on the electron cyclotron heating for TCV is being shared with the C-GT170 test facility during the first prototype tests.

Power supplies

The Body Power Supply (BPS) was delivered and commissioned in Oct. 2006.

During 2007 the work on the other power supply, the MHVPS, has continued. CRPP is following the contract through several progress meetings at OCEM premises. The delivery of the MHVPS is foreseen in May 2008.

Short Pulse load

The short pulse (<100ms) load (SPL), manufactured by CNR, has been delivered and is ready for use. A picture of the load with the associated vacuum pumping system is shown below.

A long-pulse (CW) load (CWL) is under manufacture at CNR Milano (Italy) and will be delivered in 2008.

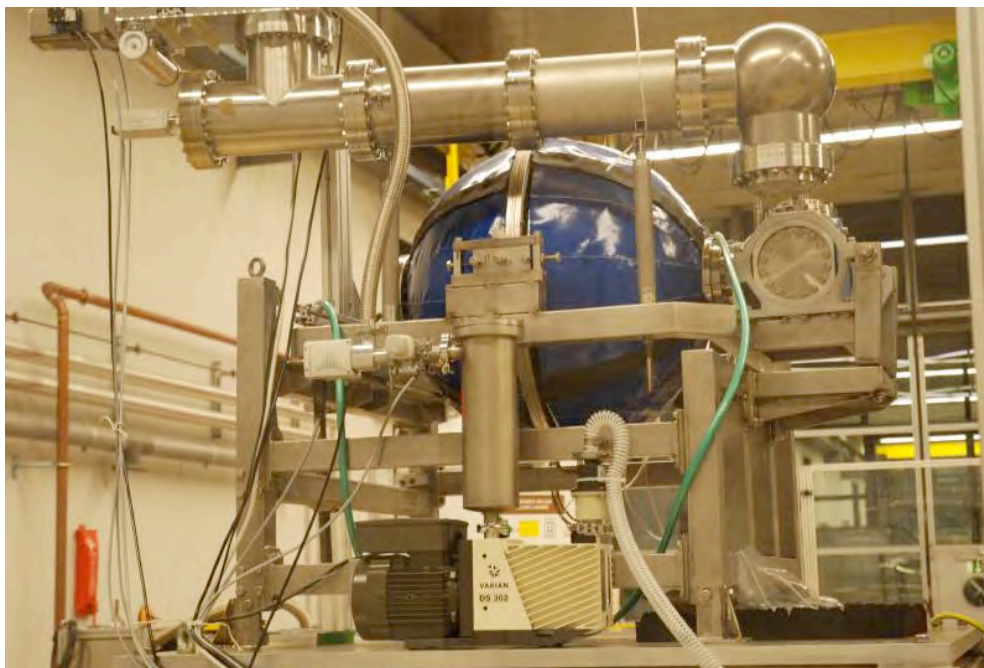


Fig. 3.8.2 Picture of the 170GHz/2MW short pulse load (SPL)

RF box

A 2x2x3m³ metallic box, to host a target and an infrared camera to measure the gyrotron radiation profile, has been built at CRPP and is nearly ready for use.

3.9 Gyrotron for Dynamic Nuclear Polarization Enhanced Magic Angle Spinning Nuclear Magnetic Resonance

The primary interest of Nuclear Magnetic Resonance (NMR) is that it probes specific atomic sites at energies far smaller than the mean molecular energies at room temperature, so the probed system remains unperturbed. The downside of these weak nuclear spin excitations is the poor sensitivity of NMR. Large signal enhancements were demonstrated by transferring the larger polarization of electron spins to nuclear spins before the NMR experiments, via Dynamics Nuclear Polarisation (DNP. Enhanced magic angle spinning (MAS) solid-state NMR experiment (DNP MAS-NMR) requires the application of a continuous microwave field at the electron resonance frequency and cryogenic temperatures to attenuate spin-lattice relaxation processes that might otherwise compete with the polarisation transfer.

For DNP MAS-NMR, since the very large gas flow required by low temperature MAS make it impossible to form a resonator around the sample, this in situ enhancement must rely on the use of relatively powerful microwave sources. The frequencies needed to operate DNP-MAS NMR in high field spectrometers are in the range of hundreds of GHz. Hence gyrotrons are the source of choice.

The recent impressive progress in this field of research¹ has motivated different groups (ISIC-EPFL, LRMB-EPFL) within EPFL to investigate the possibility to use the DNP technique on the numerous NMR spectrometers existing at EPFL. Since gyrotrons are a key element for DNP, CRPP has been contacted to evaluate the possibility of develop such a gyrotron for this application.

Thanks to a special fund of the Faculty of Basic Sciences of EPFL a design of a modular low-power (10-50W) high-frequency gyrotron (200-530GHz) for DNP-enhanced MAS-NMR spectroscopy has been carried out at CRPP since October this year. For covering this wide range of frequencies, a 9.5T helium-free superconducting magnet (SCM) with a warm bore diameter of 75mm is planned. Considering the wide frequency range, the SCM field level is compatible with operation of the gyrotron at both the fundamental or second harmonic of the electron cyclotron frequency. The gyrotron design is based on a triode electron gun ($V_k=15\text{kV}$, $I_b=100\text{mA}$, $V_a= \pm 5\text{kV}$) which is very flexible for adapting the electron beam properties to a wide variety of cavities operating at the fundamental or at the second harmonic. The gyrotron is designed for an axial output and a quasi-optical mode-converter to a Gaussian mode will be placed after the gyrotron window.

The reference parameters for the first application of DNP-enhanced NMR spectroscopy on a 400MHz (1H) spectrometer are: frequency = 263.5GHz, frequency tunability = 0.12%, rf-power = 10-50W. The modularity of the gyrotron refers to the possibility to change only some elements like the cavity-uptaper system to be adapted to the wide range of NMR spectrometers existing at EPFL. An assembly drawing of the designed system is shown in Fig. 3.9.1. Starting from this design, funding requests to develop and integrate such a system on an NMR spectrometer are being to the Swiss Science National Foundation (Requip and Sinergia). This new line of research has been carried out within the frame of the Swiss DNP Initiative (<http://ipn2.epfl.ch/LPMN/sdnpi/index.htm>) and is an activity outside the EURATOM Association.

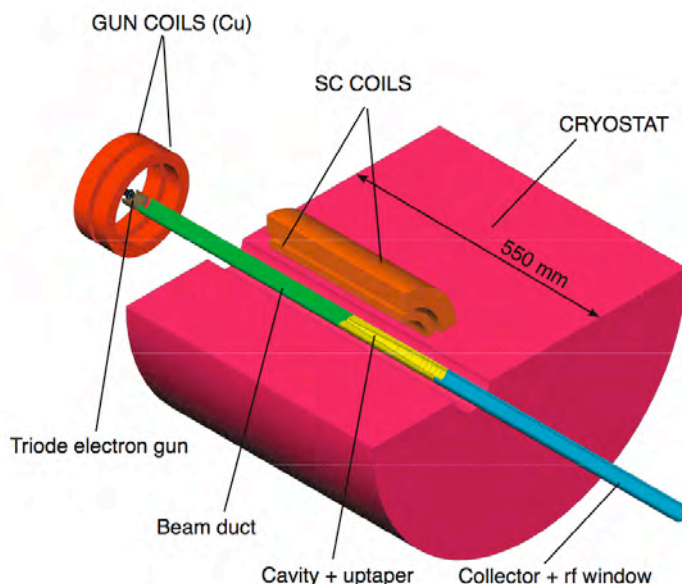


Fig. 3.9.1 Layout of the designed gyrotron system for DNP MAS-NMR spectroscopy.

4 INTERNATIONAL AND NATIONAL COLLABORATIONS

4.1 *Exploitation of the JET facilities*

4.1.1 *Control of MHD instabilities*

A successful experiment related to the physics of neoclassical tearing modes (NTMs) and of the sawtooth instability was co-led by CRPP personnel within Task Force M in the C18 campaign in 2007. This experiment resulted in the first demonstration of the effectiveness of ion cyclotron current drive (ICCD) in preventing $m=3$, $n=2$ NTMs by destabilising sawteeth in the presence of a strong fast-ion component and at β_{pol} well above marginal stability, i.e. at values at which NTMs are routinely triggered under identical conditions without ICCD. Long sawteeth are known to provide seed islands for NTMs, which can then become unstable at lower β and have the potential to significantly reduce the fusion performance in a reactor. The suprathreshold ions, which emulate the effect of α -particles in a reactor, were generated by ICRF applied in the plasma core. The experiment thus required the concomitant use of two different ICRF frequencies and antenna phasings. At $\beta_N=1.25-1.35$, the sawtooth period was kept consistently shorter than 200ms by the application of 3MW ICCD, whereas the control cases without ICCD exhibited durations in the range 500-900ms, resulting in NTMs in some instances (see Fig. 4.1.1). Crucially, this study has revealed the extreme sensitivity of the kink destabilisation effect to the location of the ICCD resonance: an accuracy of better than $\sim 0.5\%$ in the ICCD frequency is required for effective and reliable NTM prevention (see Fig. 4.1.2). This indicates that some form of feedback control of the frequency would be highly desirable in the eventual application of this technique in a fusion reactor.

4.1.2 *JET, S1 support for NTM avoidance*

ELMy H-modes discharges at high current and plasma shaping in JET usually suffer from the presence of Neoclassical tearing modes. These modes are usually triggered at a sawtooth crash which occurs after a long sawtooth period during the transition from L to H-mode. In this transient evolution, the current profile changes such as to stabilize the sawteeth and sawtooth periods in excess of 0.5s can be observed. Several specific discharges have demonstrated that by reducing the plasma shaping, increasing the q_{95} value or reducing the plasma density at the L-H transition are all beneficial for inhibiting these long sawtooth periods and hence the triggering of NTMs. If NTMs are avoided during the L-H transition, they are usually not triggered during the stationary flat top. It has also been shown that by adding LHCD or ICRH before the L-H transition, one can keep regular sawteeth during the transition and avoid NTMs

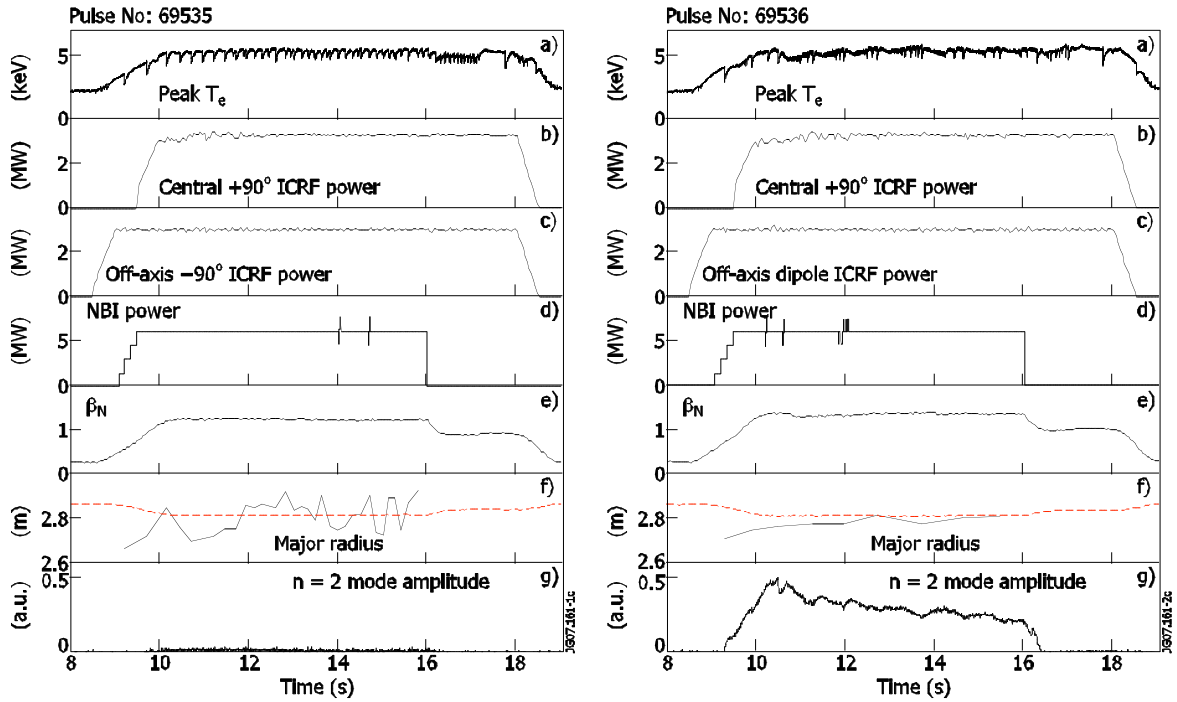


Fig. 4.1.1 JET discharges 69535 (left) and 69536 (right): (a) peak electron temperature; (b) ICRF power at 42.2MHz; (c) ICRF power at 46.2MHz; (d) NBI power; (e) normalised beta; (f) midplane major radius of sawtooth inversion (solid) and 46.2MHz ICRF resonance (dashed); (g) $n=2$ MHD mode amplitude. The average sawtooth period in the combined ICRF/NBI phase is 180ms in shot 69535 and 700-800ms in shot 69536. An $m=3, n=2$ NTM is destabilised early in shot 69536.

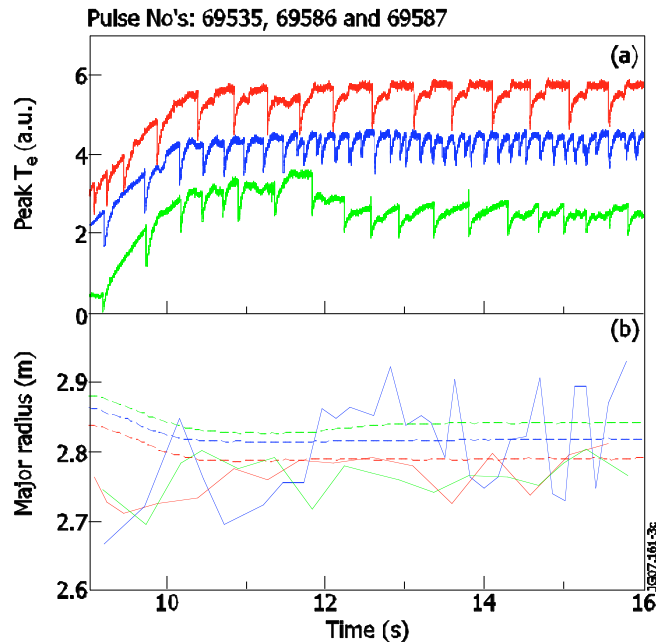


Fig. 4.1.2 JET discharges 69535 ($B_T=2.83T$, blue), 69586 ($B_T=2.85T$, green) and 69587 ($B_T=2.81T$, red): (a) peak electron temperature (keV with shifted offsets for clarity); (b) midplane major radius of sawtooth inversion (solid) and 46.2MHz ICRF resonance (dashed). The average sawtooth period in the combined ICRF/NBI phase is 180ms in shot 69535, 410ms in 69586 and 470ms in 69587.

4.1.3 Particle transport

JET H-mode experiments performed during the C15-C19 campaigns were analyzed and a database for density peaking study was established. Two independent density profile measurements were used, provided by LIDAR Thomson scattering for one and by the Far Infrared Interferometer, inverted using a regularized Abel inversion algorithm. The good agreement between two diagnostics allows us to be fully confident in the experimental results.

On the basis of the 2006-2007 experimental database, scaling laws for the density peaking factor were derived. The general results from the previous studies were confirmed. The effective collisionality is the main factor which determines the shape of density profile in H-mode, the neutral beam particle source being of secondary importance. At low collisionality an effect of the internal inductance l_1 has been identified. From this work, the peaking factor for the ITER baseline H-mode plasma scenario is expected to be $n_0/\langle n \rangle \sim 1.5$, consistently with earlier extrapolations. A vast effort to interpret this behaviour using GS2 gyrokinetic calculations in the quasilinear approximation is under way.

4.1.4 Collaboration on Alfvén waves and fast particles studies

The study of Alfvén waves and their interaction with fast particles is an important topic in the JET programme. During 2007, JET has been in operation until early April, with the second part of the year devoted to a shutdown during which, between other activities, the second set of TAE antennas (built by CRPP and delivered to JET at the end of March 2005) as been installed. Our activities have mainly focused on the operation of the new Alfvén Eigenmodes Diagnostic system (KC1T), designed and built by CRPP, and on installation and preparation work for the re-commissioning of the system in 2008.

In 2005, CRPP completed the manufacturing and the testing of the two new AE antenna frames and of the related control and protection electronics, which were delivered to the JET facilities on schedule. However, due to delays in the procurement of the feedthroughs (not CRPP responsibility), only one antenna frame could be installed during the 2005 shutdown, with the in-vessel installation completed successfully on June 2005 by the JET remote handling group. This was then followed by the installation of the ex-vessel hardware, completed by the end of September 2005. The second antenna frame and the associated ex-vessel hardware were installed in-vessel in early October 2007.

Following the completion of the technical commissioning of the new KC1T diagnostic system, which started in November 2005, the system has been in routine operation during the 2007 experimental campaigns, during which it was operated, and collected data, on about 80% of the JET discharges.

Furthermore, we have also contributed to the analysis of the data obtained with a new fast digitiser system (KC1M), with particular focus towards the measurements of the mode amplitude and radial eigenfunction combining external magnetics and internal (core-localised) X-mode reflectometry data.

The following sections present the main results of these activities, followed by a list of publications.

Further collaborations outside JET.

Part of the work reported here on the installation of the ex-vessel hardware for the new AE antennas has been performed in collaboration with staff from MIT-PSFC.

Operation of the new AE diagnostic system – KC1T.

The previous antenna geometry limited the active AE excitation to low toroidal mode numbers, $n=0\div 2$, whereas intermediate or high toroidal mode numbers characterise the most unstable AEs, which are already detected in JET and are similarly predicted for ITER. Hence, a direct excitation and tracking of the same modes is of clear interest for preparing the next step experiment. To this end, two antenna structures optimised for the excitation and detection of AEs with $n\approx 10-15$ were designed and built by CRPP: one was installed in-vessel during the 2005 JET shutdown, and the second set in October 2007, Fig. 4.1.3

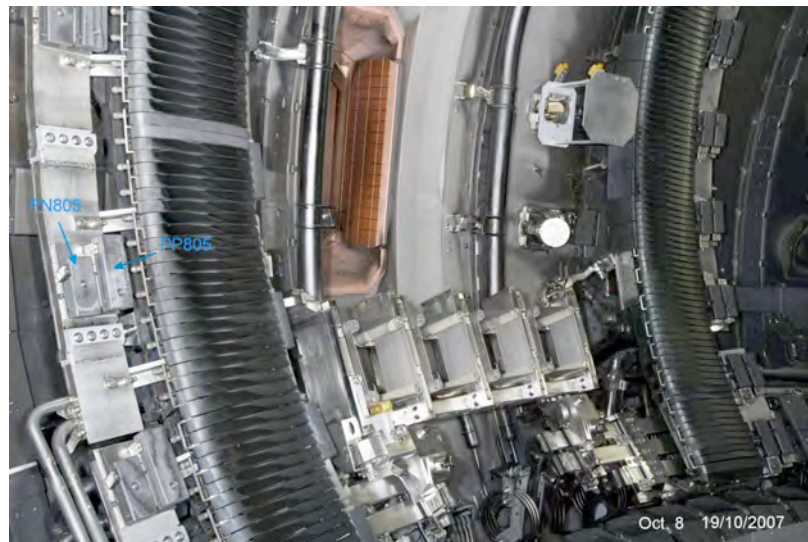


Fig. 4.1.3 *in-vessel view of the TAE antenna structure installed in octant 8, October 2007.*

Following the technical commissioning of the antenna system (KC1T diagnostics), completed towards the end of January 2007, the new antenna system has been in routine operation throughout the 2007 JET experimental campaigns. Damping rate data were obtained for about 1200 discharges, with real-time tracking of the driven plasma resonance on about a third of these, covering all the different JET operating regimes. Figure 4.1.4 shows the excitation spectra obtained for two different antenna phasing configurations, driving both low- n and high- n modes. The n -spectrum that can be excited in the plasma by the new antennas extends easily up to $n\sim 30$ also in an X-point configuration. Real-time mode tracking has been routinely obtained for all antenna excitation configurations for a variety of plasma regimes (in limiter and X-point edge shape), up to moderate heating power ($P_{\text{NBI}} < 6\text{MW}$). At higher P_{NBI} , background broadband turbulence dominates the synchronously detected signal.

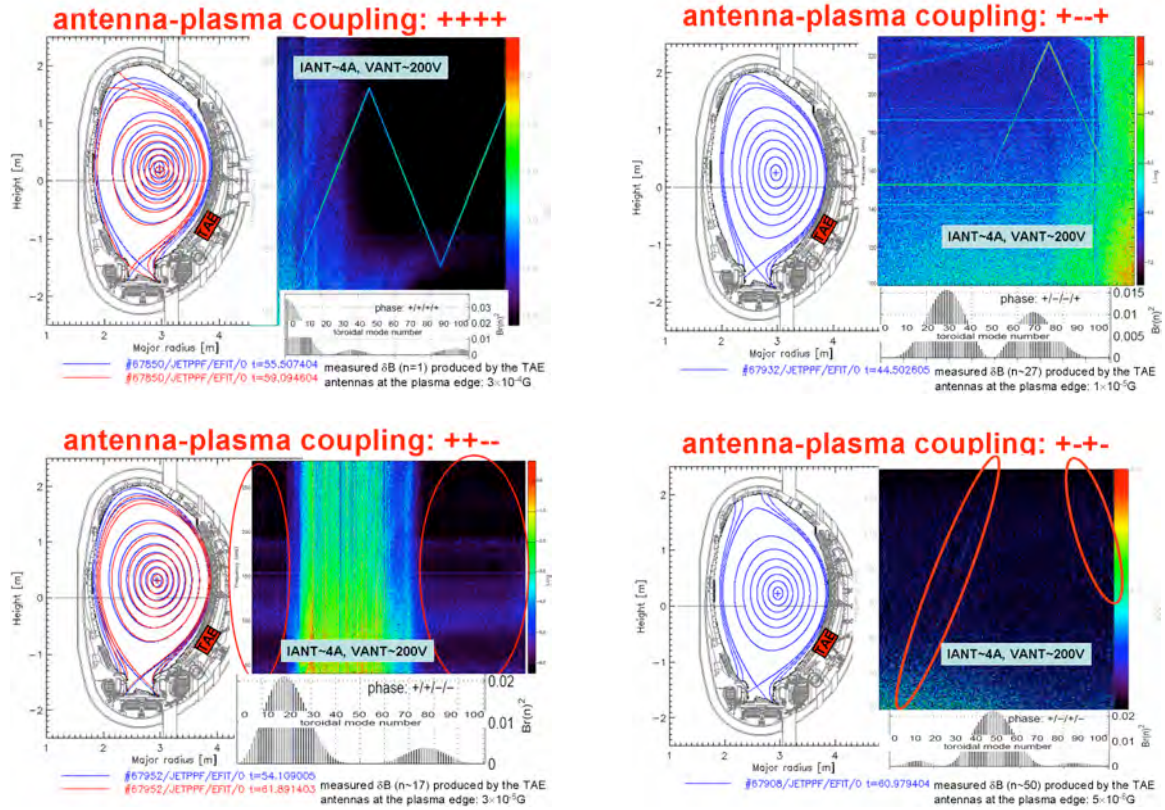


Fig. 4.1.4 Nominal vacuum and plasma excitation spectra using different antenna phasing configurations. A value of $\delta B \sim 3 \times 10^{-4} G$ is obtained for the ++++ excitation structure (low-n), whereas $\delta B \sim 1 \times 10^{-5} G$ is obtained for the +--+ excitation structure (nominal n-spectrum centred around $n \sim 25$ with HFWM ~ 10 at the antenna mouth).

First Qualitative Experimental Results for Low- to High-n AEs

We present here three examples of the first qualitative measurements of the damping rate for low- and medium- to high-n AEs with the new antennas: the n-number spectrum is inferred tentatively from the vacuum antenna excitation spectrum and allowing for an exponential decay of the driven spectrum towards the LCFS (tunnelling effect in vacuum).

As an essential verification of the data obtained with the new antennas, Fig. 4.1.5 shows that, for ohmic plasmas with low edge elongation $\kappa_{95} \sim 1.3$, the damping rate of low-n ($n \sim 1-3$) TAEs, as measured with the new antennas (excitation spectrum +++) is essentially identical to that measured with the old saddle coils. On the other hand, two general difficulties arise when using excitation spectra that drive a higher n-spectrum ($n \sim 5-20$): the first is related to the much lower antenna-driven $\delta B \sim 1 \times 10^{-5} G$ (compared to $\delta B \sim 3 \times 10^{-4} G$ for $n \sim 1-3$) achieved at the LCFS, and the second to the accurate determination of the resonant n-spectrum driven in the plasma for a broadband antenna excitation spectrum Fig. 4.1.6. These difficulties were also experienced in C-mod using similar sized antennas.

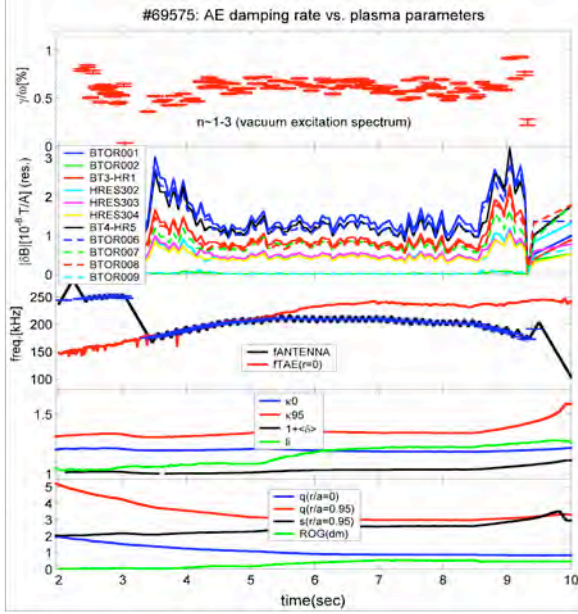


Fig. 4.1.5 Damping rate measurements for $n\sim 1-3$ TAEs in ohmic plasmas with low edge elongation.

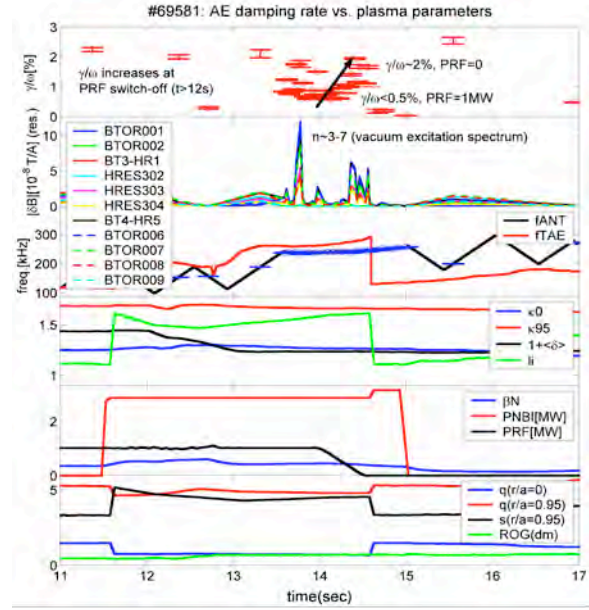


Fig. 4.1.6 Damping rate data for $n\sim 3-7$ TAEs at P_{RF} switch-off for constant plasma parameters and P_{NBI} .

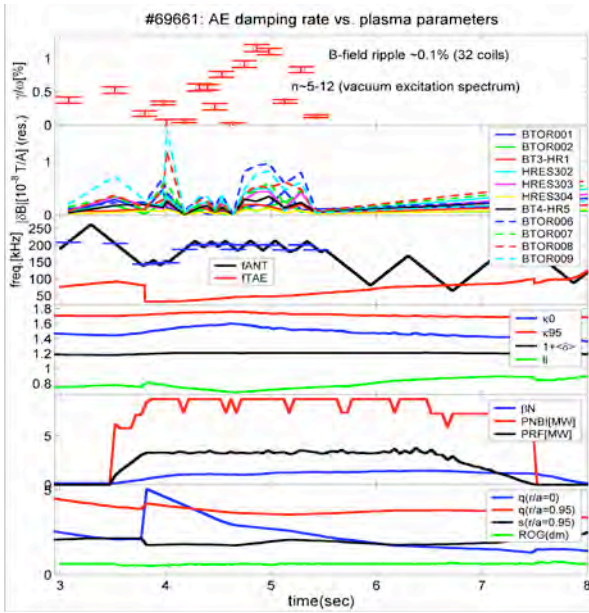
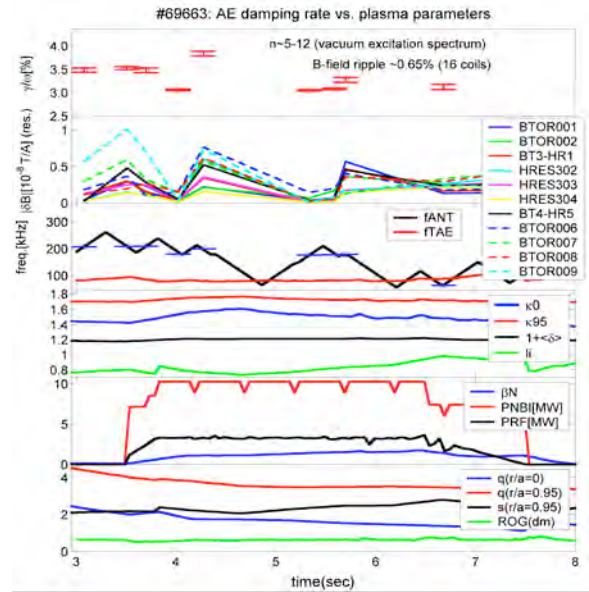


Fig. 4.1.7 Damping rate measurements for $n\sim 5-12$ TAEs as function of the B-field ripple in the presence of resonant NBI ions, $v_{||NBI}\sim v_A/3$: γ/ω increases from $\gamma/\omega=0.7\%$ without ripple to $\gamma/\omega\sim 3.5\%$ for 0.65% ripple.



Given the large bandwidth of the antenna excitation spectrum, it is difficult to separate the different harmonics and evaluate the frequency, mode number and damping for each one. This is further complicated by the limited number of (unevenly distributed) pick-up coils available to cover the toroidal cross-section, and by the fact that no internal measurements of the excited AE spectra have been so far routinely available. Various numerical tools are being assessed to resolve the uncertainty in the n -number determination. So far, the most promising method seems that to combine the vacuum antenna excitation spectrum with the numerical

tools provided by the "SparSpec" code [3]. This code has been previously used for the analysis of astrophysical data and is now being adapted for routine use on JET data. As example of the data obtained for medium-n modes, Fig. 4.1.6 shows that the damping rate γ/ω of $n\sim 3-7$ TAEs increases linearly with P_{RF} at the ICRF power switch-off for constant plasma parameters and P_{NBI} . As shown in Fig. 4.1.7, when the fast ion drive is provided by resonant NBI ions with $v_{||NBI}\sim v_A/3$, the damping rate of $n\sim 5-15$ TAEs increases to $\gamma/\omega\sim 3\%$ in the presence of a $\sim 0.65\%$ ripple in the toroidal magnetic field, compared to $\gamma/\omega\sim 1\%$ without B-field ripple.

4.2 ITER

TW5-TPO-CODAC: This task was originally foreseen to end in 2006, but was extended once to end March 2007 and then again to end July 2007. At this time CRPP refused to extend this essentially voluntary contribution (40% Euratom, 60% Swiss). The ITER team was unable to replace the CRPP staff member by 31 July 2007 and a direct contract was established from 1 September 2007 for a maximum of 6 months. This contract places the staff member ex-association for 75% of his activity. The result of the EFDA Task was presented to a CODAC Conceptual Design Review 12-14 November 2007, and it was generally approved. The missing items in the design were management issues (budget and resource loaded planning) which were outside the scope of the original Task and could not be launched without resources.

The EFDA Task final report is in the process of being submitted.

TW6-TPHE-ECHULB2: Two year contract for the design and testing of the mm-wave system of the ITER upper launcher. In addition, support of the physics analysis associated with NTM stabilization and other ECCD applications.

TW6-TPHE-ITERDREC: Four month contract (expired Oct. 2007) for investigating critical issues identified during the ITER design review that were associated with the EC transmission line and launchers.

TW6-TPHE-ECHVPS: Four month contract (expired Oct. 2007) for investigating critical issues identified during the ITER design review that were associated with the EC gyrotrons and their associated power supplies.

TW6-THHE-TFO1: One year contract (expired 15.9.07, but extended to 30.04.08 due to late delivery of equipment) to operate the gyrotron test facility and perform the investigations on the first EU ITER gyrotron.

TW6-THHE-CCGT1: One year contract (expired 15.9.07, but extended to 31.08.08 due to late delivery of equipment) to coordinate the scientific investigation and reporting of the coaxial cavity 2MW 170GHz EU ITER gyrotron.

TW5-TPDS-DIASUP, TW6-TPDS-DIADES, TW6-TPDS-DIADEV : These three EFDA tasks contribute to the development of the ITER magnetics diagnostics, for which CRPP collaborates with RFX, CIEMAT and CEA Cadarache. Activity in 2007 was significantly reduced with the departure to ITER of the key engineer involved and will gain momentum early in 2008.

4.2.1 Superconductivity

TW5-TMSC-HTSPER. HTS materials for fusion magnets.

TW5-TMSC-HTSMAG. Scoping study of HTS fusion magnets.

TW4-TDS-CLDES. Final design of HTS current leads for ITER.
TW6-TMSC-FSTEST. Participation to conductor tests and evaluation of test results.
TW6-TMSC-ASTSPH. ITER thermosyphon effect and CSMC analysis.
TW6-TMSC-TFPRO. ITER TF prototype conductor sample manufacture.
TW6-TMSC-LTPSAM. Long Twist Pitch Sultan Sample Manufacture and Solder Filling of Joints
TW5-TMSC-NEFSS. TF conductor qualification.
TW6-TMSC-PITSAM. Manufacturing of Subsize Cable-in-Conduit Conductors.
TW6-TPO-ACCOMP. Computation of AC Losses Associated with Plasma Control in ITER Magnets.
TW6-TMSP-PFWDES1. Review of PF2-PF5 Winding Design
TW6-TMSC-SULTAN07. SULTAN operation and testing 2007.
TW5-TMS-EDFAC. European dipole facility.

4.3 Collaborations on other tokamak experiments

Collaboration with the FTU group (CNR-Milano, ENEA-Frascati) at Frascati started on the topic of MHD control via ECRH.

The aim of the first step in MHD control with ECRH is to develop a stationary MHD mode in ohmic FTU discharges, at an adequate amplitude, frequency and radial location, as a target for MHD control with ECRH. The possibility of using FTU elongation capability to reduce the mode amplitude was tested but came out too small to have a significant effect on mode amplitude. Based on TCV toroidal rotation measurements, the frequency of the mode in FTU was also found to grow with edge safety factor. Somewhat lower mode frequencies could be generated in hollow temperature profile discharges with important central radiation cooling. Thus, this study of mode rotation frequencies in FTU as a function of operational parameters provides a useful data set for mode stabilisation experiments with ECH/CD.

4.4 Plasma surface interactions in collaboration with the University of Basel

The growing interest about the use of rhodium (Rh) as a material for the first mirrors in ITER and the necessity of using it as a thin film deposited on a polished substrate has raised the necessity of the development of a robust deposition technique for the preparation of high-reflectivity mirrors. Preparation of Rh-coated mirrors by magnetron sputtering has been studied in Basel, and Rh layers with a thickness of 2 microns have been produced so far with a negligible amount of impurities in the layers. Different deposition conditions such as gas pressure, deposition rate and substrate temperature were investigated.

The films have a low roughness and their structure exhibit nanometric crystallites with a dense columnar structure. Amongst all investigated parameters, only the gas pressure during deposition was observed to have an influence on the optical properties of the film. Otherwise, the measured reflectivity is close to the reflectivity calculated from optical constants of pure rhodium. Storage of the samples in air did not affect the reflectivity. The first laboratory test of erosion by deuterium ions and also annealing cycles are promising in view of diagnostic mirror applications. It is also important to note that the layer survived under erosion conditions in real tokamak (TEXTOR), although the reflectivity was decreased after exposure in tokamak plasmas, further tokamak exposures are scheduled.

A robust method for the finishing of high quality mirrors was successfully tested at the University of Basel. Cleaning of the mirror surface by hydrogen glow discharge is now routinely applied before detailed optical characterisations for mirrors to be exposed in different tokamaks. The optimization of the mirror reflectivity by such technique is a prerequisite for a successful mirror test.

Such experiments are ongoing in the present project and a modified plasma chamber enables us *in-situ* monitoring of the mirror reflectivity during cleaning in deuterium RF plasma. A molybdenum mirror exposed in the deposition dominated area of TEXTOR was used for this test. Removal of the carbon layer is achieved by chemical erosion and enhanced by increasing the surface temperature. However, for all the conditions investigated, no complete recovery of the reflectivity was achieved. The reason for that seems to be the presence of molybdenum carbide at the interface between the molybdenum substrate and the carbon film. Such carbide can not be removed by chemical sputtering only and an increase of the ion energy to values higher than the physical sputtering threshold would be necessary.

4.5 Socio-Economic Studies

Contract: TW5-TRE-NEWSO EFDA 05-1255

“Agenda for Social Science Research Related to Long-term Energy Options (ASRELEO)”, Energy Science Center (ESC), ETH Zurich

Long-term energy-environment issues (40 to 100 years hence) pose complex technical and societal problems as society and technologies develop over time. The inadequacy of technology introduction as a “technical” solution to these problems argues for a larger role for the social sciences. Non-technical aspects of energy systems have become highly relevant if not decisive in forging a sustainable energy future. Processes of technological innovation and institutional and societal decision making about energy futures are embedded within and shaped by a host of social, economic, and political factors. The need for greater engagement, reflection, and cooperation of the technical sciences with the wider social-science community was the driving force of the project ASRELEO. It aimed at defining the role and responsibility of the social sciences in long-term energy and technology research and at taking steps toward an energy-related research agenda in the social sciences. This presupposes that the social sciences speak for and explain themselves. Methodologically this goal was achieved through an extensive participatory process with two international workshops that served as important milestones. One workshop was attended by scientists from social-science energy research; the other brought together scientists and practitioners from research policy and research promotion. This allowed for an extensive overview of the diversity and significance of existing social-science energy research, as well as future challenges. There are good reasons why there cannot be *the* voice of social science. After all, the various disciplines and their approaches to problems are too diverse. Nonetheless, the goal remained to (1) clearly elaborate and (2) communicate the basic consensus on the role and significance, responsibility, ability and potential of the social sciences in long-term energy research, as well as the key topics as raw material for a research agenda.

Society faces a wide range of serious problems connected to the energy system and its foreseeable development. Main energy-related challenges are Security and Access, Climate Change and other Environmental Impacts, Economic and Social Development, Knowledge Management and Knowledge Integration across Boundaries. Social science is already active in long-term oriented energy research (*viz.*, in the area of defined energy challenges) and can point to significant

achievements. Among these are the various activities in transformation management. Nevertheless, the contribution of social science as a whole to long-term oriented energy research has fallen short of its true potential. The project compiled the building blocks of an agenda for social-science research on long-term energy options. The 27 project sketches outlined in the final report are meant to inspire the readers to formulate their own topics. It is not a "final" research agenda but extensive raw material for other topics and a tool for compiling research agendas. The report is therefore not only aimed at individual researchers but also at all the governmental and non-governmental bodies involved in research policy and promotion on all levels. Furthermore, there is a need for communication, embedding and community building: The basic consensus must be communicated competently and to the right audience if social sciences are to be repositioned and become securely embedded in long-term national and international energy research programmes and in research and teaching in universities and polytechnics.

Final report:

Flüeler, T., Goldblatt, D., Minsch, J., Spreng, D. (2007): Meeting global energy challenges: Towards an agenda for social-science research. Final report for EFDA and BP. Energy Science Center, ETH Zurich. Oct. 2007, Zurich.

4.6 Collaborations with other EURATOM Associations

P. Angelino, X. Garbet, Ph. Ghendrih, V. Grandgirard, G. Falchetto, Association EURATOM-CEA, France, "*Gyrokinetic global turbulence simulations*"

K. Avramidis, Association Euratom Hellenic Republic, Greece, "*Studies of high-power gyrotrons for ITER*"

J-F. Artaud, V. Basiuk, Association EURATOM-CEA, France, "*Coupling of the DINA-CH and CRONOS codes to simulate the ITER hybrid scenario*"

X. Bonnin, LIMHP, CNRS-UPR 1311, Université Paris, France, "*SOLPS5 (B2.5-Eirene) modelling of parallel scrape-offlayer flows in TCV*"

I. Chapman, UKAEA Fusion, UK, "*Sawtooth Stability with Fast Ions*"

A. dellaCorte, Association EURATOM-ENEA, Italy, **D. Ciazynski**, Association EURATOM-CEA, France, "*Participation to conductor test and evaluation of test results*" (TW6-TMSC-FSTEST).

L.-G. Eriksson, CEA Cadarache, France, "*Ion cyclotron current drive, heating, and sawteeth*"

O. E. Garcia, A. Nielsen, Association EURATOM-Risø National Laboratory, Roskilde, Denmark, "*Modelling and simulation of turbulence interchange dynamics in the TCV tokamak scrape-off layer*"

R. Heller, Association EURATOM-FzK, Germany, "*Final design of HTS current leads for ITER*" (TW4-TDS-CLDES)

M. Hirsch, IPP-Greifswald, **E. Holzhauer**, University of Stuttgart, Germany, "*Loan of two homodyne single-frequency reflectometers and participation in reflectometer measurements and analysis on TCV*"

J. Horacek, Association EURATOM/IPP.CR, Czech Academy of Sciences, Praha, Czech Republic, "*Electrostatic turbulence measurements in the TCV tokamak scrape-off layer*"

T. Johnson, Stockholm University, Sweden "*Ion cyclotron current drive, heating, and sawteeth*"

A. Koenies, V. Kornilov, A. Mishchenko, S. Sorge, IPP Greifswald, Germany, **A. Bottino, A. Peeters**, IPP Garching, Germany, **R. Hatzky**, Rechenzentrum MPG Garching, Germany "*Linear and nonlinear gyrokinetic code developments and simulations*"

A. Krämer-Flecken, Forschungszentrum Jülich, Germany, "*Fluctuation studies by reflectometry on the TCV and TEXTOR tokamaks*"

H.P. Laqua, IPP Greifswald, Germany **A. Mueck**, IPP Garching, Germany, "*Electron Bernstein Waves on TCV*"

E. Lazzaro, M. Lontano, G. Grosso, EURATOM-ENEA-CNR Association, Italy, "*Development of a linear plasma device for basic wave-particle interactions studies*"

M. Lewandowska, EURATOM-Poland Association, Un. Of Stectin, "*Hydraulic experiments and modeling of CICC*"

Y. Peysson, J. Decker, Association EURATOM-CEA, France, "*Quasilinear Fokker-Planck simulations and modelling of hard X-ray emission in TCV*"

V. Piffli, IPP Prague, Czech Republic, "*Study the carbon ionisation equilibrium using Charge Exchange Spectroscopy and infer transport coefficients for carbon ions*"

A. Rodrigues, L.A. Pereira, C. Varandas, CFN Lisbon, Portugal, "*Advanced plasma control for TCV*".

S. Shibaev, Association UKAEA Fusion, UK, "*Data acquisition for fast framing camera on TORPEX and TCV*"

I. Tigelis, S. Mallios, Association Euratom Hellenic Republic, Greece, "*Modelling of the EM field distribution at 2.45GHz in the empty TORPEX torus*"

I. Tigelis, G. Latsas, Association Euratom Hellenic Republic, Greece, "*Instability calculations in the 170GHz coaxial-cavity-gyrotron beam-duct*"

G. Veres, S. Kalvin, M. Berta, A. Bencze, Association EURATOM-HAS, KFKI Research Institute for Particle & Nuclear Physics, Budapest, Hungary.

This is a continuous collaboration under an Article 1.1b staff movement agreement (from HAS to CRPP). A number of projects are being pursued: design and fabrication of a fast gas injection valve for disruption mitigation and impurity transport studies, analysis and tomographic inversion of foil bolometer and AXUV fast diode camera arrays, analysis of ELM structure and turbulence using in-vessel, tile embedded Langmuir probes and 1D STRAHL modelling of impurity transport.

C. Wahlberg, Uppsala University, Sweden, "*MHD aspects of the sawtooth instability*"

M. Windridge, Association UKAEA Fusion, UK, "*Non-linear modelling of MAST*"

M. Wischmeier, IPP- Garching, Germany, "*SOLPS5 modelling of the effect of parallel flows on detachment thresholds in TCV*"

4.7 Other international collaborations

D. Ernst, Plasma Science and Fusion Center, M.I.T., Cambridge, MA, USA, *"Implementation of a synthetic tangential phase contrast imaging diagnostic in the gyrokinetic code GS2 for TCV"*

J. Egedal, W. Fox, M. Porkolab, PFSC, MIT, USA, *"Investigation of the physics of magnetic reconnection in the collisionless regime in a dedicated laboratory device, the Versatile Toroidal Facility"*

R. Ganesh, J. Chowdury, Inst. For Plasma Research, Bhat, Gandhinagar, India, *"Effects of non-adiabatic electron dynamics in gyrokinetic simulations of microinstabilities"*

R. Gruber, EPF-Lausanne, Switzerland, **S.P. Hirshman**, ORNL, USA, **K.Y. Watanabe, H. Yamada, S. Okumara, Y. Narushima, S. Sakakibara, C. Suzuki, T. Yamaguchi**, NIFS, Japan, **K. Yamazaki**, Nagoya Univ., Japan, *"3D anisotropic pressure equilibrium and fluid magnetohydrodynamic stability"*

R.W. Harvey, A.P. Smirnov, E. Nelson-Melby, CompX, San Diego, CA, USA, *"Modelling of electron cyclotron wave propagation and electron cyclotron emission in TCV"*

W. Heidbrink, H. Boehmer, UC Irvine, USA, *"Sources for energetic ions for a simple magnetized torus"*

S.P. Hirshman, Oak Ridge National Laboratory, USA, *"Three-dimensional anisotropic pressure free boundary equilibria: the ANIMEC code"*

M.Yu. Isaev, Russian Research Centre Kurchatov Institute, Moscow, Russia *"Development of the VENUS-df Code for Bootstrap Current and Neoclassical Transport in Stellarators"*

M.Yu. Isaev, Kurchatov Inst. Moscow, Russia, **H. Maassberg, C. Beidler, J. Nuehrenberg, M. Schmidt, J. Geiger**, IPP-Greifswald, Germany, **A. Bergmann**, IPP Garching, Germany, *"Montecarlo-delta-f neoclassical transport in 3D systems"*

K. Kim, KBSI, South Korea, **K. Okuno**, JAERI, Japan, **J. Miller**, ORNL, USA, **S. Egorov**, Efremov Inst., Russian Fed., and **P. Weng**, CAS, China, *"Preparation of ITER conductor qualification samples"*

N. Martowetsky, ORNL, USA, *"Test of TFAS1 sample with solder filled termination" (EFDA Task LTPSAM)*

S.Yu. Medvedev, A.A. Martynov, A.A. Ivanov, Yu.Yu. Poshekhonov, Keldysh Institute of Applied Mathematics, Moscow, Russia, **M.Yu. Isaev, V.D. Shafranov, A.A. Subbotin**, RRC Kurchatov Institute, Moscow, Russia, *"Equilibrium and Stability of 2D and 3D plasma configurations"*

M. Mikhailov, A. Subbotin, V.D. Shafranov, M.Yu. Isaev, M. Samitov, Russian Research Centre Kurchatov Institute, Moscow, Russia; **J. Nuehrenberg**, Max Planck Institut fuer Plasma Physik, Greifswald *"Optimisation of Advanced Stellarator Systems"*

G. Moritz, GSI Darmstadt, Germany, and **V. Vysotsky**, All-Russia Scientific Cable R&D Institute, Moscow, Russian Fed., *"INTAS Project"*

V. Naulin, O.E. Garcia, Risoe, Denmark, *"Adaptation of the ESEL fluid code for modelling of turbulence in the TORPEX device"*

G.R. Odette, Univ. California Santa Barbara (UCSB), Santa Barbara, CA, USA, *"Fracture mechanics and small specimen test technology"*

V. Pantsyrny, ASRIIM, Russian Fed., *"Preparation of ITER conductor qualification samples"* (EFDA Task NEFSS)

B. Rogers, Dartmouth College, USA, *"Theoretical characterization of turbulence in TORPEX plasmas"*.

P. Savrukhin, A. Sushkov, D. Kravtsov, RRC Kurchatov Institute, Moscow, Russian Federation, *"Design and fabrication of a tangential X-ray diagnostic for TCV"*

F. Skiff, Univ. of Iowa, USA, *"Basic wave-particle interactions and turbulence studies in TORPEX"*

P. Smeibidl, HMI, Berlin, Germany, *"Design of superconductor for 30T Hybrid Magnet"*

J. Snipes, R. Parker, M. Porkolab, J. Freidberg, J. Sears, PFSC, MIT, USA, *"Fast particle physics, Alfvén waves, and active MHD mode excitation on the Alcator C-Mod tokamak plasma"*

A. Sushkov, Nuclear Fusion Institute, Kurchatov, Moscow, Russia, *"Electron heat transport at switch-off in sawtooth-less TCV discharges"*, and *"Development, commissioning and use of DMPX soft X-ray wire chamber towards Te measurements"* and *"Tangential hard-X-ray imaging"*

A.D. Turnbull, General Atomics, San Diego, USA, *"Stability studies of ARIES stellarator configurations"*

E. Valeo, Princeton University, USA, and **R. Berger**, Lawrence Livermore National Laboratory, USA, *"Development of numerical methods for Vlasov simulations"*

F. Volpe, General Atomics, San Diego, CA, USA, *"Electron Bernstein wave (EBW) modelling with the ART ray tracing code, planning of EBW experiments on TCV"*

K.Y. Watanabe, S. Okamura, Y. Narushima, H. Yamada, S. Sakakibara, National Institute for Fusion Science, Toki, Japan, *"MHD stability in LHD"*

Y. Wu, Institute of Plasma Physics, Chinese Academy of Sciences, Hefei, P.R. China, *"Effects of irradiation in SING on the Chinese Low Activation Martensitic steel (CLAM)"*

J. Yu, China Institute of Atomic Energy (CIAE), Beijing, P.R. China, *"Modelling of radiation damage and radiation effects"*

4.8 Other collaborations within Switzerland

E. Cadoni, University of Applied Sciences of Southern Switzerland, Canobbio, *"High strain rate tensile testing of the EUROFER 97 RAFM steel"*

Besides the activities in the field of plasma wall interaction with the University of Basel, of the socio-economics with the LASE (EPFL) and CEPE (ETHZ), the CRPP also collaborates with the PSI in the field of material under irradiation.

The Industrial Plasma Group has close collaborations with the following Swiss Industries: Charmilles SA, OC Oerlikon SA, Ruag, Sulzer Metco and Tetra Pak.

P. Ott, S. Pavon, Laboratoire de Thermique Appliquée et Turbomachines, EPFL,
P. Leyland, Laboratoire d'Ingénierie Numérique, EPFL, Swiss National Science Foundation Project: *"Influence of a weakly ionised boundary layer on transonic and supersonic air flows"*.

5 THE EDUCATIONAL ROLE OF THE CRPP

The CRPP plays a role in the education of undergraduate and postgraduate students, particularly in the Faculté des Sciences de Base (FSB) of the EPFL. Advanced education and training in fusion physics and technology and plasma physics topics is carried out as part of the research activities of the Association. Section 5.1 presents the 6 courses given to physics undergraduates and to engineering undergraduates. In their fourth and final year, physics undergraduates spend time with a research group at the EPFL, typically 12 hours per week for the whole year. During this period, they perform experimental or theoretical studies alongside research staff, discovering the differences between formal laboratory experiments and the “real” world of research. After successful completion of the first year of the Master Programme (4th year of studies), physics students are required to complete a “master project” with a research group, lasting a full semester. This master project is written up and defended in front of external experts. The CRPP plays a role in all of these phases of an undergraduate’s education, detailed in Sections 5.2 and 5.3.

As an academic institution, the CRPP supervises many Ph.D. theses, also in the frame of the Physics Section of the EPFL. 4 PhDs were awarded in 2007. At the end of 2007 we had 39 PhD students supervised by CRPP members of staff, mostly in Lausanne but also at the PSI site in Villigen. Their work is summarised in Section 5.4.

5.1 Undergraduate courses given by CRPP staff

S. Alberti, *Chargé de cours* – “*Plasma Physics I*”

This course is an introduction to plasma physics aimed at giving an overall view of the essential properties of a plasma and at presenting the approaches commonly used to describe its behaviour. We study single particle motion, the fluid description and the kinetic model. The relation between plasma physics and developing a thermonuclear reactor is presented and illustrated with examples.

N. Baluc, *Chargée de cours* – “*Materials Physics*”

Basic course on materials physics, presented as an option to 3rd year Physics students. The course covers the theory of diffusion, dislocations and plasticity as well as the characterization of materials. Ways of production, structures, microstructures, physical and mechanical properties are presented for pure metals, intermetallic alloys, superalloys, shape memory alloys, steels, quasicrystals, glasses, gels, liquid crystals, aggregates, ceramics, composites, polymers, and nuclear materials for fission and fusion reactors.

A. Fasoli, Associate Professor – “*Plasma physics II*”

One semester option course presented to 4th year Physics students, introducing the theory of hot plasmas via the foundations of kinetic and magnetohydrodynamic theories and using them to describe simple collective phenomena. Coulomb collisions and elementary transport theory are also treated. The students also learn to use various theoretical techniques like perturbation theory, complex analysis, integral transforms and solutions of differential equations.

A. Fasoli, Associate Professor – “*General Physics II*”

This course completes the introduction to mechanics provided in the first semester with the basic concepts of statics, oscillations and special relativity. It also covers the whole of thermodynamics, from the introduction to heat, temperature and

kinetic theory to the first and second principles, including entropy and thermal engines, ending with a treatment of transport and non-equilibrium phenomena in open systems.

J.B. Lister, *Maître d'Enseignement et Recherche (MER) – "Plasma Physics III"*

An introduction to controlled fusion, presented as a one semester option to 4th year Physics students. The course covers the basics of controlled fusion energy research. Inertial confinement is summarily treated and the course concentrates on magnetic confinement from the earliest linear experiments through to tokamaks and stellarators, leading to the open questions related to future large scale fusion experiments.

M.G. Tran, *Professor - "General Physics III and IV"*

This course, given to the Mathematics Section, covers hydrostatic, hydrodynamics waves and electromagnetism (General Physics III) and quantum mechanics (General Physics IV).

L. Villard, *Professeur Titulaire – "Numerical Physics I-II"*

Full year course given to students in their 2nd year in Physics. The course covers various time and space integration techniques for ordinary and partial differential equations, and is applied to various physics problems ranging from particle dynamics, hydrodynamical equilibrium, electromagnetism and waves. It includes a strong practical work aspect.

H. Weisen, *Chargé de cours, "Physique Générale I SV &MX"*

This is a classical mechanics course on basic kinematics and dynamics, systems dynamics and rotation taught during the autumn term to a class of 170 first year life science and mechanical engineering students. It features two weekly hours of classroom lectures followed by two hours of exercises.

5.2 Undergraduate work performed at the CRPP

EPFL 4th year students

Urs AMHERD: *"Study of Suprathermal Electron Dynamics in TCV"*

Sébastien BOUTINARD ROUELLE: *"Champ magnétique et courant dans un réacteur LEPECVD"*

Alexandre BOVET: *"Étude des lois d'échelle du rayon d'inversion des instabilités en dents de scie dans le tokamak JET"*

Laurent DECOSTERD: *"Simulation numérique de l'équation Vlasov-Poisson unidimensionnelle dans l'espace des phases : écoulement libre et amortissements Landau linéaire et non-linéaire"*

Martin GIRARD: *"Sonde Magnétique tridimensionnelle"*

Benoît SCHALLER: *"Etude de l'activité dent de scie dans le Tokamak à Configuration Variable"*

Luca SULMONI: *"Confinement vers les hautes densités dans TCV"*

Alice BURKEL: *"Production and detection of a suprathermal ions beam in a low temperature toroidal plasma"*

Jérôme GURTEL: *"Etude numérique des orbits des particules dans un RFP"*

Christian LUCAS: *"Caméra d'observation TCV"*

Sergio Daniel Marques dos Santos: *"Preliminary characterization of the microstructure and mechanical properties of ODS ferritic steels after mechanical alloying and HIPping". Powders of a 14Cr oxide dispersion strengthened ferritic steel*

were prepared by mechanical alloying and compacted by hot isostatic pressing (HIPping). Both the mechanically alloyed powders and HIPped ingots were characterized in terms of density, chemical composition, microstructure, microhardness and Charpy impact behaviour.

External students

Wynne EVANS (ERASMUS student): *"Studies of plasma flow and turbulence in TCV using Doppler reflectometry"*

The characteristics of a new prototype microwave Doppler reflectometer have been studied and documented in the laboratory. Analysis was performed on reflectometry data collected in the last TCV campaign to determine the ExB velocity profile and attempt to find evidence of geodesic acoustic modes.

5.3 EPFL Master degrees awarded in 2007

Karim DAOUK: *"Simulation du transport électronique d'énergie et de particules"*

Electron density and temperature profiles measured in the TCV tokamak during internal transport barriers (eITBs) have been modeled using the ASTRA code. Various profiles of the thermal and particle transport coefficients have been used. The work has been able to determine the typical radial shape of these coefficients in order to be compatible with the measured profiles. This allowed to determine the typical location of the foot of the barrier and the width of the barrier. In addition, it was shown that the measurements are more consistent with an increased transport in the very center, where the current density is very small. Although new experiments with more central heating are needed to finalize this preliminary observation.

Michaël CHESEAUX: *"Déposition de silicium microcristallin par plasma dc à haut courant d'arc"*

The dominant optical emission from lines of ionic species proved that the high current DC arc is a plasma source with exceptionally-high degrees of depletion, dissociation, and ionisation of silane and hydrogen. Consequently, deposition of silicon thin films was obtained at rates up to 10 times faster than for conventional RF plasma sources, with a wide accessible range of crystallinity, and low hydrogen content.

Christian THEILER: *"Electrostatic turbulent structures in TORPEX plasmas"*

(ETH - Zurich and CRPP-EPFL - Lausanne)

Poloidally localized, propagating structures of increased plasma density (blobs) are reported from the scrape-off layer of various Tokamaks. The physics leading to blobs are investigated in the simple magnetized toroidal plasma of TORPEX. This talk focuses on the role of the radial density gradient in the blob ejection mechanism. For this purpose, ion saturation current measurements from a two-dimensional imaging probe are analyzed with conditional sampling and related techniques. Two scenarios leading to blobs at two different vertical positions are investigated. In one case, the blob originates from a positive wave crest of an interchange mode, which suddenly elongates. In the other case, the conditional sampling result shows blobs ejected from a rather slab-like plasma profile. In both cases, a monotonic dependence between the magnitude of instantaneous negative density gradients and the probability for the ejection of blobs is found.

5.4 Postgraduate studies

Postgraduate courses given in 2007

N. Baluc, D. Gavillet, R. Schäublin, Ph. Spätig: *"Effects of Radiation on Materials"*
This 28-hours course (2 credits) is part of the EPFL's doctoral programme in Materials Science and Engineering (MX-002). The course is given by three lecturers from the CRPP and one lecturer from the PSI (Dr. D. Gavillet). It is aimed at providing extensive information on the effects of irradiation (neutrons, protons, ions) on the structure, microstructure and mechanical properties of materials for nuclear installations. It is divided into five chapters: 1) introduction to radiation damage and radiation effects, 2) radiation damage and analysis tools, 3) radiation damage and fracture mechanics, 4) radiation effects on materials for fusion reactors, 5) radiation effects on materials for fission reactors.

Ch. Hollenstein and A.A. Howling *"Plasma in Industry: Physics basis and applications"* (PY-10) Doctoral school EPFL, winter semester 2007-2008

Doctorate degrees awarded during 2007

Mario PODESTA: *"Plasma production and transport in a simple magnetized toroidal plasma"* (EPFL Thesis No. 3765(07))

This Thesis addresses questions related to transport phenomena and the plasma production mechanisms by injection of microwaves in the electron-cyclotron frequency range in the simple magnetised toroidal plasma TORPEX.

The mechanisms of the interaction between the injected microwaves and the plasma are identified. The experimental results highlight the different roles played by the electron-cyclotron and upper-hybrid plasma resonances in the absorption of the microwave power by the plasma.

The effects of the plasma-wave interaction on the electron distribution function are investigated, confirming that the high-energy electrons that are able to ionise the neutral gas mainly come from interactions at the upper-hybrid resonance. Based on the experimental results, an expression is derived for the particle source term, which can be used in numerical codes simulating the plasma dynamics on TORPEX.

The plasma production mechanisms are then related to the properties of the time-averaged plasma profiles. A set of control parameters, including the injected microwave power and the vertical magnetic field, are identified. These allow one to vary in a systematic way the plasma profiles, as needed for a systematic study of plasma instabilities and related transport.

The study of particle and heat transport is then undertaken. A number of experimental and analysis techniques, including a method based on the combination of 'conditional-average sampling' and 'boxcar-averaging', are applied to identify and quantify specific contributions to the total fluxes. The two-dimensional temporal behaviour of density, electron temperature and plasma potential is simultaneously reconstructed, thus contributing significantly to the characterisation of transport mechanisms at play in TORPEX plasmas.

Two clearly distinct mechanisms are mainly responsible for the transport across the magnetic field. They are respectively associated to unstable low-frequency electrostatic modes, identified as drift waves and interchange modes, and to intermittent high-density plasma structures (or blobs). It is shown that the blobs originate from the intermittent radial expansion of the unstable modes in a region of strongly sheared ExB flow.

Francesca POLI *"Electrostatic instabilities and turbulence in a toroidal magnetized plasma"* (EPFL Thesis No. 3849 (2007))

This Thesis aims at characterizing the linear properties of electrostatic drift instabilities arising in a toroidal plasma and the mechanisms leading to their development into turbulence. The experiments are performed on the TORoidal Plasma EXperiment (TORPEX).

The first part of the Thesis focuses on the identification of the nature of the instabilities observed in TORPEX, using a set of electrostatic probes, designed and built for this purpose. The global features of fluctuations, analyzed for different values of control parameters such as the magnetic field, the neutral gas pressure and the injected microwave power, are qualitatively similar in different experimental scenarios. The maximum of fluctuations is observed on the low field side, where the pressure gradient and the gradient of the magnetic field are co-linear, indicating that the curvature of the magnetic field lines has an important role in the destabilization of the modes. The power spectrum is dominated by electrostatic fluctuations with frequencies much lower than the ion cyclotron frequency. Taking advantage of the extended diagnostics coverage, the spectral properties of fluctuations are measured over the whole poloidal cross-section. Both drift and interchange instabilities develop and propagate on TORPEX, with the stability of both being affected by the curvature of the magnetic field. It is shown that modes of different nature are driven at separate locations over the plasma cross-section and that the wavenumber and frequency spectra, narrow at the location where the instabilities are generated, broaden during convection, suggesting an increase in the degree of turbulence.

The transition from coherent to turbulent spectral features and the role of nonlinear coupling between modes in the development of turbulence are treated in the second part of this work. It is found that nonlinear mode-mode coupling is responsible for the redistribution of spectral energy from the dominant instabilities to other spectral components and that this mechanism is independent of the nature of the instabilities. Nonlinear interactions between the mode and its nonlinearly generated harmonics are responsible for the filling of the spectral regions between harmonics. Later in the development along the convection path, the unstable mode transfers energy to spectral components with significantly larger frequencies. This transfer of energy can be interpreted in the investigated plasma scenarios as a forward cascade in wavenumbers, with transfer of energy from large to small scales.

Alban SUBLET: *"Caractérisation de décharges à barrières diélectriques atmosphériques et sub-atmosphériques et application à la déposition de couches d'oxyde de silicium"* EPFL Thesis No. 3801 (2007)

The first part of this work concerns the study of the effect of pressure (10mbar to 1000mbar) on a DBD in non-reactive gases (helium, argon and nitrogen), then in neutral gas/oxygen mixture with electrical measurements (discharge current and applied voltage), high-speed imaging and time-resolved optical emission spectroscopy. In N₂, the exploration of discharge regimes as a function of pressure shows a progressive transition from Townsend to multi-peaks regime between 320 and 160mbar. High-speed imaging of a multi-peaks discharges in N₂ and He shows that each multi-peak corresponds to a new spatially homogeneous discharge. The inversion of Paschen's curves of Ar and He shows the importance of metastable energies and capabilities to ionize almost all impurities, in the case of He, allowing a breakdown under a lower electric field than in Ar. Time-resolved spectroscopy of a glow discharge in He as a function of pressure and impurities showed the metastables evolution within a discharge and the role of impurities in quenching or creation rate of metastables. In He and N₂, the very first microseconds of discharge are filamentary and change after 2-3 periods (~200μs) to the glow or Townsend regime respectively. The adjunction of O₂ (electronegative and metastable quencher gas) makes the discharge turn to filamentary when a proportion of more than

1500ppm is added at atmospheric pressure. This rate is increased to 2% in N₂ at 350mbar. The presence of a polymer substrate reduced this Townsend working domain due to the increase of impurities in the discharge caused by polymer etching. However, this process in pure N₂ is very efficient for implanting nitrogen functional groups on the surface of polymer films (till 23% on PET).

The second part of this work was dedicated to SiO_x barrier coating characterization as a function of pressure in oxygen/hexamethyldisiloxane (HMDSO) gas mixture highly diluted in nitrogen and to powder characterization. An admixture of HMDSO (even for ~100ppm) make the discharge turn to filamentary regime. A pressure below 40mbar must be reached to obtain a multi-peak regime. This high pressure process is fast and deposition rate of 17nm/s could be obtained at 500mbar. FTIR, AFM and SEM characterization of the coatings showed an inhomogeneous composition and structure of the layer between entrance and exit of the discharge along the gas flow. The geometry of the discharge cell (6cm by 6cm, 2mm gap) with gas injection from one side, leads to a different chemistry along the gas flow resulting in an organic, dense and smooth coating at the entrance whereas rough and quasi-stoichiometric coating at the exit. These differences are explained by heterogeneous reactions, comparable to PECVD process (surface chemistry) close to the gas input and a progressive transition to homogeneous reactions at the exit of the discharge (volume chemistry) which result in particle formation of nanometric size. Analysis of these particles by laser light scattering (LLS) shows a pressure threshold of 200mbar at the end of the discharge cell, with a constant gas mixture and flow within all the pressure range. From 200 to 1000mbar, this threshold becomes closer and closer to the discharge entrance, but it always corresponds to a residence time of the gas in the discharge of around 30ms representative of the characteristic formation time of detectable particles. This threshold varies linearly with the power injected in the discharge, the higher the power the faster the particles appear. Spatio-temporal LLS measurements show a cyclic (T~1-2s) formation of particles : rapid growth and trapping in the discharge when they reach ~200nm, when their size or density increases (~240nm) they are collected on the electrodes or expelled by the flow drag force which becomes preponderant in comparison with the electrostatic trapping force. Finally, they agglomerate at the exit of the discharge up to ~300nm size. Then a new cycle starts.

Benjamin STRAHM: *"Investigation of radio-frequency, capacitively-coupled large area industrial reactor: Cost-effective production of thin film microcrystalline silicon for solar cells"* (EPFL Thesis No. 3895(07))

Microcrystalline silicon ($\mu\text{c-Si:H}$) intrinsic layer for application in micromorph tandem photovoltaic solar cells has to be optimized in order to achieve cost-effective mass production of solar cells in large area radio frequency capacitively-coupled PECVD reactors. However, since the first use of $\mu\text{c-Si:H}$ in a solar cell in 1992, the approach is almost essentially empirical. This is because of the tiny process window for solar grade mc-Si:H – at the boundary between a-Si:H and $\mu\text{c-Si:H}$ deposition – and because the basic mechanisms at the origin of $\mu\text{c-Si:H}$ deposition are still not fully understood.

The plasma composition has been measured using Fourier transform infrared absorption spectroscopy and optical emission spectroscopy. It has been shown that the deposited films can be classified into three categories (amorphous, transitional and microcrystalline) as a function of silane concentration in the plasma, while it is impossible to do so as a function of all other process parameters (silane input concentration, RF power, pressure, etc...) if they are all varied simultaneously. This means that the common way to deposit microcrystalline silicon by strongly diluting the silane with hydrogen (< 5 %) is not unique. This is because the plasma composition does not depend only on the gas composition, but also on the fraction of silane depleted in the plasma. Analytical and numerical plasma chemistry modeling have shown that this is because the silane concentration in the plasma determines the species flux towards the growing film surface. Hence, in agreement

with existing phenomenological models of microcrystalline growth, the lower the silane concentration in the plasma, the higher the H to SiH_x flux ratio towards the surface and the higher the crystallinity.

This has been used to demonstrate the feasibility of the growth of microcrystalline silicon in large area reactors using radio-frequency excitation (40 MHz) even from pure silane gas. Moreover, it has been shown that the optimum in terms of deposition rate and deposition efficiency tends towards pure silane and not to the common H₂-diluted regime. Following this conclusion, an optimization strategy has been constructed by varying only the hydrogen flow rate and the working pressure. Guidelines for the selection of the initial process parameters have been given in order to achieve high deposition rate (> 10 Å/s) and high gas utilization efficiency (> 80 %) of good quality microcrystalline silicon with a high input silane concentration (> 10 ; 20 %) by using the optimization strategy.

Furthermore, it has been shown by using time-resolved plasma composition measurement and modeling that the time necessary to reach chemical steady-state is about 1 second in large area Plasma-Box™ reactors. This time is much shorter than times reported for small laboratory reactors, which are typically of about 1 minute. It is demonstrated by using two-dimensional modeling that this is due to back-diffusion of the silane molecules from the vacuum chamber to the plasma zone in laboratory reactors, whereas the plasma fills the whole volume in large area Plasma-Box™ reactors, making the plasma composition quasi-instantaneously uniform at plasma ignition. This is of importance for the film microstructure uniformity across the thickness of the layer.

Ph.D. Theses supervised by CRPP staff at the end of 2007

Mattia ALBERGANTE: *"Alpha Particles and Turbulence"*

My studies were focused on discovering how turbulence might drive anomalous heat and particle transport of alpha particles using a flux tube code, GENE11. This code has the possibility to solve the gyrokinetic Vlasov equation and calculate particle and heat fluxes for several geometric configurations where multiple populations of charged species evolve in time. So far, results have shown how traces of alpha particles (and heat) fluxes can be strongly driven inwards under particular conditions. These pinches appear when alphas temperature gradient is large enough with respect to the density gradient: preliminary results show that the sign of the pinch changes with the sign of the diamagnetic drift frequency. Meanwhile, the strength of the pinch can be correlated with the resonance between the frequency of the turbulent mode and the bounce averaged curvature drift frequency for trapped particle. Then, an explanation for this kind of anomalous transport can be found in a resonant interaction between the turbulent state and the particle curvature drift, especially trapped particle one's as seen from the development of a semi-analytical model. These results, however, are still very preliminar and future plans include a collaboration with an Italian university in order to confirm what has been found so far using another code capable of solving single particle equations of motion.

Mathieu BERNARD: *"Impurity transport in TCV tokamak plasmas"*

The aim of this work is to document and tentatively interpret the experimental carbon density profile behaviour in the TCV tokamak in the framework of different semi-empirical models.

During this year, the experimental information was compiled into a database of carbon density profiles in steady state measuring with Charge Exchange Spectroscopy. The Database contained nearly 800 samples and covered a wide range of discharge conditions, including low confinement discharge, ECH and some EITB discharge.

The database was used to find a correlation between the carbon density profile and the current density profile for the ohmic L-mode discharge. We also found that the semi-empirical models need a correction depending of the deposition position of power for the ECH discharge.

The gyrokinetic codes KINZERO and GS2 were to investigate specific turbulence issues concerning the TCV tokamak.

Alessandro BORTOLON: *"Plasma rotation and momentum transport studies in the TCV Tokamak based on Charge Exchange Spectroscopy measurements"*.

The experimental activity focused on momentum transport in Ohmic L-mode plasma discharges. In particular, the inversions of toroidal rotation observed in limited and diverted plasmas, has been studied as a function of plasma parameters as B_ϕ , I_p , and shape ($-0.3 < \delta < 0.6$ and $1.3 < \kappa < 1.6$). For selected discharges, the toroidal momentum transport has been characterized by means of a phenomenological model, estimating the viscous and the non diffusive contributions to the momentum fluxes. The main results can be listed as: 1) core plasma rotation is sustained by core momentum transport processes, and not driven by the edge; 2) the diffusive fluxes (e.g. viscosity) are similar for co and counter current rotation regimes ($\chi_\phi \sim 0.2 \text{ m}^2/\text{s}$); 3) non diffusive momentum fluxes in the core cannot be expressed in the classical form of pinch fluxes (i.e. proportional to v_ϕ); 4) rotation inversion may be modelled by a change of sign of such non diffusive fluxes (outward to inward). Further studies will compare these experimental results with proposed underlying physical mechanisms (micro turbulence, MHD, etc.).

The second part of the year has been also devoted to the upgrade of CXRS diagnostic, in view of the 2008 experimental campaign. This upgrade concerned both Low and High field side observation systems, now equipped with high quantum efficiency, back illuminated CCD detectors and 40 optical fibres transmission lines. This activity comprehended installation and setup of detectors and spectrometers, as well as the installation of the optic fibres. Both LFS and HFS systems have been aligned, and absolutely calibrated, and are now ready to measure, carbon density, temperature and toroidal rotation profiles with improved spatial resolution (1 cm) and spatial coverage (95% of plasma diameter, up to $\rho=1$ in the LFS region).

Loïc CURCHOD: *"Heating of High Density Plasmas in the TCV Tokamak"*

Above a density limit depending on their frequency, electron cyclotron waves (ECW) for standard EC resonant heating (ECRH) are reflected at the edge of high-density plasmas in low to medium field tokamaks like TCV. The electrostatic electron Bernstein waves (EBW) from mode conversion of externally launched EC waves encounter no plasma cutoff. EBW can thus provide a heating technique (EBWH) with the same advantages as ECRH – local deposition of high power, operation flexibility – without any upper density limit.

After the demonstration of O-X-B-conversion EBWH deposition at the edge of TCV H-modes, initial equatorial modulated EC power injections show promising results of EBWH in the plasma center and on both sides of the magnetic axis with absorption up to 60%. The difficulty of determining the power deposition location amongst strong central sawtooth activity is partly overcome using a slope-breaking method applied on high spatial and temporal resolution soft X-ray signals. Discrepancies in the power deposition radial location between some of the experimental results and simulations from the non-relativistic single ray tracing code ART will be further investigated with the fully relativistic ray-tracing and Fokker-Planck codes LUKE and DKE.

A loop-antenna for the detection of lower-hybrid waves generated at the X-B conversion layer is under construction. The transmission line of a steerable antenna for oblique ECE and EBW Emission (EBE) is being improved. Both diagnostics will help optimizing the ECW-EBW coupling at high power.

Overdense EBWH extends TCV operation to high-density H-modes, the standard operation scenario for ITER. In particular, EBWH allows heat transport and confinement studies in highly-collisional plasmas; high-power (2 MW) long-pulse EBW injection seems to provide a stationary overdense regime to be investigated along with similar stationary conditions achieved in X3 heating experiments.

Cornelis DE MEIJERE: *"Study of plasma fluctuations in tokamaks"*

The primary goal of this recently started project is to investigate density fluctuations in TCV, initially employing a newly installed microwave reflectometer and later a tangential laser imaging system, focusing in particular on the edge region.

Lukas DERENDINGER: *"Design of low-energy plasma sources"*

After it was realised last year that a ring anode will never produce stable conditions, a complete change of the anode design was carried out. The new anode is an internally-cooled copper cone placed in the centre of the reactor bottom. Additionally bigger Helmholtz coils were installed for a stronger magnetic field of about 60 Gauss, which is a configuration comparable to the older generation of the LEP reactor. And finally the idea of Hall effect measurements to localise the plasma current led to the construction of a 24 sensors Hall effect probe with a rotatable vacuum feedthrough. Some first measurements and a probe calibration have been made by a fourth year student for his laboratory work.

In the meantime the older BAI reactor was reactivated for a complete analysis of its capacity as a novel plasma source for solar cell applications. Several questions and problems have to be answered and resolved: one dimensional homogeneity along the plasma column, crystallinity of at least 60% in the $\mu\text{c-Si}$ -films, understanding of observed deposition rate limits below the theoretical maximum and contamination of the films with oxygen and metals e.g. tungsten coming from the heating filament. In order to increase linear homogeneity of the film growth rate, the ring shaped process gas shower in the upper part of the reactor was replaced by a linear gas shower installed in front of the plasma column. In particular, for high deposition rates obtained with more than 100 sccm of silane, the increase of the homogeneity is significant compared to the ring shower. The effect of the new shower on the homogeneity of crystallinity is less important.

Since low oxygen contamination is crucial for applications, several films produced under different conditions were analysed with an FTIR. The lowest base concentration and the lowest increase when exposing the film to the air was found with a long term outgassing of the samples and the reactor and a final capping of the $\mu\text{c-Si}$ -film with an a-Si-film of about 500nm. First SEM measurements show that the microcrystalline structure is different from typical $\mu\text{c-Si}$ -films e.g. those produced in large surface RF reactors, but possible influence on solar cell capacity is not yet determined.

Emiliano FABLE: *"Simulation of plasma transport"*

The theoretical study of particle transport characteristics in electron Internal Transport Barriers has been continued with analytical and numerical work using the gyrokinetic GS2 code. The main achievement of this work has been to show that the anomalous pinch is of a thermodiffusive nature and is carried by the trapped electrons. The pinch usually called 'Turbulent Equipartition Pinch' is found to be negligible. The resulting density peaking is maximized at the transition between the two main turbulent instabilities: the ion temperature gradient mode and the trapped electron mode: the latter has to be subdominant. The passing electrons start to contribute relevantly at finite and high collisionality. The comparison of the theoretical results with the experimental observations needs detailed knowledge of

the ion parameters, thus new experiments have been planned for the next experimental campaign in TCV.

Federico FELICI: *"Real-time ECH control aimed at studies of Neoclassical Tearing Modes"*

Control of tokamak plasmas using ECH is an important topic for fusion plasmas and has many potential applications. One application in particular is to suppress NTMs (neoclassical tearing modes) which degrade reactor performance and are expected to appear in ITER. Activities towards ECH control in general, and NTM control in particular have focused on study of ECH beam deposition detection algorithms using ECE, Soft X and DMPX diagnostics, as a preparation for experiments on TCV. In order to develop a simulation model for ECH control on TCV, a system identification procedure was carried out on the X2 launchers yielding a dynamical model of the poloidal mirror dynamics. Finally, work has been done on the use of the TORAY ray tracing code for analysis of oblique ECE emission data obtained using the 7th launcher as a receiver. Work has recently started on nonlinear NTM modeling for the Integrated Tokamak Modeling task force.

Silvano GNESIN: *"Design of a tomographic set of hard X-ray detector arrays for the TCV tokamak"*

This thesis focuses on suprathreshold electron dynamics in the TCV tokamak, primarily resulting from the application of ECCD, but also in relation to MHD phenomena and runaway electron generation. The focus of the work thus far has been the design of a new diagnostic, namely a tomographic set of energy-resolved hard X-ray (HXR) cameras. A preliminary design for up to nine cameras has been carried out, based on a novel tungsten collimator design adapted from the Soller collimator concept.

A substantial fraction of this year's work has consisted of an extensive simulation study to aid in the optimisation of the diagnostic design. Tomographic reconstructions of a wide range of simulated plasma emissivity patterns have been performed using a minimum Fisher information algorithm with the specific aim of determining the optimum number and orientation of the cameras and of assessing the improvement of the tomographic performance with each additional camera. Other tomographic algorithms and a parallel design assessment based on Bayesian statistic evaluation method are also foreseen to be implemented in the near future. Based on these studies, a complete diagnostic proposal is expected to be submitted early in 2008.

Work has also started on quasilinear Fokker-Planck modelling of ECRH wave-particle interaction, using the recently developed code LUKE in collaboration with CEA-Cadarache. The code includes a HXR emission module permitting a direct comparison with experimental measurements. It is envisioned that this code will be employed extensively in support of the diagnostic measurement campaign as well as of ECCD experiments in general. Current work is focusing on the interpretation of past experiments on the anomalous absorption of 3rd harmonic ECRH in a plasma pre-heated with 2nd harmonic ECRH.

Alexandr GUDOZHNIK: *"Numerical and experimental validation of sawtooth control using ECCD"*

Several experiments with ECCD stabilisation of sawteeth were performed on TCV. The sawtooth dependence on the toroidal injection angle of ECH beam was studied. The same type of experiment was simulated numerically using TORAY code. To explain revealed discrepancies and describe more thoroughly the results obtained, theoretical research and detailed simulations using Mathematica package are being performed. The evolution of q profile during sawtooth ramp has been analyzed taking into account the ICCD effects. The effect of different resistivity profiles and initial q-profiles on the sawtooth development and control is being studied. The

modeling of fast ions impact and developing a model of these phenomena for the ITER case is planned.

Barbora GULEJOVA: *"Exploitation of the new AXUV diagnostic"*

First successful attempt at modeling the inter-ELM phase of TCV Type III ELMy ohmic H-mode using the coupled fluid-Monte Carlo SOLPS5 code has been extended to include a time-dependent model, allowing ELMs to be simulated. The earlier ELM-free solution was time-independent and in order to launch the time-dependent simulation of ELM event it was thus first necessary to obtain the truly time-dependent pre-ELM solution requiring the Monte-Carlo neutral code (EIRENE) to be run with time steps, Δt equivalent to those of the fluid code (B2.5) to avoid artificial compression of the neutral timescale. A time step $\Delta t = 10^{-6}$ s has been chosen, providing 100 points during the ELM ($t_{\text{ELM}} = 100 \mu\text{s}$). The ELM event was simulated as an increase of the diffusive heat and particle transport coefficients used to simulate the pre-ELM state for the ELM duration, t_{ELM} , such that the total energy expelled during this time is compatible with that measured experimentally. A Gaussian poloidal distribution centred on the outside midplane has been applied and different multiplying factors of the pre-ELM transport coefficients chosen. In addition to the magnitude increase, the shape of transport coefficients radial profiles must also be modified compared with the pre-ELM values to account for the collapse of the edge transport barrier and provide the best match with upstream and target experimental data. Compared with the larger Type I ELMs commonly studied elsewhere, the Type III ELM that has been the starting aim of these simulations is a small event in terms of stored energy loss ($\Delta W_{\text{ELM}}/W \sim 2\%$) and absolute energy ($\Delta W_{\text{ELM}} \sim 0.5 \text{ kJ}$). It is therefore perhaps more appropriate to use the necessarily fluid approximation required for a description with SOLPS5 code. Preliminary results are encouraging in terms of absolute agreement with experimental upstream (Thomson scattering) and target (Langmuir probes and IR camera) measurements, but more work is required to understand discrepancies in the time evolution of target electron and ion temperatures. The decrease in simulated ion temperature after the ELM "switch-off" is significantly faster than expected on the basis of ion sonic transit time from upstream to target. The ELM is inherently a kinetic event and simulations with BIT1 code (1D kinetic particle-in-cell simulation) are running at the time of writing for these TCV ELMs in order to provide comparison with the fluid simulations.

At the end of 2006 in collaboration with Dr. Bonnin drift terms were activated in the SOLPS5 inter-ELM simulations but later a number of issues have been uncovered concerning the way in which SOLPS5 internally treats the direction of magnetic field components. During the visit to IPP Garching in May 2007, the efforts have been focused on the issue of modelling of the drifts for TCV for the shots with both forward and reversed toroidal magnetic field and promising simulations are in progress.

A significant part of the research program in 2007 was devoted to JET. During the modellers meeting in the beginning of 2007 familiarity with the JET data system has been developed and SOLPS5 simulations of pre-ELM phase of Type I ELMs at JET have been started. One additional aim of these JET simulations will be benchmarking of the SOLPS5 and EDGE2D codes, in particular comparing SOLPS5 results with those obtained with EDGE2D in an earlier published study.

Seyed Masood HAFEZ HAGHIGHAT: *"Multiscale modeling of irradiation induced effects on the plasticity of Fe"*

This research is focused on the investigation by multiscale modeling of the effect of irradiation on the plasticity of pure Fe. This work is aimed at determining as precisely as possible the plasticity mechanisms and their amplitude influenced by irradiation-induced effects at the level nanoscale, by molecular dynamics, and microscale, by dislocation dynamics simulations. So far the molecular dynamics

was used to simulate the interaction between a moving dislocation and a defect, such as a void or a He cavity. The stress-strain curves are obtained under imposed strain rate condition using various interatomic potentials and as a function of He content in the cavity, temperature, and cavity size. Various interatomic potentials are used, consisting of Ackland, Mendeleev, and Dudarev-Derlet for Fe-Fe interaction, Wilson-Johnson and Juslin for Fe-He interactions, and Beck for He-He interaction. The stress-strain response obtained under imposed strain rate indicated that a 2 nm void is a stronger obstacle than a He bubble at low He contents while at high He content it is weaker. With increasing temperature the escape stress and strain decrease and at the same time the discrepancy between responses induced by the various potentials decreases. It appears that this is due to compression of the Fe lattice around the cavity, which levels differences in behavior. In addition, empirical potentials with short-range induce a seemingly more reasonable dislocation-defect interaction behavior than the long-range one. Dislocation defect interaction are analyzed using the Peach and Koehler force, $\mathbf{f}=(\sigma \cdot \mathbf{b}) \times \mathbf{u}$, taking into account (1) the stress field around the cavity deduced from MD and (2) the applied stress. It appears that He atoms and favorable stress field around the He cavity assist the dislocation passage, whereas at high He contents, the He bubble becomes a stronger obstacle due to the loop punching.

Davoud IRAJI: *"Turbulence imaging in a toroidal magnetised plasma"*

Recently a fast camera has been acquired by CRPP to take the advantages of plasma imaging for both TCV and TORPEX. The PHOTRON ULTIMA APX-RX consists of 1024×1024 CMOS diodes in a dimension of 17μm×17μm. The frame rate at full resolution can be increased up to 3000f/s. By choosing a lower resolution the acquisition rate could be increased to 250000 f/s.

Using a fast camera set of diagnostics including more than 100 Langmuir probes distributed inside the TORPEX plasma will be completed to study plasma turbulence. The camera has been tested on TCV and also TORPEX. Obtained images indicate filaments in both machines' plasmas.

Next steps will be imaging of turbulence structures using Gas Puffing Imaging as well as study of light intensity correlation with density and temperature and also test the validity of proposed models of plasma emission.

Sudheer Kumar JAWLA: *"Phase Retrieval of Gyrotron Microwave Beam from Intensity Measurements"*

Experiments were performed on a 118GHz/500kW gyrotron for TCV to measure the profile of the output microwave beam. The microwave beam profile in a transverse plane was measured by irradiating a target material using output beam and the temperature elevation was recorded using an Infrared Camera. Measurements were done in several planes at different positions with respect to the gyrotron window using different target materials. Several theoretical / experimental issues were studied e.g. closest possible measurement plane, optimal target (and its thickness) for the irradiation, optimal positions for the beam profile measurements based on the optical field propagation technique, quadratic phase factor sampling (which restricts the propagation to specific locations because of severe aliasing effects due to foldover frequencies) and Iterative phase reconstruction algorithm. Several other issues which affect the phase retrieval algorithm like reconstruction in the presence of noise, effect of measurement plane misalignment w.r.t. the correct optical axis etc. were taken care in the Infrared image data processing after measurements. The Iterative phase reconstruction algorithm was then applied to the measured data using two different propagation methods i.e. Fresnel Propagation and by solving the full Rayleigh-Sommerfeld diffraction integral using circular convolution/2D-FFT technique.

Sébastien JOLLIET: *"Non-linear gyrokinetic simulations including kinetic electrons"*

Gyrokinetic theory is a useful tool for studying microinstabilities, such as ITG and TEM modes, which are commonly held responsible for anomalous transport observed in tokamaks. From a numerical point of view, simulating TEM and ITG simultaneously is a difficult task due to disparate spatial and time scales. The aim of this work is the implementation of kinetic electrons in the nonlinear, global PIC code ORB5. A model for studying collisionless TEM turbulence has been implemented in this code. Linear convergence of the growth rates and the real frequencies with respect to the main physical parameters has been achieved. A linear benchmark with other gyrokinetic code has been performed. Nonlinear TEM simulations show a small effect of turbulent detrapping for collisionless time scales, which validates the model. Simulations of ITG turbulence with trapped electrons show a strong increase of the ion diffusivity peak. Preliminary simulations of pure TEM turbulence (i.e. with linearly stable ITG modes) reveal a persistent radial structure of zonal flows with short wavelengths. This new results is in contrast with the typical radial structure of zonal flows in ITG turbulence, where long wavelengths rapidly establish.

Martin JUCKER: *"Toroidal precession drift frequency in anisotropic pressure equilibria"*

New exact Hamiltonian equations of motion have been introduced into the single particle orbit code VENUS. Together with the new anisotropic versions of VMEC and TERPSICHORE, the effects of pressure anisotropy on the toroidal drift frequency of trapped and passing ions in a fully shaped tokamak could be investigated. It was shown that the diamagnetic effect on the precession drift is in fact due to the perpendicular part of the pressure tensor and its derivative, and not the total pressure. Also, anisotropic equilibria allow for strong poloidal dependence of the pressure and thus a strong dependence of the toroidal drift frequency on the bounce angle of trapped particles on one hand, and a deepening of a poloidal magnetic well in tight aspect ratio tokamaks on the other hand, allowing for particles to be trapped away from the midplane (tear drop orbits).

Sun Hee KIM: *"Full tokamak discharge simulations using DINA-CH"*

The full tokamak discharge simulator, which has been developed by combining DINA-CH and CRONOS codes, is upgraded for the application of plasma current ramp-up phase simulation. The simulation of the plasma current ramp-up phase requires considerations on the non-linear evolution of the plasma with the response to the surrounding conducting systems and the operational constraints on CS and PF coils. As a first practical application, the feasibility of the plasma current ramp-up phase of ITER reference scenario 2 is studied. The ITER reference scenario 2 is designed to use the maximum inductive current ramp-up capability. Therefore, the risks of violating operational coil current limits and limiting the duration of plasma burn still exist in the previously proposed reference scenario. Non-linear plasma current ramp-up simulations show that several plasma parameters evolve with poorer values than the assumed ones in the reference scenario. Lower plasma poloidal beta related to the ohmic flux consumption causes the violation of CS1 coil current limit. This has been shown to be avoidable either by applying additional heating power or by modifying the reference coil current inputs for control. Higher plasma inductance, which can make the plasma more unstable for the vertical movement, is also investigated.

Xavier LAPILLONNE: *"Gyrokinetic Simulations using Eulerian Approach"*

The flux tube eulerian code GENE solves the non-linear gyrokinetic equations in order to simulate microinstabilities in Tokamak devices. The geometry of the code has been extended from an ad-hoc equilibrium, the so-called $s - \alpha$ model, which consists of circular shifted flux surfaces, to general axisymmetric geometry using an

interface with the ideal MHD equilibrium code CHEASE. Results from simulations using the $s - \alpha$ model and real geometry have been compared in the standard 'cyclon' test case and significant differences have been observed, in particular linear growth rates are found to differ by almost a factor of two. Finite aspect ratio effects, not retained in the $s - \alpha$ model, have been identified as the origin of these differences. Motivated by experimental results from TCV, showing important effects of triangularity on energy transport, the geometry interface has been used to study the effects of shaping on microinstabilities. First simulations in the ITG regime however show very little effect of triangularity and further investigations, in particular in the TEM regime, are required.

Boris LEGRADIC: *"Parasitic plasmas in industrial plasma reactors"*

In March 2007 I started investigating parasitic plasmas in industrial radio-frequency discharges for thin-film deposition, following a mandate of Oerlikon/SwissElectric. In particular I was concerned with the ignition of hollow cathode discharges and in pumping grids and shower-heads, as well as the formation of plasmoids. These discharges can severely shorten the lifetime of industrial plasma reactors, and can even lead to catastrophic failure. It soon became apparent that both hollow cathodes and plasmoids were strongly linked to the type of gas utilized in the discharge, with Argon proving to be particularly susceptible. The physical mechanisms behind this behaviour are still under investigation, but it is quite possible that metastables play a significant role.

Bin LONG: *"Investigation of LBE Embrittlement Effects on the Fracture Properties of T91"*

The susceptibility to liquid metal embrittlement (LME) of the T91 steel was studied by performing 3-point bending tests on specimens of T91 exposed to liquid lead-bismuth eutectic (LBE), and for comparison, in argon (Ar) atmosphere as well. Specimens of T91 with different heat treatments were tested to assess the hardening effect on the fracture toughness of the steel after exposure to LBE. The results demonstrate that the hardening of the T91 steel has a significant influence on its susceptibility to LBE-induced embrittlement. The 500°C tempered specimens with highest hardening appear more sensitive to LBE embrittlement, which results in brittle fracture at low temperatures and substantial reduction of fracture toughness up to 400°C. The 600°C tempered specimens with medium hardening appear quite sensitive to LBE embrittlement as well. The J-values reduced more than 50% in a temperature range of 200 to 400°C. Specimens of the non-hardened T91 steel show only slight embrittlement effect. The J-values reduced just 10-15% in presence of LBE.

Alessandro MARINONI: *"Experimental study of plasma fluctuations in tokamaks"*

The main aim of this work is to investigate plasma density fluctuations in the core region of the tokamak TCV. This is to be accomplished through a tangential laser imaging diagnostic employing the phase contrast method. A significant fraction of this year has been occupied with the finalization of the diagnostic design and procurement of components. All the in-vessel components have been fabricated and are currently being installed in TCV, with the goal of commencing measurements at the start of TCV operations early next year. The research planned will focus in particular on electron internal transport barriers.

In parallel with this work, modeling has continued with the gyrokinetic codes GS2 and KINEZERO. These codes were initially employed to aid in the choice of the diagnostic design parameters. From this activity a specific project has evolved, consisting of the nonlinear gyrokinetic modeling of a TCV experimental study of the dependence of confinement on triangularity. The salient features of the experiment

were reproduced successfully by the simulations, and the results were presented at the EPS meeting on plasma physics in the summer.

Work was also performed in support of a recently installed Doppler reflectometer diagnostic, which is used to study turbulence and plasma flows in high-density plasmas in TCV. The work included analysis software development and participation in initial data collection and analysis.

Janos MARKI: *"TCV divertor infrared measurements"*

At the end of the experimental campaign early this year, the new, vertically viewing fast Thermosensorik IR camera purchased and prepared in the latter half of 2005 has been routinely operated to gather data on ELMs during various discharges on TCV. The camera has been subsequently calibrated during the 2007 shutdown making use of a newly-acquired high-temperature blackbody source and allowing the results obtained during the TCV experiments to be formulated in terms of real surface temperatures. These first experiments yielded temperature rises exceeding 500°C during ELMs in X3 ECRH heated discharges. This figure is significantly higher than that expected for pure bulk carbon (the material of the divertor target tiles) and is proof of the existence of thick, thermally poorly coupled deposited layers on the floor tiles used as lower divertor legs on TCV. Operating the camera in sub-array mode provides time resolution for a thin radial slice of the outer divertor on the order of 40μsec, with integration times down to 4μsec. In turn this allows the power flux density due to individual ELMs to be easily observed and provides excellent data with which to benchmark models of parallel ELM transport in the scrape-off layer. Anomalies have already been noted in the apparent propagation time for the ELM pulse from upstream to divertor target when comparing Type III ELMs in low power ohmic H-mode discharges and their much higher energy counterparts (probably Type I ELMs) obtained in X3 heated H-modes. Preliminary evidence has also been found for in-out asymmetries in the ELM energy deposition by inference from the energy deposited at the outer divertor. Apparent strike point splitting at the outer divertor has been noted in low density plasmas and is thought to be due to field line ergodisation as a result of locked modes.

For JET, a total of approximately 3 months were spent working on the KL3B divertor-viewing IR camera system. Initially, an attempt was made to enable line-by-line fast (up to 21 microsecond time resolution) readout data analysis for five weeks on site, however, the difficulties encountered suggested the need for a recalibration of the system. Since JET was also shut down for maintenance this year, another 2 weeks were spent in October at the Culham site, with the goal of performing these calibration measurements on the system, easily accessible off the torus.

Mikhail MASLOV: *"Particle transport and confinement in TCV and JET"*

The aim of this work is to identify the key parameters which influence the particle transport properties in tokamaks in order to predict the density profiles behavior in burning plasma devices, ITER in particular.

JET H-mode experiments performed during the C15-C19 campaigns were analyzed and a database for density peaking study was established. Two independent density profile measurements were used, provided by LIDAR Thomson scattering for one and by the Far Infrared Interferometer, inverted using a regularized Abel inversion algorithm. The good agreement between two diagnostics allows us to be fully confident in the experimental results. On the basis of the 2006-2007 experimental database scaling laws for the density peaking factor were derived. The general results from the previous studies were confirmed: effective collisionality remains the major factor defining the density peaking in H-mode, all other parameters appeared to have much smaller effect.

Although in TCV X3-heated H-modes moderately peaked density profiles are observed at all collisionalities, which appeared to be in contradiction with JET observations. In order to help interpreting these observations, a series of quasilinear gyrokinetic simulations using the GS2 code was undertaken for both

machine conditions. The result suggests that in case of weak electron-ion coupling the ITG mode can be responsible for inward particle pinch even in high collisionality plasmas.

Nicolas MELLET: *"Extension of the LEMAN code to include finite temperature effects in the dielectric tensor to resolve singular mode structures and study effects of mode conversion without having to include gyroradius effects as in the PENN code"*

A comparison between the full warm model with consistent formulation of the parallel wave vector and a version of the code that uses different approximations of the latest has been performed in the Alfvén domain for a JET case. The different evaluations used seem to have a small impact on the TAE frequency but influence considerably the damping. The better agreement with the full warm model is found for the approximation of the parallel wave vector that corresponds to the cold dispersion relation. In other more complicated geometries like LHD or a helix with a toroidal component, simulations have been performed within the full warm model. Usual behaviour occurring in the Alfvén domain like global modes or eigenmodes of the Kinetic Alfvén Wave has been found. In the ICRF domain, the warm computation of an ion-ion hybrid resonance scenario has been done in a JET equilibrium. Finally, the optimisation and migration of the code to a SP5 cluster now permit to reach 2000 Fourier harmonics for the discretisation in the poloidal and toroidal directions and allow complex stellarator ICRF computation. The case of a magnetic beach in a 6-period quasi-isodynamic stellarator has been studied.

Pablo MUELLER: *"Fracture study on reduced activation tempered martensitic steels"*

Because of limited irradiation volume of current and future materials irradiation facilities, it is necessary to be able to assess toughness of structural ferritic steels from a limited number of small sized specimens. This work has been undertaken to better understand the size and temperature effects as well as the inherent scatter of the fracture toughness in the brittle regime and transition region. Compact tension fracture specimens of the tempered martensitic Eurofer97 steel were performed in the middle to upper ductile-to-brittle transition region. Two specimen sizes have been tested, namely 0.35T and 0.87T (crack front length of 9 and 22 mm respectively). The aim of these experiments was to assess the shape of the fracture toughness versus temperature curve and to study the size effects on toughness. Fracture data was analyzed using the ASTM E1921 master curve approach. With the new data it was possible to identify relevant differences in the shape of the toughness-temperature curve between the Eurofer97 and the fission reactor pressure vessel steels. Thus, an adjusted master curve was calibrated in order to be able to predict the ductile-brittle transition reference temperature of Eurofer97 using small specimens tested at in the lower part of the transition. 3D finite elements simulations of compact specimens were done and compared with previous plane strain 2D simulations, to investigate the effects of in plane and out of plane constraint loss. We showed that only the 3D FE simulations reproduce well the experimental load-displacement curves while the linear slope of plane strain 2D simulations is too steep and the general yield load is too high.

Theodoros PANIS: *"Alfvén Eigenmode stability in tokamak plasmas"*

The work during the past year concerned the optimization of the performance of the TAE antenna system on JET, which is used to study properties of the Alfvén Eigenmodes in tokamak plasmas.

It was understood that the electrical model which had been developed during the last months of 2006 was in disagreement with some of the impedance measurements on various stages of the system and therefore, it should be improved in order to proceed to an efficient matching unit design. Using measurements taken on the distribution and isolation units, it was possible to build transformer equivalent models in the frequency range of interest and thus enhance the overall

performance of a new four-antenna model that was in good agreement with the impedance measurements.

Comparison of the electrical model with the voltage and current measurements on various points of the system revealed important inconsistencies of the measured quantities. This led to recalibration of the corresponding signals and to new measurements so as to ascertain the reliability of the voltage and current measurements.

A solution to the matching problem was then investigated. Three resonant matching circuits were designed for the bands 60–90, 120–160 and 170–230kHz. It was shown that various constraints which are due to the system structure (e.g., the antennas are in-vessel) and to the JET operation (e.g., restricted access to the space near the torus) impose significant limitations on the matching possibilities.

Finally, a more complete model has been lately constructed in which it is possible to study the effects of the inductive coupling between the closely-spaced antennas. The most important effect predicted by the model is the fact that, in a frequency band around 200 kHz, the antenna currents do not have the phasing combination imposed at the distribution unit. This effect is critical for the ability of exciting and detecting a mode in the plasma and various ways of dealing with it are being considered.

Ilya PAVLOV: *"Plasma response to modulated electron cyclotron heating in TCV tokamak in presence of sawteeth"*

Modulated electron cyclotron heating (MECH) experiments on TCV have been analyzed from the point of view of MECH-sawtooth coupling. The main framework of this study is to compare the measurements obtained in dedicated experiments on TCV with modeling with the ASTRA transport code. This is undertaken by analyzing the plasma response at different MECH localized depositions, different ECRH power levels, and different modulation frequencies. We used Higher Order Spectral Analysis to quantitatively characterize the effect of nonlinear coupling between MECH and ST. The purpose is to obtain insight of phenomenon of MECH-ST non-linear interaction and to establish the boundaries where the conventional type of modulation analysis can be successfully implemented.

Francesco PIRAS: *"Plasma shape control of TCV"*

A new Digital System Processor (DSP) has been installed in TCV, allowing the design of a modern system for the control of the plasma shape. In particular, doublet shape plasmas are going to be studied. Initiating two plasmas at two different vertical positions, it's possible to create a doublet allowing these two plasmas to grow until their reconnect. The first difficulty is to create a two magnetic quadrupoles with a very low magnetic field, even in presence of eddy currents in the vacuum vessel. To improve the breakdown phase, the magnetic field map and the plasma current distribution are evaluated using a linear regression. Once an initial doublet shape plasma can be reliably created, it is necessary to control this configuration. A linear model describing the axisymmetric behaviour of the doublet has been created (RZIP2 model). Defining a certain number of state-space variables, the evolution of the system is easily computed and the growth rate of $n=0$ modes can be evaluated. Variation of the plasma resistivity due to the plasma temperature evolution is also taken into account.

Andreas PITSCHKE: *"Improvements of the Thomson scattering diagnostic at the TCV tokamak to better resolve internal transport gradients and to achieve a higher electron temperature resolution in the edge of X3-heated H-mode plasmas as well as a robust least-square fitting data evaluation software."*

Plasma discharges with improved energy confinement properties arising from internal (ITBs) and external transport barriers (H-mode) are an essential part of

nowadays research in plasma physics. Therefore much effort has been dedicated to improve the data quality of the Thomson scattering systems (main and edge) for these plasma scenarios.

A new data fitting software to calculate electron temperature and density has been developed to overcome the drawbacks of the former data analysis software using the ratio evaluation method leading occasionally to artifacts. The requirements of a fast and reliable analysis method could be both met in programming a especially to the problem adapted algorithm using a robust least-square fitting. The results of the new method indicate a much better match with the actual measured signals when doing the backcalculation of the signals using the fitted electron temperature and density. The obtained results also indicated a bad temperature resolution capability of the Thomson edge system in X3-heated shots. Thus a third of the Thomson edge spectrometers has been adapted towards higher electron temperatures to be well adapted for the next campaign.

In terms of spatial resolution capability there has been presented a new arrangement of the viewing chords for the Thomson main system to better resolve internal electron transport barriers. All the required equipment and hardware has been commanded and is now under quality control and installation. This works includes also the re-calibration of all the spectrometers of the Thomson main system.

Gennady PLYUSHCHEV: *"Interaction of turbulence with suprathermal ions in a simple magnetized toroidal plasma"*

For the investigation supra-thermal ions source and detector (double gridded energy analyzer) were constructed and installed on TORPEX. The first test of detector in simple regime shows reasonable signals which are slightly different for first and second gridded energy analyzer part of detector. Also the strong dependence on angle between the detector and the magnetic field was found. The test of detector in differential regime is under way. The very first test of fast ions source was performed which showed that the source can sustain heating temperature about 1000°C. The new triple probe was constructed in collaboration with Budker Institute of Nuclear Physics. The tips of the probe could be heated between the shots in order to eliminate impurity from tips. The experiments shows that impurities on the tips could significantly change the signal from the triple probe.

Amuthan RAMAR: *"On the Relationship Between the Microstructure and The Mechanical Properties of an ODS Ferritic/Martensitic Steel"*

Oxide dispersion strengthened (ODS) ferritic / martensitic (F/M) steels are candidate structural materials for the future fusion reactors due to their good high temperature strength, good thermal conductivity, swelling resistance and low radiation damage accumulation relative to austenitic steel. A new ODS F/M steel with the EUROFER 97 RAFM steel as matrix material and $(Y,Ti)_xO_{1-x}$ particle as reinforcement material is being successfully developed through the classical powder metallurgy technique. The ODS alloy produced has a density of about 99.96%. As received material is normalized at 980°C for 1hr, air cooled, followed by tempering at 780°C for 1hr and air-cooled. Electron microscopy observations were done to analyse the microstructure of the material and to identify the homogeneity in the oxide dispersion in the matrix of EUROFER 97. The yttria dispersed in the matrix EUROFER97 has an average particle size of 20nm and for the one with yttria and Ti the average size of the dispersed particle is 7nm. High-resolution transmission electron microscopy observation reveals that there is lattice incoherency in between the particles and the matrix EUROFER97, which indicates that they are unsharable by mobile dislocations. In a next step, the mechanical properties and their relation to heat treatment will be studied in detail.

Marina RICCI: *"Analyses of SiO_x barrier coatings by different mixtures O₂/HMDSO"*

The plasma enhanced chemical vapor deposition (PECVD) process for coating polymer films has been used for producing SiO_x barrier coatings. By studying processes made in BEPEX, it has shown that operating with different gas mixtures of hexamethyldisiloxane (HMDSO) and O₂ (keeping constant the total gas flux) and two different values of the input power (25 and 30W), it's possible to obtain good films with a very low powder content in particular conditions. As the oxygen content increases, the growth rate of the plasma film decreases. The chemistry of the films (studied with FTIR) seems completely different to the chemistry of the powder (except for the powder collected at the top electrode). In fact, the more is the oxygen amount, the less is the CH_x content in the powder. The plasma observed is a plasma crystal, a solid phase of dusty plasmas, that consists of small particles floating in the background plasma.

Jonathan ROSSEL: *"ELMs analysis and control in TCV"*

An RMP (Resonant Magnetic Perturbation) coil is proposed as a minor upgrade of TCV. In 2007, numerical tools have been developed to assess the efficiency of the coil for ELM control and other applications (e.g. error field correction) as a function of its parameters (position, dimensions, geometrical structure and current limit). These tools have been benchmarked with similar studies provided by the DIII-D and JET teams.

Christian SCHLATTER: *"Ion physics on TCV"*

The prompt appearance of suprathermal ion populations (which are typically ~10 times more energetic than the bulk ions and comprise up to 30% of the ions) in ECCD discharges on TCV were explained in the frame of ion-acoustic turbulence (IAT). A model for the IAT was implemented in a numerical finite differences code. It was shown that the suprathermal electrons produced by ECCD (with drift speeds of about 10% the speed of light) drive ion-acoustic waves which are then Landau damped on the ions (anomalous ion heating).

Further activities include:

- Measurement of the profile of suprathermal ions by vertically displacing the plasma across the line of sight of the Compact Neutral Particle Analyzer (CNPA).
- Displacement of the CNPA on the torus with the possibility to observe the plasma obliquely (2008 campaign).
- Determination of the key parameters of the electrons by modelling the oblique ECE emission using the raytracing code NOTEC-TCV.
- Modelling of active charge exchange (injection of the Diagnostic Neutral Beam) using the Monte Carlo code DOUBLE-TCV.
- Absolute cross-calibration of the two NPA on TCV (possibility to calculate absolute neutral densities and the isotopic plasma composition).
- Launch of a collaborative Wiki on the CRPP intranet to facilitate virtual documentation, communication and collaboration in scientific, technical and administrative topics of the institute.

Christian THEILER: *"Experimental investigation of plasma turbulence and blobs in TORPEX"*

A better understanding of intermittent cross-field transport in the edge of confinement devices could allow to find ways to increase plasma confinement and divertor efficiency.

The study of curvature driven turbulence in TORPEX by a two-dimensional Langmuir probe array has shown a link between the radial density gradient and the

occurrence of intermittent transport events. The properties of intermittently occurring, isolated structures (blobs), that are ejected from the main plasma and that propagate radially outwards, are being analyzed with a pattern recognition algorithm. The goal is to validate predictions of analytical and numerical blob models. Ways to influence the ExB profile and in this way lower the cross-field transport are also being explored.

Robert TYE: *"Analysis of ELM Filament Characteristics on TCV"*

Edge Localised Modes (ELMs) are MHD instabilities associated with the steep pressure profile in H-mode plasmas. Using data from the fast-reciprocating Langmuir probe, work was carried out to investigate the rich filamentary structure of the ELMs as well as their radial dynamics. The ELM filaments were found to propagate with a radial velocity of around 1km/s which corresponds well with velocities seen in other devices, and within error bars the radial velocity is found to be constant throughout the main SOL but increases significantly upon entering the wall shadow. The ELM filaments were found to have a radial size of around 1.5cm which corresponds well with results from other machines. Observations were also made of radiation activity immediately prior to the ELM event on AXUV chords observing areas near the x-point and the top of the plasma. These observations are linked to radiation activity observed near the x-point in tomographic inversion of the AXUV data suggesting the ELM may be starting away from the ballooning region.

This work was originally started within the frame of a PhD thesis, but the work will no longer continue due to the departure of the PhD supervisor.

Lyubomira VELEVA: *"Development and Characterization of Tungsten-Base Materials for Fusion Applications"*

The first step consisted of selecting optimal compositions and manufacturing routes. Selected compositions include W-Y, W-Y₂O₃, and W-TiC materials. Selected manufacturing routes include mechanical alloying followed by sintering and/or hot isostatic pressing and/or (ev. high-speed) hot extrusion). Recent activities have been focused on the W-Y₂O₃ material. W-0.3Y₂O₃ powders (in weight percent) were prepared by mechanically alloying pure W powder particles (up to 4-6µm in diameter) with Y₂O₃ oxide particles (about 20nm in diameter) in a planetary ball mill, in an argon or a hydrogen atmosphere. The evolution of particle size and crystallite size with milling time, as well as X-ray diffractometry, showed that the milling time should not exceed 10hrs, in order to obtain small and stabilized particle sizes and crystallite sizes and to avoid important formation of W-C particles, due to contamination of the powder by the balls and walls of the milling system, which could lead to strong embrittlement of the material. No significant effect of the atmosphere on the particle size and morphology was evidenced. However, the W-0.3Y₂O₃ powders mechanically alloyed in hydrogen exhibit larger microhardness values than the W-0.3Y₂O₃ powders mechanically alloyed in Argon.

Gang YU: *"SANS analysis of irradiation-induced defects in metals and alloys"*

In the last three years preliminary small angle neutron scattering (SANS) measurements were performed on irradiated bcc materials, such as the EUROFER 97 reduced activation tempered martensitic (RAFM) steel, which confirmed that the SANS technique allows the detection of irradiation-induced defects smaller than 1 nm. These nanoscale defects cannot be resolved using transmission electron microscopy (TEM). However, it is thought that they could contribute to radiation hardening and/or embrittlement of RAFM steels at irradiation temperatures below 400°C. So, complete characterization of these small defects (type, size distribution, density) as a function of irradiation dose and temperature appears indispensable to assess the properties/microstructure

relationships in RAFM steels and then to establish their potentiality of use as structural materials for future fusion power reactors.

The results showed that the amplitude of the scattered signal is consistent with a distribution of nano-sized particles and that the dose dependence of the number density of particles follows qualitatively a reasonable trend, i.e. the number density increases with the dose. Since the irradiated tempered martensitic steels are very complex systems in term of microstructure and chemistry, it has to be pointed out that the irradiation-induced nano-defects can be of different types, such as voids, gas bubbles and/or nano-precipitates. All these irradiation-induced defects may naturally contribute to the scattered signal and therefore make a correct interpretation of the data not straightforward.

In addition, we initiated molecular dynamics (MD) simulations and TEM image simulations of all possible types of irradiation-induced defects for further comparison to experimental TEM images, as well as simulations of neutron diffraction patterns and comparison to SANS patterns, in order to gain knowledge about identification of nano-sized defects.

Alexandra ZHUCHKOVA: *"Faraday rotation measurements of the poloidal magnetic field in the TCV Tokamak, using a far-infrared polarimeter"*

A new far-infrared (FIR) polarimeter diagnostic for the TCV Tokamak is under construction and installation. The Faraday rotation measurements will improve the accuracy of the equilibrium reconstruction by the LIUQE equilibrium code.

It will allow us to measure the poloidal magnetic field and hence the current density profile in TCV plasmas. The current density $j(r)$ is linked to the safety factor q which is a key parameter for the transport models as well as for the magnetohydrodynamic (MHD) stability theory of tearing modes, sawteeth and disruptions.

The diagnostic will measure the Faraday rotation angle of FIR laser beams along 10 vertical lines of sight across the poloidal cross section of the tokamak. At the time of writing the conceptual design of the diagnostic is finished, all components of the polarimeter have been tested. Currently, the diagnostic is under installation on TCV and the LIUQE equilibrium code is under modification in order to include the information from the new diagnostic.

Costanza ZUCCA: *"Effects of local ECCD driven by the optimized Equatorial and Upper EC Launchers on ITER"*

The present ITER base-line design has the EC launchers providing only co-ECCD. A variant of the EC system was recently proposed to enlarge the physics programs covered by the Upper (UL) and Equatorial (EL) Launchers. This study aims to provide the potential range of the q profile control achievable by this optimization, including the possibility to drive counter-ECCD and central ECH. Since the EL can only drive co-ECCD, if ECH power is needed to assist the L-H transition during ramp-up, it can have detrimental effects on the final profiles, such as removing the reverse shear. Counter-ECCD offers greater control of the plasma current density and provides, when balanced with co-ECCD, pure ECH with no net driven current. The performance of the EL in tailoring the q profile by adding co-/counter-ECCD has been analyzed. Effects of current drive and deposition width on sawtooth control by UL have also been investigated. The modelling has been carried out with both equilibrium and transport codes.

Moreover, the investigation started during 2006 on swing ECCD (SECCD) has been carried on with a dedicated set of experiments aiming to study the transport properties at large s with off-axis deposition of SECCD and thus to investigate if, at high values of s , $T_e(\text{cnt}) > T_e(\text{co})$ as predicted by micro-turbulence.

APPENDICES

APPENDIX A *Articles Published in Refereed Scientific Reviews During 2007*

(see CRPP archives at <http://crppwww.epfl.ch/archives>)

S. Alberti, *The gyrotron: a tool for plasma heating and tailoring the current profile in ITER.*, Nature Physics 3(6) 376-377 (2007)

E. Asp, J. Weiland, X. Garbet, V. Parail, P. Strand and the EFDA-JET contributors, *Critical gradient response of the Weiland model*, Plasma Phys. Control. Fusion 49 (2007) 1221-1243

N. Baluc, D.S. Gelles, s. Jitsukawa, A. Kimura, R.L. Klueh, G.R. Odette, B. van der Schaaf, *Status of reduced activation ferritic/martensitic steel development*, J. Nucl. Mater. 367-370, 33-41 (2007)

N. Baluc, K. Abe, J.L. Boutard, et al., M.Q. Tran, *Status of R&D activities on materials for fusion power reactors*, Nucl. Fusion 47, S696-S717 (2007)

R. Behn, A. Alfier, S.Yu. Medvedev et al, *Edge profiles of electron temperature and density during ELMy H-mode in ohmically heated TCV plasmas*, Plasma Phys. Control. Fusion 49 (2007) 1289-1308

R. Bonade, P. Spaetig, N. Baluc, *Fracture toughness properties in the transition region of the Eurofer97 tempered martensitic steel*, J. Nucl. Mater. 367-370, 581-586 (2007)

R. Bonade, P. Spaetig, *The Evolution of the Mobile Dislocation Density during Successive Stress Relaxation Transients*, Materials Science and Engineering (2007), doi:10.1016/j.msea.2006.10.196

A. Bottino, A.G. Peeters, R. Hatzky, S. Jolliet, B.F. McMillan, T.M. Tran, L. Villard, *Nonlinear low noise particle-in-cell simulations of electron temperature gradient driven turbulence*, Phys. Plasmas 14, 010701 (2007)

L. Bottura, P. Bruzzone, J.B. Lister, C. Marinucci, A. Portone, *Computations of AC losses in the ITER magnetics during fast field transients*, IEEE Trans. Appl. Supercond., 17, 2, 2438-2441 (2007)

L. Bottura, P. Bruzzone, M. Calvi, R. Herzog, C. Marinucci, *Simulation of the flow-reversal effect in dual channel CICC for ITER*, Cryogenics 47, 553-562 (2007)

P. Bruzzone, M. Bagnasco, D. Ciazynski, et al., R. Herzog, B. Stepanov, R. Wesche, *Test results of two ITER TF conductor short samples using high current density Nb3Sn strands*, IEEE Trans. Appl. Supercond., 17, 2, 1370-1373 (2007)

P. Bruzzone, R. Herzog, B. Stepanov, M. Vogel, R. Wesche, *Test results of a large size, forced flow Nb3Sn conductor, based on a design alternative to the cable-in-conduit*, IEEE Trans. Appl. Supercond., 17, 2, 1473-1476 (2007)

P. Bruzzone, B. Stepanov, R. Dettwiler, F. Staehli, *Results of contact resistance distribution in NbTi and Nb3Sn ITER conductor termination*, IEEE Trans. Appl. Supercond., 17, 2, 1378-1381 (2007)

P. Bruzzone, B. Stepanov, R. Wesche, M. Vogel, *Design, manufacture and first results of a novel, large size, Nb₃Sn force flow conductor*, Proc. ICMC'06 (ISBN 978-80-239-8884-0), 123-126 (2007)

Y. Camenen, F. Hofmann, A. Pochelon, A. Scarabosio, S. Alberti, G. Arnoux, P. Blanchard, S. Coda, T.P. Goodman, M.A. Henderson, E. Nelson-Melby, L. Porte, O. Sauter, *Current profile tailoring using localised electron cyclotron heating in highly elongated TCV plasmas*, Nucl. Fusion 47, 586-596 (2007)

Y. Camenen, A. Pochelon, R. Behn, A. Bottino, A. Bortolon, S. Coda, A. Karpushov, O. Sauter, G. Zhuang and the TCV team, *Impact of plasma triangularity and collisionality on electron heat transport in TCV L-mode plasmas*, Nucl. Fusion 47 (2007) 510-516

A.V. Chankin, D.P. Coster, N. Asakura, et al., R.A. Pitts, *A possible role of radial electric field in driving parallel ion flow in scrape-off layer of divertor tokamaks*, Nucl. Fusion 47, 762 (2007)

A.V. Chankin, D.P. Coster, N. Asakura, X. Bonnin, G.D. Conway, G. Corrigan, S.K. Erements, W. Fundamenski, J. Horacek, A. Kallenbach, M. Kaufmann, C. Konz, K. Lackner, H.W. Muller, J. Neuhauser, R.A. Pitts, M. Wischmeier, *Discrepancy between modelled and measured radial electric fields in the scrape-off layer of divertor tokamaks: a challenge for 2D fluid codes?*, Nucl. Fusion 47, 479 (2007)

R. Chavan, M. Henderson, R. Bertizzolo, J.-D. Landis, F. Sanchez, H. Shidara, *The ECH front steering launcher for the ITER upper port*, Fusion Eng. & Design 82, 867-872, (2007)

J.P. Coad, P. Andrew, S.K. Erements, D.E. Hole, J. Likonen, M. Mayer, R.A. Pitts, M. Rubel, J. D. Strachan, E. Vainonen-Ahlgren, A. Widdowson, and JET-EFDA Contributors, *Erosion and deposition in the JET MkII-SRP divertor*, Journal of Nuclear Materials 363–365 (2007) 287–293

S. Coda, E. Asp, E. Fable, T.P. Goodman, O. Sauter, V.S. Udintsev, R. Behn, M.A. Henderson, A. Marinoni, G.P. Turri, C. Zucca and the TCV team, *The Physics of Electron Internal Transport Barriers in the TCV Tokamak*, Nucl. Fusion 47, 714-720 (2007)

W.A. Cooper, J.P. Graves, M. Jucker, K.Y. Watanabe, Y. Narushima, T. Yamaguchi, *Fluid Magnetohydrodynamic Stability in a Heliotron with Anisotropic Fast Particle Species*, Plasma Phys. Control. Fusion 49 (2007) 1177-1191

G.A. Cooper, M. Jucker, W.A. Cooper, J.P. Graves, M. Yu. Isaev, *Exact canonical drift Hamiltonian formalism with pressure anisotropy and finite perturbed fields*, Physics of Plasmas 14 (2007) 102506

G. De Temmerman, R. A. Pitts, V.S. Voitsenya, L. Marot, G. Veres, M. Maurer, P. Oelhafen, *First mirror tests for ITER: Influence of material choice on the erosion/deposition mechanisms affecting optical reflectivity*, Journal of Nuclear Materials 363–365 (2007) 259–263

B.P. Duval, A. Bortolon, A. Karpushov, R.A. Pitts, A. Pochelon, A. Scarabosio, *Bulk Plasma Rotation in the TCV Tokamak in the Absence of External Momentum Input (Invited paper)*, Plasma Phys. Control. Fusion 49 (2007) B195

T. Eich, A. Kallenbach, R.A. Pitts, S. Jachmich, J. C. Fuchs, A. Herrmann, J. Neuhauser, ASDEX Upgrade Team and JET-EFDA Contributors, *Divertor power deposition and target current asymmetries during type-I ELMS in ASDEX Upgrade and JET*, Journal of Nuclear Materials 363–365 (2007) 989–993

- T. Eich, P. Andrew, A. Herrmann, W. Fundamenski, A. Loarte, R.A. Pitts and JET-EFDA Contributors**, *ELM resolved energy distribution studies in the JET MKII Gas-Box divertor using infra-red thermography*, Plasma Phys. Control. Fusion 49 (2007) 573
- D. Fasel, S. Alberti, T. Bonicelli, E. Droz, T. Goodman, M.-A. Henderson, J.P. Hogge, X. Llobet, B. Marletaz, Ph. Marmillod, A. Perez, L. Porte, U. Siravo, M.Q. Tran**, *Installation and commissioning of the EU test facility for ITER gyrotrons*, Fusion Eng. & Design 82, 881-886, (2007)
- G.Y. Fu, M. Isaev, L.P. Ku, M. Mikhailov, M.H. Redi, R. Sanchez, A. Subbotin, W.A. Cooper, S.P. Hirshman, D.A. Monticello, A. Reiman, M. Zarnstorff**, *Ideal Magnetohydrodynamic Stability of the NCSX*, Fusion Sci. & Technol. 51(2), 218-231 (2007)
- W. Fundamenski, R.A. Pitts and JET-EFDA Contributors**, *ELM-wall interaction on JET and ITER*, Journal of Nuclear Materials 363-365 (2007) 319-324
- O.E. Garcia, R.A. Pitts, J. Horacek, A. H. Nielsen, W. Fundamenski, J.P. Graves, V. Naulin, J. Juul Rasmussen**, *Turbulent transport in the TCV SOL*, Journal of Nuclear Materials 363-365 (2007) 575-580
- O.E. Garcia, J. Horacek, R.A. Pitts, A.H. Nielsen, W. Fundamenski, V. Naulin, J. Juul Rasmussen**, *Fluctuations and transport in the TCV scrape-off layer*, Nucl. Fusion 47, 667-676 (2007)
- O.E. Garcia, R.A. Pitts, J. Horacek, J. Madsen, V. Naulin, A.H. Nielsen, J. Juul Rasmussen**, *Collisionality dependent transport in TCV SOL plasmas*, Plasma Phys. Control. Fusion 49 (2007) B47
- V. Grandgirard, Y. Sarazin, P. Angelino, A. Bottino, N. Crouseilles, G. Darmet, G. Dif-Pradalier, X. Garbet, P. Gendrih, S. Jolliet, G. Latu, E. Sonnendruecker, L. Villard**, *Global full-f gyrokinetics simulations of plasma turbulence*, Plasma Phys. Control. Fusion 49, 12B (2007)
- J.P. Graves, C. Wahlberg**, *Safety factor corrections to the magnetohydrodynamic internal kink mode in a tokamak*, Phys. of Plasmas 14, 082504-1 (2007)
- B. Gulejova, R.A. Pitts, M. Wischmeier, R. Behn, D. Coster, J. Horacek, J. Marki**, *SOLPS5 modelling of the type III ELMing H-mode on TCV*, Journal of Nuclear Materials 363-365 (2007) 1037-1043
- A.A. Howling, L. Sansonnens, Ch. Hollenstein**, *Electromagnetic sources of nonuniformity in large area capacitive reactors*, Thin Solid Films 515, 5059-5064 (2007)
- A.A. Howling, B. Strahm, P. Colsters, L. Sansonnens, Ch. Hollenstein**, *Fast equilibration of silane/hydrogen plasmas in large area RF capacitive reactors monitored by optical emission spectroscopy*, Plasma Sources Sci. Technol. 16, 679-696 (2007)
- Y. Idomura, M. Ida, S. Tokuda, L. Villard**, *New conservative gyrokinetic Vlasov code and its comparison to gyrokinetic delta-f particle-in-cell code*, J. Comput. Phys. 226 (2007) 244-262
- S. Jachmich, T. Eich, W. Fundamenski, A. Kallenbach, R.A. Pitts and JET-EFDA Contributors**, *Divertor particle and power deposition profiles in JET ELMy H-mode discharges*, Journal of Nuclear Materials 363-365 (2007) 1050-1055

S. Jolliet, A. Bottino, P. Angelino, R. Hatzky, T.M. Tran, B.F. McMillan, O. Sauter, Y. Idomura, L. Villard, A global collisionless PIC code in magnetic coordinates, Computer Phys. Commun. 177(5), 409-425 (2007)

M. Jucker, V.P. Pavlenko, On the kinetic stability of magnetic structures in electron drift turbulence, Phys. Plasmas 14, 032303 (2007)

M. Jucker, V.P. Pavlenko, On the modulational stability of magnetic structures in electron drift turbulence, Phys. Plasmas 14, 102313 (2007)

B. Labit M. Ottaviani, Comparison between fluid Electron Temperature Gradient-driven simulations and Tore Supra experiments on electron heat transport, J. Plasma Phys. 73(2), 199-206 (2007)

B. Labit, I. Furno, A. Fasoli, A. Diallo, S.H. Mueller, G. Plyushchev, M. Podesta, F.M. Poli, Universal statistical properties of drift-interchange turbulence in TORPEX toroidal plasmas, Phys. Rev. Letters 98, 2550022 (2007)

J.-D. Landis, R. Bertizzolo, R. Chavan, M. Henderson, F. Sanchez, Design of the critical components in the ITER ECH upper launcher steering mechanism, Fusion Eng. & Design 82, 897-904 (2007)

A. Laorte, B. Lipschultz, A.S. Kukushkin et al., R.A. Pitts, Power and particle control, Nucl. Fusion 47, S203 (2007)

B. Lipschultz, X. Bonnin, G. Counsell, et al., R.A. Pitts, Plasma– surface interaction, scrape-off layer and divertor physics: implications for ITER, Nucl. Fusion 47, 1189 (2007)

J.B. Lister, J.W. Farthing, M. Greenwald, I. Yonekawa, The ITER CODAC conceptual design, Fusion Eng. & Design 82, 1167-1173, (2007)

X. Litaudon, J.P.S. Bizzaro, C.D. Challis, et al. R.A. Pitts and the JET EFDA contributors, Prospects for steady-state scenarios on JET, Nucl. Fusion 47, 1285 (2007)

X. Litaudon, G. Arnoux, M. Beurskens, et al., R.A. Pitts, Development of steady-state scenarios compatible with ITER-like wall conditions, Plasma Phys. Control. Fusion 49 (2007) B529

A. Litnovsky, P. Wienhold, V. Philipps, et al., R.A. Pitts, Diagnostic mirrors for ITER: A material choice and the impact of erosion and deposition on their performance, J. Nucl. Mater. 363–365 (2007) 1395-1402

G.E. Lucas, G.R. Odette, H. Matsui, A. Moeslang, P. Spaetig, J. Rensman, The role of small specimen test technology in fusion materials development, Journal of Nuclear Materials 367-370 (2007) 1549-1556

D. Maisonnier, D. Campbell, I. Cook, et al., M.Q. Tran, Power plant conceptual studies in Europe, Nucl. Fusion 47, 1524-1532 (2007)

C. Marinucci, L. Bottura, P. Bruzzone, B. Stepanov, Analysis of the transverse heat transfer coefficients in a dual channel ITER-type cable-in-conduit conductor, Cryogenics 47, 563-576 (2007)

J. Marki, R.A. Pitts, T. Eich, A. Herrmann, J. Horacek, F. Sanchez, G. Veres, Sheath heat transmission factors on TCV, Journal of Nuclear Materials 363–365 (2007) 382–388

A. Mueck, Y. Camenen, S. Coda, L. Curchod, T.P. Goodman, H.P. Laqua, A. Pochelon, L. Porte, V.S. Udintsev, F. Volpe, and the TCV Team, Electron

Bernstein Wave Heating and Emission in the TCV Tokamak, Fusion Sci. & Technol. 52, 221-229 (2007)

A. Mueck, L. Curchod, Y. Camenen, S. Coda, T.P. Goodman, H.P. Laqua, A. Pochelon, L. Porte, F. Volpe, *Demonstration of Electron Bernstein Wave Heating in a Tokamak via O-X-B Double Mode Conversion*, Phys. Rev. Letters 98, 175004 (2007)

P. Mueller, R. Bonade, P. Spaetig, *Fracture Properties of Notched and Pre-Cracked Specimens of a Tempered Martensitic Steel at Low Temperature*, Materials Science and Engineering A, (2007) doi:10.1016/j.msea.2006.09.172

G.R. Odette, T. Yamamoto, H. Kishimoto, M. Sokolov, P. Spaetig, W.J. Yang, J.-W. Rensman, G.E. Lucas, *A master curve analysis of F82H using statistical and constraint loss size adjustments of small specimen data*, J. Nucl. Mater 329-333, 1243-1247 (2007)

R.A. Pitts, J. Horacek, W. Fundamenski, O.E. Garcia, A.H. Nielsen, M. Wischmeier, V. Naulin, J. Juul Rasmussen, *Parallel SOL flow on TCV*, Journal of Nuclear Materials 363-365 (2007) 505-510

R.A. Pitts, P. Andrew, G. Arnoux, T. Eich, W. Fundamenski, A. Huber, C. Silva, D. Tskhakaya and JET EFDA Contributors, *ELM transport in the JET scrape-off layer*, Nucl. Fusion 47, 1437 (2007)

R.A. Pitts, P. Andrew, G. Arnoux, T. Eich, W. Fundamenski, A. Huber, C. Silva, D. Tskhakaya, and JET EFDA Contributors, *ELM Transport in the JET Scrape-Off Layer*, Nucl. Fusion 47, 1437-1448 (2007)

A. Pochelon, A. Mueck, L. Curchod, Y. Camenen, S. Coda, B.P. Duval, T.P. Goodman, I. Klimanov, H.P. Laqua, Y. Martin, J.-M. Moret, L. Porte, A. Sushkov, V.S. Udintsev, F. Volpe and the TCV Team, *Electron Bernstein wave heating of overdense H-mode plasmas in the TCV tokamak via O-X-B double mode conversion*, Nucl. Fusion 47, 1552-1558 (2007)

M. Podesta, A. Diallo, A. Fasoli, I. Furno, B. Labit, S.H. Mueller, F.M. Poli, *Characterization of the electron distribution function in an*, Plasma Phys. Control. Fusion 49 (2007) 175-182

F.M. Poli, M. Podesta A. Fasoli, *Development of electrostatic turbulence from drift-interchange instabilities in a toroidal plasma*, Phys. Plasmas 14(5), 052311 (2007)

L. Porte, S. Coda, S. Alberti, G. Arnoux, P. Blanchard, A. Bortolon, A. Fasoli, T. Goodman, I. Klimanov, Y. Martin, M. Maslov, A. Scarabosio, H. Weisen, *Plasma dynamics with second and third harmonic ECRH and access to quasi-stationary ELM-free H-mode on TCV*, Nucl. Fusion 47, 952-960 (2007)

A. Ramar, N. Baluc, R. Schaeublin, *Effect of irradiation on the microstructure and the mechanical properties of oxide dispersion strengthened low activation ferritic/martensitic steel*, J. Nucl. Mater. 367-370, 217-221 (2007)

M.J. Rubel, J.P. Coad, R.A. Pitts, *Overview of co-deposition and fuel inventory in castellated divertor structures at JET*, J. Nucl. Mater. 367-370, Part 2, 1432-1437 (2007)

L. Savoldi Richard, P. Bruzzone, N. Mitchell, P.L. Ribani, R. Zanino,, *Assessment of the effect of current non-uniformity on the ITER Nb3Sn good joint short sample DC performance*, IEEE Trans. Appl. Supercond., 17, 2, 1382-1385 (2007)

A. Scarabosio, A. Pochelon, Y. Martin, *Plasma shape stabilisation of current rise MHD instabilities in TCV*, Plasma Phys. Control. Fusion 49 (2007) 1041-1060

P. Spaetig, E.N. Campitelli, R. Bonade, N. Baluc, *Assessment of plastic flow and fracture properties with small specimen test techniques for IFMIF-designed specimens*, Nucl. Fusion 45, 635-641 (2007)

P. Spaetig, R. Bonade, G.R. Odette, J.W. Rensman, E.N. Campitelli, P. Mueller, *Plastic flow properties and fracture toughness characterization of unirradiated and irradiated tempered martensitic steels*, J. Nucl. Mater. 367-370, 527-538 (2007)

R. Stoenescu, R. Schaeublin, D. Gavillet, N. Baluc, *Welding-induced mechanical properties in austenitic stainless steels before and after neutron irradiation*, J. Nucl. Mater. 360, 255-264 (2007)

R. Stoenescu, R. Schaeublin, D. Gavillet, N. Baluc, *Mechanical properties-microstructure correlation in neutron irradiated heat-affected zones of austenitic stainless steels*, J. Nucl. Mater. 362, 287-292 (2007)

B. Strahm, A.A. Howling, L. Sansonnens, Ch. Hollenstein, *Optimization of the microcrystalline silicon deposition efficiency*, J. Vac. Sci. Technol. A 25(4), 1198-1202 (2007)

B. Strahm, A.A. Howling, L. Sansonnens, Ch. Hollenstein, Ch. Ellert, J. Meier, U. Kroll, L. Feitknecht, C. Ballif, *Microcrystalline silicon deposited at high rate on large areas from pure silane with efficient gas utilization*, Solar Energy Mater Solar Cells 91, 495-502 (2007)

B. Strahm, A.A. Howling, L. Sansonnens, Ch. Hollenstein, *Plasma silane concentration as a determining factor for the transition from amorphous to microcrystalline silicon in SiH₄/H₂ discharges*, Plasma Sources Sci Technol 16, 80-89 (2007)

B. Strahm, A.A. Howling, Ch. Hollenstein, *Plasma diagnostics as a tool for process optimization: the case of microcrystalline silicon*, Plasma Phys. Control. Fusion 49 (2007) B411-B418

V.S. Udintsev, G. Turri, E. Asp, Ch. Schlatter, T.P. Goodman, O. Sauter, H. Weisen, P. Blanchard, S. Coda, B.P. Duval, E. Fable, A. Gudozhnik, P.F. Isoz, M.A. Henderson, I. Klimanov, X. Llobet, Ph. Marmillod, A. Mueck, L. Porte, *Recent electron cyclotron emission results on TCV*, Fusion Sci. & Technol. 52, 161-168 (2007)

V.S. Udintsev, G. Turri, E. Asp, Ch. Schlatter, T.P. Goodman, O. Sauter et al, *Overview of Recent Results of ECE on TCV*, Fusion Sci. & Technol. 52, 161 (2007)

G. Veres, R.A. Pitts, M. Wischmeier, B. Gulejova, J. Horacek, S. Kalvin, *Radiation distributions in TCV*, J. Nucl. Mater. 363-365 (2007) 1104-1109

C. Wahlberg, J. P. Graves, *Stability analysis of internal ideal modes in low-shear tokamaks*, Phys. Rev. Letters 14, 110703 (2007)

R. Wesche, R. Heller, P. Bruzzone, W.H. Fietz, R. Lietzov, A. Vostner, *Design of high-temperature superconductor current leads for ITER*, Fusion Eng. and Design 82, 1385-1390 (2007)

R. Wesche, F. Roth, P. Bruzzone, *Comparison of the dc performance of various Nb₃Sn strands used in cable-in-conduit conductors for fusion*, Proc. ICMC'06 (ISBN 978-80-239-8884-0), 145-148 (2007)

L. Zani, D. Ciazynski, A. Torre, P. Bruzzone, B. Stepanov, R. Dettwiler, F. Staehli, *Analysis of DC properties and current distribution TFAS ITER conductor samples using high J_c Nb₃Sn advanced strands*, IEEE Trans. Appl. Supercond., 17, 2, 1374-1377 (2007)

R. Zanino, M. Astrov, M. Bagnasco, et al., R. Wesche, Predictive analysis of the ITER poloidal field conductor insert (PFCI) test program, IEEE Trans. Appl. Supercond., 17, 2, 1353-1356 (2007)

APPENDIX B Conferences and Seminars

(see CRPP archives at <http://crppwww.epfl.ch/archives>)

B.1 Conference and conference proceedings published in 2007

S. Alberti, G. Arnoux, J. Berrino, Y. Camenen, S. Coda, B.P. Duval, T.P. Goodman, J-M. Moret, J.I. Paley, L. Porte and TCV team, *Experiments with real-time controlled ECW on the TCV Tokamak*, 4th IAEA Technical Meeting on "ECRH Physics and Technology for ITER", IAEA Headquarters, Vienna, AUSTRIA, 06.06. - 08.06.2007

P. Angelino, V. Grandgirard, Y. Sarazin, G. Dif-Pradier, S. Jolliet, A. Bottino, X. Garbet, Ph. Ghendrih, B.F. McMillan, T.M. Tran, L. Villard, *Benchmark of a semi-Lagrangian and a Lagrangian code for gyrokinetic simulations*, 12th US-EU Transport Taskforce Workshop, San Diego, Ca, US, 17.04. - 20.04.2007

P. Angelino, V. Grandgirard, Y. Sarazin, G. Dif-Pradier, S. Jolliet, A. Bottino, X. Garbet, Ph. Ghendrih, B.F. McMillan, T.M. Tran, L. Villard, *Effects of Plasma Elongation on Geodesic Acoustic Modes*, International Sherwood Fusion Theory Conference, Annapolis, MD, USA, 23.04. - 25.04.2007

G. Arnoux, P. Andrew, M. Beurskens, S. Brezinsek, C. Challis, P. De Vries, W. Fundamenski, E. Gauthier, C. Giroud, A. Huber, S. Jachmich, X. Litaudon, R.A. Pitts, F. Rimini and JET EFDA contributors, *Plasma-wall heat loads in ITER-like advanced Tokamak scenarios on JET*, 34th EPS Conference on Plasma Physics, Warsaw Congress Centre, Poland, 02.07. - 06.07.2007

E. Asp, W. Horton, L. Porte, S. Alberti, E. Fable, J. Kim, Y. Martin, O. Sauter, G. Turri and the TCV Team, *Transport analysis of multi-phase H-mode shot at TCV*, International Sherwood Fusion Theory Conference, Annapolis, MD, USA, 23.04. - 25.04.2007

E. Asp, J. Kim, W. Horton, L. Porte, S. Alberti, E. Fable, Y. Martin, O. Sauter, G. Turri and the TCV Team, *ETG modelling of a TCV multi-phase H-mode shot*, 49th APS Conf., Orlando, Florida, USA, 12.11. - 16.11.2007

E. Asp, V. Udintsev, T.P. Goodman, O. Sauter and G. Turri, *Global Plasma Oscillation Regime and Its Suppression on TCV*, 49th APS Conf., Orlando, Florida, USA, 12.11. - 16.11.2007

N. Baluc, *Reduced activation materials*, GCEP Workshop, Princeton University, USA, May 2006

N. Baluc, *Fusion reactor materials - challenge for the next decades*, Euroscience Open Forum (ESOF 2006), Muenich, Germany, July 2006

N. Baluc, *Status of European R&D in the field of SSTD*, IEA Workshop on Fusion Reactor Materials, Tokyo, Japan, July 2006

N. Baluc, *Status of European R&D in the field of ODS steels*, IEA Workshop on Fusion Reactor Materials, Tokyo, Japan, July 2006

N. Baluc, *Modelling needs for fusion materials*, 14th European Fusion Physics Workshop (EFPW14) on Computational Plasma Physics for ITER and Beyond, Greoux-les-Bains, France, December 2006

N. Baluc, *Platform for high temperature materials (PHiTEM)*, Annual Meeting of the Swiss Society of Physics, February 2007

A. Bencze, R.A. Pitts, O.E. Garcia, M. Berta, G. Veres, *On the statistics of ELM filaments measured by fast low field side wall Langmuir probes on TCV*, 34th EPS Conference on Plasma Physics, Warsaw Congress Centre, Poland, 02.07. - 06.07.2007

A. Bencze, R. A. Pitts, O. E. Garcia, M. Berta, G. Veres and the TCV Team, *On the statistics of ELM filaments measured by fast low field side wall*, 34th EPS Conference on Plasma Physics, Warsaw Congress Centre, Poland, 02.07. - 06.07.2007

M.N.A. Beurskens, G. Arnoux, P. de Vries, C. Giroud, P. Lomas, F.G. Rimini, A.S. Brezinsek, C. Challis, E. de la Luna, W. Fundamenski, S. Gerasimov, E Giovannozzi, E. Joffrin, A. Huber, S.Jachmich, X. Litaudon, T. Loarer, J. Mailloux, *Edge pedestal characterisation in high triangularity Advanced Tokamak with impurity seeding at JET*, 34th EPS Conference on Plasma Physics, Warsaw Congress Centre, Poland, 02.07. - 06.07.2007

A. Bortolon, B.P. Duval, A. Scarabosio, A. Karpushov, A. Pochelon, *Toroidal momentum transport in limited and diverted TCV Ohmic plasmas*, 12th US-EU Transport Taskforce Workshop, San Diego, Ca, US , 17.04. - 20.04.2007

V.R. Boshuk, W.A. Cooper, M.I. Mikhailov, J. Nuehrenberg, V.D. Shafranov, *Search for very high-beta MHD stable quasi-isodynamic configurations*, Joint Conference of 17th International Toki Conference on Physics of Flows and Turbulence in plasmas and 16th International Stellarator/Heliotron Workshop, Toki, Japan , 15.10. - 19.10.2007

V.R. Bovshuk, W.A. Cooper, M.Yu. Isaev, M.I. Mikhailov, J. Nuehrenberg, V.D. Shafranov, A.A. Subbotin, R. Zille, *Search for quasi-isodynamic configurations with diminished Pfirsch-Schlueter current*, 34th EPS Conference on Plasma Physics, Warsaw Congress Centre, Poland, 02.07. - 06.07.2007

S. Brunner, T.M. Tran, X. Lapillonne, M. Brunetti, *Development of a Semi-Lagrangian Gyrokinetic Simulation Code*, 49th APS Conf., Orlando, Florida, USA, 12.11. - 16.11.2007

R. J. Buttery, S. Coda, R. J. La Haye, E. Strait, the DIII-D team and JET-EFDA contributors, *Neoclassical tearing mode stability at low rotation and implications for ITER*, 3rd IAEA-TM on Theory of Plasma Instabilities, University of York, York, UK, 26.03. - 28.03.2007

R. J. Buttery, S. Coda, D. F Howell, A. Isayama, R. J. La Haye, D. Raju, A. Sen, E. Strait, DIII-D team, JET-EFDA contributors, *Neoclassical tearing mode stability at ITER-like parameters*, 34th EPS Conference on Plasma Physics, Warsaw Congress Centre, Poland, 02.07. - 06.07.2007

A.V. Chankin, D.P. Coster, G. Corrigan, S.K. Erents, W. Fundamenski, A. Kallenbach, K. Lackner, J. Neuhauser, R.A. Pitts, the ASDEX Upgrade Team and JET-EFDA Contributors, *Mechanisms Affecting Radial Electric Field in the Tokamak SOL*, 34th EPS Conference on Plasma Physics, Warsaw Congress Centre, Poland, 02.07. - 06.07.2007

I.T. Chapman, S.D. Pinches, J.P. Graves, R.J. Akers, L.C. Appel, R.V. Budny, S. Coda, N.J. Conway, M. de Bock, L.-G. Eriksson, R.J. Hastie, T.C. Hender, G.T.A. Huysmans, T. Johnson, H.R. Koslowski, A. Kraemer-Flecken, M. Lennholm, Y. Lian, *The Physics of Sawtooth Stabilisation (invited paper)*, 34th

EPS Conference on Plasma Physics, Warsaw Congress Centre, Poland, 02.07. - 06.07.2007

R. Chavan, R. Bertizzolo, M. A. Henderson, J.D. Landis, F. Sanchez, *Design and material selection for a pressure controlled bellows actuator for the angular positioning of the steering mirror in the ITER ECRH upper port plug*, Euromat 2007, N_rnberg, Germany , 10.09. - 13.09.2007

S. Coda, L.-G. Eriksson, M. Lennholm, J. Graves, T. Johnson, J.H. Brzozowski, M. De Baar, D.F. Howell, S. Jachmich, V. Kiptily, R. Koslowski, M.-L. Mayoral, A. Mueck, S. Pinches, G. Saibene, M.I.K. Santala, M.F. Stamp, M. Valisa, JET-EFD, *NTM prevention by ICCD control of fast-ion-stabilised sawteeth*, 34th EPS Conference on Plasma Physics, Warsaw Congress Centre, Poland, 02.07. - 06.07.2007

S. Coda, O. Sauter, M.A. Henderson, T.P. Goodman and the TCV Team, *Steady-state, fully bootstrap-sustained discharges in the TCV tokamak*, 34th EPS Conference on Plasma Physics, Warsaw Congress Centre, Poland, 02.07. - 06.07.2007

S. Coda, O. Sauter, M.A. Henderson, T.P. Goodman and the TCV Team, *Steady-state, fully bootstrap-sustained discharges in the TCV tokamak*, 34th EPS Conference on Plasma Physics, Warsaw Congress Centre, Poland, 02.07. - 06.07.2007

W.A. Cooper, J.P. Graves, M. Jucker, K.Y. Watanabe, Y. Narushima, *Fluid Plasma Stability in Stellarators with Anisotropic Energetic Species*, 3rd IAEA-TM on Theory of Plasma Instabilities, University of York, York, UK, 26.03. - 28.03.2007

G.A. Cooper, M. Jucker, W.A. Cooper, J.P. Graves, M. Yu. Isaev, *Exact canonical drift Hamiltonian formalism with pressure anisotropy and finite perturbed fields*, 49th APS Conf., Orlando, Florida, USA, 12.11. - 16.11.2007

T. Dannert, S. Guenter, T. Hauff, F. Jenko, *Turbulent transport of energetic ions*, 12th European Fusion Theory Conf (EFTC), Madrid, 24.09. - 26.09.2007

A. Descoedres, C. Hollenstein, G. Waelder, R. Demellayer, R. Perez, *Time- and spatially-resolved characterization of electrical discharge machining plasma (Invited lecture)*, XXVIII International Conference on Phenomena in Ionized Gases (ICPIG 2007), July 2007, Prague, Czech Republic

A. Diallo, A. Fasoli, B. Labit, I. Furno, S.H. Mueller, M. Podesta, F.M. Poli, P. Ricci, F. Skiff, *Drift Wave Antenna Excitation in TORPEX Low-field Side*, 34th EPS Conference on Plasma Physics, Warsaw Congress Centre, Poland, 02.07. - 06.07.2007

J.-L. Dorier, Ch. Hollenstein, *(Strongly coupled) micro-plasma formation during opening of a low current electrical contact*, 18th International Symposium on Plasma Chemistry (ISPC18), Kyoto, Japan , 26.08. - 31.08.2007

B.P. Duval, A. Bortolon, A. Karpushov, R.A. Pitts, A. Pochelon, A. Scarabosio, *Bulk Plasma Rotation in the TCV Tokamak in the Absence of External Momentum Input (Invited paper)*, 34th EPS Conference on Plasma Physics, Warsaw Congress Centre, Poland, 02.07. - 06.07.2007

B.P. Duval, *Spontaneous Plasma Rotation Scaling in the TCV Tokamak*, 49th APS Conf., Orlando, Florida, USA, 12.11. - 16.11.2007

A. Encheva, G. Vayakis, R. Chavan, A. Karpouchov, J.-M. Moret, *3D Thermal and CFD Simulations of the Divertor Magnetic Coils for ITER*, NAFEMS World

Congress (Simul. Technol. for the Eng. Analysis Community), Vancouver, Canada, 22.05. - 25.05.2007

E. Fable, C. Angioni, A. Bottino, S. Brunner, T. Dannert, F. Jenko, O. Sauter, *The role of electron-driven microinstabilities in particle transport during electron ITBs*, 34th EPS Conference on Plasma Physics, Warsaw Congress Centre, Poland, 02.07. - 06.07.2007

J.W. Farthing, A.J. Capel, N. Cook, et al., J.B. Lister, *Data management at JET with a look forward to ITER*, ICALEPCS conference, Knoxville, USA, October 2007

A. Fasoli, *Peculiarities of burning plasmas and fast particle dynamics*, Burning plasma diagnostics, Varenna, Italy, 24.09. - 28.09.2007

A. Fasoli, A. Diallo, I. Furno, D. Iraj, B. Labit, S.H. Mueller, M. Podesta, G. Plyushchev, F.M. Poli, P. Ricci and C. Theiler, *Fluctuations, turbulence and related transport in the TORPEX magnetised toroidal plasma*, 49th APS Conf., Orlando, Florida, USA, 12.11. - 16.11.2007

I. Furno, A. Diallo, A. Fasoli, B. Labit, S.H. Mueller, M. Podesta, F.M. Poli, P. Ricci and C. Theiler, *Mechanism for plasma blob generation and related transport in the TORPEX toroidal plasma*, 12th US-EU Transport Taskforce Workshop, San Diego, Ca, US, 17.04. - 20.04.2007

I. Furno, A. Diallo, A. Fasoli, B. Labit, S.H. Mueller, M. Podesta, *Experimental investigation of blob physics in the TORPEX toroidal plasma*, 49th APS Conf., Orlando, Florida, USA, 12.11. - 16.11.2007

O.E. Garcia, J. Horacek, J.S. Larsen, S. Madsen, V. Naulin, A.H. Nielsen, R.A. Pitts, J.J. Rasmussen, *Convective transport by filamentary structures in scrape-off layer plasmas*, 34th EPS Conference on Plasma Physics, Warsaw Congress Centre, Poland, 02.07. - 06.07.2007

O.E. Garcia, R.A. Pitts, J. Horacek, J. Madsen, V. Naulin, A.H. Nielsen, J. Juul Rasmussen, *Collisionality dependent transport in TCV SOL plasmas*, 34th EPS Conference on Plasma Physics, Warsaw Congress Centre, Poland, 02.07. - 06.07.2007

S. Gnesin, S. Coda, *Design of a tomographic hard X-ray spectrometer for suprathreshold electron studies with ECRH*, Burning plasma diagnostics, Varenna, Italy, 24.09. - 28.09.2007

T.P. Goodman, S. Coda, S. Alberti, B.P. Duval, D. Fasel, M.A. Henderson, J.-P. Hogge, P.F. Isoz, P. Lavanchy, J. Lister, B. Marletaz, Ph. Marmillod, J.-M. Moret, L. Porte and TCV team, *Ten Years of Experience in Integrated Control of the Multi-Megawatt*, 4th IAEA Technical Meeting on "EC--RH Physics and Technology for ITER", IAEA Headquarters, Vienna, AUSTRIA, 06.06. - 08.06.2007

T.P. Goodman, V.S. Udintsev, F. Felici, C. Zucca, Ch. Schlatter, *Co- and Counter-viewing oblique ECE measurements during ECH and ECCD on the TCV tokamak*, 34th EPS Conference on Plasma Physics, Warsaw Congress Centre, Poland, 02.07. - 06.07.2007

J.P. Graves, *Asymmetric Distributions of Energetic Circulating Ions and Sawtooth Control using ICCD and Unbalanced NBI*, 12th European Fusion Theory Conf (EFTC), Madrid, 24.09. - 26.09.2007

B. Gulejova, R.A. Pitts, X. Bonnin, D. Coster, R. Behn, J. Horacek, J. Marki, *Time-dependent modelling of ELMing H-mode at TCV with SOLPS5*, 34th EPS Conference on Plasma Physics, Warsaw Congress Centre, Poland, 02.07. - 06.07.2007

M.A. Henderson, R.Chavan, R. Bertizzolo, A. Bruschi, S. Criant, J. Duron, D. Farina, R. Heidinger, J.-D. Landis, E. Poli, G. Ramponi, G. Saibene, O. Sauter, H. Shidara, V.S. Udintsev, H. Zohm, C. Zucca, *The Enhanced Performance Launcher Design For The ITER Upper Port ECH Antenna*, 17th Topical Conference on Radio Frequency Power in Plasmas, Clearwater, Florida, USA, 07.05. - 09.05.2007

M.A. Henderson, R. Chavan, R. Bertizzolo, A. Bruschi, E. Ciattaglia, S. Cirant, A. Collazos, I. Danilov, F. Dolizy, J. Duron, D. Farina, R. Heidinger, J.-D. Landis, A. Moro, P. Platania, E. Poli, G. Ramponi, G. Saibene, F. Sanchez, O. Sauter, A. Serikov, H. Shidar, *Design Status of the ITER Upper Port Launcher*, 4th IAEA Technical Meeting on "ECRH Physics and Technology for ITER", IAEA Headquarters, Vienna, AUSTRIA, 06.06. - 08.06.2007

M.A. Henderson, G. Saibene, T. Bonicelli, R. Chavan, D. Farina, D. Fasel, R. Heidinger, E. Poli, G. Ramponi, O. Sauter, H. Zohm, *Interface Issues associated with the ITER ECH system*, 4th IAEA Technical Meeting on "ECRH Physics and Technology for ITER", IAEA Headquarters, Vienna, AUSTRIA, 06.06. - 08.06.2007

M.A. Henderson, R. Chavan, R. Bertizzolo, A. Bruschi, S. Cirant, A. Collazos, F. Dolizy, D. Farina, W. Kasperek, J.-D. Landis, A. Moro, P. Platina, B. Plaum, E. Poli, G. Ramponi, G. Saibene, F. Sanchez, H. Shidara, V.S. Udintsev, *mm-wave Optical System of the ITER Upper Port EC Launcher*, Workshop on RF Heating Technology of Fusion Plasmas 2007, Heidelberg, Germany, 10.09. - 12.09.2007

M.A. Henderson, G. Saibene, F. Albajar, S. Alberti, T. Bonicelli, R. Chavan, M. de Baar, D. Farina, D. Fasel, R. Heidinger, I. Pagonakis, B. Piosczyk, G. Ramponi, O. Sauter, M. Thumm, C. Zucca, *Critical Issues Associated with the ITER ECH System*, Workshop on RF Heating Technology of Fusion Plasmas 2007, Heidelberg, Germany, 10.09. - 12.09.2007

J.-P. Hogge, F. Albajar, S. Alberti, P. Benin, T. Bonicelli, S. Cirant, D. Fasel, T. Goodman, S. Illy, S. Jawla, C.Li_vin, I. Pagonakis, A. Perez, B. Piosczyk, L. Porte, T. Rzesnicki, M. Thumm, M.Q. Tran, *The European 2MW, 170GHz Coaxial Cavity Gyrotron for ITER (Invited paper)*, IRMMW-THz 2007, Cardiff, UK, 02.09. - 07.09.2007

W. Horton, J.-H. Kim, E. Asp, L. Porte, *Electron transport analysis in TCV*, 49th APS Conf., Orlando, Florida, USA, 12.11. - 16.11.2007

A.A. Howling, *Electromagnetic effects in very high frequency capacitive discharges*, Workshop on Radio Frequency Discharges, 11-13 June 2007, Dublin, Ireland

A. Huber, R. A. Pitts, V. Philipps, A. Loarte, P. Andrew, S. Brezinsek, J.P. Coad, W. Fundamenski, S. Jachmich, A. Korotkov, J. Marki, G.F. Matthews, K.McCormick, Ph. Mertens, J. Rapp, G. Sergienko, M. Stamp and JET EFDA contributors, *Divertor radiation distribution during ELMs in JET*, 34th EPS Conference on Plasma Physics, Warsaw Congress Centre, Poland, 02.07. - 06.07.2007

A.A. Ivanov, S.Yu. Medvedev, Yu.Yu.Poshekhonov, R. Behn, O. Sauter, L. Villard, R.R. Khayrutdinov, *Reconstruction of Tokamak Equilibria with Pedestal Profiles Using the SPIDER Code*, 34th EPS Conference on Plasma Physics, Warsaw Congress Centre, Poland, 02.07. - 06.07.2007

S. Jachmich, W. Fundamenski, R. A. Pitts, M. Beurskens, C. Giroud, H.R. Koslowski, Y. Liang, F. Rimini, and JET-EFDA contributors, *Langmuir probe measurements of particle and heat fluxes at the JET MkII-HD divertor targets*,

34th EPS Conference on Plasma Physics, Warsaw Congress Centre, Poland, 02.07. - 06.07.2007

S. Jolliet, A. Bottino, B. F. McMillan, P. Angelino, T. M. Tran, X. Lapillonne, Y. Idomura, L. Villard, *Nonlinear global gyrokinetic PIC simulations of Collisionless TEM turbulence*, 49th APS Conf., Orlando, Florida, USA, 12.11. - 16.11.2007

M. Jucker, V.P. Pavlenko, *Generation and Stability of Large Scale Magnetic Structures in Electron Drift Turbulence*, 12th European Fusion Theory Conf (EFTC), Madrid, 24.09. - 26.09.2007

M. Jucker, J.P. Graves, W.A. Cooper, *Single particle orbits in anisotropic fully shaped plasmas*, 12th European Fusion Theory Conf (EFTC), Madrid, 24.09. - 26.09.2007

A.N. Karpushov, B.P. Duval, Ch. Schlatter, *Ion Temperature Fluctuations in ELMy H-mode of the X3 EC-heated Plasmas on TCV*, International Conference on Research and Applications of Plasmas (PLASMA-2007), Greifswald, Germany, 16.10. - 19.10.2007

S.H. Kim, J.-F. Artaud, V. Basiuk, V. Dokouka, R.R. Khayrutdinov, J.B. Lister, V.E. Lukash, *Plasma Current Ramp-up Phase Simulation of ITER*, 34th EPS Conference on Plasma Physics, Warsaw Congress Centre, Poland, 02.07. - 06.07.2007

S.H. Kim, J.-F. Artaud, V. Basiuk, V. Dokouka, R.R. Khayrutdinov, J.B. Lister, V.E. Lukash, *Plasma Current Ramp-up Phase Simulation of ITER*, 34th EPS Conference on Plasma Physics, Warsaw Congress Centre, Poland, 02.07. - 06.07.2007

N. Kobayashi, T. Bonicelli, S. Cirant, G. Denisov, R. Heidinger, M. Henderson, J-P. Hogge, S.L. Rao, D. Rasmussen, G. Saibene, K. Sakamoto, K. Takahashi, R.J. Temkin, M. Thumm, M.Q. Tran, A.G.A. Verhoeven, H. Zohm, *Design of Electron Cyclotron Heating and Current Drive System of ITER*, 17th Topical Conference on Radio Frequency Power in Plasmas, Clearwater, Florida, USA, 07.05. - 09.05.2007

B. Labit, A. Fasoli, A. Diallo, I. Furno, D. Iraj, S.H. Mueller, G. Plyushchev, M. Podesta, F.M. Poli, P. Ricci, C. Theiler, J. Horacek, *Statistical properties of electrostatic turbulence in toroidal magnetized plasmas (Invited paper)*, 34th EPS Conference on Plasma Physics, Warsaw Congress Centre, Poland, 02.07. - 06.07.2007

B. Labit, A. Diallo, A. Fasoli, I. Furno, D. Iraj, P. Ricci, C. Theiler, *Toroidal rotation in the TORPEX magnetized plasmas*, 49th APS Conf., Orlando, Florida, USA, 12.11. - 16.11.2007

J.D. Landis, R. Chavan, M.A. Henderson, R. Bertizzolo, A. Collazos, F. Sanchez, H. Shidara, *Design status of the ITER ECH upper steering mirror mechanism*, 22nd IEEE/NPSS Symp on Fusion Engineering (SOFE07), Albuquerque, New Mexico, USA, 17.06. - 21.06.2007

X. Lapillonne, T. Dannert, O. Sauter, A. Marinoni, Y. Camenen, A. Pochelon, L. Villard, S. Brunner, *Gyrokinetic simulations of shaping effects on turbulent heat and particle transport.*, 12th European Fusion Theory Conf (EFTC), Madrid, 24.09. - 26.09.2007

J.B. Lister, J.W. Farthing, M. Greenwald, I. Yonekawa, *The status of the ITER CODAC conceptual design*, IAEA Technical Coordination Meeting on Data Acquisition and Remote Participation, Inuyama, Japan, June 2007

J.B. Lister, J.W. Farthing, M. Greenwald, I. Yonekawa, *Status of the ITER CODAC conceptual design*, Icalepcs conference, Knoxville, USA, October 2007

J.B. Lister, J.W. Farthing, M. Greenwald, I. Yonekawa, *Overview of the ITER CODAC conceptual design*, IEEE Real-Time Conference, Batavia, USA, June 2007

J.B. Lister, *ITER CODAC*, ITER Business Forum, Nice, France, November 2007

V.E. Lukash, J.-F. Artaud, V. Basiuk, V. Dokouka, R.R. Khayrutdinov, S.H. Kim, J.B. Lister, *Combined DINA-CH and CRONOS Simulation of TCV plasma*, 34th EPS Conference on Plasma Physics, Warsaw Congress Centre, Poland, 02.07. - 06.07.2007

M.J. Mantsinen, B. Alper, C. Angioni, R. Buttery, S. Coda, L.-G. Eriksson, J.P. Graves, T. Hellsten, D. Howell, L.C. Ingesson, T. Johnson, V. Kiptily, M. Lennholm, M.-L. Mayoral, A. Mueck, F. Nabais, F. Nave, J.-M. Noterdaeme, J. Ongena, *Modification of sawtooth oscillations with ICRF waves in the JET tokamak*, 17th Topical Conference on Radio Frequency Power in Plasmas, Clearwater, Florida, USA, 07.05. - 09.05.2007

A. Marinoni, S. Brunner, Y. Camenen, S. Coda, J.P. Graves, M. Jucker, X. Lapillonne, A. Pochelon, L. Villard, and the TCV Team, *The impact of triangularity on plasma confinement: TCV experiments vs non-linear gyrokinetic modelling*, 34th EPS Conference on Plasma Physics, Warsaw Congress Centre, Poland, 02.07. - 06.07.2007

J. Marki, R.A. Pitts, and TCV Team, *Infra Red thermography of ELM-divertor target interactions on TCV*, 34th EPS Conference on Plasma Physics, Warsaw Congress Centre, Poland, 02.07. - 06.07.2007

Y. Martin and ITPA-CDBM working group, *Power requirements for accessing the H-mode in ITER*, 11th IAEA Technical Meeting on "H-mode Physics and Transport Barriers", Tsukuba, Japan, 26.09. - 28.09.2007

A.A. Martynov, S.Yu. Medvedev, L. Villard, *Tokamaks with Reversed Current Density: Current Holes, AC Operation and Axisymmetric Stability*, 34th EPS Conference on Plasma Physics, Warsaw Congress Centre, Poland, 02.07. - 06.07.2007

B.F. McMillan, S. Jolliet, A. Bottino, P. Angelino, T.M. Tran, L. Villard, *Noise control in global gyrokinetic particle simulations.*, 49th APS Conf., Orlando, Florida, USA, 12.11. - 16.11.2007

S.Yu. Medvedev, A.A. Ivanov, A.A. Martynov, Yu.Yu. Poshekhonov, S.H. Kim, J.B. Lister, Y.R. Martin, O. Sauter, L. Villard, *Edge Stability and Boundary Shaping in Tokamaks*, 34th EPS Conference on Plasma Physics, Warsaw Congress Centre, Poland, 02.07. - 06.07.2007

N. Mellet, W.A Cooper, L. Villard, P. Popovich, S. Brunner, T.M. Tran, *3D warm effects for low-frequency wave propagation in magnetically confined plasmas*, 12th European Fusion Theory Conf (EFTC), Madrid, 24.09. - 26.09.2007

Y. Narushima, K.Y. Watanabe, R. Sakamoto, Y. Suzuki, S. Sakakibara, S. Ohdachi, H. Yamada, LHD experimental group, W.A. Cooper, *3-D ideal MHD stability of super dense core plasma in LHD*, Joint Conference of 17th International Toki Conference on Physics of Flows and Turbulence in plasmas and 16th International Stellarator/Heliotron Workshop, Toki, Japan, 15.10. - 19.10.2007

Z. Oksiuta, P. Olier, Y. de Carlan, N. Baluc, *Effects of Y2O3 and Fe2Y particles on the microstructure and Charpy impact properties of an ODS ferritic steel*, Proc. Intern. Powder Metallurgy Congress and Exhibition, Toulouse, France, October 2007

I.Gr. Pagonakis, J.-P. Hogge, S. Alberti, K.A. Avramides, J.L. Vomvoridis, *A new concept for the collection of an electron beam guided by an externally applied magnetic field*, IRMMW-THz 2007, Cardiff, UK, 02.09. - 07.09.2007

I.Gr. Pagonakis, J.-P. Hogge S. Alberti, *Numerical study of the effect of stray magnetic field on the beam quality of the 170 GHz, 2MW gyrotron gun for ITER*, IRMMW-THz 2007, Cardiff, UK, 02.09. - 07.09.2007

J.I. Paley, S. Coda, Y. Camenen and the TCV Team, *Real time plasma current and elongation control using ECRH actuators*, 34th EPS Conference on Plasma Physics, Warsaw Congress Centre, Poland, 02.07. - 06.07.2007

J.I. Paley, S. Coda, S. Alberti, *Real time control using ECRH actuators on TCV*, Burning plasma diagnostics, Varenna, Italy , 24.09. - 28.09.2007

L. Pangione, J.B. Lister, *Matlab modeling of ITER CODAC*, IAEA Technical Coordination Meeting on Data Acquisition and Remote Participation, Inuyama, Japan, June 2007

B. Piosczyk, F. Albajar, S. Alberti, D. Fasel, T.P. Goodman, J.-P. Hogge, M.G. Tran, *Status of the 2 MW, 170 GHz coaxial cavity gyrotron for ITER*, 4th Workshop on ECRH, Vienna, Austria, June, 2007

R.A. Pitts, J. Horacek and the TCV Team, *Neoclassical and transport driven parallel SOL flows on TCV*, 34th EPS Conference on Plasma Physics, Warsaw Congress Centre, Poland, 02.07. - 06.07.2007

R.A. Pitts, J. Horacek, TCV team, *Neoclassical and transport driven parallel SOL flows on TCV*, 34th EPS Conference on Plasma Physics, Warsaw Congress Centre, Poland, 02.07. - 06.07.2007

R.A. Pitts, *Tokamak edge physics and plasma-surface interaction*, Burning plasma diagnostics, Varenna, Italy , 24.09. - 28.09.2007

R.A. Pitts, JET-EFDA Contributors, *Progress in ITER-relevant exhaust physics at JET*, 49th APS Conf., Orlando, Florida, USA, 12.11. - 16.11.2007

A. Pochelon, A. Bortolon, Y. Camenen, B.P. Duval, A. Marinoni, H. Reimerdes, A. Scarabosio, S. Alberti, C. Angioni, R. Behn, A. Bottino, S. Brunner, S. Coda, K. Daouk, A. Fasoli, I. Furno, T.P. Goodman, J. Graves, M.A. Henderson, F. Hof, *Physics insight from plasma shaping experiments in the TCV tokamak*, 49th APS Conf., Orlando, Florida, USA, 12.11. - 16.11.2007

F.M. Poli, A. Fasoli, A. Diallo, I. Furno, B. Labit, S.H. Mueller, M. Podesta, *Experiments in a basic plasma device in support of the comparison with linear and nonlinear theories of electrostatic instabilities*, 3rd IAEA-TM on Theory of Plasma Instabilities, University of York, York, UK, 26.03. - 28.03.2007

L. Porte and the TCV Team, *Vertical launch third harmonic electron cyclotron emission heating of H-mode on TCV and access to quasi-stationary ELM-free H-mode*, 17th Topical Conf. on Radio Frequency Power in Plasmas, Clearwater, Florida 7-9 May 2007

L. Porte, S. Alberti, E. Asp, G. Arnoux, A. Bortolon, Y. Martin, M. Maslov, O. Sauter, A. Scarabosio, H. Weisen, *Vertical Launch Third Harmonic Electron Cyclotron Resonance Heating of H-mode on TCV and Access to Quasi-Stationary ELM-free H-mode*, 17th Topical Conference on Radio Frequency Power in Plasmas, Clearwater, Florida, USA, 07.05. - 09.05.2007

L. Porte & the TCV Team, *Vertical Launch Third Harmonic Electron Cyclotron Resonance Heating of H-mode on TCV and Access to Quasi-Stationary ELM-free H-*

mode, 17th Topical Conference on Radio Frequency Power in Plasmas, Clearwater, Florida, USA, 07.05. - 09.05.2007

L. Porte and the TCV Team, *Vertical Launch Third Harmonic Electron Cyclotron Resonance Heating of H-mode on TCV and Access to Quasi-Stationary ELM-free H-mode*, 17th Topical Conference on Radio Frequency Power in Plasmas, Clearwater, Florida, USA, 07.05. - 09.05.2007

L. Porte, S. Coda, S. Alberti, R. Bertizzolo, R. Chavan, J.-M. Mayor, A. Simonetto, V.S. Udintsev, *A Vertical ECE Diagnostic for TCV*, 49th APS Conf., Orlando, Florida, USA, 12.11. - 16.11.2007

L. Porte, S. Alberti, E. Asp, A. Bortolon, A. Karpushov, Y. Martin, O. Sauter, *Stationary ELM-free H-mode on TCV*, 49th APS Conf., Orlando, Florida, USA, 12.11. - 16.11.2007

F. Sanchez, R. Chavan, J. Duron, M.A. Henderson, J.D. Landis, H. Shidara, *Design status of ITER ECH upper launcher mirrors*, 22nd IEEE/NPSS Symp on Fusion Engineering (SOFE07), Albuquerque, New Mexico, USA, 17.06. - 21.06.2007

Ch. Schlatter, B.P. Duval, A.N. Karpushov, T.P. Goodman and the TCV team, *Ion-Acoustic Turbulence in ECCD-driven TCV plasmas*, 49th APS Conf., Orlando, Florida, USA, 12.11. - 16.11.2007

P. Spaetig, P. Mueller, G.R. Odette, *Assessment of irradiation embrittlement after 590 MeV proton irradiation of the Eurofer97 steel using mini pre-cracked bend bars*, 13th Int. Conf. on Fusion Reactor Materials, Nice, December 2007 (oral presentation)

J.D. Strachan, P. Coad, G. Corrigan, J. Spence, G.F. Matthews, M. Airila, J. Likonen, M. Rubel, R.A. Pitts, A. Kirschner, V. Phillips, A. Kallenbach and JET-EFDA Contributors, *Carbon migration during JET 13C experiments*, 34th EPS Conference on Plasma Physics, Warsaw Congress Centre, Poland, 02.07. - 06.07.2007

B. Strahm, A.A. Howling, L. Sansonnens, Ch. Hollenstein, *Optimization of microcrystalline silicon deposition efficiency*, AVS 53rd International Symposium & Exhibition, San Francisco, 12.11. - 17.11.2006

B. Strahm, A.A. Howling, Ch. Hollenstein, *Plasma diagnostics as a tool for process optimization*, 34th EPS Conference on Plasma Physics, Warsaw Congress Centre, Poland, 02.07. - 06.07.2007

S.K. Jawla, J.-P. Hogge, S. Alberti, *Analysis of Iterative Phase Retrieval Approach to Optimize Amplitude Measurement Parameters*, IRMMW-THz 2007, Cardiff, UK, 02.09. - 07.09.2007

D. Testa, A. Fasoli, A. Klein, P. Beaumont, R. Bertizzolo, R. Chavan, F. Dolizy, P. Lavanchy, N. Lam, S. Mills, S.G. Sanders, J.A. Snipes, J. Thomas, P. Titus, L. Villard, M. Way, and JET-EFDA contributors, *First Measurement of the Damping Rate of High-n Toroidal Alfvén Eigenmodes in JET Tokamak Plasmas*, 34th EPS Conference on Plasma Physics, Warsaw Congress Centre, Poland, 02.07. - 06.07.2007

M.G. Tran, *DEMO concepts and their roles within the fusion programme*, 8th Int. Symposium on Fusion Nuclear Technology, Heidelberg, Germany, 30 September - 5 October, 2007 (Invited key note)

M.G. Tran, J. Pamela M.T. Westra D. Ward, *The potential of fusion as a future source of energy (oral presentation)*, World Energy Conference 2008, 12-15 November 2007, Rome, Italy

M.G. Tran, J. Pamela M.T. Westra D. Ward, *The potential of fusion as a future source of energy (oral presentation)*, 20th World Energy Congress, 12-15 November 2007, Rome, Italy

D. Tskhakaya, R.A. Pitts, W. Fundamenski, T. Eich, S. Kuhn and JET-EFDA Contributors, *PIC simulations of ELM particle and heat loads to the JET divertor targets*, 34th EPS Conference on Plasma Physics, Warsaw Congress Centre, Poland, 02.07. - 06.07.2007

G. Turri, O. Sauter, E. Asp, T.P. Goodman, A. Martynov, S.Yu. Medvedev, V.S. Udintsev, C. Zucca, G. Zhuang, *MHD detrimental effect on the confinement during flat-top eITB plasmas on TCV*, 5th IAEA TM on Steady State Operations of Magnetic Fusion Devices, Daejeon, Korea , 14.05. - 17.05.2007

G. Turri, S. Coda, J.-M. Moret, Y. Martin, O. Sauter, *The Effect of MHD Noise on the Vertical Observer in Tokamaks*, 49th APS Conf., Orlando, Florida, USA, 12.11. - 16.11.2007

V.S. Udintsev, E. Asp, O. Sauter, H. Shidara, F. Turco, G. Turri, S. Coda, G. Falchetto, T.P. Goodman, X. Llobet, T.I. Madeira, Ph. Marmillod, H. Weisen, *Control of the oscillatory regime by local current perturbation in ECCD plasmas on TCV*, 34th EPS Conference on Plasma Physics, Warsaw Congress Centre, Poland, 02.07. - 06.07.2007

G. Veres, R.A. Pitts, A. Aranyi, A. Bencze, M. Berta, B. Gulejova, S. Kalvin and the TCV Team, *Fast Radiation Dynamics during ELMs in TCV*, 34th EPS Conference on Plasma Physics, Warsaw Congress Centre, Poland, 02.07. - 06.07.2007

L. Villard, T.M. Tran, S.J. Allfrey, P. Angelino, A. Bottino, S. Brunner, W.A. Cooper, T. Dannert, G. Darmet, X. Garbet, Ph. Ghendrih, V. Grandgirard, J.P. Graves, R. Hatzky, Y. Idomura, F. Jenko, S. Jolliet, M. Jucker, X. Lapillonne, *Computational fusion plasma physics (invited talk)*, CCP 2007, Conference on Computational Physics, Brussels, Belgium , 05.09. - 08.09.2007

M. Maslov, H. Weisen, *Density profile behavior in JET and extrapolations to ITER*, 49th APS Conf., Orlando, Florida, USA, 12.11. - 16.11.2007

M.K. Zedda, D. Testa, B. Cannas, A. Fanni, F. Piccolo, F. Sartori, P. Sonato, and JET-EFDA contributors, *An example of a new approach for the development of Disruption Protection Tools for JET: the mode-lock disruption class*, 34th EPS Conference on Plasma Physics, Warsaw Congress Centre, Poland, 02.07. - 06.07.2007

C. Zucca, O. Sauter, M.A. Henderson, D. Farina, G. Ramponi, *Effects of local ECCD driven by the optimized equatorial and Upper EC launchers on ITER*, 49th APS Conf., Orlando, Florida, USA, 12.11. - 16.11.2007

B.2 Seminars presented at the CRPP in 2007

A. Encheva, CRPP-EPFL, Lausanne, Switzerland, "Design and simulations of the divertor coils and in-vessel high frequency magnetic coils for ITER"

Ch. Rasouli, Univ. Teheran, Iran, "Imaging of plasma current in the Damavand tokamak"

J. Kim, Dept. of Physics, Korea Advanced Inst. of Sci. And Technol., Daejeon, Korea, *"Visualization of the sawtooth crash in highly elongated TCV plasmas using soft X-ray tomography"*

J.P. Friconneau, CEA-LIST, Service de Robotique Interactive, Fontenay-aux-Rose, France, *"Maintenance d'ITER: robotique et inspection"*

Dr. I. Kjølberg, System Engineering Division, CSEM, Neuchâtel, Switzerland, *"CSEM SA in Neuchâtel and its high tech development projects: Short review of public instrumentation developments for the astrophysical community; What might we do together for ITER?"*

Dr. G. De Temmerman, Inst. of Physics, Univ. Basel, Switzerland, *"On the lifetime of the first mirrors in the diagnostic systems of ITER"*

A. Feltrin, IMT Neuchâtel Switzerland, *"Recent developments in microcrystalline solar cell deposition in KAI-S systems"* and **J. Bailat**, IMT Neuchâtel, Switzerland, *"Substrate surface morphology and growth of microcrystalline solar cells"*

T. Shimosuma, National Inst. for Fusion Science, Toki-City, Japan, *"Present status, application and prospect of the ECRH system in large helical device"*

M. Albergante, Univ. Bicocca (Milano), Italy, *"Fast ions dynamics effects on neutron emission spectroscopy at JET"*

R. Tye, Imperial College London, UK, *"Improvement of diamagnetic measurement of TCV"*

Dr. J. Decker, CEA Cadarache, France, *"Current drive by electron Bernstein waves"*

M. Podesta, CRPP-EPFL, Lausanne, Switzerland, *"Plasma production and transport in a simple magnetized toroidal plasma"*

Ch. Theiler, ETHZ Zürich, Switzerland, *"Electrostatic turbulent structures in TORPEX plasmas"*

Prof. J. Yu, China Institute of Atomic Energy, Beijing, P.R. China, *"Fission-Fusion neutron source"*

Dr. J. Horacek, IPP Prague, Czech Republic, *"Reinstallation of tokamak COMPASS-D in IPP Prague"*

Prof. N. Thomas, Planetary Imaging Group, Physikalisches Institut, Univ. Bern, Switzerland, *"The Jovian moon, Io and its plasma torus"*

K. Daouk, CRPP-EPFL Lausanne, Switzerland, *"Simulating perpendicular transport of energy and particles in the tokamak TCV"*

Dr. S.M. Kayel, Plasma Physics Lab., Princeton Univ., Princeton, USA, *"Physics results from the National Spherical torus Experiment"*

K. de Meijere, Faculty of Applied Physics, Delft Univ. of Technology, The Netherlands, *"Determination of recycling rate in Tore Supra using Mach probe measurements in the SOL"*

Prof. T. Carter, Dept. of Physics and Astronomy, UCLA, USA, *"Studies of turbulence and transport in a linear magnetized plasma: intermittency and shear suppression of transport"*

Dr. E. Gnansounou, Energy Planning Group, ENAC-EPFL, Lausanne, Switzerland, *"Contribution potentielle de l'énergie de fusion à l'approvisionnement en électricité au 21^{ème} siècle: une approche prospective"*

Dr. Y. Idomura, Japan Atomic Energy Agency, Tokyo, Japan, *"Gyrokinetic toroidal full-f 5D Vlasov code GT5D"*

Z. Lin, Dept. of Physics and Astronomy, Univ. of California at Irvine, USA, *"Turbulent transport in collisionless plasmas: eddy mixing or wave-particle decorrelation"*

Dr. H. Reimerdes, Columbia Univ., New York, USA, *"Resistive wall mode stabilization in slowly rotating high beta DIII-D plasmas"*

Prof. P. Muggli, Electrical Engineering and Electrophysics Dept., Univ of Southern California, Los Angeles, USA, *"Energy doubling of the stanford linear accelerator collider electrons in a meter-scale plasma-based accelerator"*

Prof. D.L. Brower, Dept. of Physics, the Univ. of Texas at Austin & Dept. of Physics and Astronomy, Univ. of California, Los Angeles, USA, *"Tearing mode driven particle transport, momentum transport and flow generation"*

G.A. Cooper, Univ. of the South, Sewanee, Tennessee, USA, *"Exact canonical drift Hamiltonian formalism with pressure anisotropy and finite perturbed fields"*

J. Rossel, EPFL Lausanne, Switzerland, *"Method of tomography inversion accounting for the presence of magnetic islands and based on the measurements of a single pin-hole soft X-ray camera"*

Dr. Y. Poitevin, EFDA CSU Garching, Germany, *"The European test blanket modules for ITER"*

F.M. Poli, CRPP-EPFL Lausanne, Switzerland, *"Electrostatic instabilities and turbulence in a toroidal magnetized plasma"*

Dr. A. Kraemer-Flecken, IPP Forschungszentrum Jülich, Germany, *"Recent reflectometry results from the TEXTOR tokamak"*

Prof. R.L. Dewar, Research School of Physical Sciences and Engineering, The Australian National Univ., Australia, *"Quantum chaos? Genericity and nongenericity in the MHD spectrum of nonaxisymmetric toroidal plasmas"*

Dr. R. Ganesh, Inst. for Plasma Research, Bhat, India, *"Electron plasma in a tight torus: experiments and simulations"*

Dr. M. Goniche, DRFC-CEA, Cadarache, France, *"Identification of fast particle triggered modes by means of correlation ECE on Tore Supra"*

Dr. J.-M. Fürbringer, LGPP-STI-EPFL, Lausanne, Switzerland, *"An apology for the design of experiments (DOE)"*

Dr. A. Pochelon, CRPP-EPFL Lausanne, Switzerland, *"Physics insight from plasma shaping experiments in the TCV tokamak"*

Dr. G. Turri, CRPP-EPFL Lausanne, Switzerland, *"The effect of MHDnoise on the vertical observer in tokamaks"*

Dr. F. Doveil, Turbulence Plasma, PIIM, CNRS/Université de Provence, Marseille, France, *"Observation and control of Hamiltonian chaos in wave-particle interaction"*

Dr. P. Angelino, DRFC-CEA, Cadarache, France, *"Effects of plasma elongation on ITG turbulence, zonal flows and Geodesic Acoustic Modes"*

B.3 Other external presentations in 2007

N. Baluc, *Warsaw, Poland, 16 Oct 2007*, "Materials for fusion reactors"

N. Baluc, *Vienna, Austria, 24 Oct 2007*, "ExtreMat SP3: radiation resistant materials"

W.A. Cooper, *Dept. of Physics, Univ. of California, Los Angeles, USA, 20 Nov 2007*, "3D anisotropic pressure equilibria and selfconsistent guiding centre orbits"

W.A. Cooper, *Univ. of the South, Sewaonee, Tennessee, USA, 28 Nov 2007*, "Computational plasma physics"

G. Turri , O. Sauter, S. Alberti, L. Porte, T.P. Goodman, V.S. Udintsev, *IAEA TM H-Mode Physics and Internal Transport Barriers, 28 Sep 2007*, "The Role of MHD in the Sustainment of Electron Internal Transport Barriers and H-Mode in TCV"

A. Howling, *Workshop “_c-Si depositon Processes”, Inst. fuer Photovoltaik, Forschungszentrum Juelich, Germany, 06 Feb 2007*, "Electromagnetic sources of non-uniformity in large area RF capacitive plasma reactors"

S. Jolliet, T.M. Tran, B.F. McMillan, L. Villard, X. Lapillonne, A. Bottino, P., *Princeton Plasma Physics Laboratory, Princeton, USA, 19 Nov 2007*, "Nonlinear Global Gyrokinetic Simulations of Collisionless TEM Turbulence"

J.B. Lister, *DESY, Hamburg, Germany, 28 Feb 2007*, "ITER - a global challenge"

A. Pochelon, *PPPL, Princeton, USA, 19 Nov 2007*, "Plasma shaping effects on heat transport, rotation, MHD and Electron Bernstein wave heating experiments in TCV"

O. Sauter, *4th Technical Meeting on ECRH Physics and Technology for ITER, Vienna, 2007, 08 Jun 2007*, "Summary of EC wave physics and experiments"

B. Strahm, *Workshop “_c-Si depositon Processes, 06 Feb 2007*, "Optimization of the microcrystalline silicon deposition efficiency"

V. Udintsev, G. Turri, O. Sauter, *DRFC/SCCP/CEA Cadarache, France, 25 Apr 2007*, "Oscillations of the Plasma Current and Electron Temperature in ECCD plasmas on TCV"

C. Zucca, O. Sauter, M.A.Henderson, E. Fable, D. Farina, E. Poli, G.Ramponi, G. Saibene, H. Zohm, *Princeton Plasma Physics Laboratory, Princeton, USA, 19 Nov 2007*, "Effects of local ECCD driven by the optimized Upper and Equatorial EC Launchers on ITER"

APPENDIX C External activities of CRPP Staff during 2007

C.1 National and international committees and ad-hoc groups

MEMBERSHIP

- N. Baluc Scientific and Technical Advisory Committee (STAC), Euratom
Chairwoman of an ad-hoc group for monitoring the EFDA 2006 activities on long-term technology and safety
International Organizing Committee of the SOFT Conference (Symposium on Fusion Technology)
International Advisory Committee of the ICFRM Conference (International Conference on Fusion Reactor Materials)
IEA Annex II Executive Committee
IEA Fusion Materials Agreement Executive Committee
Steering Committee CRPP-PSI on Materials for Nuclear Applications (SCMATNUC).
Swiss Society for Optics and Microscopy (SSOM)
Task Coordinator of the Euratom Task TTMS-003 entitled 'Compatibility of Steels with Hydrogen and Liquids' of the Tritium Breeding and Materials Programme of EFDA
Task Coordinator of the subproject entitled 'Radiation-Resistant Materials' of the EXTREMAT Integrated Project (IP) of the 6th European Framework Programme
- P. Bruzzone International Magnet Technology Conference Organizing Committee
ITER Magnet Expert Group
EFDA Dipole Design Advisory Group
Wendelstein 7-X Magnet Advisory Group
GSI Magnet Advisory Group
- W.A. Cooper Chairman, CSCS Large users assembly, Switzerland
- J.-L. Dorier Member of the committee of the Swiss Vacuum Society
Member of the scientific committee of the 7th Workshop on Frontiers in Low Temperature Plasma Diagnostics, Beverley (UK), April 2007
- A. Fasoli Visiting Professor, MIT Physics Department
Scientific and Technical Advisory Committee, Euratom
ASDEX Upgrade Programme Committee, Germany
Scientific Expert for Switzerland at Fusion Power Coordination Committee of the International Energy Agency
International Tokamak Physics Activities: MHD and Energetic Particles Topical Group
Chairman of ad-hoc group of STAC for the monitoring of 2004 activities and 2006 work program of JET
Scientific Committee, 11th IAEA Technical Meeting on Energetic Particles in Magnetic Confinement Systems, 2007
Audit Committee, Laboratory for Ion and Molecular Interactions, Université de Provence, France
- Ch. Hollenstein Expert for Habilitation University of Bochum, D
Member of the Wissenschaftlicher Beirat Leibniz-Institut für Oberflächenmodifizierung Leipzig
Editorial Board Plasma Chemistry and Plasma Processing Kluwer Academic/Plenum Publisher
Member of the IUVSTA Plasma Division
President of the Swiss Vacuum society

- J.B. Lister International Tokamak Physics Activities: MHD, Disruption and Control Topical Group
34th EPS Conference Programme Committee, Warsaw 2007
35th EPS Conference Programme Committee, Crete 2008
- C. Marinucci CHATS-AS, Board
- P.J. Paris Member of the CCEF
- R.A. Pitts Leader of the EFDA-JET Exhaust Physics Task Force (TF-E)
CRPP Representative of the EFDA EU Task Force on Plasma-Wall Interactions
- A. Pochelon Member of the Committee of the SWISS NUCLEAR FORUM
Member of the Commission for Training and Formation of the Swiss Nuclear Forum "Aussschuss Wissenschaft"
Member of the FORATOM Committee, in particular of the "Research and Development Task Force (R&D.TF)
- O.Sauter Scientific Committee of the 13th European Fusion Theory Conference 2007
Member of ITPA on Transport Physic
- R. Schäublin Member of the board of the Swiss Society for optics and microscopy
- M.Q. Tran Director of the Inst. of Physics of Energy and Particle, EPFL
Member of the EFDA Steering Committee
Consultative Committee for the Euratom Specific Research and Training Programme in the field of Nuclear Energy, Fusion (CCE-FU)
Chairman of the Scientific and Technical Advisory Committee, Euratom (STAC) (until fall 2007)
Chairman of the Technical Advisory Panel of the Joint Undertaking Fusion for Energy (F4E)
Swiss delegate to the Governing Board of F4E
Chairman of the Ad'hoc Group for the Monitoring of W7-X
Chairman of the Ad'hoc Group for the assessment of the JET Risk
Member of the Ad'hoc Group for the Socio Economic Programme of EFDA
Member of the Core Commission for the nomination of Max-Planck Plasma Physics Director
Chairman of the CCE-FU Ad'hoc Group on Expenses Overrun
Standing Committee of the International Symposium on Fusion Nuclear Technology
Expert on the IAEA International Fusion Research Council
Member of the Steering Committee of the Center of Competence on Energy and Mobility of the the CEPF
Member of the International Committee of the IRMWW and THZ conference
Swiss delegate at the Fusion Power Coordinating Committee
- L. Villard Expert Group on High Performance Computing, EFDA
- H. Weisen Coordinator for particle transport at the JET Transport Task Force
Coordinator for particle transport ('spokesperson') of the working group on particle transport within the ITPA database and modelling workgroup
Member of the Diagnostics Working Group within the ITPA
Member of the ad'hoc expert group for the application for preferential support for the proposal "Enabling a programme of ITER relevant plasma studies by transferring and installing COMPASS-D to the Institute of Plasma Physics AS CR, Association EURATOM-IPP.CR".

PARTICIPATION

- B. Duval Remote Participation Users Group, EFDA-JET
34th EPS Local Organising Committee
- Y.R. Martin International Tokamak Physics Activity: Confinement Database and
Modelling Topical Group
- R.A. Pitts International Tokamak Physics Activity: SOL & Divertor Topical Group
- A. Pochelon Auditor of the Swiss Physical Society Committee
- L. Villard Ad-Hoc Group for the assessment of an application for a Cost-Sharing
Action by the Bulgarian Academy of Sciences

C.2 Editorial and society boards

- S. Coda Editorial Board of Plasma Physics and Controlled Fusion
- Ch. Hollenstein Editorial Board Plasma Chemistry and Plasma Processing Kluwer
Academic/Plenum Publisher
- J.B. Lister Chairman of the European Physical Society Plasma Physics Division
Deputy Editor of Plasma Physics and Controlled Fusion
- Y.R. Martin Chairman of the Association Vaudoise des Chercheurs en Physique
- P.J. Paris EFDA Information Network (PIG)
"Fédération Romande de l'Energie" Committee
Chairman of the "International Association of Specialists in Energy"
(AISEN)
- A. Pochelon Auditor of the Swiss Physical Society Committee

C.3 EPFL committees and commissions

- N. Baluc Commission Ecole Doctorale en Science et Génie des Matériaux
- J-L. Dorier Commission du Doctorat de la Section de Physique, FSB-EPFL
- A. Fasoli Commission d'Enseignement de la Section de Physique, FSB-EPFL
Comité des 'Bourses Ecole Doctorale', EPFL
Comité de nomination "Professeur de Théorie des Plasmas"
- J-Ph. Hogge Commission du Doctorat de la Section de Physique, FSB-EPFL
- O. Sauter Commission du Doctorat de la Section de Physique, FSB-EPFL
- M.Q. Tran Commission du Doctorat de la Section de Physique, FSB-EPFL
Commission stratégique de la Section de Physique, EPFL
Membre du Comité de Sélection du Prix de la meilleure thèse EPFL
Comité de nomination "Professeur de Théorie des Plasmas"
- T.M. Tran Groupe de travail technique du Comité de Pilotage HPC/MPC, EPFL
- L. Villard Délégué à la mobilité, Section de physique, FSB-EPFL
Commission d'Ethique, EPFL

Commission d'Enseignement de la Section de Physique, FSB-EPFL
Groupe de travail technique HPC (High Performance Computing) – EPFL
Steering Committee, HPC (High Performance Computing) – EPFL
Steering Committee, Blue Gene Project - EPFL

APPENDIX D Lausanne Reports (LRP)

(see CRPP archives at <http://crppwww.epfl.ch/archives>)

M. Podesta, *Plasma production and transport in a simple magnetised toroidal plasma (EPFL Thesis 3765(07))*, LRP 829/07

P. Bauer P. Bruzzone A. Portone F. Roth M. Vogel A. Vostner K. Weiss, *review of material properties, past experiences, procedures, issues and results for a possible solder filled cable as Plan B conductor for the EFDA dipole magnet (Draft Vs 1)*, LRP 830/07

P. Marmy, R. Betemps, B. Gross, W. Meier, P. Vladimirov, M. Wohlmuther, *IFMIF facility: Test rig actuator for in situ creep-fatigue tests and concept for the medium flux test area (Final report on task: TW5-TTMI-003/Del No. 7)*, LRP 831/07

A. Sublet, *Caracterisation de decharges a barrieres dielectriques atmospheriques et sub-atmospheriques et application a la deposition de couches d'oxyde de silicium (these EPFL 3801(07))*, LRP 832/07

E. Asp, W. Horton, J.Kim, L. Porte, Stefano Alberti, E. Fable, Yves Martin, O. Sauter, G. Turri and the TCV Team, *Transport analysis of multi-phase H-mode shot at TCV*, LRP 833/07

F. Poli, *Electrostatic instabilities and turbulence in a toroidal magnetized plasma (EPFL thesis 3849(07))*, LRP 834/07

B. Strahm, *Investigation of radio-frequency, capacitively-coupled large area industrial reactor: cost-effective production of thin film microcrystalline silicon for solar cells (EPFL thesis 3895(07))*, LRP 835/07

APPENDIX E The basis of controlled fusion

E.1 Fusion as a sustainable energy source

Research into controlled fusion aims to demonstrate that it is a valid option for generating power in the long term future in an environmentally, politically and economically acceptable way. Controlled fusion is a process in which light nuclei fuse together to form heavier ones: during this process a very large amount of energy is released. For a fusion reactor it is planned to use the two isotopes of hydrogen: deuterium (D) and tritium (T), which fuse together much more readily than any other combination of light nuclei according to the following reaction:

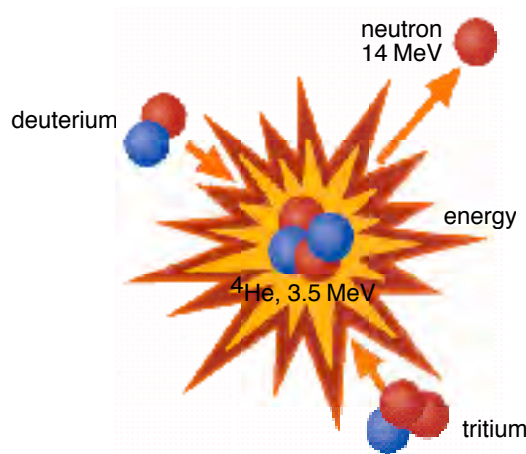
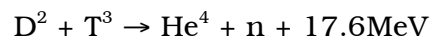
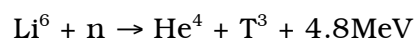


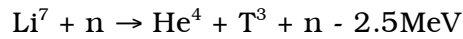
Fig. E.1 Schematic of a fusion reaction between deuterium and tritium nuclei. The products are 3.5MeV 4He , the common isotope of helium, and a 14MeV free neutron.

The end products are helium and neutrons (n). The total energy liberated by fusing one gram of a 50:50% mixture of deuterium and tritium is 94000kWh, which is 10 million times more than from the same mass of oil. 80% of this energy is carried by the neutrons with an energy of 14MeV while the remaining 20% is carried by the helium nucleus. Most of this energy eventually becomes heat to be stored or converted by conventional means into electricity.

The temperature at which fusion reactions start to become significant are above a few tens of millions of degrees. For the D-T reaction, the optimal temperature is of the order of 70-200 million degrees. At such temperatures the D-T fuel is in the plasma state.

Deuterium is very abundant on the earth and can be extracted from water (0.034g/l). Tritium does not occur naturally, since its half-life is only 12.3 years, but it can be regenerated from lithium using the neutrons produced by the D-T fusion reactions. The two isotopes of natural lithium contribute to this breeding of tritium according to the reactions:





The relative abundance of the two lithium isotopes Li^6 and Li^7 are 7.4% and 92.6%, respectively. The known geological resources of lithium both in the earth and in the sea water are large enough to provide energy for an unlimited time.

E.2 Attractiveness of fusion as an energy source

The inherent advantages of fusion as an energy source are:

- The fuels are plentiful and their costs are negligible because of the enormous energy yield of the reaction;
- The end product of the reaction is helium, an inert gas;
- No chain reaction is possible: at any time only a very small amount of fuel is in the reacting chamber and any malfunction would cause an immediate drop of temperature and the reaction would stop;
- No after-heat problem can lead to thermal runaway;
- None of the materials required by a fusion power plant are subject to the provisions of the non-proliferation treaties.

Its further potential advantages are:

- Radioactivity of the reactor structure, caused by neutrons, can be minimised by careful selection of low-activation materials resulting in a manageable quantity of long lived radioactive waste;
- The release of tritium in normal operation can be kept at a very low level. The inventory of tritium in the breeding section of the reactor and on the site can be sufficiently small so that the worst possible accident could not lead to a harmful release to the environment requiring evacuation of the nearby population.

APPENDIX F Glossary

The following is a general purpose glossary for the field of controlled fusion and plasma physics.

Additional heating: Usually with reference to a plasma which is initially heated by a toroidal current induced in the plasma (ohmic heating), additional heating designates other means of heating a plasma (absorption of electromagnetic waves or of injected fast neutral particles).

Advanced Tokamak Scenarios: Tokamaks normally generate natural profiles of plasma current and plasma pressure. External non-inductive current drive and local control of the current and pressure profiles can allow access to enhanced regimes and even steady state operation, generally referred to as Advanced Tokamak Scenarios.

ALCATOR C-MOD: High field, high density tokamak at MIT (USA) with an elongated, diverted plasma and metallic walls.

Alfvén gap modes: The toroidal nature of tokamak plasmas produces gaps in the otherwise continuous spectrum of Alfvén waves, populated by discrete, weakly damped Alfvén gap modes. Under certain conditions these modes can be destabilised by resonant energy transfer from energetic particles, e.g. α -particles from fusion reactions.

Alfvén waves: A fundamental plasma wave, which is primarily magneto-hydrodynamic in character with an oscillation of the magnetic field and, in some cases, plasma pressure. In tokamaks, these waves are typically strongly damped. See also fast Alfvén wave.

Alfvén velocity: The velocity of propagation of Alfvén waves in the direction of the magnetic field; it is proportional to the magnetic field strength, and inversely proportional to the square root of the mass density.

alpha particle, or α -particle He^4 : The nucleus of the helium atom, composed of two protons and two neutrons, is one of the two products of the DT fusion reaction (the other one is a neutron). The α -particles, being electrically charged, are trapped by the magnetic confinement field and therefore can release their energy to the plasma contrary to the neutrons which escape from the plasma and transfer their energy in the blanket surrounding the plasma core. The plasma

heating which is provided by these α -particles as they slow down due to collisions is essential for achieving ignition.

Alternative lines: Magnetic confinement development other than the tokamak.

Analytic/Computational modelling: Analytic: algebraic solution of basic equations. Computational: numerical solution of basic equations.

Anomalous transport: Measured heat and particle loss is anomalously large compared with collisional theory of heat transport in toroidal plasmas.

ASDEX-Upgrade: Medium-sized Tokamak at Garching (Association Euratom-IPP, Germany) with an elongated, diverted plasma.

Aspect ratio: The ratio between the large radius and the small radius of a torus.

Auxiliary heating: See additional heating.

Ballooning instability: A local instability which can develop in the tokamak when the plasma pressure exceeds a critical value; it therefore constrains the maximum β that can be achieved. It is analogous to the unstable bulge which develops on an over-inflated tyre.

Beta (β): Ratio of plasma pressure to magnetic field pressure. One of the figures of merit for magnetic confinement: the magnitude of the magnetic field pressure determine the cost of the field coil that generates it; since fusion reactivity increases with the square of the plasma pressure, a high value of β indicates good performance. The highest values achieved in tokamaks reach 40% (START).

Beta-normalised (β_N): The ratio of plasma current (in MA) to the product of minor radius (in m) and magnetic field (in T) characterises the limit to the achievable β imposed by ideal MHD. β -normalised is the ratio of β (as a percentage) to the above ideal MHD parameter. Generally $\beta_N \sim 3$ should be achievable, but techniques for obtaining higher values have been found experimentally.

Blanket: A structure containing lithium or lithium compounds surrounding the plasma core of a fusion reactor. Its functions are to breed tritium, via lithium-neutron reactions, and to absorb most of

the fusion energy to be used for electricity generation.

Bootstrap current: Theory developed in 1970 predicted that a toroidal electric current will flow in a tokamak which is fuelled by energy and particle sources that replace diffusive losses. This diffusion driven "Bootstrap current", which is proportional to β and flows even in the absence of an applied voltage, could be used to provide the poloidal magnetic field: hence the concept of a Bootstrap tokamak, which has no toroidal voltage. A Bootstrap current consistent with theory was observed many years later on JET and TFTR; it now plays a role in optimising advanced tokamaks.

Breakeven: The fusion performance of a power plant is denoted by Q , which is the ratio of the power released by fusion reactions to that used to heat the plasma. As a convention, scientific breakeven corresponds to $Q=1$ and ignition to $Q=\infty$. A fusion power plant would operate at $Q\sim 50$.

Breeding ratio: The number of tritium atoms produced in the blanket of a fusion power station per tritium nucleus burned in the fusion plasma.

Burn: The fusion process of consuming DT fuel in a reactor, releasing energy.

CCE-FU: The Consultative Committee for the Euratom Specific Research and Training Programme in the field of Nuclear Energy, Fusion. Formerly the CCFP.

CEA: Commissariat à l'Énergie Atomique, France. Partner in the Association EURATOM-CEA which operates the TORE SUPRA tokamak.

CFI: Committee on Fusion-Industry.

Charge exchange measurement: Measures the plasma ion temperature. Neutral atoms in the plasma (for example from a neutral beam) donate electrons to hot plasma ions, which are thereby neutralised. These hot atoms are no longer confined by the magnetic field and leave the plasma. Their energy is measured by a neutral particle analyser.

CIEMAT: Centro de Investigaciones Energéticas Medioambientales y Tecnológicas, Spain. Partner in the Association EURATOM-CIEMAT. Operates the flexible heliac stellarator TJ-II.

Classical transport: Collisions between the individual particles of a plasma allow

them to move across the magnetic field. Theories which describe this mechanism are called "classical" (or "neo-classical" when additional effects due to the toroidal geometry are included). The measured heat and particle transport is usually higher than predicted by these theories.

Collisionality: Non-dimensional parameter, which is the inverse ratio of the mean free path of plasma particles between collisions to a characteristic length of the magnetic field configuration.

Compact torus: Class of closed magnetic configurations in which no material elements (coils, conductors or walls) need to link through the bore of the plasma torus. Thus the vessel of compact tori can be spherical or cylindrical.

COMPASS: COMPact ASSEMBly, a tokamak for studies of plasma stability, at Culham, UK (Association EURATOM-UKAEA). Originally with circular vessel (COMPASS-C), later with D-shaped vessel (COMPASS-D).

Confinement time: In a fusion plasma neither particles nor energy are perfectly confined. Particle confinement time is the time during which the particles, on average, stay confined. The energy confinement time, which is usually shorter than the particle confinement time, is defined in steady state as the ratio of the plasma energy content to the total power input to the plasma and is a measure of how fast a plasma would cool if there were no heating.

CRPP: Centre de Recherches en Physique des Plasmas. Fusion laboratories of the Association EURATOM-Swiss Confederation at the Ecole Polytechnique Fédérale de Lausanne and the Paul-Scherrer Institute, Villigen (CRPP-Fusion Technology).

Current drive (non-inductive): In a tokamak, plasma current can be driven inductively, with the toroidal plasma acting as a secondary winding of a transformer whose primary coil is at the central column of the device. Continuous current cannot be driven by transformer action. 'Non-inductive' current drive methods are applied either by injecting particles with directed momentum into the plasma or by accelerating electrons by electromagnetic waves so that they carry the current. Also being applied to control instabilities and to optimise confinement by modifying the current profile. The bootstrap effect also drives current.

Current profile (current distribution): The distribution of current density across the minor radius of the plasma.

Current ramp-up (down): The increase (decrease) of plasma current either at the start of operation or during operation.

Cyclotron frequency: Charged particles in a magnetic field have a natural frequency of gyration in the plane perpendicular to the magnetic field - the cyclotron frequency. For electrons in a tokamak, the cyclotron frequency is typically a few tens of GHz (28GHz per Tesla), and for ions, a few tens of MHz (7.5MHz per Tesla for deuterium).

Cylindrical approximation: An approximation to the true tokamak geometry in which the torus is straightened, so that the toroidal direction becomes the cylinder axis. There are two directions of symmetry: along the axis (the 'toroidal' direction) and about the axis (the 'poloidal' direction).

DCU: Dublin City University, Ireland. Partner in the Association EURATOM-DCU.

DEMO: Demonstration Reactor (the first device in the European fusion strategy intended to produce significant amounts of electricity).

Deuterium: A stable isotope of hydrogen, whose nucleus contains one proton and one neutron. In heavy water, normal hydrogen is replaced by deuterium. Sea water contains, on average, 34g deuterium per m³. Deuterium plasmas are used routinely in present-day experiments; in a fusion power plant the plasma will consist of a mixture of deuterium and tritium which fuse more readily than two deuterium nuclei.

DG Research (DG RTD): The Directorate-General of the European Commission, Brussels, responsible for Research and Development. Formerly DG XII.

Diagnostic: Apparatus used for measuring one or more plasma quantities (temperature, density, current, etc.).

Diffusion, thermal (or particle): The random flow of heat (or particles) in the presence of a thermal (or density) gradient.

DIII-D: The largest operating US tokamak, run by General Atomics, San Diego. It has a flexible configuration and studies core and divertor physics with intense additional heating.

D-He³: Deuterium-³Helium: A potential fuel mix for fusion with low release of neutrons, but which would require a much higher fusion triple product ($nT\tau$) than DT to reach ignition. ³Helium is an isotope of helium which is not available in appreciable quantities on Earth.

Disruption, Disruptive instability: A complex phenomenon involving MHD instability which results in a rapid release of energy to the wall and strong electromechanical forces in a tokamak. Plasma control may be lost, triggering a VDE (q.v.). This phenomenon places a limit on the maximum density, pressure and current in a tokamak.

Distribution function: Describes both the space and velocity distribution of plasma particles.

Divertor: A magnetic field configuration with a separatrix, affecting the edge of the confinement region, designed to remove heat and particles from the plasma, i.e. divert impurities and helium ash to divertor plates in a target chamber. Alternative to using a limiter to define the plasma edge.

Double null: See Single/double null divertors.

Drift kinetic theory: Kinetic theory which describes plasma processes which have spatial scales much greater than the particle Larmor radii.

Drift orbits: Particle motion is tied to straight magnetic field lines. However, electric fields and gradients of the magnetic field give an additional drift perpendicular to the magnetic field creating drift surfaces displaced from the magnetic surfaces.

Driven current: Plasma current produced by a means external to the plasma, inductively or non-inductively.

Driver: In inertial confinement fusion, the laser or particle beam system used to compress a target pellet.

DTE: The deuterium-tritium experiment at JET which in 1997 set new records for fusion power production. Followed the Preliminary Tritium Experiment of 1991.

ECCD: Electron Cyclotron Current Drive. Non-inductive current drive technique using directed electron cyclotron resonance waves.

ECE: Electron Cyclotron Emission. Radiation emitted by electrons as a result of their cyclotron motion around magnetic field lines. Used to measure electron temperature.

ECH: Electron-Cyclotron Heating. Radio wave heating near the resonance frequency (or its multiple) of the electron gyration in a magnetic field. In present and future machines ECH is at typically 60-170GHz, depending on the magnetic field strength in a machine.

EFDA: European Fusion Development Agreement. The organisational framework of the EU fusion activities for the exploitation of the JET Facilities, international collaboration (including ITER) and supporting technology.

EFET: European Fusion Engineering & Technology; a fusion technology oriented European Economic Interest Grouping.

Electron temperature: A measure of electron thermal energy in units of degrees or electron volts (1eV ~ 10⁴ degrees Kelvin).

ELM: Edge localised mode. An instability which occurs in short periodic bursts during the H-mode in divertor tokamaks. It modulates and enhances the energy and particle transport at the plasma edge. These transient heat and particle losses could be damaging in a reactor.

ENEA: Ente per le Nuove Tecnologie, l'Energia e l'Ambiente, Italy. Partner in the Association EURATOM-ENEA.

Energetic particle: In terms of energy, the particles in a plasma can be divided into two classes. The more numerous thermal particles are characterised by a temperature typically in the range 1–30keV for modern tokamaks. The less numerous class of energetic particles has significantly higher energy up to several MeV. Energetic particles can be created by electric fields, fusion reactions, neutral beam injection or RF heating.

EPS: European Physical Society. Its Plasma Physics Division hosts the major European annual conference on Plasma Physics.

Error fields: The magnetic coils of a tokamak are designed to give the desired magnetic field configuration. The finite number of coils and imperfections in their construction lead to unwanted deviations from this configuration known as error fields. These could lead to disruptions and are of particular concern for larger tokamaks.

EXTRAP T-II: External Trap II, a medium-sized reversed field pinch (RFP) at the Royal Institute of Technology, Stockholm (Association EURATOM-NFR),

built for RFP transport and shell stabilisation studies in support of RFX.

EURATOM: European Atomic Energy Community.

Faraday rotation: The rotation of the plane of polarisation of light passing through a magnetised plasma.

Fast Alfvén wave: The fast Alfvén wave exists over a broad frequency spectrum, from the ion cyclotron range of frequencies (ICRF) where its character is electromagnetic, down to magnetohydrodynamic frequencies. Its velocity is comparable to the Alfvén velocity. The fast Alfvén wave is used routinely for high-power (~20MW) ICRF heating on JET, as it is efficiently absorbed in the plasma by the mechanism of ion cyclotron resonance. Although usually stable in tokamaks, the wave can be excited by energetic ion populations.

Fast wave current drive: Current drive produced by a fast wave. The wave can penetrate the plasma more easily than a lower hybrid wave.

Feedback: Use of measurements of plasma parameters to control the parameters, shape or profiles of the plasma to obtain desired conditions.

Field lines, Flux surfaces: Imaginary lines marking the direction of a force field. In a tokamak these define a set of nested toroidal surfaces, to which particles are approximately constrained, known as flux surfaces.

Field reversed configuration: A compact torus with a strongly elongated plasma. The plasma is contained in a cylindrical vessel inside a straight solenoid. The confining magnetic field usually has only a poloidal component. Not to be confused with reversed field pinch.

FIR: Far infra-red (e.g. wavelength ~ 0.2 to 1mm). FIR lasers are used to measure the magnetic field and plasma density.

"Fishbones": Rapid bursts of MHD activity sometimes observed when neutral beam heating is used in tokamaks (fishbone refers to the shape of the bursts in oscillating magnetic field when plotted as a function of time).

First wall: The first material boundary that surrounds the plasma. Today, the first wall in many machines is protected by low-Z materials (such as carbon tiles, boron or beryllium coating). Future tokamaks will require metallic walls.

Flat-top current: Constant current during quasi-stationary operating conditions.

Fokker-Planck Code: A computer code to calculate the velocity distribution of plasma particles allowing for collisional relaxation and plasma heating. Calculates distribution functions (q.v.).

FOM: Stichting voor Fundamenteel Onderzoek der Materie (Foundation for basic investigations of matter), The Netherlands. Partner in the Association EURATOM-FOM.

FTU: Frascati Tokamak Upgrade, a high density, high current tokamak at Frascati, Italy (Association EURATOM-ENEA).

Fusion triple product: Product of (ion) density, (ion) temperature and energy confinement time. A measure of the proximity to break-even and ignition.

Fusion product: The product of a fusion reaction, for example an α -particle or neutron in a deuterium-tritium plasma.

Fusion reactivity: Fusion reaction rate. For present typical tokamak conditions, it increases with the square of the density and the ion temperature of the plasma.

Full wave theory: Wave theory which includes complete accounting of wave energy (transmitted, reflected and absorbed, including energy transferred to other waves) for studying RF heating.

FZK: Forschungszentrum Karlsruhe, Germany. Partner in the Association EURATOM-FZK, active in fusion technology and, with the development of gyrotrons, in plasma engineering.

FZJ: Forschungszentrum Jülich GmbH, Germany. Partner in the Association EURATOM-FZJ, operating the tokamak TEXTOR.

GSI: Gesellschaft fuer Schwerionenforschung, Darmstadt, Germany. Studying heavy-ion physics, and driver physics with possible application for inertial confinement fusion.

Gyro-kinetic theory: Version of kinetic theory in which the Larmor radius is not assumed to be small. An essential theory for investigating fine-scale instabilities which might be responsible for driving turbulence, which may in turn be responsible for anomalous transport.

Gyrotron: Device used for generating high power microwaves in the electron cyclotron range of frequencies (50 - 200GHz). This UHF wave is mostly used to heat the plasma at the electron cyclotron resonance frequency. It also could be used to diagnose the plasma.

Heliac: Stellarator configuration with a central toroidal coil around which the plasma column is wound helically. Because of its high capability of investigating a wide range of stellarator configurations, it is used for TJ-II.

Helias: Optimised stellarator configuration, used with modular coils for Wendelstein VII-X (Germany) and SHEILA (Australia).

H-mode: A High confinement regime that has been observed in tokamak plasmas. It develops when a tokamak plasma is heated above a characteristic power threshold, which increases with density, magnetic field and machine size. It is characterised by a sharp temperature gradient near the edge (resulting in an edge "temperature pedestal"), ELMs and typically a doubling of the energy confinement time compared to the normal "L" regime. Today, a variety of high confinement modes have been identified in divertor and in limiter configurations (e.g. the I-mode), which, in part, have been obtained by special tailoring of the radial plasma current profile.

H-transition (or L-to-H transition): Transition into the H-regime from the L-regime, usually quite sudden, at a certain threshold power of additional heating and specific plasma parameters.

Halo currents: See Vertical Displacement Event.

Helicity injection: The helicity of a toroidal plasma is related to a linkage of toroidal and poloidal magnetic fluxes, and is approximately conserved throughout a discharge. If additional helicity can be injected, the plasma current could be sustained or even increased.

Helium ash: Fusion reactions in a deuterium-tritium plasma produce energetic α -particles (helium nuclei), which heat the plasma as they slow down. Once this has happened, the α -particles have no further use: they constitute helium ash, which dilutes the fuel and must be removed to maintain a burning plasma.

High beta (β): Condition in which the plasma energy is a significant fraction of the energy in the magnetic field. An alternative measure is the ratio between the

plasma energy and the energy in the poloidal magnetic field, the poloidal β .

High field ECH launch: Electron cyclotron waves can be launched from the inside of the plasma torus. This allows higher density plasma to be heated.

Hydrogen: The lightest element; the nucleus consists of only one proton, the atomic shell of one electron. Isotopes of hydrogen, with one or two additional neutrons in the nucleus, are deuterium and tritium respectively.

IAEA: International Atomic Energy Agency (of the United Nations), Vienna, Austria. The ITER-EDA is undertaken under the auspices of the IAEA.

ICE: Ion Cyclotron Emission. Observed in JET and TFTR as a suprathreshold signal, apparently driven by collective instability of energetic ion populations such as fusion products and injected beam ions.

ICF: Inertial Confinement Fusion. Intense beams of laser light or light or heavy ion beams are used to compress very rapidly and heat tiny target pellets of fusion fuel to initiate fusion burn in the centre. Sufficient fusion reactions must occur in the very short time before the fuel expands under its own pressure. The inertia of the pellet's own mass determines the time scale during which fusion reactions occur, hence the name inertial confinement.

Ideal: In the context of MHD, 'ideal' implies that the magnetic field and the plasma always move together. For this to occur, the electrical resistivity of the plasma must be negligible.

Ideal internal kink modes: An MHD instability of the central region of a tokamak. This, or its close relative the resistive internal kink mode, may be involved in the Sawtooth disruptions which occur in most Tokamaks.

IEA: International Energy Agency (of the OECD), Paris, France. Implementing agreements for international collaboration on specific topics in fusion have been set up in the frame of the IEA.

Ignition condition: Condition for self-sustaining fusion reactions: heat provided by fusion α -particles replaces the total heat losses. External sources of plasma heating are no longer necessary and the fusion reaction is self-sustaining. Ignition is not required for energy gain in a power station. Retaining a level of external heating or current drive will be required

to control the plasma pressure and current profiles, to optimise the performance, leading to a so-called "driven burn".

Impurities: Ions, other than the basic plasma ion species, which are unwanted as they lose energy by radiation and dilute the plasma.

Impurity screening: The prevention of impurities from entering the plasma.

Internal kink: A type of MHD instability that can occur within the central region of the plasma (where $q < 1$) reducing the peak temperature and density.

Internal Reconnection Event (IRE): An instability which breaks magnetic field lines and reconnects them with a different topology to reduce the system to a lower energy state - associated with the operating limits of spherical tokamaks.

Ion Bernstein wave: A wave which only exists in a hot plasma and is supported by the ions. It propagates at right angles to the magnetic field, when it is undamped, at harmonics of the ion cyclotron frequency. There is also an electron Bernstein wave which propagates at harmonics of the electron cyclotron frequency.

Ion Cyclotron Current Drive (ICCD): Non-inductive current drive using ICRH.

Ion Cyclotron Resonance Heating (ICRH)/Ion Cyclotron Resonance Frequencies (ICRF): Additional heating method using RF waves at frequencies (~20-50MHz) matching the frequency at which ions gyrate around the magnetic field lines.

IPP: Max-Planck-Institut fuer Plasmaphysik, Garching, Germany. Partner in the Association EURATOM-IPP, operating the tokamak ASDEX-Upgrade and the stellarator Wendelstein VII-AS. Also has sites in Berlin and in Greifswald, where the construction of the large superconducting stellarator Wendelstein VII-X is in progress. The name is also used for the Czech Republic Association.

IR: Infra Red part of the electromagnetic spectrum.

IRE: Internal Reconnection Event.

IST: Instituto Superior Técnico, Portugal. Partner in the Association EURATOM-IST.

ISTTOK: Tokamak, for study of non-inductive current drive, at the Instituto Superior Técnico (IST), Lisbon, Portugal.

ITER: International Thermonuclear Experimental Reactor (the next step as a

collaboration between EURATOM, Japan, China, India, Korea, the Russian Federation and the USA, under the auspices of the IAEA). After a conceptual design phase - CDA (1988-1990), and engineering design activities (ITER-EDA, 1992-2001), now under the Coordinated Technical Activities (CTA).

JAEC: Japan Atomic Energy Commission, Tokyo, Japan.

JAEA: Japan Atomic Energy Agency. Headquarters in Tokyo, Japan.

JET: Joint European Torus. The largest tokamak in the world, sited at Abingdon, UK. Operated as a Joint Undertaking (JET Joint Undertaking), until the end of 1999. The scientific exploitation of the JET facilities is now guaranteed by the Euratom fusion Associations within the EFDA framework. The operation of the facility is the responsibility of the Association Euratom-UKAEA.

JT-60U: Japanese tokamak at Naka. The largest Japanese tokamak and second largest operating experiment after JET, but not designed for use with D-T fuel.

keV: Kilo-electronvolt. Energy which an electron acquires passing a voltage difference of 1000 volts. Also used to measure the temperature of a plasma (1 keV corresponds to 11.8 million degrees Kelvin).

Kinetic instability: Oscillation which is unstable as a result of the energy distribution of ions or electrons.

Kinetic theory: A detailed mathematical model of a plasma in which trajectories of electrons and ions are described. More complex than fluid and two-fluid theories, it is necessary in the study of RF heating and some instabilities, particularly when energetic particles are involved.

L-H transition: Change from L regime to H regime (usually quite sudden).

L-mode: As opposed to the H mode. Regime with degradation of confinement, in additionally heated plasmas, with respect to plasmas heated ohmically by the plasma current.

Langmuir probe: Electrical probe inserted into the edge of a plasma for measurements of density, temperature and electric potential.

Larmor radius: Radius of the gyrotory motion of particles around magnetic field lines.

Large scale ideal modes: A large scale mode has a wavelength which is a significant fraction of the plasma dimensions and assumes ideal MHD.

Laser ablation: Use of lasers to produce a sudden influx of impurities into the plasma from a solid surface.

Last closed flux surface: The boundary separating those magnetic field lines that intersect the wall (open lines) from the magnetic field lines that never intersect the wall (closed lines).

Lawson criterion: The value of the confinement time multiplied by the ion density (at the required temperature) which must be exceeded in a fusion reactor to reach ignition.

Limiter: A material surface within the tokamak vessel which defines the edge of the plasma and thus avoids contact between the plasma and the vessel. A pumped limiter can also be used to remove heat and particles and is an alternative exhaust system to the divertor.

LLNL: Lawrence Livermore National Laboratory, Livermore, USA.

Locked modes: MHD modes that cease rotating (though they can still grow).

Low-activation materials: Materials which do not develop high, long-lived radioactivity under neutron irradiation.

Low aspect ratio: Low ratio of major to minor radius of the torus.

Lower hybrid current drive (LHCD): Non-inductive current drive using lower hybrid waves.

Lower hybrid heating (LHRH): Plasma heating by radio frequency waves at the "lower hybrid" resonance frequency in the plasma. Typical frequencies are a few GHz.

Lower hybrid (LH) wave: A plasma wave of frequency between the ion and electron cyclotron frequencies. It has a component of electric field parallel to the magnetic field, so it can accelerate electrons moving along the field lines.

Magnetic axis: The magnetic surfaces of a tokamak form a series of nested tori. The central 'torus' defines the magnetic axis.

Magnetic Confinement Fusion (MCF): Confinement and thermal insulation of a plasma within the reactor core volume by the action of magnetic fields. In toroidal magnetic confinement, usually both toroidal and poloidal components of the magnetic field are needed (the field lines are

threaded like the filaments of a cable which is bent into a ring).

Magnetic islands: Islands in the magnetic field structure caused either by externally applied fields or internally by unstable current or pressure gradients. See tearing magnetic islands.

Magnetic surfaces (flux surfaces): In toroidal magnetic confinement, the magnetic field lines lie on nested toroidal surfaces. The plasma pressure, but not the amplitude of the magnetic field, is a constant on each magnetic surface.

Magneto-acoustic cyclotron instability: This instability results from an exchange of energy between the fast Alfvén wave (or magneto-acoustic wave) and an ion Bernstein wave which has a source of free energy through the presence of a population of energetic (non-thermal) ions, e.g. fusion products. The instability occurs for propagation perpendicular to the equilibrium magnetic field.

Major radius: The distance from the tokamak symmetry axis to the plasma centre.

Marfe: A localised and radiating thermal instability sometimes observed near the edge of tokamak plasmas.

Marginal Stability: Close to the transition from stability to instability.

MAST: Mega Amp Spherical Tokamak at Culham (Association EURATOM-UKAEA), twice as big as START. Began operation in 1999.

MeV: Mega-electronvolt, unit for nuclear energies. Energy which an electron acquires passing a voltage difference of 1 million volts.

MHD (Magnetohydrodynamics): A mathematical description of the plasma and magnetic field, which treats the plasma as an electrically conducting fluid. Often used to describe the bulk, relatively large-scale, properties of a plasma.

MHD instabilities: Unstable distortions of the shape of the plasma/magnetic field system.

Microinstabilities: Instabilities with characteristic wave-lengths similar to the ion Larmor radii, rather than to the tokamak dimensions. These are thought to be responsible for the fine scale turbulence in tokamaks, and hence anomalous transport.

Minor radius: Half the small diameter of the tyre-shaped toroid.

Mirnov coils: Pick-up coils at the edge of the plasma for measuring the time variation of magnetic fields arising from instabilities.

Mirror: A linear magnetic confinement concept with a weaker magnetic field in a central region and with strong fields at both ends which reflect contained particles by the mirror effect. Some variants exist to increase the magnetic field in all directions from the centre or to improve the closure of the bottlenecks. The Tandem Mirror confinement concept also involves electrostatic fields.

MIT: Massachusetts Institute of Technology, Boston, USA. Operates the high-field divertor tokamak ALCATOR C-MOD.

Mode: A resonant wave or oscillation in a plasma. Also used as a synonym for an operating regime.

Mode number: Characterises the wavelength of a mode normalised to the device size.

Monte Carlo code: A statistical technique used in numerical calculations where events may occur many times, each with a certain probability.

Motional Start Effect (MSE): The measurement of shifts and splitting of spectral lines emitted from particles moving in a local electric field. This can be interpreted to give the local magnetic field inside the tokamak if the particle velocity is known, and is a major diagnostic on some tokamaks to deduce the current profile.

MPG: Max-Planck-Institut fuer Quantenoptik, Garching, Germany. Active, within its programme, in ICF (laser fusion) related physics. Partially supported by Euratom, for a "keep in touch activity" in ICF.

Negative ion beam: To produce neutral beams, negative ions (obtained by the addition of electrons to neutral atoms) are accelerated and then neutralised before entering the plasma. The efficiency of creating neutral beams from positive ions is too low at the beam energy required for a fusion power station, of the order of 1 MeV.

Neo-classical theory: Classical collisional plasma transport theory, corrected for toroidal effects. The neoclassical theory predicts the existence of the bootstrap current.

Neo-classical tearing mode: The magnetic island produced by a tearing mode perturbs the bootstrap current which further amplifies the island and degrades confinement or leads to a disruption.

NET: Next European Torus, a design for the Next Step which had been prepared by the NET team (located at the Association EURATOM- IPP in Garching) and which largely influenced the ITER design.

Neural network: A computer algorithm that uses incoming data to derive plasma parameters, having previously been "trained" on a series of examples of a non-linear input-output mapping.

Neutrons: Neutral particles in the nucleus. Products of Deuterium-Tritium and other fusion reactions.

Neutral beams: Since charged particles cannot easily penetrate the magnetic confinement fields of the plasma, high energy beams of neutral atoms are injected into the plasma for fuelling, heating and current drive. Within the plasma, the atoms of the beam are ionized and are then confined.

Neutron multiplier: The fusion of deuterium and tritium consumes one tritium nucleus per reaction, producing one neutron. Since in the blanket of a power station not every neutron reacts with lithium to produce a new tritium atom, a neutron multiplying element may be used in the blanket to enhance the tritium production so as to make the power station self-sufficient in tritium supply.

Next Step: The next experimental device in the strategy of the European Fusion Programme. Presently pursued via the ITER EDA, with a European activity as a fall-back option. The generic name for an experimental reactor with a long pulse burning plasma at high fusion gain.

NFR: Naturvetenskapliga Forskningsrådet (Natural Science Council), Sweden. Partner in the Association EURATOM-NFR.

NIFS: National Institute for Fusion Science, Nagoya, Japan.

NRIM: National Research Institute for Metals, Sakura-mura, Japan.

Non-inductive heating and current drive: See additional heating and current drive.

NSTX: Spherical tokamak at Princeton, USA. A similar size to MAST, but of different design. Started operation in 1999.

Ohmic heating (OH): The resistive heating resulting from a current flowing within the plasma corresponding to the heating of a wire by a current flowing through it. Ohmic heating in a tokamak is insufficient to reach thermonuclear temperatures since, contrary to a wire, the resistance of a plasma decreases strongly with increasing temperature, thus making Ohmic heating weak at high temperatures.

ORNL: Oak Ridge National Laboratory, USA.

Operating limits: See tokamak operating boundaries.

Optimised shear: Adjusting the current profile to optimise tokamak.

PbLi: Eutectic lithium-lead alloy considered for use as blanket breeding material.

Peeling mode: An edge MHD instability which exists when the current density at the plasma edge is non-zero. It may be associated with ELMs.

Pellet: In inertial confinement concepts, the fuel is contained in tiny spheres, called pellets, which are compressed by laser or particle beams. In magnetic fusion, pellets of frozen hydrogen, deuterium, tritium, accelerated up to several kilometres per second, are used to refuel the plasma and to obtain very high densities.

PIREX: Proton Irradiation Experiment, material test facility (Association Euratom-Switzerland, CRPP-FT, PSI, Villigen, CH).

Plasma: State of matter above a few thousand degrees where atoms are broken into their constituents, ions and electrons, thereby creating an electrically conducting medium. Plasmas can therefore interact strongly with electric and magnetic fields.

Plasma confinement: Retention of plasma energy or particles within a given region, including the heat and particle losses from the plasma.

Plasma parameters: Physical quantities which characterise the plasma and which must be measured experimentally, such as current, density, temperature, confinement time, β .

Plasma pressure: Proportional to the product of plasma density and temperature. There is an electron and an ion pressure and the plasma pressure is the sum of the two. In magnetic

confinement devices, this pressure is counterbalanced by magnetic pressure.

Plasma shape: Describes the plasma vertical cross-section, circular, elongated, D-shape, diverted, single null, double null.

Polarimetry: Measurement of the rotation of the plane of polarisation of light passing through a magnetically confined plasma; used to measure the local magnetic field and thus the safety factor (see Faraday rotation).

Poloidal field: Component of the magnetic field perpendicular to the toroidal direction and the major radius. The poloidal field is essential for confinement and is generated in a tokamak by the plasma current and the external coils.

Power threshold: The L-H transition and improved performance regimes related to reversed shear occur when the power exceeds a certain threshold value - the power threshold.

PPPL: Princeton Plasma Physics Laboratory, New Jersey, USA.

Preliminary Tritium Experiment (PTE): Three plasma discharges on JET, November 1991, into which a significant amount of tritium was injected for the first time in a tokamak. The power liberated from fusion reactions (~ 2MW for ~ 2 seconds) was in accordance with expectations. Followed by the more ambitious DTE in 1997.

Profile: Variation of plasma parameters with minor radius.

Profile control: Controlling the profiles of pressure, density or current, in order to control instabilities.

PSI: Paul-Scherrer-Institut, Villigen, Switzerland, active, in muon physics among others fields. The Association EURATOM-Swiss Confederation has their fusion technology activities working in superconductor and materials technology located at Villigen.

Pumped divertor: Divertor field lines directed into a pumped chamber surrounding the target plate.

q, q_{95} : See Safety factor.

Q: Ratio of fusion power to total additional heating power. At $Q=\infty$, no external power is required and the plasma is said to be ignited. A power station

should operate with $Q\sim 50$ to be economical.

Radial electric field: Arises when there is a charge imbalance in the plasma.

Radio frequency (RF) heating: Heating with waves in the radiofrequency range at resonance frequencies of the plasma (see ECH, ICRH, LHH).

Reflectometry: Use of reflected microwaves to measure plasma density.

Relaxation: The evolution of a plasma to a lower energy state.

Resistive ballooning modes: A class of ballooning mode which would be stable in the absence of resistivity, but can be unstable in its presence. Related to tearing modes, but topologically different.

Resistive instability: Instability due to diffusion and rearrangement of magnetic field lines. When the plasma resistivity is small, these instabilities have a slow growth rate.

Resistivity: The tendency to resist the flow of electric current, thereby dissipating energy. Plasmas are very good conductors of electric current, so that their resistivity can often be neglected. In this case, 'ideal' magnetohydrodynamics may be applied.

Resonant ions/electrons: Resonance occurs when one of the characteristic frequencies of particle motion in the plasma (for example, the cyclotron frequency) matches the frequency of some applied perturbation (for example, an RF wave).

Resonant magnetic perturbation (RMP): An externally applied magnetic perturbation matched to the spatial structure and optionally the frequency and phase of an instability.

Reverse Field Pinch (RFP): A toroidal magnetic confinement device, similar to a tokamak, in which the poloidal and toroidal fields are of comparable magnitude. Capable of higher plasma current and pressure for a given external magnetic field. They require a conducting shell close to the plasma for stabilisation.

Reverse (magnetic) shear: In a tokamak the current density is usually greatest at the magnetic axis, in which case the safety factor increases from the centre to the edge of the plasma. Using non-inductive current drive and/or the bootstrap current the current density can be made to increase away from the centre. In this "reverse shear" case, the safety factor has a minimum away from the plasma centre.

Using reverse or low shear ("optimised shear") some tokamaks, notably DIII-D and TFTR in the US and more recently JT-60U in Japan and JET, have shown greatly improved plasma performance. Reverse shear is an attractive option for advanced tokamak scenarios.

RF: Radio-Frequency.

RFX: Reversed Field pinch Experiment at CNR-Padova, Italy (Association EURATOM-ENEA).

RISØ: Forskningscenter Risø, Denmark. Partner in the Association EURATOM-RISØ.

Rotational transform: Measure of the ratio of poloidal to toroidal flux defining the pitch of the helical field lines. The q -value of the tokamak is proportional to the reciprocal of the rotational transform.

RTP: Rijnhuizen Tokamak PETULA, for study of transport in a plasma, at Nieuwegein (Rijnhuizen), the Netherlands (Association EURATOM-FOM). Ceased operation in 1998, the activities of the Association being transferred to TEXTOR, as part of the Tri-lateral Euregio Cluster.

Runaway electron: An electron with a very high energy has a decreasing probability of colliding with another charged particle and of losing its energy. Such a particle then gains more and more energy in the electric field of a tokamak, reaching 10's of MeV.

Safety factor: Number of turns the helical magnetic field lines in a tokamak make round the major circumference for each turn round the minor circumference, denoted q . Has no connection with the ordinary sense of "safety" other than $q=1$ surfaces are ideally unstable. For diverted plasmas q goes to infinity at the separatrix, so instead q_{95} is used to describe the safety factor near the edge, which is the safety factor of the plasma surface which contains 95% of the poloidal flux.

Sawtooth: A cyclically recurring instability which causes an energy loss from the central region of tokamak discharges. The temperature periodically falls abruptly, then slowly recovers. The jagged trace produced by plotting temperature against time gives the instability its name.

Sawtooth crash: The rapid collapse of the central temperature in a tokamak during a sawtooth cycle.

Scaling laws: Empirical or theoretical expressions for how various plasma phenomena (eg confinement, power threshold, etc) vary with tokamak parameters. They are particularly used for predicting the performance of future tokamaks.

Scrape-off-layer (SOL): The residual plasma between the "edge" of the plasma (defined by the limiter radius or the separatrix) and the tokamak vessel wall.

Semi-empirical: A theoretical approach in which the behaviour of some key quantities is deduced from experiment, rather than a priori.

SEAFP: The Safety and Environmental Assessment of Fusion Power is an extensive study conducted by several teams in the associated laboratories, NET, industry and the JRC, published in June 1995.

SEAL: The Safety and Environmental Assessment of Fusion Power Long-term is a programme, launched in 1995, being undertaken for the European Commission in the framework of the Fusion Programme.

Separatrix: Magnetic surface at which the rotational transform vanishes and the safety factor becomes infinite.

Shear: The safety factor usually varies from magnetic surface to magnetic surface across the plasma cross-section; this variation is measured by the non-dimensional quantity called "shear". Also refers to the variation of plasma flow (flow shear). If the type of shear is not specified, it usually means magnetic shear.

Single/double null: Points of zero poloidal magnetic field where the separatrix crosses itself are the X-points or nulls. Usually sited above and/or below the plasma. Tokamak divertor configurations have either one or two nulls.

Single fluid model: The set of equations which represent a plasma as a magnetised, electrically conducting fluid with the usual fluid properties of viscosity, thermal conductivity, etc. The possibility of distinct behaviour of electrons and ions (i.e. 2 "fluids") is excluded.

Small aspect ratio: Same as Low aspect ratio.

Spectroscopy: The detection and analysis of the spectrum of radiation emitted by a plasma. This can yield information about temperatures, impurities, rotation, using different parts of the electromagnetic spectrum (IR, visible, VUV, XUV, etc.)

Spherical tokamak (ST): A very low aspect ratio tokamak - it appears almost spherical, though topologically it remains a torus with a centre column. The spherical tokamak is being further investigated, with larger experiments, MAST and NSTX.

Spheromak: A spherical plasma in which comparable toroidal and poloidal currents flow. The toroidal current is not driven by transformer action.

Stability theory: The theory of how small perturbations to a system evolve in time. Spontaneous growth is due to instability. Instabilities can saturate at some small amplitude, in which case they may degrade confinement, or grow uncontrollably, in which case the equilibrium is lost leading to a disruption.

START: Small Tight Aspect Ratio Tokamak, a "spherical" tokamak with a very small aspect ratio at the Association EURATOM-UKAEA (Culham). This very fat ring-shaped configuration showed experimentally a lesser tendency to disruptions and is efficient in its use of magnetic energy. Ceased operation in 1998, replaced by MAST.

Start-up assist: Assisting plasma formation to cross a range of plasma temperature at which impurities radiate strongly, with the aim of minimising the start-up delay and transformer requirements, usually using ECH.

STAC: Scientific and Technical Advisory Committee set up by EURATOM.

Steady state power plant: A continuously (as opposed to cyclically) operated power plant.

Stellarator: Closed configuration having the shape of a three-dimensionally distorted ring in which the plasma is confined principally by an externally generated magnetic field (produced by non-planar coils outside the plasma vessel). The coils can be arranged in a modular fashion. Stellarators do not need a transformer; they need an additional heating system for the plasma start-up. Due to the fact that no toroidal plasma current is needed to maintain the confinement configuration, they naturally provide steady state operation.

SULTAN: Supra Leiter Test Anlage. Large Superconductor Test Facility, CRPP at PSI Villigen, Switzerland (Association EURATOM-Swiss Confederation).

Super Alfvénic velocity: A velocity greater than the Alfvén velocity. In a tokamak, only energetic particles have super Alfvénic velocities; because they satisfy this condition, they may resonantly transfer their energy to magnetohydrodynamic modes, which may grow as a result (eg TAE modes).

Suprathermal radiation: Electromagnetic radiation produced by energetic particles, as opposed to thermal particles.

Survey spectrometer: An instrument which gives information concerning the radiated spectrum over a large range of frequencies.

TAE modes: Toroidal Alfvén Eigenmodes. One class of Alfvén gap modes.

Target plates: See Divertor.

TCV: "Tokamak à Configuration Variable", for study of elongated and strongly shaped plasmas, at Lausanne, Switzerland (Association EURATOM-Swiss Confédération).

TEKES: Technology Centre Finland. Partner in the Association EURATOM-TEKES.

Tearing magnetic islands: The disturbance caused by a tearing mode which alters the topology of the confining magnetic field and causes transfer of heat across the affected region.

Tearing mode: A class of resistive MHD instability which has been predicted theoretically in tokamaks and positively identified in experiments.

Temperature pedestal: In an H-mode discharge there is a region of steep temperature gradient at the plasma edge. The temperature at the top of this steep gradient region is the temperature pedestal.

Tesla: Unit of magnetic field strength (more exactly the magnetic induction). $1T = 1Vs/m^2 = 10,000Gauss$.

TEXTOR: Torus Experiment for Technology Oriented Research. Tokamak at Jülich, Germany (Association EURATOM-FZJ). Refurbished and upgraded, in 1994, as TEXTOR-94.

TFTR: "Tokamak Fusion Test Reactor" at Princeton, the largest US device with a major campaign using deuterium-tritium fuel from 1993 - 1997. Ceased operation in March 1997.

Thermal cycling: Successive heating and cooling of materials can lead to cracks or

rupture, particularly at boundaries between materials that expand at different rates.

Thermal particles: As a result of collisional energy exchange, the energy of most plasma particles falls within a Maxwellian distribution which is described by a single temperature (typically 1-30keV for tokamaks). These are the thermal particles, as distinct from energetic particles which lie outside the thermal distribution.

Thomson scattering diagnostic: Diagnostic to measure temperature and density by detecting laser light scattered and Doppler shifted by the thermal plasma electrons.

Tight aspect ratio: Same as Low aspect ratio.

TJ-II: A heliac stellarator at Madrid, Spain (Association EURATOM-CIEMAT). (TJ-IU was a torsatron at CIEMAT, built and operated in preparation for TJ-II).

Tokamak: Magnetic configuration with the shape of a torus. The plasma is stabilised by a strong toroidal magnetic field. The poloidal component of the magnetic field is produced by an electrical current flowing toroidally in the plasma. This current is induced via transformer action and, for steady state, must be maintained by non-inductive current drive and by self-generation of bootstrap current inside the plasma.

Tokamak operating boundaries: The set of plasma parameters, beyond which it is impossible to operate a tokamak. Careful choice of plasma cross-sectional shapes and current and pressure profiles can increase the operating regime.

TORE SUPRA: Large tokamak with superconducting toroidal magnetic field coils and a circular plasma cross-section at the Association EURATOM-CEA in Cadarache, France. It features long high total energy plasmas.

Toroidal Alfvén Eigenmodes: See TAE modes.

Toroidal field: The component of the magnetic field along the major circumference of the torus. The largest magnetic field component in a tokamak.

Toroidal stability: Stability analysis taking account of effects due to the toroidal geometry. These are sometimes neglected to identify possible instabilities,

but must usually be included for accurate predictions of stability boundaries.

Toroidal turbulence code: A turbulence code which includes effects due to the toroidal geometry.

TOSKA: Large testing facility for superconductors (Association EURATOM-FZK, Karlsruhe, Germany).

Transformer drive: The use of a transformer action to induce plasma current.

Transport: The processes by which particles and energy move across magnetic surfaces.

Transport barrier: In certain operational scenarios (e.g. the H-mode or ITB-mode) a region of low transport exists giving rise to a steep local pressure gradient. Such a region is referred to as a transport barrier.

Transport scaling: The magnitude of heat transport may be expressed, empirically or theoretically, in terms of a simple functional dependence on a few plasma parameters. This allows us to model how the heat transport varies (scales) in response to changes in the value of these parameters.

Trapped particles: The outside (large major radius) of a tokamak plasma has a lower magnetic field than the inside. Particles with low velocity parallel to the magnetic field compared with the velocity perpendicular to the magnetic field may not enter the higher field (inside) region and become trapped on the outside. They are not free to circulate toroidally but instead bounce back and forth, performing so-called banana orbits.

Tri-lateral Euregio Cluster (TEC): A collaboration between the Associations Euratom-FZJ, -FOM and -Etat Belge, to exploit the TEXTOR tokamak at FZJ, Julich, Germany.

Tritium: An isotope of hydrogen, whose nucleus consists of one proton and two neutrons. Tritium is unstable to radioactive decay with a half-life of 12.3 years. Due to its rapid decay, tritium is almost absent on earth. For a fusion reactor, tritium will be produced in the breeding blanket surrounding the core of a fusion power station. Special tritium-handling technology is required whenever the use of deuterium-tritium plasmas is contemplated and has been developed on TFTR and JET.

Tritium inventory: The amount of tritium contained in a fusion power station or in a specified part of it.

Turbulence: Randomly fluctuating, as opposed to coherent, wave action. For example, the turbulent water beneath a waterfall can only be described in terms of its averaged properties, such as the scale and duration of fluctuations; whereas a more systematic description can be given to waves on the surface of a still pond.

Turbulent transport: Anomalous heat transport associated with plasma turbulence.

Two-fluid model and multi-fluid model: The extended set of equations which represent a plasma as interpenetrating and interacting fluids of electrons and ions, impurity ions etc.

UKAEA: United Kingdom Atomic Energy Authority. Partner in the Association EURATOM-UKAEA which operates the tokamak COMPASS-D and the spherical tokamak MAST. Also charged with the operation of the JET facilities under EFDA.

Vertical Displacement Event (VDE): An event which arises when control of the plasma is lost and the plasma moves vertically. It can lead to a "halo current" in components which surround the plasma resulting in large, potentially damaging, forces on these components. The forces are much larger in larger tokamaks and are therefore of particular concern for JET and ITER.

VUV: The "Vacuum Ultra Violet" range of the electromagnetic spectrum.

Warm plasma refuelling: Fuelling of plasma using medium energy particles or particle clusters.

WEC: World Energy Council.

WENDELSTEIN VII-AS: Advanced stellarator, at Garching, Germany (Association EURATOM-IPP).

WENDELSTEIN VII-X: Large advanced superconducting stellarator, optimised to produce a reactor-relevant plasma configuration, designed at Garching. Construction is in progress at Greifswald, Germany (Association EURATOM-IPP).

X-point: See single/double null.

XUV: The "Extreme Ultra Violet" range of the electromagnetic spectrum. Shorter wavelengths than VUV.

Acknowledgement: This glossary was adapted from the "Glossary of fusion terms" by UKAEA Culham, UK, and from the glossary of "Fusion programme evaluation", 1996, EUR 17521, European Commission.

APPENDIX G Sources of Financial Support

The work carried out at the CRPP and presented in this annual report was financed from several sources. The major financial support is provided by the Ecole Polytechnique Fédérale de Lausanne (EPFL), EURATOM, the Paul Scherrer Institute (PSI), which hosts the supraconductivity and materials science activities, and the Swiss National Science Foundation and the Centre de Compétence "Energie-Mobilité" of the CEPF. Other public and private organisations which contributed funding for our research in 2007 include, in alphabetical order: Charmilles SA., OC Oerlikon, Ruag, the Secrétariat d'Etat à l'Education et à la Recherche (SER), Sulzer Metco AG, the Swiss Commission pour la Technologie et l'Innovation (CTI), Swiss Electric AG, Tetra Pak SA and Unaxis Balzers.

The CRPP is the Host of Euratom Fellows:

- Dr. I. Pagonakis whose fellowship is entitled *"Design of the collector system for the coaxial gyrotron 170GHz/2MW/CW"*,
- Dr. J. Paley, whose fellowship is entitled *"Real-time control of multi-beam ECRH-ECCD in the TCV tokamak"*,
- Dr. P. Ricci, whose fellowship is entitled *"Plasma turbulence: comparison between theory simulations and the basic plasma physics experiments TORPEX"*, and
- Dr. G. Turri, whose fellowship is entitled *"MHD spectroscopy in the TCV tokamak, in particular to determine current density profiles"*.
- MM. A. Collazos and M. da Silva, EC-TECH "Electron cyclotron system technology for ITER"
- F. Cau, M. Bagnasco, MATEFU "Magnet Technology for Fusion"